

ABSTRACT

Title of Dissertation: BROADBAND OBSERVATIONS
 OF GAMMA-RAY BURSTS
 AND FAST RADIO BURSTS:
 ENERGETICS, AFTERGLOWS,
 AND PHYSICAL ORIGINS

Virginia A. Cunningham
Doctor of Philosophy, 2021

Dissertation Directed by: Dr. Brad Cenko
 NASA Goddard Space Flight Center

Long gamma-ray bursts (GRBs) are produced during the deaths of massive stars. They are the most powerful explosions known in the Universe and release most of their energy via a narrow cone of emission. The long-lived afterglows of the brightest GRBs detected by the *Fermi* Large Area Telescope (LAT) are visible from radio to gamma-rays, and this relative abundance of broadband data makes them excellent tools for constraining theoretical models regarding their origins. Here, we use our sample of bright GRBs to test emission models beyond the canonical on-axis, top-hat jet model which has historically been applied throughout the literature. We demonstrate that many GRBs are likely to produce emission via a structured jet. We also find that derived physical parameters are highly dependent upon the fraction, ξ , of electrons which contribute to the synchrotron emission. Our findings for ξ are contrary to what is generally assumed during GRB modeling ($\xi = 1.0$), but consistent with theoretical simulations which predict lower values. Lower pre-

dictions for ξ would impact our current understanding of GRBs, implying denser environments and higher energetics than commonly assumed.

Fast radio bursts (FRBs) are extremely bright, short-duration pulses at radio frequencies that were only confirmed as true astrophysical sources a decade ago. Although the field has experienced major leaps in recent years, many questions regarding their progenitors and emission processes remain. The identification of counterparts at higher energies is critical to understanding the physical origins of FRBs. Here, we report on an archival search of previously identified FRBs with the *Fermi* Gamma-ray Burst Monitor (GBM), the *Fermi*-LAT, and the *Swift* Burst Alert Telescope (BAT). We find no significant X-ray or gamma-ray counterparts but report upper limits on the high-energy fluence, f_γ , for each FRB in our sample. We also report lower limits on the ratio of radio to high-energy fluence (f_r/f_γ). We discuss the implications of our results on several FRB progenitor theories, including pulsar-like analogs and magnetar flares.

BROADBAND OBSERVATIONS OF GAMMA-RAY
BURSTS AND FAST RADIO BURSTS: ENERGETICS,
AFTERGLOWS, AND PHYSICAL ORIGINS

by

Virginia A. Cunningham

Dissertation submitted to the Faculty of the Graduate School of the
University of Maryland, College Park in partial fulfillment
of the requirements for the degree of
Doctor of Philosophy
2021

Advisory Committee:

Dr. Brad Cenko, Advisor/Co-Chair

Professor Stuart Vogel, Co-Chair

Professor Jordan Goodman, Dean's Representative

Professor Cole Miller

Dr. Geoff Ryan

Professor Alexander van der Horst

© Copyright by
Virginia A. Cunningham
2021

Preface

A portion of the research presented within this dissertation has been previously published. Chapter 2 is presented with only minimal modification since appearing in the *Astrophysical Journal* (ApJ) as “A Search for High-Energy Counterparts to Fast Radio Bursts” ([Cunningham et al., 2019](#)). Chapter 3 is also presented with minimal modification since appearing in ApJ as “GRB 160625B: Evidence for a Gaussian-shaped Jet” ([Cunningham et al., 2020](#)).

Dedication

I dedicate this thesis to my parents, who have never wavered in their support and enthusiasm in all my endeavors.

Acknowledgments

The final product that is this thesis is not mine alone, but can also be credited to those who have helped shape me into the person I am today.

First, I would like to thank my NASA Goddard advisor, Dr. Brad Cenko. I appreciate that he always made me feel like a priority despite the impressive number of projects in which he is constantly involved. Brad is one of the sharpest, yet also laid-back and funniest, people I know. I aspire to one day master his ability to be both incredibly efficient and completely nonchalant about it at the same time.

I would also like to thank my UMD advisor, Professor Stuart Vogel. Stuart is one of the most kind, encouraging, and supportive mentors I have ever had. He does so much for the department and I am glad to have had him in my corner. I am also especially grateful for his patience in answering my many, many CASA questions.

Dr. Geoff Ryan has been a phenomenal source of knowledge. I can always count on him to kindly break down complex theoretical topics in simple enough terms for even an observer like me to understand completely.

Thank you to Professor Cole Miller who has been a part of my thesis committee since the beginning. His enthusiasm for astronomy is inspiring and the courses I had with him were amongst some of the most useful that I have had throughout graduate school.

Of course I would not have accomplished any of this without the support of my parents and sisters. My parents instilled a love of learning and independence in me that has prepared me well for any path in life.

I would also like to thank my Aunt and Uncle for adopting me while I lived in Maryland. Having family nearby (and home-cooked meals!) meant the world to me.

All of the other graduate students made UMD such a fun place. It is hard to imagine what the past six years would have been like without all the happy hours, astro parties, road trips, late-night study breaks at Denny's, and all the adventures we had at conferences. I am so glad that I have gotten to share this journey with you all.

Thank you to the business office and professional staff at UMD who always keep things running so smoothly. I appreciated how friendly and accessible everyone is, they really made dealing with all those administrative and bureaucratic issues as painless as possible.

Lastly, I want to thank Tyler and Little Bear for keeping me sane and well-loved the last few years. Tyler kept me full of laughs and pasta and my cat, Little Bear, probably deserves co-author status on this thesis since she sat in my lap throughout almost its entire creation. Not even my thesis committee will spend more time looking at this document than she did.

Table of Contents

Preface	ii
Dedication	iii
Acknowledgements	iv
Table of Contents	vi
List of Tables	ix
List of Figures	x
List of Abbreviations	xii
Chapter 1: Introduction	1
1.1 Gamma-ray Bursts	1
1.1.1 History and Background	1
1.1.2 Observational Properties	3
1.1.3 Theoretical Considerations	9
1.2 Fast Radio Bursts	20
1.2.1 History and Background	20
1.2.2 Observational Properties	23
1.2.3 Theoretical Considerations	27
1.3 Connections between FRBs and GRBs	29
1.4 Thesis Overview	31
Chapter 2: A Search for High-Energy Counterparts to Fast Radio Bursts	35
2.1 Introduction	35
2.2 Data and Results	41
2.2.1 <i>Fermi</i> -GBM	42
2.2.2 <i>Fermi</i> -LAT	45
2.2.3 <i>Swift</i> -BAT	47
2.3 Analysis and Interpretation	54
2.3.1 Limits on the Ratio of Radio to Gamma-ray Fluence	54
2.3.2 Constraints on Theoretical Models	57
2.4 Conclusions	66

Chapter 3: GRB 160625B: Evidence for a Gaussian-Shaped Jet	69
3.1 Introduction	70
3.2 Observations and Data Reduction	74
3.2.1 Gamma-ray	74
3.2.2 X-ray	75
3.2.3 Optical	76
3.2.4 Radio	77
3.3 Afterglow Modeling	79
3.3.1 Basic Tenets	79
3.3.2 <code>Afterglowpy</code> Package	81
3.4 Discussion	89
3.4.1 Comparison to Past Works	89
3.4.2 Model Comparison with WAIC	92
3.4.3 The Participation Fraction, ξ	93
3.4.4 Sharp Edge Effects on p	94
3.4.5 Viewing Angle Effects	95
3.4.6 Local Circumburst Environment	97
3.4.7 Energetics and Central Engine	100
3.5 Conclusions	101
 Chapter 4: The Afterglows of <i>Fermi</i> -LAT GRBs: Jet Structure, Energetics, and Physical Origins	 105
4.1 Introduction	106
4.2 Observations and Data Reduction	108
4.2.1 GRB 090902B	111
4.2.2 GRB 160509A	113
4.2.3 GRB 160625B	116
4.2.4 GRB 180720B	117
4.3 Analysis and Broadband Modeling	120
4.3.1 GRB 090902B	123
4.3.2 GRB 160509A	127
4.3.3 GRB 160625B	132
4.3.4 GRB 180720B	135
4.4 Discussion	139
4.4.1 Model Comparison with WAIC	139
4.4.2 Participation Fraction, ξ	142
4.4.3 Jet Structure Shape	143
4.4.4 Energetics and Central Engine	145
4.4.5 Circumburst Densities and Birth Environments	146
4.4.6 Comparison to Other Populations of GRBs	147
4.5 Conclusions	149
 Chapter 5: Summary and Future Directions	 152
5.1 Summary of Results	152
5.2 Publication Plans for Chapter 4	155

5.3	Future Directions	156
5.3.1	High-Energy and Optical Observations of FRBs	156
5.3.2	VHE Emission from GRBs	159
5.4	Facilities and Software	161
Appendix A: FRB Observational Supplementary Material		162
A.1	FRB Observations by Instrument	162
A.2	Summary of Extraneous Signals Detected with the <i>Fermi</i> -GBM Targeted Search	164
A.2.1	Local Particle Activity	164
A.2.2	Other Unrelated Signals	165
Appendix B: MCMC Corner Plots		168
B.1	GRB 090902B	169
B.2	GRB 160509A	172
B.3	GRB 180720B	175
Appendix C: GRB Data Tables		178
C.1	GRB 090902B	178
C.2	GRB 160509A	184
C.3	GRB 160625B	194
C.4	GRB 180720B	208
Bibliography		219

List of Tables

2.1	FRB Upper Limits on f_γ	50
2.2	FRB Lower Limits on f_r/f_γ	55
3.1	X-ray Data	76
3.2	Optical Data	78
3.3	Radio Data	79
3.4	Best Fit Model Parameters.	99
3.5	Best Fit Gaussian Model Parameters for §3.4.4 and §3.4.5	102
3.6	WAIC Score Model Comparison	104
4.1	MCMC Prior Distributions and Bounds	122
4.2	Best Fit Model Parameters for GRB 090902B	125
4.3	Best Fit Model Parameters for GRB 160509A	130
4.4	Best Fit Model Parameters for GRB 160625B	134
4.5	Best Fit Model Parameters for GRB 180720B	138
4.6	Model Comparison for GRB 090902B	141
4.7	Model Comparison for GRB 160509A	141
4.8	Model Comparison for GRB 160625B	142
4.9	Model Comparison for GRB 180720B	142
4.10	Beaming-corrected γ -ray energies in units of ergs (E_γ)	149
5.1	f_γ Upper Limits	153
A.1	Available FRB Observations per Instrument	163
C.1	GRB 090902B: X-ray Data	178
C.2	GRB 090902B: Optical Data	181
C.3	GRB 090902B: Radio Data	183
C.4	GRB 160509A: X-ray Data	184
C.5	GRB 160509A: Optical Data	190
C.6	GRB 160509A: Radio Data	191
C.7	GRB 160625B: X-ray Data	194
C.8	GRB 160625B: Optical Data	197
C.9	GRB 160625B: Radio Data	205
C.10	GRB 180720B: X-ray Data	208
C.11	GRB 180720B: Optical Data	217
C.12	GRB 180720B: Radio Data	218

List of Figures

1.1	GRB Light Curve Examples	5
1.2	GRB Isotropic Energy vs Redshift	7
1.3	Short vs Long GRBs	8
1.4	Multiwavelength Light Curve of GRB 130427A	11
1.5	Jet Break Example	12
1.6	GRB SED Examples	16
1.7	FRB Light Curves	24
1.8	FRB Dispersion Measure	25
1.9	SGR 1935+2154 Light Curve	30
2.1	FRB Energy Estimate Based on Fluence Upper Limits	62
3.1	Isotropic Energies of <i>Fermi</i> and <i>Swift</i> GRBs	73
3.2	GRB 160625B Radio SED	82
3.3	Corner Plot for Top-hat Model	85
3.4	Afterglow Model Comparison	86
3.5	Corner Plot for Gaussian Model with Fixed Participation Fraction	87
3.6	Corner Plot for Gaussian Model with Variable Participation Fraction	90
3.7	Multiwavelength Light Curve with Best Fit Model	91
3.8	Model Comparison to Previous Works	91
3.9	Impact of Participation Fraction on Afterglow Fitting	98
3.10	Viewing Angle Effects on Afterglow Modeling	103
4.1	Isotropic Energy Release vs Redshift for Bright GRBs	110
4.2	Multiwavelength Light Curve of GRB 090902B	126
4.3	Multiwavelength Light Curve of GRB 160509A	131
4.4	Multiwavelength Light Curve of GRB 160625B	133
4.5	Multiwavelength Light Curve of GRB 180720B	140
4.6	ξ Parameter Ranges	144
4.7	0.3-10 keV <i>Swift</i> -XRT Light Curves	146
5.1	Radio and X-ray Fluences for FRBs	157
5.2	Synchrotron and SSC SED of GRB 190114C	160
A.1	GBM FRB Localization Skymaps	167
B.1	GRB 090902B: Top-hat	169

B.2	GRB 090902B: Gaussian with fixed ξ	170
B.3	GRB 090902B: Gaussian with free ξ	171
B.4	GRB 160509A: Top-hat	172
B.5	GRB 160509A: Gaussian with fixed ξ	173
B.6	GRB 160509A: Gaussian with free ξ	174
B.7	GRB 180720B: Top-hat	175
B.8	GRB 180720B: Gaussian with fixed ξ	176
B.9	GRB 180720B: Gaussian with free ξ	177

List of Abbreviations

AGN	Active Galactic Nuclei
AMI-LA	Arcminute Microkelvin Imager Large Array
ASKAP	Australian Square Kilometer Array Pathfinder
BAT	Burst Alert Telescope
BATSE	Burst and Transient Source Explorer
BGO	Bismuth Germanate
BH	Black Hole
CASA	Common Astronomy Software Applications
CBM	Circumburst Medium
CHIME	Canadian Hydrogen Intensity Mapping Experiment
CTA	Cherenkov Telescope Array
CTIME	Continuous Time
DSA	Deep Synoptic array
DM	Dispersion Measure
FOV	Field of View
FRB	Fast Radio Burst
FRED	Fast Rise Exponential Decay
FS	Forward Shock
GBM	Gamma-ray Burst Monitor
GCN	Gamma-ray Burst Coordinates Network
GMRT	Giant Metrewave Radio Telescope
GRB	Gamma-ray Burst
GW	Gravitational Wave
HESS	High Energy Stereoscopic System
HST	Hubble Space Telescope
INTEGRAL	International Gamma-Ray Astrophysics Laboratory
IR	Infrared

ISM	Interstellar Medium
ISS	Interstellar Scintillation
IGM	Intergalactic Medium
JWST	James Webb Space Telescope
KN	Kilonova
Λ CDM	Lambda Cold Dark Matter
LAT	Large Area Telescope
LIGO	Laser Interferometer Gravitational-Wave Observatory
LogLR	Log Likelihood Ratio
LSST	Large Synoptic Survey Telescope
MAGIC	Major Atmospheric Gamma Imaging Cherenkov
MCMC	Markov Chain Monte Carlo
MW	Multiwavelength
NaI	Sodium Iodide
NIR	Near Infrared
PI	Principal Investigator
RMS	Root Mean Square
ROI	Region of Interest
RS	Reverse Shock
SAA	South Atlantic Anomaly
SED	Spectral Energy Distribution
SGR	Soft Gamma-ray Repeater
SKA	Square Kilometer Array
SLSN	Super Luminous Supernova
SMC	Small Magellanic Cloud
SN	Supernova
SSC	Synchrotron Self-Compton
ToO	Target of Opportunity
TTE	Time-Tagged Events
UTC	Coordinated Universal Time

UV	Ultraviolet
UVOT	Ultraviolet/Optical Telescope
VHE	Very High Energy
VLA	Very Large Array
VLT	Very Large Telescope
WAIC	Widely Applicable Information Criterion
WD	White Dwarf
XRT	X-ray Telescope
XSPEC	X-Ray Spectral Fitting Package

Chapter 1: Introduction

We are sitting at the cusp of a ‘big data’ revolution in astronomy. Next generation observatories to be commissioned in a few years will generate more than 10 million alerts per night, increasing our knowledge of known transients and undoubtedly leading to the discovery of novel types of events. The work presented here focuses on two particular types of transients - fast radio bursts (FRBs) and gamma-ray bursts (GRBs). Both represent extreme systems - GRBs as the most relativistic known outflows, and FRBs as the sources with the largest brightness temperatures. As a result, the work outlined in this thesis serves as a small stepping stone towards preparing for this deluge of information as we enter this new dawn of transient astronomy.

1.1 Gamma-ray Bursts

1.1.1 History and Background

Gamma-ray bursts (GRBs) were a serendipitous discovery during the Cold War. The United States, the United Kingdom and the Soviet Union signed the 1963 Partial Test Ban Treaty to prohibit nuclear weapons testing in the atmo-

sphere, outer space, and in the ocean. Following this, the United States launched a series of satellites of which one of their purposes was to detect radiation signatures from potential treaty violations. The Vela satellites - appropriately named after the Spanish word *velar* (to keep watch over) - never confirmed any definitive illegal testing on Earth, but did lead to the discovery of several mysterious bursts of gamma-ray energy coming from outer space ([Klebesadel et al., 1973](#)).

Today we recognize these events as some of the most energetic and catastrophic explosions known to exist in the Universe, although it took several decades to confirm this fact. Early space-based gamma-ray detectors had particularly poor positional accuracy which made it difficult to localize the bursts to a host source. The lack of a distance estimate led to contentious debates over their origins ([Kulkarni, 2018](#); [Ruderman, Sutherland, 1975](#)). More theories than known bursts were proposed, astronomers found themselves taking sides in the galactic vs extragalactic debate, and whole conferences were dedicated to tackling the mystery. It was not until the 1990s that significant progress was made towards understanding their origins. The Burst and Transient Source Explorer (BATSE) on board the Compton Gamma-ray Observatory confirmed that the bursts were not only isotropically distributed (suggesting an extragalactic origin) but also could be classified into two groups - short duration, spectroscopically hard bursts versus longer, softer bursts ([Kouveliotou et al., 1993](#); [Meegan et al., 1992](#)).

It soon became clear that further progress necessitated the detection of a counterpart at lower energies. The satellite BeppoSAX ([Boella et al., 1997](#)) was the first to detect fading X-ray afterglows to GRBs and its increased positional accuracy

eventually helped facilitate the finding of the first optical and radio counterparts as well which led to the first host-galaxy associations (e.g., GRB 970228; [Costa et al. 1997](#)), thus revolutionizing the field ([Frontera, 2019](#)). Redshift measurements allowed a proper calculation of isotropic energy production,¹ suggesting GRBs were even more energetic than supernovae (SNe). Eventually, the connection between bright SNe and long GRBs (e.g., SN 1998bw; [Galama et al. 1998](#); [Iwamoto et al. 1998](#)) led to the understanding that both are produced during the collapse of massive stars, and the detection of a short GRB coincident with a gravitational wave signal (GRB 170817A/GW 170817; [Abbott et al. 2017a,c](#)) confirmed that at least some short GRBs are produced by the coalescence of two neutron stars. Despite the huge leaps made in recent history, several fundamental questions remain and the field of GRB research continues to reward us with new surprises.

1.1.2 Observational Properties

Prompt emission: Initial bursts from GRBs consist of bright emission at gamma-ray and X-ray wavelengths lasting from less than 1 s to up to 1000 s ([Pe'er, 2015](#)). The prompt emission phase of GRB light curves can vary widely in terms of behavior and structure and is thought to be directly related to the internal physics of the burst central engine (Figure 1.1). While many individual peaks follow FRED-like behavior (a fast rise followed by exponential decay), no two GRB events appear exactly the same ([Pe'er, 2015](#)). Some GRBs consist of a single peak of emission

¹Due to the uncertainty in measuring GRB beaming angles, isotropic (non-beaming-corrected) energies are often reported instead.

while others may display multiple peaks, the emission can be smooth or highly variable, and some GRBs may even exhibit delayed or long-lasting gamma-ray emission (Beloborodov et al., 2014).

Individual peaks of emission within the GRB light curve define the minimum variability timescale. This property is directly correlated with the peak isotropic luminosity (Fenimore, Ramirez-Ruiz, 2000) and also sets the physical size scale for these events, both of which are highly relevant when considering the non-thermal nature of the prompt emission (MacLachlan et al., 2013, 2012; Sonbas et al., 2013).

Spectrum: GRB prompt emission spectra are nonthermal in nature and typically peak around several hundred keV. In some bursts the spectral tail may extend into GeV energies. Spectra are well-described by the empirically-derived ‘Band’ function (Band et al., 1993).² The Band function describes the photon number flux, $N_E(E)$, and consists of a smoothly broken power law characterized by the low and high-energy power-law exponents, α and β , and the break energy, E_0 :

$$N_E(E) = \begin{cases} A \left(\frac{E}{100 \text{ keV}} \right)^\alpha \exp\left(-\frac{E}{E_0}\right) & (\alpha - \beta)E_0 \geq E, \\ A \left(\frac{(\alpha - \beta)E_0}{100 \text{ keV}} \right)^{\alpha - \beta} \exp(\beta - \alpha) \left(-\frac{E}{100 \text{ keV}} \right)^\beta & (\alpha - \beta)E_0 \leq E. \end{cases} \quad (1.1)$$

Rates and energy scales: It was quickly noted that GRBs are distributed isotropically on the sky. This was most naturally explained as indirect evidence for their extragalactic origins. On average, more than one GRB is detected per day

²More recent work has explored the potential for more physical models with multiple components in the prompt emission (Guiriec et al., 2015).

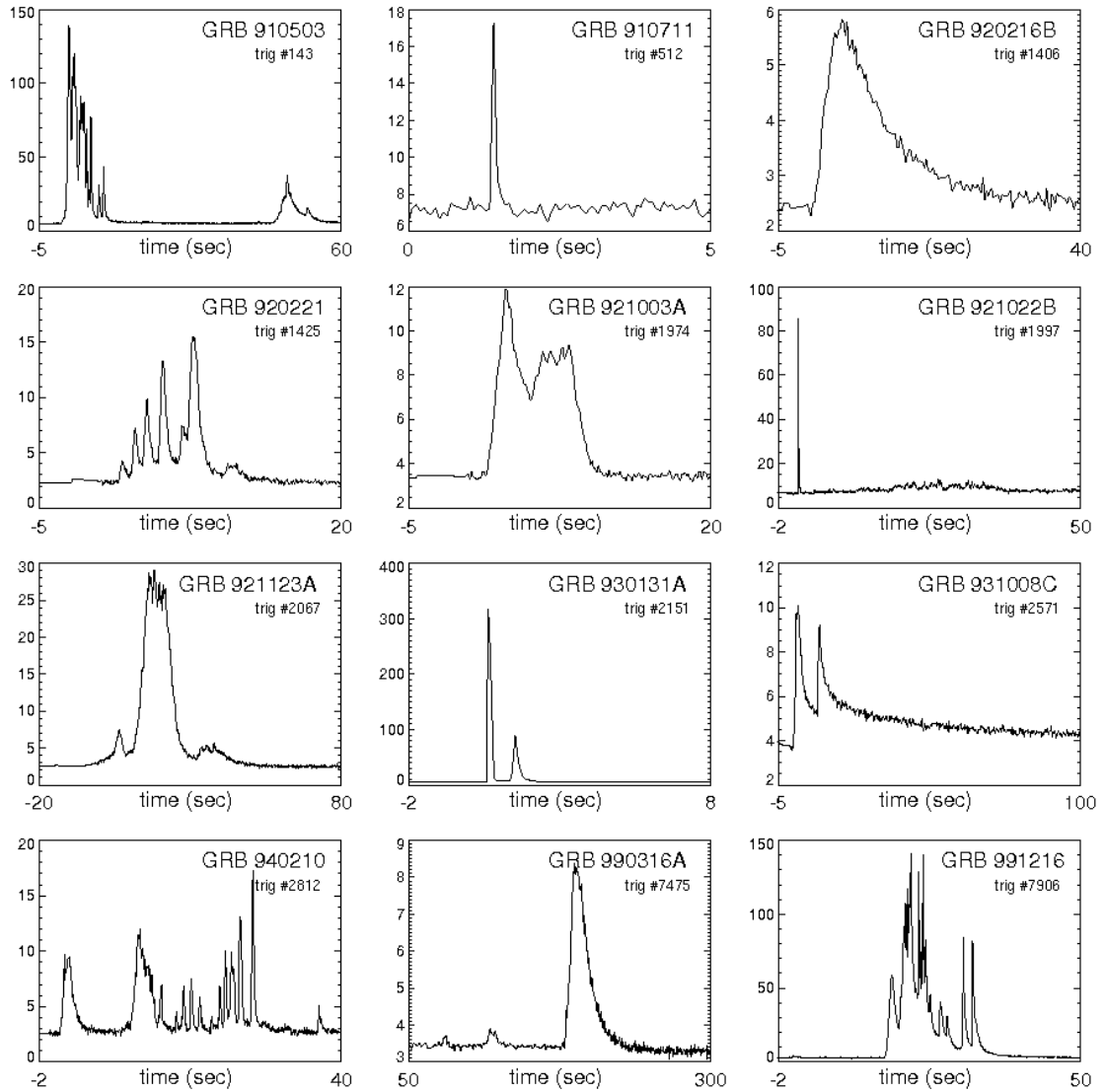


Figure 1.1: 12 GRB light curve examples highlighting their variable nature. The y-axis represents the detector count rate in counts s^{-1} . GRB prompt emission may consist of a single peak or multiple pulses and can range from a few seconds to many minutes long. Figure is taken from [Pe'er \(2015\)](#).

over the whole sky (Lien et al., 2016a; Sun et al., 2015).³ The GRB detection rate is dependent upon the detector used and the type of GRB observed (short GRBs have lower discovery rates compared to long GRBs, partially due to their on-average lower luminosities, lower event rates, and inability to be seen out to larger distances; Shahmoradi, Nemiroff 2015; Sun et al. 2015).

GRBs are known to emit most of their energy along a narrow cone of emission, or jet, which may impact estimates of both their event rates and energies. Assuming GRBs radiate isotropically, their observed luminosities, E_{iso} , typically measure between 10^{46} and $> 10^{54}$ erg s⁻¹ (Pescalli et al., 2015). Due to the uncertainty in measuring GRB jet widths it can be difficult to convert isotropic measurements into the true energy produced during each GRB explosion. Therefore, we typically report the isotropic emission rather than the true beaming-corrected energy: $E = E_{\text{iso}}(1 - \cos \theta_j) \approx E_{\text{iso}} \frac{\theta_j^2}{2}$,⁴ where E is the beaming-corrected energy of the burst, E_{iso} is the uncorrected isotropic energy, and θ_j is the jet opening angle (Bloom et al., 2001; Frail et al., 2001). Most detected long GRBs have typical isotropic energies between $10^{51} - 10^{53}$ erg (Figure 1.2).

Dual population: The duration of the burst is defined by the T_{90} parameter, which is the portion of time over which from 5% to 95% of its total measured background-subtracted counts are detected (Koshut et al., 1995). While there are known issues with using it (e.g., it is dependent on detector sensitivity and bandpass, it can be difficult to distinguish between prompt and afterglow phases, and it can be

³Depending on instrument sensitivity

⁴This equation is only valid for a simple top-hat jet.

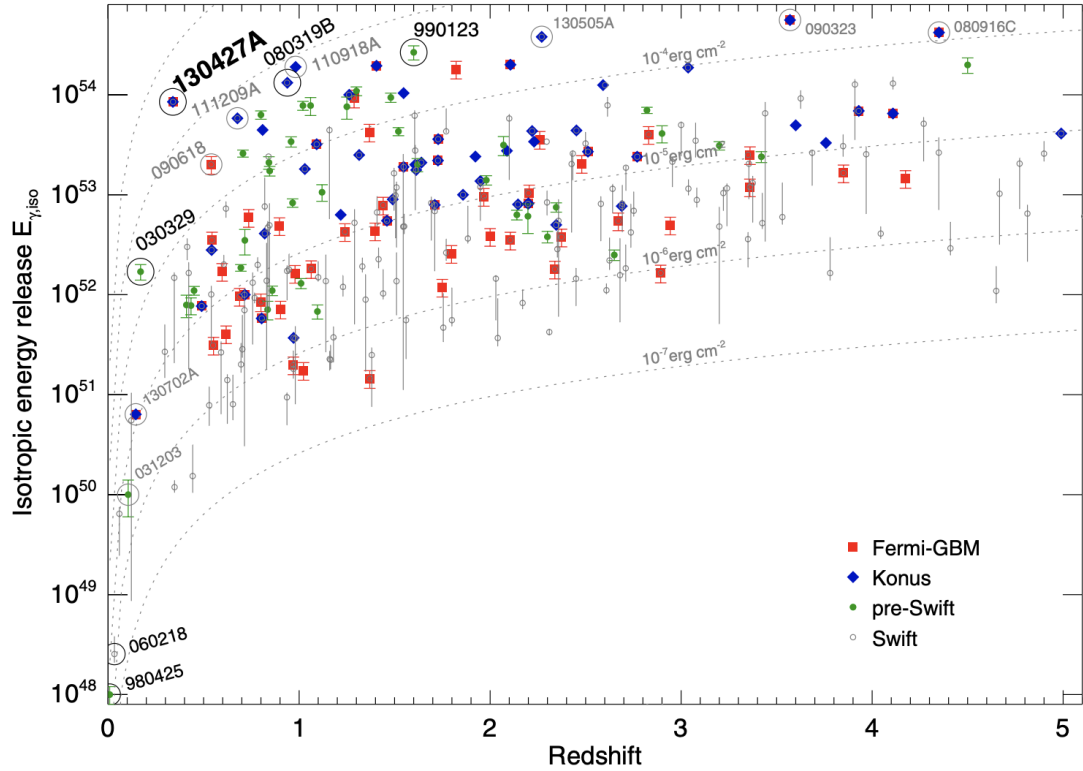


Figure 1.2: Total bolometric isotropic energy versus redshift for several GRBs detected by *Fermi*-GBM, *Konus*, *Swift*, and pre-*Swift* observatories. High-luminosity GRBs dominate at higher redshifts due to the inability to detect low-energy events at such large distances. Lines of constant fluence are denoted by the dotted curves. Particularly bright GRBs of interest are circled and labeled. Figure is taken from [Perley et al. \(2014\)](#).

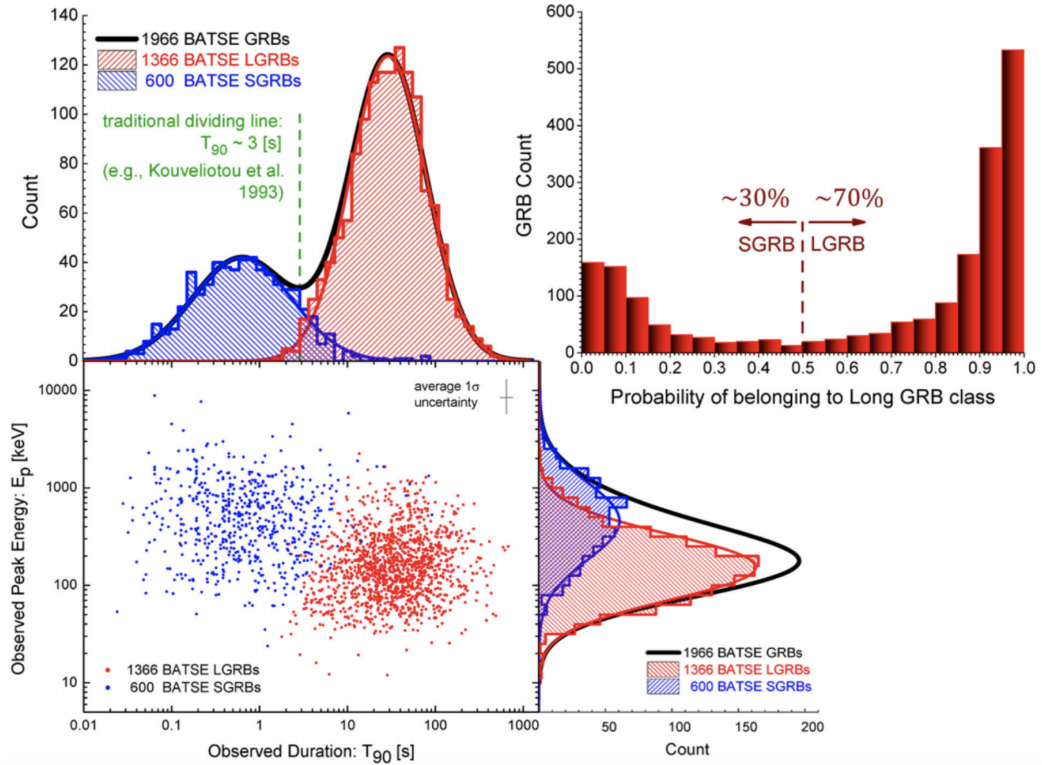


Figure 1.3: Classification of short and long BATSE GRBs based on burst duration (T_{90}) and observed peak energy (E_p). The upper right figure shows the probability that each GRB in the sample belongs to the long GRB class based upon fuzzy C-means clustering. GRBs with probabilities >0.5 are considered long GRBs. Long GRBs are defined by durations longer than $\sim 2 - 3$ s and are typically spectrally softer than short GRBs. Figure is taken from [Shahmoradi, Nemiroff \(2015\)](#).

complicated by the presence of precursors and aftershocks), T_{90} can still be a useful metric. The distribution of T_{90} is bimodal with an energy-dependent boundary around 2 seconds (Figure 1.3); thus GRBs are usually classified as being either short or long in duration ([Kouveliotou et al., 1993](#)). Generally, only around 25-30% of detected GRBs are classified as short ([Shahmoradi, Nemiroff, 2015](#)). Short GRBs also tend to have a higher hardness ratio (the difference between the exposure corrected counts in a high and low energy band) than the softer long GRBs, further supporting the idea that they are distinct populations.

1.1.3 Theoretical Considerations

Relativistic emission: The short timescales of GRBs necessitate that a significant amount of gamma-ray radiation must be produced within a compact region, i.e., the GRB is a ‘fireball’. Early theoretical works envisioned a pure fireball which would produce optically thick radiation via pair production and eventually expand and cool (Goodman, 1986; Paczynski, 1986). However, physically realistic GRB models must account for the baryons within the jet that inevitably interact with the surrounding environment (commonly referred to as ‘baryon loading’). Paczynski (1990) and Shemi, Piran (1990) found that in this more realistic situation the relativistic energy of the explosion would be converted into baryonic kinetic energy. In both situations the expected GRB spectrum would be thermal.

Counter to these early fireball theories GRB spectra are decidedly nonthermal. Given this, a ‘compactness’ problem emerged since the short variability timescales imply a compact, optically thick source. For example, a typical cosmological ($D = 3$ Gpc) GRB with a minimum variability timescale of $\delta t = 10$ ms implies a physical size of no more than $R < c\delta t \approx 3000$ km. Assuming an average GRB fluence of $F = 10^{-7}$ erg cm², the equation for optical depth to pair production becomes:

$$\tau_{\gamma\gamma} = \frac{f_p \sigma_T F D^2}{R^2 m_e c^2} \approx 10^{13}, \quad (1.2)$$

where σ_T is the Thompson cross-section, $m_e c^2$ is the electron rest energy, and f_p is the fraction of electrons satisfying the condition for pair production (Piran, 2005;

Piran, Shemi, 1993). Clearly, with such a large optical depth all photons should pair produce resulting in a thermal spectrum.

To solve this discrepancy we must invoke relativistic effects. Emitted photons have been blueshifted as they propagate towards the observer, meaning their energy is a bulk Lorentz factor, Γ , higher at the observer compared to the source. Accordingly, the fraction of photons at the source that would have the requisite energy to pair produce is then reduced by a factor of $\Gamma^{-2\alpha}$, where α is the power law spectral index of the emission. In addition, relativistic effects cause the observer to view the source radius as larger by a factor of Γ^2 , $R_{source} < \Gamma^2 c \delta t$. Therefore,

$$\tau = \frac{\tau_{\gamma\gamma}}{\Gamma^{2\alpha+4}} \quad (1.3)$$

and the compactness problem can be resolved if the emission is ultra-relativistic and $\Gamma > 10^2$.

Multiwavelength afterglows: After the prompt phase GRB light curves begin a phase of slow power law decay seen across all wavelengths (Figure 1.4). This afterglow emission is the burst ejecta interacting with the material immediately surrounding the progenitor star. However, instead of radiating isotropically, GRBs instead only emit over a small portion of their surface area; i.e., their relativistic emission is beamed into jets. Typical long GRB jet widths are between 1–10° (Rhoads, 1999; Sari et al., 1999). A GRB jet is emitted with an opening angle, θ , and a large initial Lorentz factor, $\Gamma > 100$. Over time, as the burst ejecta propagates forward and interacts with the circumburst media it will decelerate and

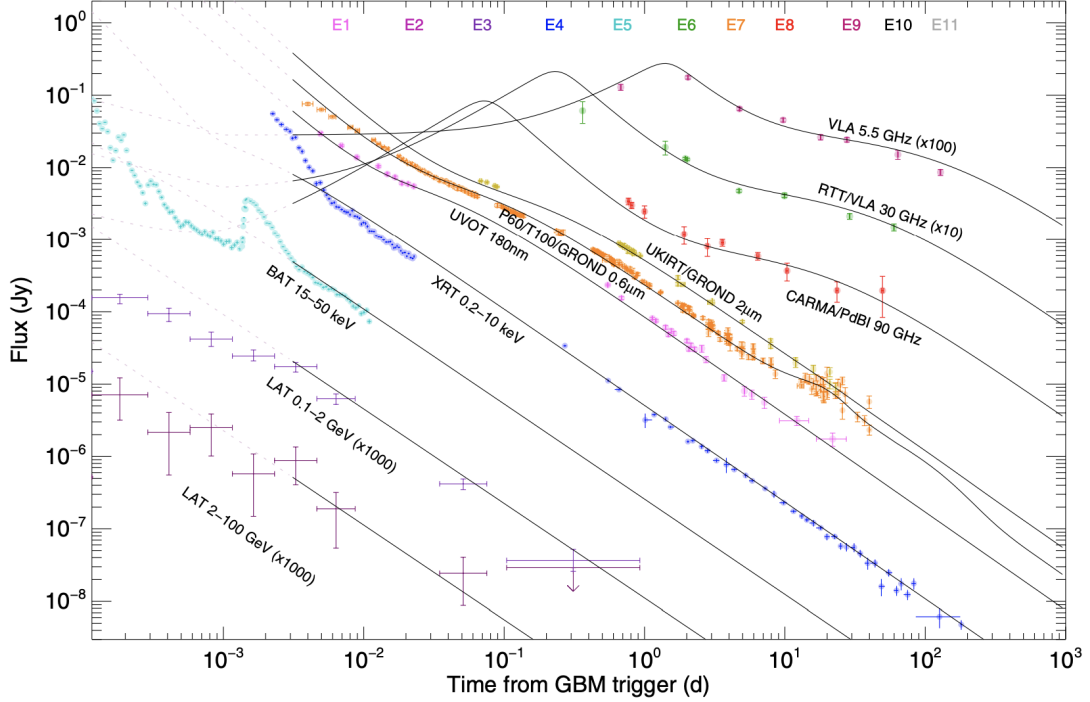


Figure 1.4: The multiwavelength afterglow of GRB 130427A at radio, millimeter, near infrared, optical, ultraviolet, X-ray, and gamma-ray wavelengths. Figure is taken from [Perley et al. \(2014\)](#).

spread laterally. Due to relativistic beaming effects at early times an on-axis observer will only see a small portion of the jet equal to Γ^{-1} ([Sari, 2000](#)). At the point when $\theta \approx \Gamma^{-1}$, beaming effects decrease significantly and the GRB afterglow begins to fade much more rapidly. This onset of rapid deceleration is referred to as the ‘jet break’ ([Figure 1.5](#)). Since the causes are purely geometrical, jet breaks are achromatic and can be seen at the same time across all observing frequencies.

Some GRB light curves may have additional components beyond the jet break such as plateau phases, flares, and additional changes in the light curve slope over time ([Zhang et al., 2006](#)). Several of the GRBs mentioned within this work have noticeable reverse shocks (e.g., GRB 160625B, [Alexander et al. 2017](#); GRB 160509A, [Laskar et al. 2016a](#)). In addition to the forward shock which produces most of the

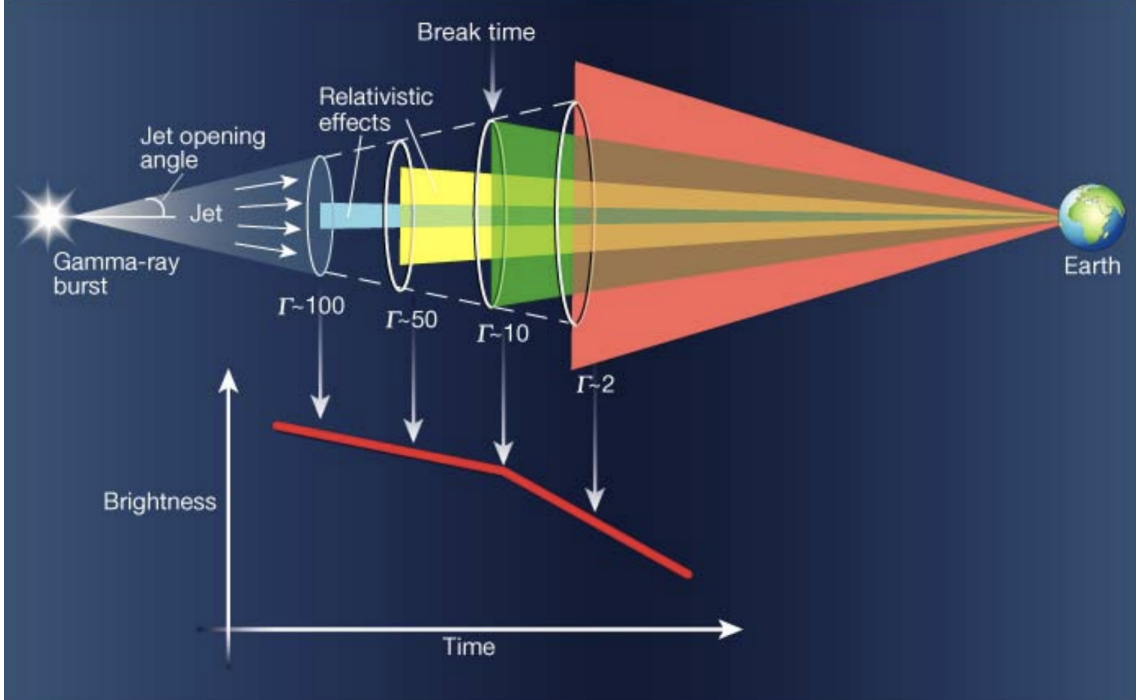


Figure 1.5: A cartoon example of a GRB jet break in a light curve. Large Γ and relativistic beaming effects influence what portion of the GRB jet is visible to an observer at early times. When the jet slows down and $\theta \approx \Gamma^{-1}$ the light curve begins to fade much more rapidly. Figure is adapted from Poonam Chandra’s slides.

long-lived afterglow there is a shorter-lived reverse shock which propagates into the GRB ejecta (Gao, Mészáros, 2015). The reverse shock typically manifests observationally as an early-time radio flare and possibly an optical/IR flash (Kobayashi, Sari, 2000; Mészáros, Rees, 1999; Sari, Piran, 1999). While in theory GRBs should produce afterglows at all wavelengths from radio to gamma-ray, in practice their detection can be limited by high GRB redshift, host galaxy absorption, limited instrument sensitivities, and observational visibility.

Gathering multiwavelength observations and precisely measuring GRB jet breaks can provide critical information about the GRB central engine, jet microphysics, surrounding circumburst medium, bulk energy properties, and jet internal structure (Lamb et al., 2021; Panaitescu, Kumar, 2002; Sari et al., 1999). There-

fore, campaigns to rapidly follow-up and observe GRB afterglows are vital for understanding their physical properties. One of the best sources of information from broadband observations came out of the joint LIGO-*Fermi*-INTEGRAL detection (GW 170817/GRB 170817A; [Abbott et al. 2017a,c](#)). Modeling of the multimessenger data showed that the event was observed at a viewing angle of $\sim 20^\circ$ and that emission was visible beyond the central core of the jet ([Fong et al., 2019](#); [Lamb et al., 2020](#); [Lazzati et al., 2018](#); [Troja et al., 2019](#)).

Synchrotron emission processes: In the fireball model we assume that the observed non-thermal afterglow emission is produced via synchrotron radiation from a spherical blast wave expanding into a surrounding medium with density, n , and accelerating electrons. The properties of the emission are directly dependent upon the post-shock magnetic field strength, B ,:

$$B^2 = 32\pi m_p \epsilon_B n \gamma^2 c^2, \quad (1.4)$$

where ϵ_B is a dimensionless parameter representing the fraction of magnetic energy, U_B , imparted to the electrons ($\epsilon_B = \frac{U_B}{e}$), e is the total thermal energy, m_p is the particle mass, and γ is the Lorentz factor of the shock front ([Sari et al., 1996, 1998](#)). We also assume that a constant fraction of thermal energy is imparted to the electrons by the shock front: $\epsilon_e = \frac{U_e}{e}$, where $U_e = 4\gamma^2 n m_p c^2$.

Electrons are accelerated via shock heating to a power law distribution of Lorentz factors:

$$N(\gamma_e) \sim \gamma_e^{-p}. \quad (1.5)$$

Values of p must be larger than 2 to prevent the distribution from diverging at large values of γ_e .⁵ Now the minimum Lorentz factor (or low energy cut-off) can be written as

$$\gamma_m = \epsilon_e \left(\frac{p-2}{p-1} \right) \frac{m_p}{m_e} \gamma. \quad (1.6)$$

The resulting synchrotron spectral energy distribution presents as a series of power laws smoothly broken at three characteristic frequencies: ν_a , below which self absorption becomes an important factor; ν_m , the frequency of the minimum energy electron; and ν_c , the minimum frequency at which electrons begin to cool efficiently. The exact shape of the spectrum (Figure 1.6) depends upon the ordering of ν_a , ν_m , and ν_c as well as whether the burst is expanding into an ISM- (interstellar medium; $\rho(r) \propto r^0$) or wind-like medium ($\rho(r) \propto r^{-2}$).

Most GRB afterglows are observed in the slow-cooling regime ($\nu_c > \nu_m$ and only a portion of the electrons can cool efficiently). To calculate the flux over a range of frequencies for an ISM-like density we integrate over Eq. 1.5 and find:

$$F_\nu \propto \begin{cases} \nu^2 & \nu < \nu_a \\ \nu^{1/3} & \nu_a \leq \nu < \nu_m \\ \nu^{(1-p)/2} & \nu_m \leq \nu < \nu_c \\ \nu^{-p/2} & \nu \geq \nu_c \end{cases} \quad (1.7)$$

⁵Cases where the electron energy distribution may be very hard (i.e., $1.0 < p < 2.0$) have been explored, e.g., [Bhattacharya 2001](#).

$$F_\nu \propto \begin{cases} t^{1/2} & \nu < \nu_a \\ t^{1/2} & \nu_a \leq \nu < \nu_m \\ t^{3(1-p)/4} & \nu_m \leq \nu < \nu_c \\ t^{(2-3p)/4} & \nu \geq \nu_c. \end{cases} \quad (1.8)$$

In the case of a wind-like medium the temporal relationships instead become:

$$F_\nu \propto \begin{cases} t^1 & \nu < \nu_a \\ t^0 & \nu_a \leq \nu < \nu_m \\ t^{(1-3p)/4} & \nu_m \leq \nu < \nu_c \\ t^{(2-3p)/4} & \nu \geq \nu_c. \end{cases} \quad (1.9)$$

Other examples of potential GRB spectra (e.g., fast cooling) can be seen in more detail in [Granot, Sari \(2002\)](#).

Broadband Afterglow Modeling: Analytical methods for describing GRB afterglows typically involve looking at the closure relations, i.e., measuring the temporal and spectral scaling relations of the SED (as described in the previous section). Historically, a full analytical description depended upon the assumption of an on-axis, uniformly collimated outflow, or ‘top-hat’ jet (e.g., [Frail et al. 2001](#)). However, a range of alternative jet structure types have been proposed in the literature – some common examples include variations of top-hat, Gaussian, and power law models ([Aloy et al., 2005](#); [Coughlin, Begelman, 2020](#); [Duffell, MacFadyen, 2013a](#); [Margutti](#)

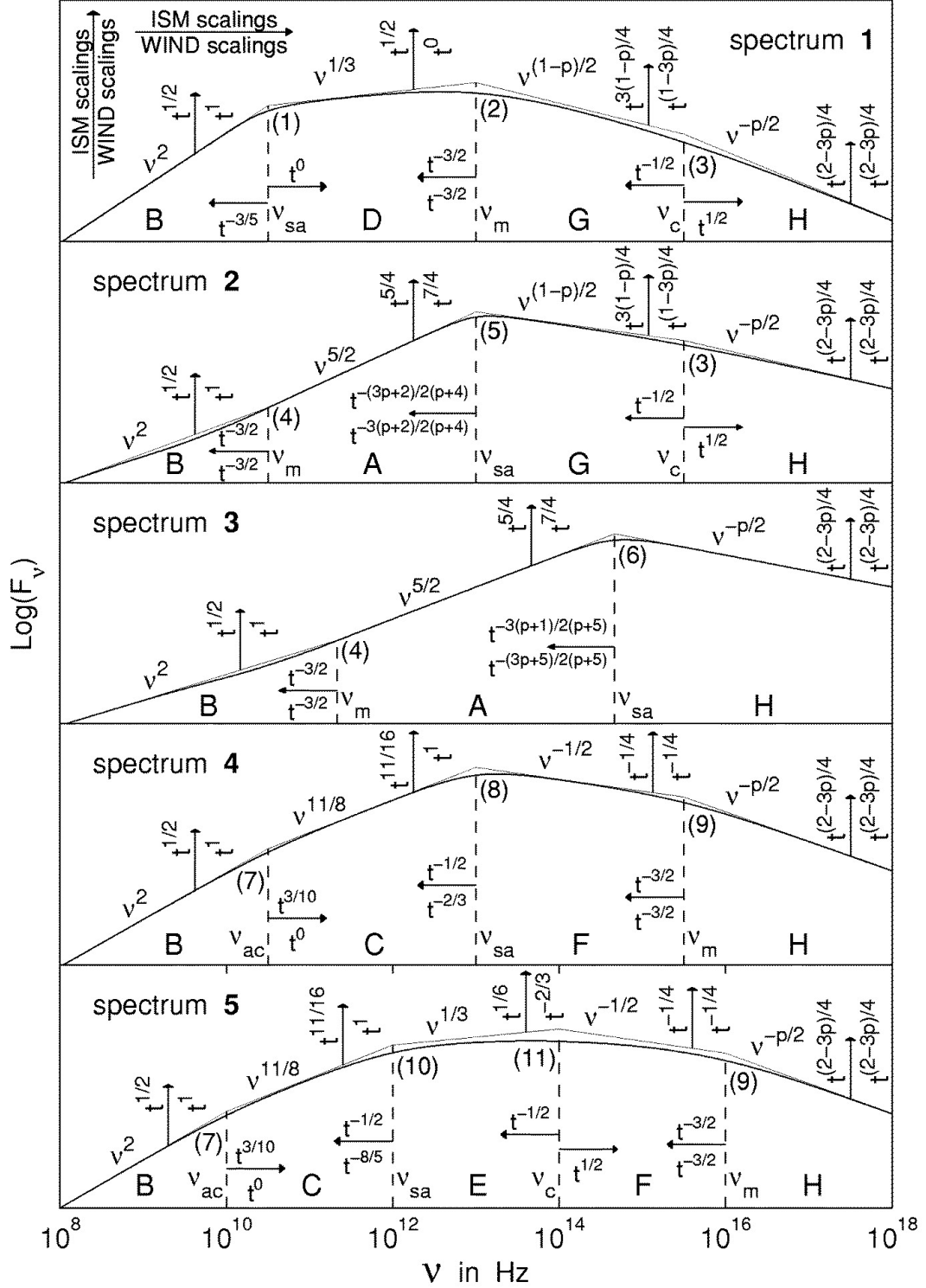


Figure 1.6: Examples of potential GRB spectral shapes, taken from [Granot, Sari \(2002\)](#). Temporal and frequency dependencies are given for both wind (bottom or right of arrow) and ISM-like (top or left of arrow) environments and a range of orderings for ν_a , ν_m , and ν_c . The break frequencies and their dependencies are denoted by dotted lines.

et al., 2018; Mészáros et al., 1998; Rossi et al., 2002, 2004; Zhang et al., 2004; Zhang, Mészáros, 2002). The exact structure of any one GRB jet may be dependent upon several factors such as the immediate circumburst environment and interactions with the stellar envelope. Given these more complicated structure types, numerical methods offer a much more comprehensive view of the physical processes within the GRB jet.

Several numerical codes have been developed within recent years to model GRB afterglows (Alexander et al., 2017; Laskar et al., 2013; Leventis et al., 2013; Perley et al., 2014; Ryan et al., 2015; van Eerten et al., 2010, 2012; van Eerten, MacFadyen, 2012). Such methods offer an advantage over the simplified approach of power law fitting since they do not necessarily require contemporaneous multiwavelength observations and offer much improved abilities to quantify physical models, estimate parameter uncertainties, and perform model comparisons since they are typically based in Bayesian inference methods. Many of these numerical codes utilize Markov-Chain Monte Carlo methods (MCMC; Foreman-Mackey et al. 2013; Goodman, Weare 2010) which efficiently handle arbitrarily complex models, multimodal solutions, and large data sets.

One of the standard tools for GRB analysis is the publicly available `BoxFit` package (van Eerten et al., 2012). `BoxFit` generates synthetic GRB light curves and spectra via two-dimensional relativistic hydrodynamic simulations. `BoxFit` produces highly accurate light curves via fully numerical methods to model the nonlinear hydrodynamics of the spherical blast wave. `ScaleFit` (Ryan et al., 2013, 2015) later expanded upon the methods of `BoxFit` by utilizing scaling relations in the

radiation equations to reduce the set of scale-invariant characteristic quantities in the model fitting.

For the following analysis we utilize the methods of the `afterglowpy` package which is a publicly available, open-source `python` code for modeling GRB afterglows (Ryan et al., 2020). `Afterglowpy` uses the single-shell approximation to semianalytically model a relativistic blast wave propagating through a surrounding medium as a function of jet structure and viewing angle. It operates under the assumption that the afterglow is produced via synchrotron emission from the forward shock. `Afterglowpy` trades some of the physical accuracy of the fully numerical methods of `BoxFit` and `ScaleFit` for greater flexibility and efficiency. `Afterglowpy` takes the broadband fluxes, observation times, and frequencies to produce model light curves based upon the following physical parameters: viewing angle, θ_v , isotropic kinetic energy released by the blastwave, $E_{K,iso}$, jet core opening angle, θ_c , circumburst density, n , spectral slope of the electron distribution, p , fraction of shock energy imparted to electrons, ϵ_e , and to the magnetic field, ϵ_B .

In addition, we also include the participation fraction of electrons, ξ , as a free parameter in some of our models. The participation fraction, ξ , describes the percentage of total electrons which are accelerated by the passing shock wave and contribute to the power-law distribution. 100% participation ($\xi = 1$) is often assumed in the literature but simulations have shown ξ can be as low as 10^{-2} (Sironi, Spitkovsky, 2011; Sironi et al., 2013) and that lower values are likely to be more physically realistic (Warren et al., 2018).

Progenitors: Short GRBs are found in both early type and star-forming

galaxies, often lack a detectable afterglow, and are not associated with supernovae or massive stars (Berger, 2014; D’Avanzo, 2015). Compact object mergers had long been a favored model given their short timescales, expected low circumburst density, and non-correlation with star formation. The joint detection of a short GRB and a GW signal in 2017 definitively confirmed that binary neutron star mergers can power short GRBs (Abbott et al., 2017a,c).

Unlike short GRBs, long GRBs are exclusively found in star-forming regions of spiral and irregular galaxies at small nuclear offsets. They are conclusively linked to massive star collapse via supernovae emission. While the association between long GRBs and the deaths of massive stars is long-standing the exact details regarding the physics of the central engine remain elusive. Currently, two popular progenitor models are favored to explain the central engines of long GRBs: magnetars and black hole systems.

The spindown of a newborn millisecond pulsar could potentially power a long GRB via a Poynting-flux dominated relativistic outflow (Thompson et al., 2004; Zhang, Mészáros, 2001). These magnetars are limited by their finite reserve of rotational energy. For a neutron star with a mass limit of $\sim 2 M_{\odot}$, a radius of 10 km, and a spin period of about 1 ms places a cap on the available energy at $\sim 10^{52}$ erg (Metzger et al., 2011, 2007). This energy cap can be increased in the case of ‘supramassive’ neutron stars that have been stabilized by centrifugal forces and therefore could accommodate rotational energies of up to 10^{53} erg (Metzger et al., 2015). However, Beniamini et al. (2017) and Metzger et al. (2018) have recently shown that the true reservoir of available energy is unlikely to reach beyond $\sim 10^{52}$

erg and so the magnetar model may be in tension with at least the most energetic long GRBs (Cunningham et al., 2020).

In the second scenario, a black hole is formed in the immediate aftermath of the death of a massive star (MacFadyen, Woosley, 1999; Woosley, 1993; Woosley, Heger, 2012). Stellar material accreting back onto the newly formed black hole may power relativistic jets. The jets burrow through the stellar envelope and provide an outlet for relativistic material to escape (Morsony et al., 2007). The typical 10-100 s durations of long GRBs correspond to the free-fall time of the star’s helium core. Unlike magnetars, these ‘collapsars’ have much less stringent caps on the potential energy which could be extracted. Theoretical predictions can easily produce energy releases greater than 10^{53} erg, however the exact mechanism via which the energy is extracted remains uncertain. Potential processes which could power this energy extraction include the Blandford-Znajek process (Blandford, Znajek, 1977) and neutrino annihilation (Popham et al., 1999).

1.2 Fast Radio Bursts

1.2.1 History and Background

Fast radio bursts (FRBs) are a more recently discovered class of transients. They were also an accidental discovery and their story parallels that of GRBs in many ways. The first FRB (FRB 010724; Lorimer et al. 2007) was discovered six years after the initial detection when Duncan Lorimer and his student were searching through archival pulsar observations from the Parkes radio telescope. Therefore, this

first burst is now often referred to as the Lorimer burst. Over the next ten years a few dozen more FRBs would be detected. FRBs were particularly intriguing due their highly dispersed signals. Dispersion measure (DM, explained in more detail in §1.2.2) is commonly used as a proxy for distance and the large DM of FRBs implied potentially cosmological origins and also distinguished them from galactic pulsars (Chatterjee, 2021; Katz, 2018; Lorimer, 2018; Petroff et al., 2019; Stappers et al., 2019; Zhang, 2020).

Many astronomers remained skeptical that FRBs were truly an astrophysical source. The first FRBs were all observed by the same instrument (Parkes Radio Telescope) and their large implied luminosities seemed extreme. When it was reported that a similar type of mystery radio event, perytons, were caused by impatient lunch-goers opening microwaves too early (Petroff et al., 2015) the outcome for FRBs looked even more grim. However, eventually FRBs were detected at other radio observatories confirming that they were not geographically constrained to Australia and probably were astrophysical in origin.

Similarly to GRBs, the initial instruments (single dish radio telescopes) used to detect FRBs did a particularly poor job of localizing the first bursts, making it difficult to perform rapid followup at other wavelengths or to identify host galaxies. The first real breakthrough in the field occurred when a repeating FRB was detected (FRB 121102; Spitler et al. 2014). Astronomers were finally able to undertake a coordinated campaign between the Arecibo telescope and the Very Large Array (VLA) to localize the FRB to within an arcsecond and identify the host galaxy (Chatterjee et al., 2017), confirming they were indeed extragalactic events.

Like the early days of GRBs, at some point there were more theories about FRBs than there were FRBs themselves. In fact, many early GRB theories were recycled to help explain FRBs (Platts et al., 2019). Unlike GRBs however, FRBs have yet to reveal a multiwavelength afterglow. The lack of an observable counterpart made placing constraints on the various theories difficult but because of their short timescales and large energetics a compact object progenitor has always been favored.

The next big break came only in 2020 when the elusive counterpart was finally observed for the first time. Several X-ray satellites observed a bright burst of emission from the soft gamma-ray repeater SGR 1935-2154 (Bochenek et al., 2021; Kirsten et al., 2020; Mereghetti et al., 2020; Zhang et al., 2020). SGRs are objects which irregularly emit extreme bursts of X-ray and gamma-ray energy and are thought to be a type of highly magnetized neutron star called a magnetar. A burst of X-ray activity from SGR 1935-2154 matched with a repeating FRB that was detected coincidentally (The Chime/FRB Collaboration et al., 2020). This provided the first evidence that at least some types of FRBs may originate from magnetar activity. The discovery is a major breakthrough in the field but many questions still remain. The field of FRBs is still in its relative infancy and much more work is required before it reaches an established state like that of GRBs.

1.2.2 Observational Properties

Burst duration: FRBs are so called due to their short durations of only a few milliseconds on average (although durations can range from sub-millisecond to tens of milliseconds; [Petroff et al. 2016](#)). For a typical FRB with an intrinsic duration of 1 ms, causality limits the size of the emitting region to be less than 300 km (barring bulk relativistic motion). This limits the potential progenitor to compact objects such as black holes and neutron stars ([Zhang, 2020](#)). FRB pulses can vary widely in shape, ranging from single peak pulses to double peaked and sometimes repeating signals (Figure 1.7).

Dispersion measure: As FRBs propagate through space they interact with ionized electrons, causing a frequency-dependent delay in the signal (Figure 1.8). The dispersion measure is defined as $DM = \int_0^{D_z} \frac{n_e(l)}{1+z(l)} dl$, where D_z is the comoving distance to a source, n_e is the number density of free electrons along the line of sight, l is the length, and z is redshift. For a radio observation between two frequencies ν_1 and ν_2 the observed time delay will be:

$$\Delta t = \frac{e^2}{2\pi m_e c} (\nu_1^{-2} - \nu_2^{-2}) DM. \quad (1.10)$$

The large DMs (100 to 2600 pc cm⁻³; [Petroff et al. 2016](#)) of FRBs imply they must come from either cosmological distances or regions of high density.

Fluence and luminosities: The typical radio fluence of an FRB is around 2 Jy ms. In cases where it can be determined the isotropic luminosity ranges from

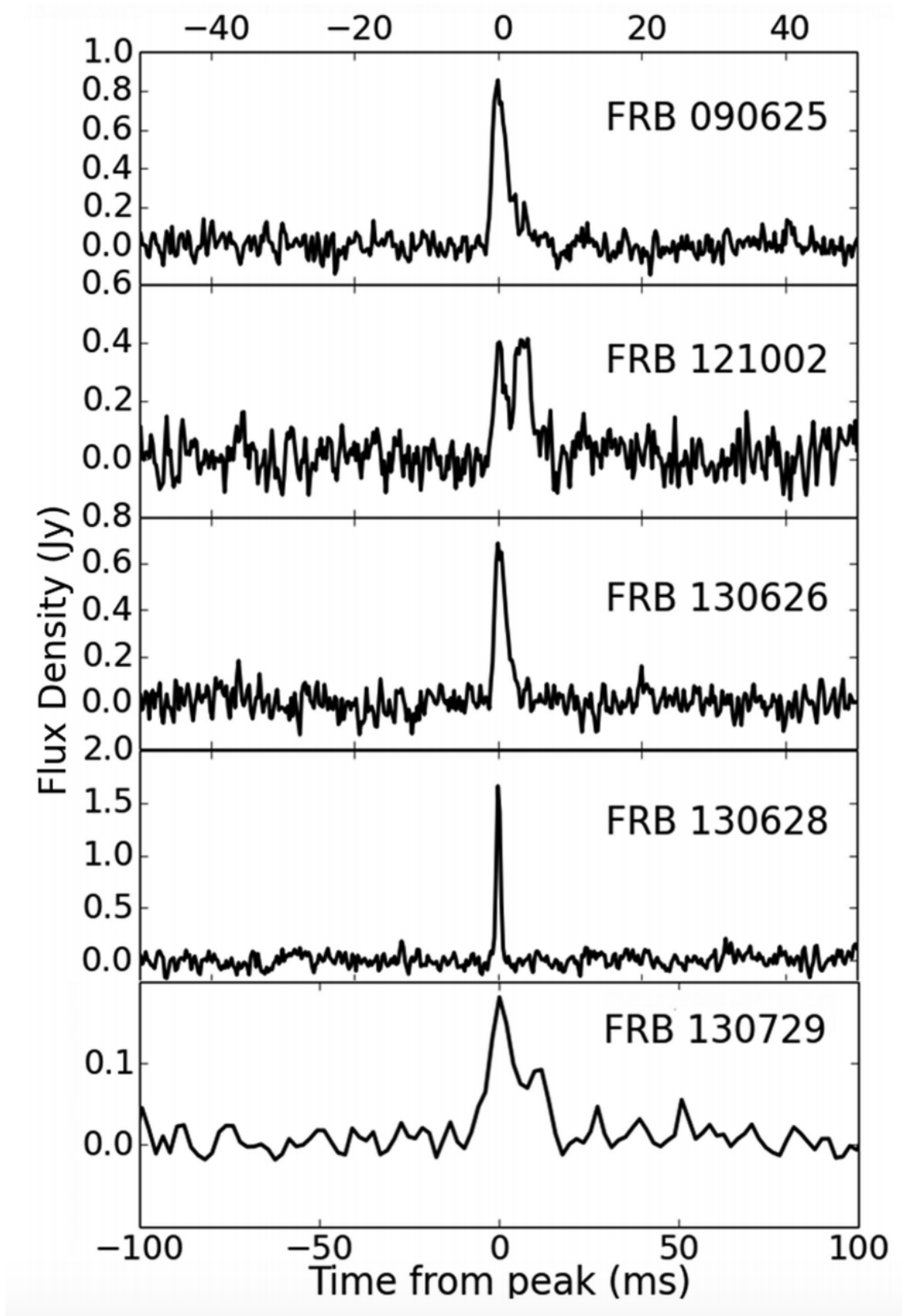


Figure 1.7: Example FRB light curves for the five FRBs reported by [Champion et al. \(2016\)](#). FRB pulses can take on a variety of shapes.

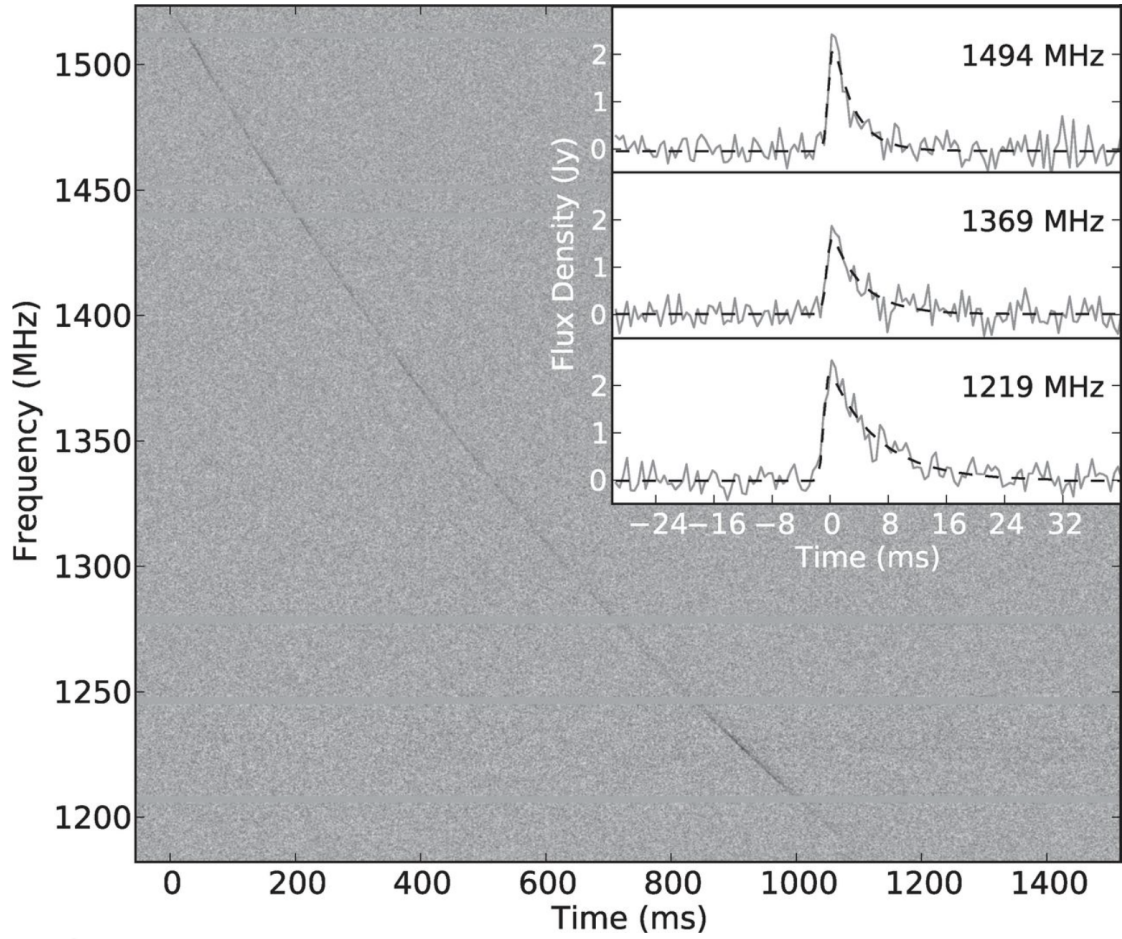


Figure 1.8: The dynamic spectrum of FRB 110220 highlighting the classic DM sweep observed in all FRBs. Figure is taken from [Thornton et al. \(2013\)](#).

$10^{38} - 10^{46}$ erg s⁻¹ (Zhang, 2020), though this does not take into consideration any potential beaming angle effects.

Spectra: FRBs have been detected at frequencies as low as 300 MHz and as high as 8 GHz (Chawla et al., 2020; Gajjar et al., 2018). The spectra of the repeating bursts from FRB 121102 are highly variable. Fitting their spectra with a power law model results in estimates of α ranging from -10 to +14 (Spitler et al., 2016). This range in spectral behavior is thought to be intrinsic to the source rather than caused by some extrinsic mechanism (e.g., scintillation or free-free absorption cannot explain the behavior alone).

Coherent emission and brightness temperatures: Any source emitting incoherently (e.g., synchrotron radiation) cannot exceed a brightness temperature of 10^{12} K (Readhead, 1994). As previously noted in the burst duration discussion, their short timescales limit the size of the emitting region to be less than 300 km. Assuming an FRB distance of ~ 1 Gpc, peak flux density of ~ 1 Jy at $\nu \sim 1$ GHz implies a brightness temperature of $T_B \geq 10^{35}$ K. For FRBs $T_B \gg 10^{12}$ K, from which we infer that FRBs must be emitting coherent radiation. Only a handful of astronomical sources are known to radiate coherently, with pulsars being the most well-known example.

Event rates: Since most FRBs have been discovered by relatively narrow field-of-view instruments, the true all-sky rate is remarkable: ~ 800 sky⁻¹ day⁻¹ above a fluence of 5 Jy ms at 600 GHz (The CHIME/FRB Collaboration et al., 2021). For comparison, this is much larger than the all-sky rate of gamma-ray bursts (\sim few per day at current detector sensitivities) and comparable to the rate

of supernovae (core-collapse and thermonuclear) out to a redshift of $z \approx 0.5$ (Li et al., 2011).

Host galaxies: The first repeating FRB 121102 was localized to a dwarf star-forming galaxy (Chatterjee et al., 2017; Tendulkar et al., 2017), consistent with the hosts of long GRBs and SLSN. However, as more and more FRBs were followed-up it became clear that 121102 was an outlier and most FRBs appear to reside in more massive galaxies with lower rates of star formation (Li, Zhang, 2020).

Non-radio counterparts: Initially, FRBs had only been observed at radio frequencies and due to the poor localization abilities of most single-dish radio telescopes it was difficult to identify a host galaxy or easily perform follow-up at other wavelengths. Therefore, the detection of a counterpart at optical or higher-energy bands was necessary and since their initial discovery several campaigns have been undertaken to identify simultaneous prompt counterparts. The first confirmed non-radio counterpart was only reported in April 2020 when an FRB-like burst of emission was detected coincident with a short hard X-ray flare during a period of heightened activity from the soft gamma-ray repeater (SGR) 1935-2154 (The Chime/FRB Collaboration et al., 2020).

1.2.3 Theoretical Considerations

Emission mechanism: Any valid FRB model must account for several observed properties - their high DM, large event rates, energetics, host galaxy properties, redshifts, etc. Although several potential progenitors have been proposed in

the literature (Zhang, 2020), the exact mechanism via which the FRB itself could be produced is not well-understood. The two most commonly invoked pathways by which one could produce an FRB are (1) magnetospheric interactions in pulsar-like compact objects and (2) relativistic shocks from GRB-like compact objects.

Like FRBs, pulsars produce coherent emission, making them an obvious choice for a theoretical starting point. However, magnetospheric plasma instability models struggle to reproduce the high brightness temperatures of FRBs (Lu, Kumar, 2018) and curvature radiation (Ruderman, Sutherland, 1975), while often invoked to explain FRBs, is difficult to maintain throughout the pulse duration (Kumar et al., 2017; Lu et al., 2020; Yang, Zhang, 2018). Most pulsar-like models require unusual circumstances, such as extreme magnetic and electric fields or volatile environments, to satisfy the observational constraints.

Similar to GRBs, a radio signal could be produced via relativistic shocks far outside the magnetosphere. These synchrotron maser models require large bulk Lorentz factors, Γ , magnetized shocks, and a compact central engine (Beloborodov, 2017; Lyubarsky, 2014). One common mechanism by which this radiation could be produced is via ultrarelativistic shock waves released through magnetar giant flares (Metzger et al., 2019).

Magnetar progenitors and SGR 1935-2154: FRB progenitor theories are complicated by the apparent discrepancy between repeating and non-repeating bursts - do they have the same progenitors? Or are they distinct from each other? In either situation neutron stars have long been favored as an explanation for FRBs due to their compact sizes, coherent emission mechanisms, and large all-sky rates.

(Bhandari et al., 2020; Bochenek et al., 2021; Heintz et al., 2020; Margalit et al., 2020)

Magnetars in particular offer several potential pathways to FRB production. Magnetars are highly-magnetized neutron stars with surface magnetic field strengths of $B_{\text{surf}} \sim 10^{14} - 10^{15}$ G (Duncan, Thompson, 1992). They are often classified as either soft gamma-ray repeaters (SGRs) or anomalous X-ray pulsars. Commonly invoked theories for powering FRBs include SGR 1806-20-like giant flares, magnetospheric shocks, magnetar remnants from core-collapse supernovae, and mergers between compact objects.

The simultaneous X-ray/FRB-like detection from SGR 1935-2154 provided the first observational proof that magnetars can produce FRBs (Mereghetti et al. 2020; The Chime/FRB Collaboration et al. 2020; Figure 1.9). Interestingly, SGR 1935-2154 is a common galactic magnetar implying that at least some FRBs do not require special or extreme conditions, although this also implies the fraction of galactic magnetars which produce FRB-like emission must be quite low (about 1 out of every 100, depending on expected timescales). Given that X-ray emission is known to be produced within the magnetosphere (Thompson, Duncan, 1995) pulsar-like emission mechanisms are then favored in this case for the FRB itself.

1.3 Connections between FRBs and GRBs

Given the relative newness of the field of FRBs and the lack of fundamental information it can be helpful to draw connections to the neighboring field of GRBs.

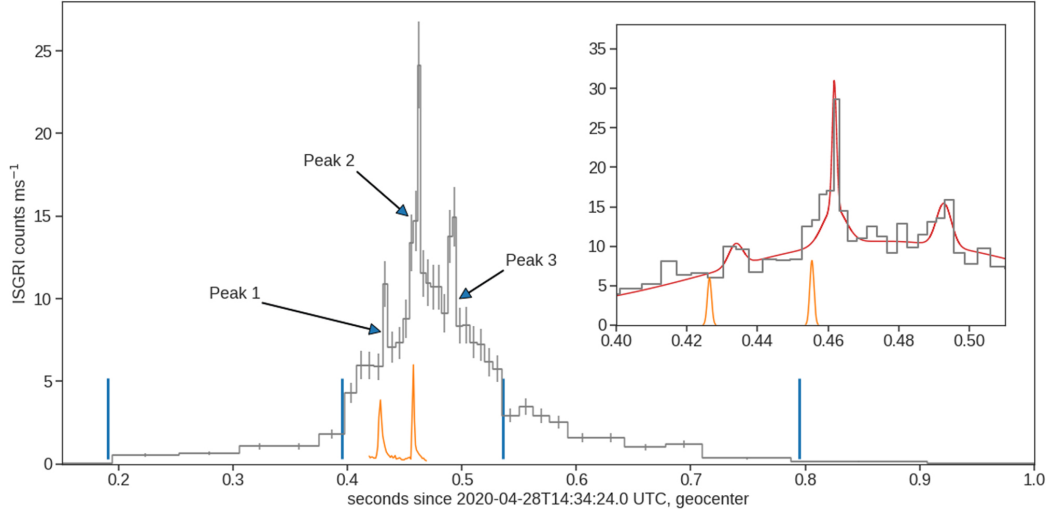


Figure 1.9: The 20-200 keV INTEGRAL light curve of SGR 1935-2154 (black) and radio pulses from CHIME (orange). The inset shows a zoomed-in portion of the pulse where the X-ray data have been fit (red) with a combination of Gaussian curves (Mereghetti et al. 2020).

As our understanding of FRBs evolves it appears that insight in that field may prove useful in regards to remaining GRB questions as well. Connections between the two fields include:

Recycling GRB theories for FRBs: Considering the large fluences, short timescales, dual populations (short versus long GRBs, repeating versus non-repeating FRBs), and isotropic distributions of both objects it was immediately obvious that some of the original theories proposed in the early days of GRBs could be recycled and applied to FRBs. These included both galactic theories - collisions with near-Earth objects, stellar flares from red dwarfs, pulsar giant flares - and extragalactic theories - collisions between compact objects, AGN flares. Although we now know that galactic magnetars produce FRB-like events, there still remains a debate over whether multiple classes of FRBs exist. If so, insights from GRBs may still be relevant in those cases especially regarding magnetar theories for SLSNe and long

GRBs.

Need for contemporaneous multiwavelength observations: Initially, both GRBs and FRBs were only observed at a single waveband - gamma-rays and radio waves, respectively. Progress within the field of GRBs only occurred after the detection of their multiwavelength afterglows. Indeed today, broadband observations are still necessary to perform proper GRB modeling and analysis. Likewise, multiwavelength counterparts will prove critical in understanding FRBs. Although one FRB now has a confirmed X-ray counterpart, the field still has a long ways to go and will require observation campaigns and rapid follow-up similar to that already in place for GRBs.

Remaining open ended questions regarding emission mechanism: Although the connections between short GRBs/compact object mergers and long GRBs/massive star collapse are well established, many questions remain regarding the emission mechanism which produces the GRB. The inner workings of neutron stars are active fields of research and major insights are yet to come. As we learn more about FRBs, the knowledge is likely to lead to progress in the field of GRBs as well.

1.4 Thesis Overview

The motivation for undertaking this thesis stems from the community-wide wave of excitement as we prepare for the next era in transient astronomy. The preparation for upcoming instruments such as the Vera Rubin Observatory ([Ivezić](#)

et al., 2019), the Nancy Grace Roman Telescope (Spergel et al., 2015), the James Webb Space Telescope (JWST; (Gardner et al., 2006)), and the Square Kilometer Array (SKA; Schilizzi et al. 2010) has fueled renewed interest in understanding all classes of transient objects, both long-standing and newer types. As such, this thesis will be structured as follows:

Chapter 2: A Search for High-energy Counterparts to Fast Radio Bursts

For FRBs - a much younger and far less well-understood field than GRBs - better localizations and working knowledge of their higher-energy counterparts are a necessary first step towards understanding their origins and role in the universe. Here, we complete an archival search for contemporaneous X-ray and gamma-ray signals from FRBs using the Burst Alert Telescope (BAT), the Gamma-ray Burst Monitor (GBM), and the Large Area Telescope (LAT). We place upper limits on the high-energy fluence produced during the event and lower limits on the ratio of the high-energy to radio fluence. We use the results of the search to constrain several possible FRB progenitor theories, including analogs of giant pulses from the Crab pulsar and hyperflares from magnetars.

Chapter 3: Evidence for a Gaussian-shaped Jet in GRB 160625B

For GRBs, our initial goals were to determine the true scale of GRB energetics via multiwavelength observations of their afterglows. This can often be difficult to do due to the lack of afterglow data from most GRBs. However, detailed analysis of the abundant broadband data associated with very bright bursts can help constrain their beaming angles and microphysical parameters, probe their birth environments, and

understand the role of the participation fraction - all of which are crucial information for understanding their central engines and relativistic jet mechanisms. Here, we model the afterglow of the exceptionally bright burst GRB 160625B with a range of structured jet models using the `afterglowpy` code described in §1.1.3. The multiwavelength data used in this analysis comes from previously published works, publicly available archives, and new observations. We use the results of the fitting to explore the role of different parameters in the modeling and to shed light on the GRB central engine.

Chapter 4: The Afterglows of *Fermi*-LAT GRBs: Jet Structure, Energetics, and Physical Origins

Here, we expand on the work outlined in Chapter 3 by applying our analysis to a larger sample of GRBs detected by the *Fermi* Large Area Telescope (LAT). GRBs detected by LAT have long been observed to be brighter and more energetic than GRBs detected by other instruments, but it is unclear whether this is because they are truly more energetic or rather because they are more narrowly beamed. The bright, multiwavelength afterglows of these GRBs provide the best opportunity to constrain their physical properties and origins. We again test multiple structured jet models on our sample of GRBs. The results of this analysis are used to test assumptions regarding LAT GRB energetics, their relativistic jet structure, and their progenitors.

Chapter 5: Summary and Future Directions

In Chapter 5, I summarize the main results of the thesis. I also outline plans,

both immediate and long-term, for future work within each field. Finally, I conclude by acknowledging the facilities and software used throughout this work.

Chapter 2: A Search for High-Energy Counterparts to Fast Radio Bursts

We report on a search for high-energy counterparts to fast radio bursts (FRBs) with the *Fermi* Gamma-ray Burst Monitor (GBM), *Fermi* Large Area Telescope (LAT), and the *Neil Gehrels Swift Observatory* Burst Alert Telescope (BAT). We find no significant associations for any of the 23 FRBs in our sample, but report upper limits to the high-energy fluence for each on timescales of 0.1, 1, 10, and 100 s. We report lower limits on the ratio of the radio to high-energy fluence, f_r/f_γ , for timescales of 0.1 and 100 s. We discuss the implications of our non-detections on various proposed progenitor models for FRBs, including analogs of giant pulses from the Crab pulsar and hyperflares from magnetars. This work demonstrates the utility of analyses of high-energy data for FRBs in tracking down the nature of these elusive sources.

2.1 Introduction

Fast radio bursts (FRBs) are bright (typical fluences of 2 Jy ms), short-duration (\sim few ms) pulses at frequencies of \sim 1 GHz (Lorimer et al., 2007; Thornton et al., 2013). FRBs can be distinguished from other short-duration radio pulses (e.g.,

pulsars) by their high dispersion measures (DM) for their Galactic latitude (100 to 2600 pc cm⁻³; [Petroff et al. 2016](#)). Because the DM derived for FRBs can be significantly in excess of the Galactic value (average of ~ 250 pc cm⁻³ for Galactic pulsars; [Manchester et al. 2016](#)), they must either reside in regions of large over-densities of free electrons if in the Milky Way or at extragalactic distances.

The first FRB was discovered in 2007 ([Lorimer et al., 2007](#)) and it was not until 2013 that their reality as a class of astrophysical objects was firmly established ([Thornton et al. 2013](#), c.f. perytons). Only ~ 70 FRBs have been published in the literature at the date of this publication (see the FRB Catalog (FRBCAT) at frbcatalog.org; [Petroff et al. 2016](#)). However, because these have been discovered by relatively narrow field-of-view instruments, the true all-sky rate is remarkable: ~ 6000 sky⁻¹ day⁻¹ above a fluence of \sim few Jy ms at ~ 1 GHz ([Champion et al., 2016](#); [Keane, Petroff, 2015](#); [Nicholl et al., 2017](#)). For comparison, this is much larger than the all-sky rate of gamma-ray bursts (\sim few per day at current detector sensitivities) and comparable to the rate of supernovae (core-collapse and thermonuclear) out to a redshift of $z \approx 0.5$ ([Li et al., 2011](#)).

Only two FRBs are known to exist as repeating bursts: FRB 121102 (“The Repeater”) and FRB 180814.J0422+73 ([Spitler et al., 2016](#); [The CHIME/FRB Collaboration et al., 2019](#)). FRB 180814.J0422+73 was reported as this work was being completed and so is not included in our following analysis. [Spitler et al. \(2016\)](#) report the detection of 12 bursts from the Repeater at 1.4 GHz from Arecibo and 5 bursts at 2 GHz from Green Bank, [Chatterjee et al. \(2017\)](#) report 9 bursts at 3 GHz from the Very Large Array (VLA), and [Scholz et al. \(2017a\)](#) report 8 bursts

at 2 GHz from Green Bank, 2 bursts at 1380 MHz from Arecibo, and 2 bursts seen by both telescopes. All repeating bursts display a consistent DM but can vary in pulse shape and spectral shape. The Repeater exhibits no evidence for periodicity, but instead appears to show episodes of enhanced activity (i.e., active and quiescent periods). Other FRBs have been reobserved, but none show repeated bursting as displayed by the two previously mentioned. In several cases it is possible to rule out repeat outbursts with the intensity and frequency of FRB 121102; however less frequent and/or fainter, repeated outbursts remain viable (Palaniswamy et al., 2018). It is therefore not currently known if all FRBs repeat, or if the known population comprises multiple classes of events (e.g., repeaters and non-repeaters; Fonseca et al. 2020).

Only the repeating FRB 121102 has been localized to within a host galaxy. No obvious host has yet been identified for FRB 180814.J0422+73. Chatterjee et al. (2017) use high angular resolution radio interferometry to place FRB 121102 within a dwarf galaxy at $z \sim 0.2$ (Tendulkar et al., 2017). The FRB location is consistent with a faint, persistent radio source of unknown origin (Chatterjee et al., 2017). While this result provides unprecedented insight into the physics of the repeating FRB, without detections from radio interferometers for the other FRBs it is impossible to localize them to such high precision using this method.

Despite being a recent discovery, FRBs have nonetheless piqued great interest in the area of high time-resolution radio astronomy. This excitement can be divided into two separate motivations: FRBs may become powerful probes of the intergalactic medium (IGM), and the emission mechanism powering these outbursts

may help clarify some long-standing issues in astrophysics, including the missing baryon problem and the nature of coherent emission (see below).

The large DM derived from FRBs suggest that the signals have encountered more free electrons than can be accounted for in the ISM of the Milky Way. While Galactic models resulting from a large local density of free electrons do exist (e.g., [Maoz et al. 2015](#)), the most natural explanation is that FRBs are of extragalactic origin (e.g., [Thornton et al. 2013](#)). In fact if all the DM were to result from electrons in the intergalactic medium (IGM), this would imply cosmological redshifts of $z \approx 0.5-1.0$ for these events.

The possibility of using FRBs to measure the density of free electrons at cosmological distances may offer a way to solve the “missing baryons” problem. In the local universe, only half of cosmic baryons reside at densities and temperatures that result in detectable emission and/or absorption ([Bregman, 2007](#); [Shull et al., 2012](#)). [McQuinn \(2014\)](#) demonstrates how the location of these baryons can be inferred from the distribution of DM (at a fixed redshift). Similarly, samples extending out to $z \approx 3$ with measured DM and redshift may even be able to constrain the equation of state of dark energy ([Zhou et al., 2014](#)).

In addition to their potential utility as cosmological probes, FRBs also offer a means to improve our understanding of coherent emission processes. Any source emitting incoherently (e.g., synchrotron radiation) cannot exceed a brightness temperature of 10^{12} K ([Readhead, 1994](#)). For a typical FRB with an intrinsic duration of 1 ms, causality limits the size of the emitting region to be less than 300 km barring bulk relativistic motion. For FRBs at distances of ~ 1 Gpc, the peak flux densities

of ~ 1 Jy at $\nu \sim 1$ GHz imply a brightness temperature of $T_B \gtrsim 10^{35}$ K. Clearly for FRBs $T_B \gg 10^{12}$ K, from which we infer that FRBs must be emitting coherent radiation. Only a handful of astronomical sources are known to radiate coherently, with pulsars being the most well-known example. Given the large uncertainties in the pulsar emission mechanism, the advent of FRBs offer the real hope of fundamental progress towards understanding coherent processes in this long-standing field.

As with many astronomical phenomena, the number of theoretical models has rapidly grown larger than the number of known FRBs. Here we consider several of the more plausible models, which must incorporate the following basic tenets: compact emission region, extragalactic distance scale, coherent emission mechanism, repeated outbursts from at least some FRBs, and large all-sky rates. We consider models for FRBs resulting from outbursting neutron stars (either magnetically or rotationally powered), as mergers between neutron star binaries, or as “cosmic combs”. We describe the models and their various predictions in greater detail in §2.3.

The goal of this paper is to search for possible counterparts at high-energy wavelengths to FRBs. We use data from the *Fermi* Gamma-ray Burst Monitor (GBM; Meegan et al., 2009), the *Fermi* Large Area Telescope (LAT; Atwood et al., 2009), and the *Neil Gehrels Swift Observatory* (Gehrels et al., 2004) Burst Alert Telescope (BAT; Barthelmy et al., 2005) to search for X-ray and gamma-ray (8 keV to 300 GeV) counterparts to FRBs. Although the energy range of the *Swift*-BAT overlaps with the *Fermi*-GBM we choose to include the BAT due to its arcminute localization, compared to the GBM. Scholz et al. (2016) use the same instruments to search for sources related to the repeating FRB but report no significant detec-

tions. They conducted another campaign coordinating observations between the Green Bank, Effelsberg, and Arecibo radio telescopes and the *Chandra X-ray Observatory* and *XMM-Newton* (Scholz et al., 2017b) but also report no significant X-ray detections. Their searches focus on a single FRB but our project extends to cover all FRBs within the field-of-view of each instrument as well as extending the timescales of interest that were analyzed. One advantage of this population study is the ability to potentially identify fundamental differences between repeating and non-repeating FRBs. There also exist upper limits for three FRBs from the INTEGRAL observatory (Savchenko et al., 2018a,b,c) which has comparable energy coverage to the *Fermi*-GBM and *Swift*-BAT. These limits are in agreement with the limits found here in this paper.

Tendulkar et al. (2016) place limits on the ratio of radio to gamma-ray emission for FRBs based on observations of SGR 106–20. We conduct a more sensitive search for high-energy counterparts in the GBM by employing the targeted search techniques developed for coincident searches for gravitational wave counterparts (Blackburn et al., 2015). We also use these ratios to compare our results with the proposed gamma-ray counterpart to FRB 131104 (DeLaunay et al., 2016). With the exception of the host galaxy for FRB 121102 (Chatterjee et al., 2017; Marcote et al., 2017; Tendulkar et al., 2017), no other electromagnetic analogs have so far been confirmed, despite rigorous efforts.

The detection of robust high-energy signals from FRBs would have a significant impact on the field as current theories predict widely differing high-energy fluences. Although a confirmed, positive detection of a high-energy counterpart

would definitively rule out many theories, a non-detection and corresponding upper limit could also eliminate many as well.

This paper is organized as follows: in §2.2 we describe the data products and analysis methods for calculating the high-energy upper limits for each FRB. In §2.3 we compare our results with various theories from the literature before we draw our conclusions in §2.4 on the likelihood and implications for each model. In this work we assume a standard Λ CDM cosmology and that the Milky Way is well-described by Galactic structure models such as NE2001 (Cordes, Lazio, 2002).

2.2 Data and Results

There are 23 published FRBs used in this analysis (taken from the FRBCAT) as of July 2017. 17 were detected with the Parkes Radio Telescope, 3 with UTMOST (Upgrade of The Molonglo Observatory Synthesis Telescope), 1 with the Arecibo Telescope, 1 with the Green Bank Telescope, and 1 with ASKAP (the Australian Square Kilometre Array Pathfinder). We search for contemporaneous high-energy emission from all these events with three different instruments: *Fermi*-GBM, *Fermi*-LAT, and *Swift*-BAT (see Table A.1 for a breakdown of available observations per FRB). We search for high-energy emission on a variety of different timescales. To place limits on a coincident (i.e., ms-long) pulse, we utilize the smallest time bin available from each relevant instrument. Where possible, we also place limits on timescales of 0-1 s, 0-10 s, and 0-100 s.¹ This spans the range from hyperflares of magnetars ($\Delta t \sim 0.1$ s) to short ($\Delta t \sim 1$ s) and long ($\Delta t \sim 10 - 100$ s) gamma-ray

¹We take the zero-point time, t_{frb} , as the arrival time of an infinite energy photon.

bursts (GRBs).

2.2.1 *Fermi*-GBM

The Gamma-ray Burst Monitor (GBM; [Meegan et al., 2009](#)) is a collection of hard-X-ray/soft gamma-ray detectors onboard the *Fermi Gamma-ray Space Telescope* sensitive to photons with energies from 8 keV to 40 MeV. *Fermi* is in a low-Earth (96 min) orbit, and the GBM is sensitive to gamma rays from the entire sky unoccluded by Earth when outside the South Atlantic Anomaly (SAA).

The GBM consists of two sets of detectors: twelve sodium iodide (NaI) scintillators cover a lower energy range from 8 keV to 1 MeV, and two bismuth germanate (BGO) scintillators cover the higher end from 300 keV to 40 MeV. The 12 NaI detectors are positioned to enable all-sky coverage, while the two omnidirectional BGO detectors are positioned on opposite sides of the spacecraft for the same reason. The 14 detectors are positioned in such a way that any burst should be seen by multiple detectors. The 12 NaI detectors are used for triggering and localization and the two BGO enable a broader energy range for spectroscopy. The rates received by each detector combined with their relative position and angle to each other allow the position of bursts to be determined to a few degrees accuracy ([Connaughton et al., 2015](#)).

Each of the 14 detectors in the GBM record several data products. The two of interest for this work are continuous time (CTIME) and time-tagged events (TTE).

The CTIME data are binned by 0.256 seconds with eight energy channels. The TTE data are continuous event data precise to 2 microseconds with 128 energy channels. Due to the short duration of FRBs, TTE data are preferred over CTIME; however continuous TTE data only started in 2012, so are not available for every FRB in our sample.

Of the 23 FRBs in our sample, 20 occurred after *Fermi*'s launch. Of those 20, 12 were visible to *Fermi* during good time intervals for GBM. Of the 38 repeat bursts of FRB 121102, 15 were visible to *Fermi* during good time intervals for GBM. To determine if a candidate counterpart exists in GBM data we ran a targeted search (Blackburn et al., 2015; Goldstein et al., 2016a) of GBM data around t_{frb} for ± 15 s for the 0.1 and 1.0 s timescales, ± 250 s for the 10 s timescales, and ± 400 s for the 100 s timescales (the 100 s timescale was only searched when the background was stable over periods of a few hundred seconds and had continuous TTE coverage).

The targeted search was designed to identify untriggered, faint, short GRB-like counterparts to gravitational-wave events, which makes it a useful tool to adapt to our purposes. We use the same three standard spectral templates described in Goldstein et al. (2016a), which generally cover the diverse range of short to long GRBs: a low-energy soft Band function (Band et al. 1993; $E_{\text{peak}} = 70$ keV), a medium-energy Band function ($E_{\text{peak}} = 230$ keV), and a power law with an exponential cutoff ($E_{\text{peak}} = 1.5$ MeV). While we calculate fluence upper limits for each of these three spectral types, the limits listed in this paper will be given for the hardest template. On average, this harder spectral template results in a factor of ~ 2.5 times the fluence of the medium-energy template and ~ 5 times the fluence of

the low-energy template.

We employ the Bayesian likelihood analysis originally developed by [Blackburn et al. \(2015\)](#) to search for contemporaneous signals around the FRB radio detections. This method calculates the likelihood of a signal matching one of the three spectral templates compared to the null hypothesis of a constant background. Owing to the highly transient universe in the gamma-ray band and GBM’s all-sky coverage there were a few real transient gamma-ray signals in GBM during time intervals of interest; however, these are known to be unrelated due to inconsistent sky localizations or classification as a known source type (e.g., a solar flare). No possibly related signal is significant over the total lifetime of the search (See the Appendix for more detail on these unrelated signals).

In the absence of any correlated gamma-ray signal with the FRBs, we estimate flux upper limits in the search time windows around each t_{frb} on timescales of 0.1, 1, 10, and 100 s using the same spectral templates that were used by the targeted search. These conservative upper limits were calculated by utilizing the NaI detector with the smallest normal angle to the FRB, and estimating the maximum 3σ count rate flux upper limit in the window based on the modeled background noise. The count rate upper limit was then converted to a flux upper limit by assuming each of the template spectra, folding them through the GBM detector responses calculated for the FRB sky location, and fitting for the amplitude of the template spectra. This procedure results in 3σ flux upper limits listed in [Table 2.1](#). Five of these FRBs are analyzed by [Tendulkar et al. \(2016\)](#) where the limiting gamma-ray fluence is estimated to be 1×10^{-8} erg cm⁻², roughly consistent with the faintest known short

GRBs detected by GBM. The targeted search used here provides consistent, though slightly shallower, limits to [Tendulkar et al. \(2016\)](#).

In addition, we consider the results derived from performing a stacking analysis of the bursts from the Repeater and a separate stacking analysis of the bursts from the non-repeating FRBs. In the case of the non-repeating FRBs we assume that all FRBs are approximately at the same redshift ($z = 0.1 - 0.3$). This assumption will be justified in §2.3 where each of the models we consider in this work limits the distance of the FRBs to no further than ~ 1 Gpc. We find no obvious potential signals which would warrant any further stacking analysis for either case.

2.2.2 *Fermi*-LAT

The Large Area Telescope (LAT; [Atwood et al., 2009](#)) is a pair-conversion telescope on board the *Fermi* satellite, sensitive to gamma rays with energies between 20 MeV and more than 300 GeV. The LAT has a wide field-of-view (FOV), scans continuously and covers approximately 20% of the sky at any given time. The LAT completes all-sky coverage every two orbits over a duration of about three hours. The timing accuracy of the LAT is better than $10 \mu\text{s}$ and its localization precision is highly energy-dependent ($\sim 5'$ for GeV photons).

We search the *Fermi*-LAT data for gamma-ray counterparts by performing an unbinned likelihood analysis using the standard analysis tools developed by the LAT team (ScienceTools version v10r01p0).² For this analysis, we use the

²<http://fermi.gsfc.nasa.gov/ssc/>

‘P8R2_TRANSIENT_V6’ instrument response functions and select ‘Transient’ class events in the 0.1–100 GeV energy range from a 12° radius energy-independent region of interest (ROI) centered on the FRB location. The size of the ROI is chosen to reflect the 95% containment radius of the LAT energy-dependent point spread function at 100 MeV. The ‘Transient’ event class is chosen because it represents looser cuts against non-photon background contamination and is typically used to study GRBs on very short timescales (Ackermann et al., 2012).

In standard unbinned likelihood analysis, the observed distribution of counts at a particular position is fit to a model that includes all known gamma-ray sources in the 3FGL catalog (Acero et al., 2015) within a radius of 30° , as well as Galactic and isotropic background components.³ The Galactic component, *gll_iem_v06*, is a spatial and spectral template that accounts for interstellar diffuse gamma-ray emission from the Milky Way. The isotropic component, *iso_transient_v06*, provides a spectral template to account for all remaining isotropic emission including contributions from both residual charged particle backgrounds and the isotropic celestial gamma-ray emission. Possible emission from a FRB is modeled as an uncatalogued point source with a power law spectrum where the normalization and photon index are left as free parameters. A likelihood-ratio test is then employed to quantify whether there exists a significant excess of counts due to the uncatalogued point source above the expected background model. If no significant new source is found, we calculate the 95% confidence level upper limits using a Bayesian method described in Ackermann et al. (2016), which we convert to a fluence limit for the rel-

³<https://fermi.gsfc.nasa.gov/ssc/data/access/lat/BackgroundModels.html>

evant timescale. Note that these fluence limits are calculated via a different method than we use for the GBM (§2.2.1) and BAT (§2.2.3) data.

The three earliest FRBs are again excluded from our analysis since they occurred before *Fermi* was launched on June 11, 2008. Of the remaining 19 non-repeating FRBs, six are located within the LAT FOV at the time of radio detection. Five of the 38 repeating bursts are in the LAT FOV as well. We examine two time intervals based on the zero-point detection time, t_{FRB} : 0 – 10 s and 0 – 100 s (Table 2.1). No photons are detected for any of the FRBs within 1 second of the initial burst.

2.2.3 *Swift*-BAT

The *Neil Gehrels Swift Observatory* (Gehrels et al., 2004) Burst Alert Telescope (BAT) is a coded-aperture instrument dedicated to triggered hard X-ray observations of GRBs. The BAT detectors have an energy range of 15 to 300 keV with a resolution of ~ 7 keV, a large FOV of 1.4 steradians (half-coded) and a positional accuracy of $\sim 3'$ (Barthelmy et al., 2005). Although the detectors are sensitive up to 300 keV, the coded mask is transparent to photons above 150 keV and so is unable to determine their direction from the sky. When running in survey mode, BAT collects detector plane histograms that are binned in ~ 300 s. These detector plane histograms can be used to generate sky images and search for sources in the BAT FOV. In addition to these spatially-resolved images, BAT

also collects raw rate data from all of the enabled detectors. The raw rate data are a continuous stream of events which can be used to search for GRB triggers not in the BAT FOV. We analyze both the five-minute time-binned survey images and the 64 ms-binned, four energy band (15-25 keV, 25-50 keV, 50-100 keV, and 100-350 keV) rate data lightcurves using the standard *Swift*-specific tools provided by the HEASoft package (version 6.18).

Only FRB 110626, FRB 150215, and FRB 160410 were within the BAT FOV at the time of radio detection. The three earliest FRBs occurred prior to *Swift*'s launch on November 20, 2004 so they are excluded from the analysis. Of the 19 non-repeating FRBs examined 10 of the bursts were out of the FOV, and one did not occur during recorded observations (i.e., the telescope was most likely slewing to a new location), 3 were within the FOV while the BAT was in the SAA, and 1 occurred while the BAT was slewing. 30 of the 38 repeating signals from FRB 121102 were not within the FOV at the time of detection and six occurred while the BAT was in the SAA. Three of the bursts (FRB 131104 and bursts 2 and 3 of FRB 121102) were located right on the edge of the BAT FOV but are excluded from analysis due to their low partial coding fraction. It is standard practice to remove pointings with partial coding fractions corresponding to less than 10% of the array being illuminated (Krimm et al., 2013).⁴

The survey images provide more accurate positional information compared to the rate data. The rate data are the cumulative sum of all counts seen within and

⁴DeLaunay et al. (2016) report a *Swift*-BAT counterpart to FRB 131104 with a partial coding fraction of 2.9%. A more detailed analysis of this event is currently underway for a separate work (Sakamoto et al., in prep).

around the BAT FOV. It can be difficult to definitively attribute a significant rise in counts to any single FRB as it could also be due to a nearby source. In the survey images the precise timing information is lost due to the 300-second binning of the counts. While the rate data are useful for identifying sudden significant changes in the aggregate background emission on short timescales, the survey images are more accurate for producing limits for the specific FRB locations. The fluence limits derived from the rate data are shallower than, yet still consistent with, the limits derived from the survey images.

We find no significant counterpart detections at 3σ confidence level for FRB 110626, FRB 150215, and FRB 160410, but we are able to determine upper limits to the high-energy fluence. We produce 8-channel spectra using the mask-weighted background variation counts detected in the survey images, and estimate the flux that would have been equivalent to a 3σ detection. Assuming a simple power law function with index 2.0 for the FRB spectra, we calculate an estimate of the flux within XSPEC based on the spectral fit over an energy range of 15 to 350 keV (Arnaud, 1996). We use the FRB location on the BAT FOV to generate the instrument response matrix corresponding to the respective grid ID on the BAT detector (Lien et al., 2014). The fluence limits are listed in Table 2.1 for 300-second timescales. Here we find comparable limits for those same FRBs analyzed by Tendulkar et al. (2016) with *Swift*-BAT.

For comparison we also examine the raw rate data for FRB 150215 and

FRB 160410.⁵ We model the rate background emission over a total of 500 seconds as a linear fit in time. If necessary we use a low-order polynomial fit instead. We compute the root mean square of the background level in 200 second duration bins at ± 50 seconds from the time region of interest and denote the total number of counts in the bins as N_{bins} . We assume that the scatter within the region of interest also follows this scatter as well. From there we calculate 3σ upper limits on the count rate assuming Poisson statistics. We then use XSPEC to convert the count rate limit to a fluence over the same energy range as the survey data. We find consistent results between the event rate data and survey images.

Table 2.1: 3σ upper limits to f_γ in different time ranges and energy bands for each FRB. Values listed for f_γ are the fluence for the spectral template of a power law with an exponential cutoff ($E_{peak} = 1.5$ MeV). We also explore two softer spectral templates. See §2.2.1 for more information.

FRB Name	Bandpass	Date [yyyy-mm-dd]	Time [hh:mm:ss]	RA	Dec	Δt [s]	f_γ [$10^{-6} \frac{\text{erg}}{\text{cm}^2}$]
090625	8 keV-40 MeV	2009-06-25	21:53:51	46.95	-29.93	100	<7.9
						10	<2.5
						1	<0.82
						0.1	<0.28
110523	8 keV-40 MeV	2011-05-23	15:06:20	326.30	-0.16	100	<7.5
						10	<2.3
						1	<0.76
						0.1	<0.26
110626	8 keV-40 MeV	2011-06-26	21:33:16	315.75	-44.73	100	<7.5
						10	<2.3
						1	<0.76
						0.1	<0.26
110703	8 keV-40 MeV	2011-07-03	18:59:39	352.50	-2.87	100	<8.2
						10	<2.6
						1	<0.84

continued . . .

⁵A flare from a nearby X-ray binary occurred at the same time as FRB 110626 and so we exclude those results for the rate data here.

... continued

FRB Name	Bandpass	Date [yyyy-mm-dd]	Time [hh:mm:ss]	RA	Dec	Δt [s]	f_γ [$10^{-6} \frac{\text{erg}}{\text{cm}^2}$]
						0.1	<0.29
130628	8 keV-40 MeV	2013-06-28	03:57:59	135.76	3.44	100	<6.6
						10	<2.1
						1	<0.7
						0.1	<0.24
130729	8 keV-40 MeV	2013-07-29	09:01:51	205.34	-6.00	100	<7.1
						10	<2.3
						1	<0.75
						0.1	<0.26
131104	8 keV-40 MeV	2013-11-04	18:04:00	101.04	-51.28	100	<8.4
						10	<2.7
						1	<0.87
						0.1	<0.3
150215	8 keV-40 MeV	2015-02-15	20:41:39	274.36	-4.90	100	<7.0
						10	<2.2
						1	<0.73
						0.1	<0.25
150418	8 keV-40 MeV	2015-04-18	04:29:05	109.12	-19.04	100	<7.1
						10	<2.3
						1	<0.74
						0.1	<0.25
150807	8 keV-40 MeV	2015-08-07	17:53:55	340.10	-55.27	100	<6.9
						10	<2.2
						1	<0.73
						0.1	<0.25
160317	8 keV-40 MeV	2016-03-17	09:00:30	118.45	-29.61	100	<7.0
						10	<2.2
						1	<0.73
						0.1	<0.25
160608	8 keV-40 MeV	2016-06-08	03:52:57	114.17	-40.80	100	<7.7
						10	<2.4
						1	<0.79
						0.1	<0.27
121102 3	8 keV-40 MeV	2015-05-17	17:51:41	82.99	33.15	100	<7.6
						10	<2.4
						1	<0.78
						0.1	<0.26
121102 4	8 keV-40 MeV	2015-06-02	16:38:08	82.99	33.15	100	<6.5
						10	<2.1
						1	<0.69
						0.1	<0.24
121102 5	8 keV-40 MeV	2015-06-02	16:47:36	82.99	33.15	100	<6.7
						10	<2.1

continued ...

... continued

FRB Name	Bandpass	Date [yyyy-mm-dd]	Time [hh:mm:ss]	RA	Dec	Δt [s]	f_γ [$10^{-6} \frac{\text{erg}}{\text{cm}^2}$]
						1	<0.69
						0.1	<0.24
121102 17	8 keV-40 MeV	2015-12-08	04:54:40	82.99	33.15	100	<7.2
						10	<2.3
						1	<0.75
						0.1	<0.25
121102 18	8 keV-40 MeV	2016-08-23	17:51:24	82.99	33.15	100	<7.6
						10	<2.4
						1	<0.79
						0.1	<0.26
121102 19	8 keV-40 MeV	2016-09-02	16:19:00	82.99	33.15	100	<7.2
						10	<2.3
						1	<0.76
						0.1	<0.26
121102 20	8 keV-40 MeV	2016-09-02	16:41:02	82.99	33.15	100	<7.7
						10	<2.4
						1	<0.79
						0.1	<0.27
121102 21	8 keV-40 MeV	2016-09-07	11:59:06	82.99	33.15	100	<8
						10	<2.6
						1	<0.84
						0.1	<0.29
121102 22	8 keV-40 MeV	2016-09-12	10:58:31	82.99	33.15	100	<7.3
						10	<2.4
						1	<0.78
						0.1	<0.26
121102 24	8 keV-40 MeV	2016-09-15	11:11:03	82.99	33.15	100	<7.5
						10	<2.4
						1	<0.78
						0.1	<0.27
121102 27	8 keV-40 MeV	2016-09-17	10:29:09	82.99	33.15	100	<7
						10	<2.2
						1	<0.73
						0.1	<0.25
121102 28	8 keV-40 MeV	2016-09-18	04:10:17	82.99	33.15	100	<8
						10	<2.5
						1	<0.83
						0.1	<0.28
121102 29	8 keV-40 MeV	2016-09-18	05:14:14	82.99	33.15	100	<8.5
						10	<2.7
						1	<0.89
						0.1	<0.3
121102 33	8 keV-40 MeV	2017-01-12	01:39:26	82.99	33.15	100	<7.2

continued ...

... continued

FRB Name	Bandpass	Date [yyyy-mm-dd]	Time [hh:mm:ss]	RA	Dec	Δt [s]	f_γ [$10^{-6} \frac{\text{erg}}{\text{cm}^2}$]
						10	<2.3
						1	<0.76
						0.1	<0.26
121102 34	8 keV-40 MeV	2017-01-12	02:25:12	82.99	33.15	100	<6.6
						10	<2.1
						1	<0.69
						0.1	<0.24
121102 35	8 keV-40 MeV	2017-01-12	02:36:30	82.99	33.15	100	<6.8
						10	<2.2
						1	<0.72
						0.1	<0.25
121102 37	8 keV-40 MeV	2017-01-12	03:16:33	82.99	33.15	100	<6.8
						10	<2.2
						1	<0.71
						0.1	<0.24
121102 38	8 keV-40 MeV	2017-01-12	03:26:24	82.99	33.15	100	<7.5
						10	<2.3
						1	<0.75
						0.1	<0.25
090625	60 MeV-100 GeV	2009-06-25	21:53:51	46.95	-29.93	100	<0.31
130628	60 MeV-100 GeV	2013-06-28	03:57:59	135.76	3.44	100	<0.83
150215	60 MeV-100 GeV	2015-02-15	20:41:39	274.36	-4.90	100	<1.5
150418	60 MeV-100 GeV	2015-04-18	04:29:05	109.12	-19.04	100	<0.31
160317	60 MeV-100 GeV	2016-03-17	09:00:30	118.45	-29.61	100	<0.77
160608	60 MeV-100 GeV	2016-06-08	03:52:57	114.17	-40.80	100	<0.38
121102 18	60 MeV-100 GeV	2016-08-23	17:51:24	82.99	33.15	100	<0.45
121102 19	60 MeV-100 GeV	2016-09-02	16:19:00	82.99	33.15	100	<1.4
121102 22	60 MeV-100 GeV	2016-09-12	10:58:31	82.99	33.15	100	<0.73
121102 27	60 MeV-100 GeV	2016-09-17	10:29:09	82.99	33.15	100	<0.5
121102 34	60 MeV-100 GeV	2017-01-12	02:25:12	82.99	33.15	100	<1.4
110626	15-350 keV	2011-06-26	21:33:16	315.75	-44.73	300	<4.8
150215	15-350 keV	2015-02-15	20:41:39	274.36	-4.90	300	<2.3
						100	<0.065
						10	<0.055
						1	<0.027
						0.064	<0.0092
160410	15-350 keV	2016-04-10	08:33:38	130.35	6.08	300	<1.6
						100	<0.17
						10	<0.08
						1	<0.021
						0.064	<0.0048

2.3 Analysis and Interpretation

We report no significant excess in high-energy emission from the *Fermi*-GBM, *Fermi*-LAT, or *Swift*-BAT for any of the individual FRBs or repeats from FRB 121102. The expected high-energy fluence from FRBs is highly model-dependent. Given the number of theories in the literature we take a two-fold approach in this work. First, we compare our results with previously reported observations of high-energy counterparts to FRBs, such as that claimed for FRB 131104. Second, we consider the implications of our non-detections for some of the more plausible models that have been considered.

2.3.1 Limits on the Ratio of Radio to Gamma-ray Fluence

A recent paper by DeLaunay et al. (2016) reports a possible connection of FRB 131104 to a *Swift*-BAT long GRB with fluence $f_\gamma \approx 4 \times 10^{-6} \text{ erg cm}^{-2}$ and duration $T_{90} = 377 \text{ s}$, where T_{90} is defined as the time over which a burst emits from 5% of its total measured counts to 95%. With the reported radio fluence for FRB 131104 of 2.33 Jy ms, this implies a ratio of radio to gamma-ray emission of $\approx 6 \times 10^5 \text{ Jy ms erg}^{-1} \text{ cm}^2$. For consistency with the DeLaunay result we consider fluences on 100 s timescales. The radio fluences are taken from the FRBCAT. We find that $f_r/f_\gamma \gtrsim 10^5 - 10^7 \text{ Jy ms erg}^{-1} \text{ cm}^2$ for the non-repeating FRBs in our sample and we find $f_r/f_\gamma \gtrsim 10^4 - 10^5 \text{ Jy ms erg}^{-1} \text{ cm}^2$ for the repeating bursts of FRB 121102 (Table 2.2). None of the limits derived from the *Swift*-BAT or

Fermi-LAT are consistent with the DeLaunay result, providing lower limits to the radio to gamma-ray emission ratio that exceed their reported values. However nine out of the eleven non-repeating FRBs and all of the repeating bursts from the *Fermi*-GBM are consistent.

We then compare our limits to those expected from magnetar hyperflares (see §2.3.2.2), given observations of SGR1806–20. [Tendulkar et al. \(2016\)](#) find upper limits of $f_r/f_\gamma < 10^7$ Jy ms erg⁻¹ cm² for the giant flare event on December 27, 2004, based on archival observations of FRBs taken with the Konus-Wind gamma-ray spectrometer, the *Swift*-BAT, and the *Fermi*-GBM. Although the timescales and the bandpass of the Konus-Wind (10 keV to 10 MeV) are not identical to our analysis, this is inconsistent with four of the non-repeating FRBs yet consistent with all of the repeating bursts (10 in our sample) for limits on timescales of order 0.1 s (Table 2.2).

We also compare our ratios to those of [Scholz et al. \(2017b\)](#) who find a lower limit on f_r/f_γ of $> 2 \times 10^8$ based on *Fermi*-GBM observations of the Repeater. Although they look at bursts on finer timescales of a few hundred milliseconds this is consistent with all of our *Fermi*-GBM limits on timescales of 0.1 s.

Table 2.2: Maximum 3σ ratio of radio to high-energy emission on 100 s and 0.1 s timescales.

FRB Name	Bandpass	Δt [s]	f_r [Jy ms]	f_γ [10 ⁻⁶ erg cm ⁻²]	$\log(f_r/f_\gamma)$ [Jy ms erg ⁻¹ cm ²]
090625	8-4e4 keV	100	2.19	<7.9	>5.44
		0.1		<0.28	>6.89
110523	8-4e4 keV	100	1.04	<7.5	>5.14
		0.1		<0.26	>6.60

continued ...

... continued

FRB Name	Bandpass	Δt [s]	f_r [Jy ms]	f_γ [10^{-6} erg cm^{-2}]	$\log(f_r/f_\gamma)$ [Jy ms erg^{-1} cm^2]
110626	8-4e4 keV	100	0.56	<7.5	>4.88
		0.1		<0.26	>6.33
110703	8-4e4 keV	100	1.80	<8.2	>5.34
		0.1		<0.29	>6.80
130628	8-4e4 keV	100	1.22	<6.6	>5.26
		0.1		<0.24	>6.70
130729	8-4e4 keV	100	3.43	<7.1	>5.68
		0.1		<0.26	>7.13
131104	8-4e4 keV	100	2.33	<8.4	>5.45
		0.1		<0.3	>6.89
150215	8-4e4 keV	100	1.96	<7	>5.45
		0.1		<0.25	>6.90
150418	8-4e4 keV	100	1.76	<7.1	>5.39
		0.1		<0.25	>6.84
150807	8-4e4 keV	100	44.80	<6.9	>6.81
		0.1		<0.25	>8.26
160317	8-4e4 keV	100	69.00	<7	>7.00
		0.1		<0.25	>8.44
160608	8-4e4 keV	100	37.00	<7.7	>6.68
		0.1		<0.27	>8.14
121102 3	8-4e4 keV	100	0.10	<7.6	>4.12
		0.1		<0.26	>5.58
121102 4	8-4e4 keV	100	0.20	<6.5	>4.49
		0.1		<0.24	>5.93
121102 5	8-4e4 keV	100	0.09	<6.7	>4.13
		0.1		<0.24	>5.58
121102 17	8-4e4 keV	100	0.09	<7.2	>4.10
		0.1		<0.25	>5.55
121102 28	8-4e4 keV	100	0.36	<8	>4.65
		0.1		<0.28	>6.11
121102 29	8-4e4 keV	100	0.29	<8.5	>4.53
		0.1		<0.3	>5.98
121102 33	8-4e4 keV	100	0.62	<7.2	>4.93
		0.1		<0.26	>6.38
121102 35	8-4e4 keV	100	0.03	<6.8	>3.65
		0.1		<0.25	>5.09
121102 37	8-4e4 keV	100	0.22	<6.8	>4.51
		0.1		<0.24	>5.96
121102 38	8-4e4 keV	100	0.10	<7.5	>4.13
		0.1		<0.25	>5.60
090625	60-1e5 MeV	100	2.19	<0.31	>6.85
130628	60-1e5 MeV	100	1.22	<0.83	>6.17
150215	60-1e5 MeV	100	1.96	<1.5	>6.10

continued ...

...continued

FRB Name	Bandpass	Δt [s]	f_r [Jy ms]	f_γ [10^{-6} erg cm $^{-2}$]	$\log(f_r/f_\gamma)$ [Jy ms erg $^{-1}$ cm 2]
150418	60-1e5 MeV	100	1.76	<0.31	>6.75
160317	60-1e5 MeV	100	69.00	<0.77	>7.95
160608	60-1e5 MeV	100	37.00	<0.38	>7.99
150215	15-350 keV	100	1.96	<0.065	>7.48
		0.1		<0.0092	>5.60
160410	15-350 keV	100	34.00	<0.17	>8.29
		0.1		<0.0048	>9.85

2.3.2 Constraints on Theoretical Models

Given that there are dozens of theories put forth attempting to explain FRBs, because of their implied small sizes (<300 km), we choose to favor models involving compact objects like neutron stars. We cannot examine all models in our analysis here so we consider only those models which satisfy the criteria of a compact emission region, extragalactic distance scale, coherent emission mechanism, repeated outbursts from at least some FRBs, and large all-sky rates. Here we consider the ramifications of our results in reference to some of the more probable theories.

2.3.2.1 Rotationally-powered Pulses from Neutron Stars

The Crab pulsar exhibits rare, giant radio pulse behavior at GHz frequencies. Giant pulse occurrences are random in time but are correlated with the pulsar's main pulse or interpulse periods. About 1% of pulses from the Crab are giant pulses. These giant bursts can exceed 0.5 MJy over a duration of a few nanoseconds

(Cordes, Wasserman, 2016). The most extreme event was a 0.4 ns pulse with a flux density of 2.2 MJy at 9 GHz (Hankins, Eilek, 2007). The short durations, large fluxes, and non-periodic nature of giant pulses make them an excellent test for comparison with FRBs.

The Crab emits across all frequencies and also exhibits giant pulse behavior in the gamma- and X-ray as well (Bühler, Blandford, 2014). Mickaliger et al. (2012) examine the correlation between radio giant pulses and high-energy photons from 0.1 to 100 GeV and find no significant association.

If FRBs are powered by giant pulses from pulsars then we would expect them to be nearby. Cordes, Wasserman (2016) show that even the most extreme giant pulse from the Crab could not provide the necessary radio fluences of ~ 2 Jy ms at 1 Gpc (the reported distance of the Repeater). For these observed fluences they find a maximum distance for Crab-like giant pulses of ~ 100 Mpc.

An extremely energetic burst of gamma rays from the Crab occurred in April 2011 with a luminosity of $L_\gamma = 4 \times 10^{36}$ erg s⁻¹ (Buehler et al., 2012; Striani et al., 2011). If we assume this energy scale for FRBs, then at 1 Gpc we would expect to observe a fluence around 20 orders of magnitude fainter than the background level. The expected flux density is orders of magnitude too small at 1 Gpc to account for the radio emission observed. However, if indeed the FRBs are located at these Galactic distances this would imply that most of the DM is local to the source, rather than from the IGM. Although the distances derived here are inconsistent with that of the Repeater we still consider giant Crab-like pulses as a viable model for FRBs since the energy scale and lack of high-energy emission are consistent

with that observed for FRBs.

2.3.2.2 Magnetically-powered Pulses from Neutron Stars

Magnetars are highly-magnetized neutron stars with surface magnetic field strengths of $B_{\text{surf}} \sim 10^{14} - 10^{15}$ G (Duncan, Thompson, 1992). They are known to regularly emit hard X-ray/soft gamma-ray flares of duration < 1 s with total energy 10^{41} erg (Kouveliotou et al., 1998). Distinct from these “average flares”, magnetars can also emit hyperflares which are several orders of magnitude higher in energy. A hyperflare is marked by a millisecond rise time, hard X-ray peak, and an oscillating tail lasting for minutes. Although there are ~ 30 magnetars known to date, there are only three observed hyperflare events, with the SGR 1806–20 event being the most energetic (Hurley et al., 2005, 1999; Mazets et al., 1979; Palmer et al., 2005).

Magnetar hyperflares are a popular theory for FRBs (Kulkarni et al., 2015; Lyubarsky, 2014; Pen, Connor, 2015; Popov, Postnov, 2013). They have sub-second time variation, extreme energetics, and (depending on assumptions made about the underlying magnetar population) comparable event rates (Nicholl et al., 2017). Magnetars are thought to be correlated with recent star formation and should therefore be enshrouded in dense gas and dust. This would imply a significant portion of an FRB’s DM can be attributed to its local environment, rather than to the IGM, placing them at extragalactic, but not necessarily cosmological, distances. The properties of the host galaxy of the repeating FRB (e.g., a low mass, low

metallicity, star-forming dwarf galaxy at redshift $z \sim 0.2$) is consistent with where we might expect to find magnetars (Tendulkar et al., 2017).

If FRBs are caused by magnetar-like hyperflares we can place constraints on their distances by assuming a similar energy release to the SGR1806–20 event. The total flare energy of this event is 10^{47} erg and could only have been observed out to 40 Mpc before falling below the threshold of most X-ray/gamma-ray telescopes. Figure 2.1 shows the inferred E_γ for each FRB at different distances, neglecting k-corrections.⁶ We can be conservative and consider possibilities that other hyperflares could be stronger than the SGR1806–20 event, therefore pushing the maximum energy release to $E_\gamma = 10^{49}$ erg. For fluence upper limits set by the harder spectral template in GBM we find the FRBs should be located no nearer than about 0.5 Gpc, which is consistent with the distance of the Repeater at 1 Gpc.

There are a few caveats with this picture. One is that, based on the SGR1806–20 event, we may not expect to see any radio emission from these hyperflares (see §2.3.1). On the other hand, Lyutikov (2002) proposes a model where radio counterparts could be seen at ~ 1 Gpc distances. We note that we are extrapolating the properties of all giant magnetar flares from a total sample of three and that it is impossible to yet know what other subclasses of magnetar hyperflares might actually exist. Another issue with the theory is that, based on constraints from the DM, optical depth, and expansion of the supernova (SN) ejecta surrounding the magnetar, the age of the source must be less than 100 years (Metzger et al.,

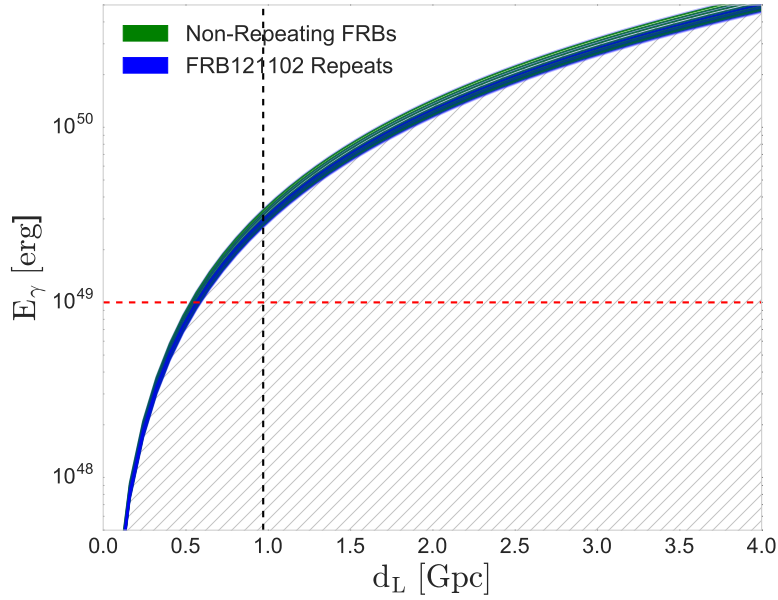
⁶K-corrections allow a conversion between a measurement at a redshift, z , to its equivalent rest-frame value.

2017). This implies that as the remnant expands in time we should expect to see the observed DM evolve as well, despite there being no such evidence for this based on the DM of the repeating bursts from FRB 121102. However, given these caveats we still consider the theory that FRBs originate as magnetar hyperflares as plausible.

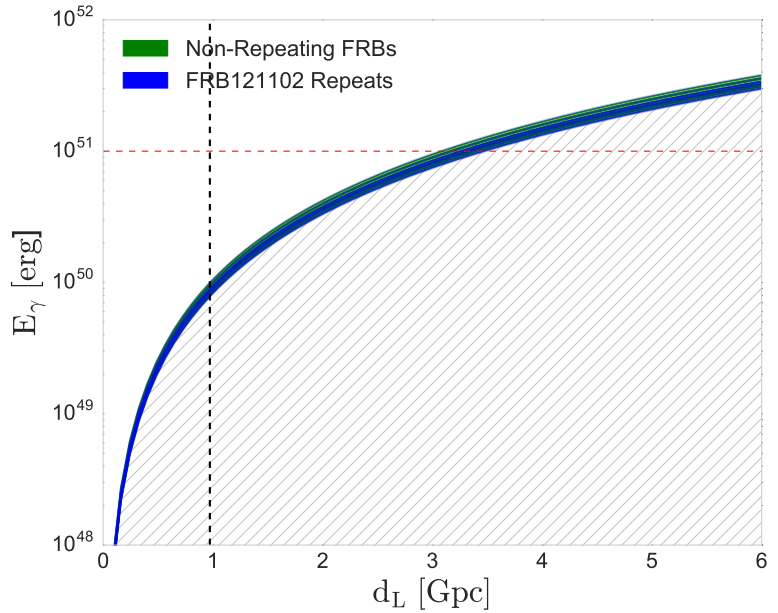
2.3.2.3 Coalescence Models

[Dokuchaev, Eroshenko \(2017\)](#) propose a model where FRBs are caused by collisions between neutron stars in the centers of evolved galaxies. This coalescence is suggested to generate short GRBs and the extreme energies produced have led some to suggest they could also power FRBs ([Berger, 2014](#); [Takami et al., 2014](#)). The model predicts that a binary merger is not necessary to generate an FRB signal. As the neutron stars inspiral, their magnetic fields become synchronized with the binary rotation. This can result in magnetic reconnections which produce coherent radio emission.

The inferred rate of FRBs is much higher than that of neutron star - neutron star mergers. Only the most optimistic binary neutron star merger rates could begin to compare with the lowest expected FRB rates ([Callister et al., 2016](#)). Assuming this is the case however would imply that the majority of binary neutron star mergers will result in an observable FRB. This is in apparent conflict with the small number of known FRBs - only 70 to date (FRBCAT) - and the lack of any associated FRB with the recent GRB170817A/GW 170817 event ([Abbott et al.,](#)



(a)



(b)

Figure 2.1: Given the fluence upper limits on varying timescales (Table 2.1) we can predict how far away FRBs can be observed as predicted by different models. The hatched pattern represents viable parameter space. The black dashed line is the reported distance of the host galaxy of FRB 121102. (a.) The red dashed line represents the energy cut-off for magnetar hyperflares ($E_\gamma < 10^{49}$ erg). (b.) The red dashed line represents the energy cut-off for coalescence models ($E_\gamma < 10^{51}$ erg).

2017c). However we caution that radio observations of GW170817 did not begin until approximately 12 hours after the merger, making firm conclusions difficult to draw.

With the notable exception of GRB170817A (a highly sub-luminous event; Abbott et al. 2017b), the prompt isotropic energy release of short GRBs is $\sim 10^{51} - 10^{52}$ erg (Berger, 2014). The divide between short and long GRBs occurs at about 2 s (Kouveliotou et al., 1993), so therefore we consider time scales of high-energy emission of 1 s. We take a similar approach to the magnetar model and constrain distances out to which we should expect to see FRBs if they are powered by coalescence (Figure 2.1). We find that colliding neutron stars must reside outside of ~ 3 Gpc to account for the lack of detected high-energy emission we observe. This is inconsistent with the FRB 121102 result and the observed DMs of the other FRBs. If we attribute all of the observed DM to propagation through the IGM then we would expect FRBs to reside at distances of no more than ~ 3 Gpc (Thornton et al., 2013). In addition, low-luminosity, GRB170817A-like events must be located at distances further than a few hundred Mpc to account for a lack of radio emission. This is inconsistent with the merger’s reported distance of only 40 Mpc (Abbott et al., 2017c).

If FRBs are the result of collisions between neutron stars then the absence of gamma-ray emission is puzzling. Dokuchaev, Eroshenko (2017) propose that the GRB occurred off-axis and we are left seeing only the radio afterglow. In addition, they propose that collisions of this kind may also produce relativistic fireballs which can be lensed by the central supermassive black hole. The effects of this lensing

is to produce a range of achromatic flashes of varying wavelengths. In this case the gas produced by the collision could absorb some of the high-energy emission. However, given the inconsistencies between this model and the FRB rate, observed FRB DMs, and the distances of the Repeater and GRB 170817A we consider it unlikely that FRBs are caused by binary neutron star mergers.

2.3.2.4 “Cosmic Combs”

Zhang (2017) proposes a model that can reproduce the variety of observations associated with FRBs (e.g., the gamma-ray signal associated with FRB 131104, the active galactic nucleus (AGN) possibly coincident with FRB 150418,⁷ and the repeating nature of FRB 121102). The magnetosphere of a cosmological pulsar can be “combed” by a passing astrophysical plasma stream and accelerated by magnetic reconnections to produce a FRB. The origins of the plasma stream will determine what signatures are detected. For example, Zhang proposes that the radio flare associated with the FRB 150418 event is in fact the original plasma stream which combed a pulsar to create the observed FRB. Also, they suggest that the repeater could be powered by irregular emission from a supernova remnant. Anything from AGN, GRBs, SNe, tidal disruption events, or stellar flares could be responsible for combing these signals from pulsars. The only condition needed to produce such a phenomenon is that the ram pressure of the plasma stream from these objects

⁷Keane et al. (2016) use the coincidence of FRB 150418 to a fading radio transient to identify a host galaxy at $z \sim 0.5$. Williams, Berger (2016) claim that the radio source is instead AGN variability and is not connected to the FRB.

exceeds the magnetic pressure of the magnetosphere of the pulsar.

Similar to §2.3.2.3, we consider the proposition that FRBs are caused by short GRBs originating from binary neutron star collisions. If we consider FRBs as counterparts to combed GRB signals then we can use a statistical approach to determine the maximum percentage of events that must come from GRB-like sources in order to account for the observed high-energy non-detections. We assume a binomial distribution of cosmic comb outcomes where p is the probability of a cosmic comb event originating from a GRB and take our sample size to be the $n = 12$ non-repeating FRBs in Table 2.1. Therefore the probability of getting k observed high-energy events is:

$$P = \binom{n}{k} p^k (1 - p)^{n-k}. \quad (2.1)$$

Since we report no significant high-energy counterparts, the probability of getting $k=0$ events is $<17.5\%$ (at 90% confidence). If instead we calculate the probability of finding $k=0$ events over all observations (both repeating and non-repeating, $n = 30$) then this decreases to $<7.4\%$. Therefore we disfavor GRB cosmic combs as a plausible explanation for the origins of FRBs.

2.3.2.5 Other Compact Object Models

To date, there exist dozens of theories in the literature describing FRB origins. In this section we summarize additional models involving compact objects which we feel do not warrant the full analytical treatment exhibited in previous

sections.

FRBs could be produced by collapsing supramassive neutron stars (Falcke, Rezzolla, 2014; Zhang, 2014). While the timescale of collapse is consistent with that of FRBs, it fails to explain any repeating phenomena or the production of the radio emission itself. Similarly to §2.3.2.3, binaries involving neutron stars and white dwarfs have been proposed (Gu et al., 2016; Lin et al., 2018) although are specifically invoked to explain only the Repeater. Several models exist involving neutron star interactions with black holes (Abramowicz et al., 2018; Bhattacharyya, 2017), black hole interactions with white dwarfs (Li et al., 2018), and events from various other types of black holes and AGN (Vieyro et al., 2017; Zhang, 2016), but these theories all remain highly speculative.

For a full treatment of all plausible theories on FRB origins we direct the reader to recent reviews which cover models involving both compact and non-compact sources (Katz, 2018; Lorimer, 2018).

2.4 Conclusions

We searched for high-energy counterparts to FRBs in *Fermi*-GBM, *Fermi*-LAT, and *Swift*-BAT. We detect no significant high-energy emission on timescales of several 0.1 to 100 s. We report upper limits to the emission in Table 2.1 for each timescale (0.1, 1, 10, and 100 s) and energy range (15-350 keV, 300-40,000 keV, and 60-100,000 MeV) and also report limits on the ratio of radio to high-energy fluence

for timescales of 0.1 and 100 s (Table 2.2).

We consider the implications of non-detections in the context of several theoretical models. We regard the neutron star coalescence model as highly unlikely as it is inconsistent with the observed FRB DMs, the number of observed FRBs to date, and the distance of the FRB 121102 host galaxy. In addition, if the cosmic comb model explains FRBs then it is unlikely that FRBs are caused by GRBs “combing” pulsars.

Two of the more promising theories - magnetically or rotationally powered neutron stars - remain viable. We place lower limits on the distance for magnetar hyperflares which are consistent with the observed FRB DMs and the FRB 121102 result. While the non-detection of high-energy emission agrees with the rotationally powered theory, it does not agree with the distance of the repeater.

Although we exclude FRB 131104 due to its low partial coding fraction we compare our results from the other FRBs with that of its claimed counterpart in BAT (DeLaunay et al., 2016). If FRBs are caused by similar events as that reported by DeLaunay then for the majority of our sample the observed gamma-ray fluence should have been larger than reported here.

As this paper was being written new FRBs have been reported, including the second repeating burst FRB 180814.J0422+73 (see the FRB Catalog at frbcat.org (Petroff et al., 2016)). We will continue to explore the high-energy properties of these (and any other future FRBs) with the same methods as described in this paper. However for best results a dedicated, multi-wavelength follow-up procedure needs to be put in place. Ideally there would exist a joint campaign between

telescopes for co-observing candidates so that data at other wavelengths would be immediately available. If there are in fact no counterparts to FRBs at other wavelengths, then future progress in the field will require precise localization from radio measurements, in particular interferometry.

Chapter 3: GRB 160625B: Evidence for a Gaussian-Shaped Jet

We present multiwavelength modeling of the afterglow from the long gamma-ray burst GRB 160625B using Markov Chain Monte Carlo (MCMC) techniques of the `afterglowpy` Python package. GRB 160625B is an extremely bright burst with a rich set of observations spanning from radio to gamma-ray frequencies. These observations range from ~ 0.1 days to >1000 days, thus making this event extremely well-suited to such modeling. In this work we compare top-hat and Gaussian jet structure types to find best fit values for the GRB jet collimation angle, viewing angle, and other physical parameters. We find that a Gaussian-shaped jet is preferred ($2.7\text{-}5.3\sigma$) over the traditional top-hat model. Our estimate for the opening angle of the burst ranges from 1.26° to 3.90° , depending on jet shape model. We also discuss the implications that assumptions on jet shape, viewing angle, and particularly the participation fraction of electrons have on the final estimation of GRB intrinsic energy release and the resulting energy budget of the relativistic outflow. Most notably, allowing the participation fraction to vary results in an estimated total relativistic energy of $\sim 10^{53}$ erg. This is two orders of magnitude higher than when the total fraction is assumed to be unity, thus this parameter has strong relevance for placing constraints on long GRB central engines and concerning details

of the circumburst media.

3.1 Introduction

Long gamma-ray bursts (GRBs)¹ are amongst the most violent and energetic phenomena in the Universe. Despite observations of thousands of GRBs over the last few decades, key open questions – such as the nature of the central engine and the structure and composition of the relativistic jets – remain unsolved.

One key to unraveling these mysteries lies in accurately measuring their energetics. Estimates of the total relativistic energy released by a GRB can have major implications for constraining their physical characteristics and origins. Precise measurements could potentially distinguish between different progenitor systems. Two popular theories include rotationally-powered magnetars (Metzger et al., 2015; Thompson et al., 2004; Zhang, Mészáros, 2001) and the collapse of a massive star into a black hole (MacFadyen, Woosley, 1999; Woosley, 1993; Woosley, Heger, 2012).

GRBs are known to be highly collimated explosions with jet opening angles typically between 1–10° (Rhoads, 1999; Sari et al., 1999). The true value of the intrinsic energy release of a GRB is dependent upon this collimation angle: $E_\gamma = E_{\gamma,\text{iso}}(1 - \cos \theta_j) \approx E_{\gamma,\text{iso}} \frac{\theta_j^2}{2}$, where E_γ is the beaming-corrected gamma-ray energy of the burst, $E_{\gamma,\text{iso}}$ is the uncorrected isotropic gamma-ray energy, and θ_j is the jet half-opening angle (Bloom et al., 2001; Frail et al., 2001).² This jet collimation correction

¹The primary focus throughout this paper will be on long-duration GRBs, unless otherwise noted.

²This equation is only valid for the simple top-hat jet. More complicated jet structure types are discussed in §3.3.2.2

can affect the value of E_γ by a factor of 10 – 100 (Frail et al., 2001). Therefore a precise measurement of θ_j is imperative for understanding the true energetics of GRBs.

Making a precise measurement of the collimation angle can be difficult however, as it usually requires sustained, detailed, multiwavelength observations of the GRB afterglow and the identification of a ‘jet-break’, i.e., a change in the temporal slope of the light curve associated with the observer becoming aware of the edge of the jet (Goldstein et al., 2016b; Kocevski, Butler, 2008; Panaitescu, 2007; Racusin et al., 2009; Sari et al., 1999). Alternatively, the energy of the explosion can be inferred via non-relativistic calorimetry (Berger et al., 2004; Frail et al., 2000). At late times the ejecta slows to a non-relativistic spherical blastwave and can be modeled independently of the jet collimation angle. This is of course only possible when sufficiently late-time radio data exists.

Here we focus on events detected at GeV energies by the Large Area Telescope (LAT; Atwood et al. 2009) on *Fermi*. This sample is well-suited for studying GRB energetics since *Fermi*-LAT tends to select events with high values of $E_{\gamma,\text{iso}}$. This effect can be partly explained by both the Amati Relation ($E_{\text{peak}} - E_{\gamma,\text{iso}}$, Amati et al. 2009) and also the lower sensitivity of the LAT compared to X-ray instruments. LAT-detected GRBs often display values of $E_{\gamma,\text{iso}} > 10^{53}$ erg (Figure 3.1; Cenko et al. 2011, 2010; Perley et al. 2014; Xu et al. 2013) and their afterglows can generally be well modeled by a series of more simple power laws (Yamazaki et al., 2019).

We are conducting a campaign to model the broadband behavior of a sample of LAT-detected GRBs. Here we present the methodology and apply this to one

example, that of GRB 160625B - an exceptionally bright long-GRB at $z=1.406$ (Xu et al., 2016). Future work will discuss the broader population in the hopes of identifying whether LAT GRBs in fact represent a unique group and if so, how they differ from the rest of the GRB population (e.g., jet shape, local environments, magnetar vs black hole central engines; Racusin et al. 2011).

Several previous works have already performed detailed afterglow analysis of GRB 160625B (Alexander et al. 2017; Kangas et al. 2020; Troja et al. 2017, hereafter T17, A17 and K20, respectively). We expand on these works by combining and including all available data as well as undertaking new late-time observations with the Very Large Array (VLA). We also expand the analysis by considering additional models for the internal structure of the GRB jet beyond the canonical top-hat model as well as taking into account viewing angle effects, quantifying the uncertainty of derived parameters, and investigating the role individual afterglow parameters, such as the participation fraction, ξ , have on the model fitting.

For our modeling of GRB 160625B, we make use of the new `afterglowpy` software package (Ryan et al., 2020). `Afterglowpy` is a publicly available open-source Python package for the numerical computation of structured jet afterglows. This package is unique in its ability to test a range of jet structures such as top-hat, Gaussian, and power law while leaving the viewing angle and jet collimation angle as free parameters. There is evidence to suggest that the interaction between the GRB jet and the surrounding medium could take on a variety of forms - based on numerical simulations (Aloy et al., 2005; Duffell, MacFadyen, 2013a; Margutti et al., 2018) and observations of GW 1701817/GRB 170817A (Lazzati et al., 2018;

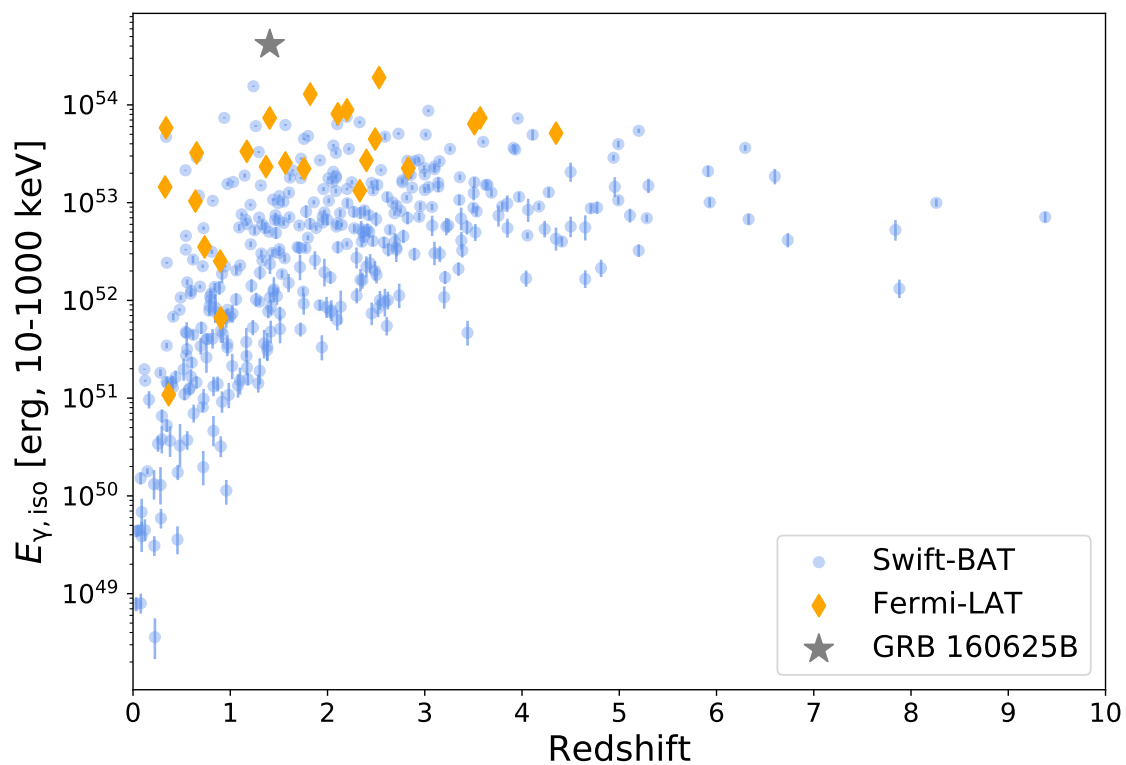


Figure 3.1: Bolometric (10-1000 keV) isotropic energy release vs redshift compared between LAT-detected and BAT-detected GRBs. In general, GRBs detected by LAT tend to be brighter, more energetic events and GRB 160625B is itself extreme even for this population. Data are taken from [Lien et al. \(2016b\)](#) and [Ajello et al. \(2019b\)](#).

Troja et al., 2018). In fact, most GRB jets probably deviate significantly from the simple on-axis top-hat model (e.g., Ryan et al. 2015) and Strausbaugh et al. (2019) has already suggested GRB 160625B can be modeled as a structured jet so it is imperative to consider this when modeling GRB afterglows.

This paper is organized as follows: we describe the available data products and our data reduction methods in §3.2. In §3.3 we define the details of the GRB afterglow modeling. We discuss the implications of our results in §3.4 and summarize our conclusions in §3.5. All error bars correspond to 1σ uncertainties and we assume a standard Λ CDM cosmology (Planck Collaboration et al., 2018) throughout the analysis.

3.2 Observations and Data Reduction

3.2.1 Gamma-ray

The *Fermi* Gamma-ray Burst Monitor (GBM; Meegan et al., 2009) first triggered on GRB 160625B at 22:40:16.28 UT on 25 June 2016 (UT times are used throughout this work) and again at 22:51:16.03. The burst is characterized by three ‘sub pulses’ separated by two relatively quiescent periods over a duration of $t_{90} = 460$ s (50-300 keV) and the spectral shape of the burst is well modeled by a Band function (Burns, 2016). The fluence in the 10-1000 keV bandpass was $(6.4256 \pm 0.0019) \times 10^{-4}$ erg cm⁻² (von Kienlin et al., 2020).

The *Fermi* Large Area Telescope (LAT; Atwood et al., 2009) triggered on the second pulse at 22:43:24.82. The GRB location was in the LAT field-of-view for

~ 1000 seconds after its initial trigger (20 MeV to 300 GeV, [Dirirsa et al. 2016](#)). The highest energy photon observed in the rest-frame was 15.3 GeV which occurred ~ 345 seconds after the first GBM trigger ([Ajello et al., 2019b](#)).

The GRB was also detected by *Konus-Wind* ($9.44 \pm 0.16 \times 10^{-4}$ erg cm²) from 20 keV to 10 MeV, [Svinkin et al. 2016](#)), SPI-ACS/INTEGRAL ([Kann, 2016](#)), and CALET ([Nakahira et al., 2016](#)). For the analysis presented here we choose t_0 to be that corresponding to the first GBM trigger.³

3.2.2 X-ray

The *Neil Gehrels Swift Observatory* ([Gehrels et al., 2004](#)) began observing GRB 160625B 2.5 hours after the initial GBM trigger ([Evans, 2016](#)). The X-ray Telescope (XRT; [Burrows et al. 2005](#)) on board *Swift* observed GRB 160625B for 47 days. XRT data are taken from the publicly available online *Swift* burst analyzer tool.⁴ For details of how these light curves were produced, see [Evans et al. \(2009, 2007\)](#). The hardness ratio appears relatively constant over time so we assume a single spectrum that can be described as an absorbed power law with the Galactic neutral hydrogen column fixed to 9.76×10^{20} cm⁻² ([Willingale et al., 2013](#)). Using a photon index of $\Gamma_x = 1.86_{-0.09}^{+0.10}$, assuming an intrinsic host absorption of $n_{\text{H,int}} = 1.8 \times 10^{21}$ cm⁻², an unabsorbed counts-to-flux conversion factor of 4.4×10^{-11} erg cm⁻² ct⁻¹, and a redshift of 1.406 ([Xu et al., 2016](#)) we convert the 0.3-10 keV flux light curves

³Most other analyses reference t_0 to that of the LAT trigger, but since we are ignoring very early data we consider any differences negligible.

⁴https://www.swift.ac.uk/burst_analyser/00020667/

Δt [day]	Energy [keV]	Flux Density [nJy]	Instrument
0.12	5	4787 ± 1076	<i>Swift</i> /XRT
0.12	5	4358 ± 981	<i>Swift</i> /XRT
0.12	5	5671 ± 1244	<i>Swift</i> /XRT
0.12	5	4772 ± 1073	<i>Swift</i> /XRT
...
41.31	5	1.34 ± 0.38	<i>Swift</i> /XRT
47.16	5	1.06 ± 0.47	<i>Swift</i> /XRT
69.76	5	0.61 ± 0.12	<i>Chandra</i> /ACIS-S
144.36	5	0.13 ± 0.03	<i>Chandra</i> /ACIS-S

1. Times are in reference to the first GBM trigger (Jun 25 2016 22:40:16.28 UTC).
2. This table is available in its entirety in a machine-readable format. A portion is shown here for guidance regarding its form and content.
3. A full printout of this table is also shown in Appendix C.

Table 3.1: X-ray Data

to a flux density at an energy of 5 keV.⁵ We choose only to include data taken during photon counting mode, which begins 0.1 days after the burst. In addition to the XRT data we include the late-time *Chandra* observations taken by K20 at 69.8 and 144 days after the burst. Example X-ray observations are available in Table 3.1.

3.2.3 Optical

One defining feature of GRB 160625B is its extremely bright optical afterglow and the presence of an optical ‘bump’ around the time of the jet-break. [Strausbaugh et al. \(2019\)](#) suggest this excess emission could be the result of an edge-brightened jet while K20 suggest it could instead be produced by density fluctuations within the circumburst medium or angular brightness differences.

A17 utilized several optical instruments to observe the GRB – the 2 m Faulkes Telescope North (FTN) operated by Las Cumbres Observatory (LCO), the 2 m

⁵Assuming the standard data reduction methods used by the *Swift*-XRT light curve repository (https://www.swift.ac.uk/xrt_curves/00020667/).

Liverpool Telescope (LT) at Roque de los Muchachos Observatory (ORM), and the Low Dispersion Survey Spectrograph 3 (LDSS3) at Magellan – ranging from 0.56 to 37 days post trigger. T17 observed the GRB with the Reionization And Transients InfraRed camera (RATIR) beginning 8 hours after the trigger until it faded beyond detection at ~ 50 days and also reported u-band observations taken with the Ultraviolet/Optical Telescope (UVOT; [Roming et al. 2005](#)) on board *Swift*. In addition, several observations used in this work were compiled from the Gamma-ray Burst Coordinates Network (GCN) Circulars by [Zhang et al. \(2018\)](#) and appropriately converted to flux densities. Late time Hubble Space Telescope (HST) observations were reported by K20 71.5 and 140.2 days post trigger. The flux contribution from the host was already subtracted out by K20 and we account for Galactic extinction in the direction of the GRB, $E(B-V) = 0.1107$ mag ([Schlafly, Finkbeiner, 2011](#)), by assuming the extinction law described in [Fitzpatrick \(1999\)](#). Example optical observations are available in Table 3.2.

3.2.4 Radio

We consolidate previous Karl G. Jansky VLA observations (Program IDs 15A-235 and S81171, PIs Berger and Cenko, respectively) from 1.37 to 209 days after the burst for the most complete sample of radio data (A17, K20). We obtained additional late time observations of GRB 160625B taken at 6 GHz (C-band) on 4 Feb 2020 15:14:24 (1319 days post-burst; Program ID SC1031, PI Cenko) for an on-source integration time of 1.8 hours. The data were reduced using the standard VLA

Δt [day]	Filter	AB Mag	Frequency [$\times 10^{14}$ Hz]	Flux Density [μJy]	Instrument
0.37	r	18.24 ± 0.01	4.82	240 ± 2	RATIR
0.39	r	18.29 ± 0.01	4.82	229 ± 2	RATIR
0.41	r	18.35 ± 0.01	4.82	216 ± 2	RATIR
0.43	r	18.43 ± 0.01	4.82	202 ± 2	RATIR
...
37.92	R	23.68 ± 0.10	4.68	1.57 ± 0.15	SAORAS/BTA
40.29	R	23.52 ± 0.10	4.68	1.82 ± 0.18	Maidanak/AZT-22
44.34	R	23.90 ± 0.11	4.68	1.28 ± 0.14	Maidanak/AZT-22
44.34	R	<23.01	4.68	<2.91	Maidanak/AZT-22

1. Magnitudes are not corrected for extinction, while flux densities are. Times are in reference to the first GBM trigger (Jun 25 2016 22:40:16.28 UTC).
2. This table is available in its entirety in a machine-readable format. A portion is shown here for guidance regarding its form and content.
3. A full printout of this table is also shown in Appendix C.

Table 3.2: Optical Data

calibration pipeline provided by the Common Astronomy Software Applications package (CASA; McMullin et al. 2007). We use J2049+1003 as the complex gain calibrator and 3C286 as both the bandpass and flux calibrator. Imaging is done using the TCLEAN algorithm in CASA. We do not detect any emission at the afterglow location and so report a 3σ upper limit of $7.4 \mu\text{Jy}$. We calculate this limit as three times the RMS uncertainty at the position of the GRB. In addition, we include data from the Australian Telescope Compact Array (ATCA) taken by T17 between 4.5 and 29 days post burst. Example radio observations are available in Table 3.3.

Δt [day]	Frequency [GHz]	Flux Density [μJy]	Instrument
1.37	5.00	163 ± 34	VLA
1.37	7.10	232 ± 22	VLA
1.35	8.50	288 ± 23	VLA
1.35	11.00	507 ± 35	VLA
...
58.25	6.10	75 ± 10	VLA
58.25	22.00	52 ± 12	VLA
208.95	6.10	16 ± 5	VLA
1319	6.10	2.46	VLA

1. Times are in reference to the first GBM trigger (Jun 25 2016 22:40:16.28 UTC).
2. This table is available in its entirety in a machine-readable format. A portion is shown here for guidance regarding its form and content.
3. A full printout of this table is also shown in Appendix C.

Table 3.3: Radio Data

3.3 Afterglow Modeling

3.3.1 Basic Tenets

The primary focus of this section is to model the broadband afterglow emission of GRB 160625B with the goal of measuring the total energy output of the GRB central engine, the jet opening angle, and the geometry of the jet structure. Here, we assume the standard fireball model for the afterglow where the observed emission is synchrotron radiation from electrons in the circumburst medium accelerated by the relativistic blast wave (Granot, Sari, 2002; Sari et al., 1998). The emitting electrons are accelerated to a power-law distribution of energies with an index of $-p$ and a minimum Lorentz factor of γ_m . The resulting spectral energy distribution (SED) can be described by a series of power law segments smoothly broken at three characteristic frequencies – ν_{sa} , the self-absorption frequency, ν_m , the frequency of

the lowest energy electron in the distribution, and ν_c , the cooling frequency. The values of the frequencies depend on the structure of the surrounding medium of the explosion as well as the jet shape, jet microphysics, energy produced, and viewing angle.

Before calculating detailed models, we infer the circumburst density profile via the temporal decline rate of the observations. From $t \sim 0.1$ days to $t = 20$ days the optical and X-ray data can be well approximated by a single power law. Then at around 20 days the decay steepens, signifying the jet-break.⁶ For the early time i-band data we find $\alpha_i = -1.00 \pm 0.02$ and for the early XRT observations we find $\alpha_X = -1.26 \pm 0.02$. The steepening of the slope between the optical and X-ray observations suggests that the cooling frequency, ν_c , lies between these two regimes. In the case of a slow-cooling constant-density (ISM-like) profile $\alpha_{\text{ISM}} = \frac{3(1-p)}{4}$ ($\nu < \nu_c$) which yields an estimate for p , the index of the electron energy distribution, of 2.33 ± 0.03 (Granot, Sari, 2002). In the slow-cooling wind-like scenario $\alpha_{\text{wind}} = \frac{(1-3p)}{4}$ which yields $p = 1.67 \pm 0.03$. When $\nu > \nu_c$ the decline rate can be described by $\alpha = \frac{(2-3p)}{4}$ for both the wind and ISM-like profiles. Using $\alpha_X = -1.26 \pm 0.02$ we find $p = 2.35 \pm 0.03$, consistent with the ISM result. Despite fewer observations available at later times (> 20 days) the optical decline rate of $\alpha_{i,\text{late}} = -1.61 \pm 0.16$ produces $p = 2.15 \pm 0.21$ ($\alpha = \frac{3p}{4}$) and the X-ray decline rate of $\alpha_{X,\text{late}} = -2.10 \pm 0.15$ produces $p = 2.46 \pm 0.20$ ($\alpha = \frac{3p-1}{4}$; Ryan et al. 2020).⁷ The spectral index of the 0.3-10 keV XRT data ($\beta_x = 0.86 \pm 0.10$) produces a lower estimate of $p = 1.72 \pm 0.20$.

⁶Strausbaugh et al. (2019) place the jet-break slightly earlier during the peak of the optical bump at ~ 13 days

⁷The closure relations for structured jets derived in Ryan et al. (2020) reduce to those of Granot, Sari (2002) for on-axis ($\theta_v < \theta_c$) cases.

[Alexander et al. \(2017\)](#) interpret this to mean that the cooling break is only slightly below that of the XRT observations, meaning the power law index is transitioning at this frequency. The general early and late-time behavior are consistent; thus throughout this work we assume an ISM-like density profile for GRB 160625B.⁸

There are significant features present in the early time radio data of GRB 160625B which are likely not related to the forward shock emission (Figure 3.2). A17 attribute these effects to the combination of a reverse shock and interstellar scintillation. Therefore when modeling the forward shock we conservatively choose to only include post-jet-break radio data ($\gtrsim 20$ days) and at frequencies above 10 GHz (except for our late-time observation at 6.1 GHz) to mitigate these effects. A17 found there is negligible extinction due to dust within the GRB host galaxy and so we choose to ignore those effects in our analysis. Due to a systematic offset between the r- and i-band data of A17 and T17 we choose to only include that of T17 and none from A17 in our forward shock modeling as it is a larger dataset and observations were directly compared to the PanSTARRS magnitude system (see also K20).

3.3.2 Afterglowpy Package

`Afterglowpy` uses the single-shell approximation to numerically and analytically model a blast wave propagating through an ISM-like circumburst medium as a function of viewing angle and jet type ([Ryan et al., 2020](#)). A range of jet structure types have been proposed in the literature – some common examples include

⁸A17, T17, K20 and other works come to the same conclusion.

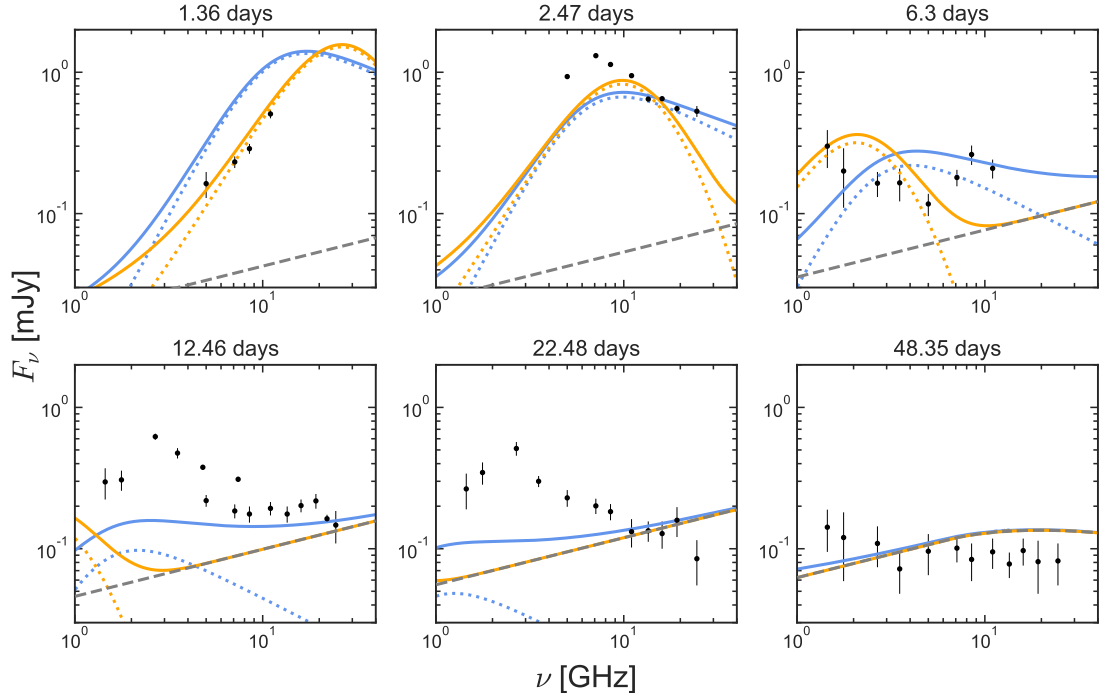


Figure 3.2: The observed spectral energy distributions (SEDs) for the radio data at various epochs overplotted with forward and reverse shock models. Our forward shock model (gray dashed line) is as described in §3.3.2.3. The two reverse shock models (dotted lines) are taken from A17 and represent different assumptions for the location of the SED peak, ν_p : $\nu_p = \nu_a$ (blue) and $\nu_p = \nu_c$ (orange). The solid lines represent the combination of both the forward and reverse shock models. Clearly the reverse shock, regardless of which model is used, dominates at early times (< 20 days) and lower frequencies (< 10 GHz).

variations of top-hat, Gaussian, and power law models (Aloy et al., 2005; Coughlin, Begelman, 2020; Duffell, MacFadyen, 2013a; Margutti et al., 2018; Mészáros et al., 1998; Rossi et al., 2002, 2004; Zhang et al., 2004; Zhang, Mészáros, 2002). The exact structure of any one GRB jet may be dependent upon several factors such as the immediate circumburst environment and interactions with the stellar envelope. Compared to other available afterglow modeling codes (e.g., BoxFit; van Eerten et al. 2012) `afterglowpy` is advantageous for its ability to probe this complex inner structure of the GRB jet.

We employ the statistical sampling techniques of the EMCEE Python package for Markov-Chain Monte Carlo (MCMC; Foreman-Mackey et al. 2013) analysis with the `afterglowpy` models, as outlined in Troja et al. (2018). `Afterglowpy` generates samples from the entire posterior distribution for each of the models we consider here in this work. As input, our fit takes broadband fluxes, observation times, and instrument frequencies. As output, it produces samples from the posterior distribution for the viewing angle, θ_v , the isotropic kinetic energy released by the blastwave, $E_{K,iso}$, jet core opening angle, θ_c , circumburst density, n , the spectral slope of the electron distribution, p , the fraction of shock energy imparted to electrons, ϵ_e , and to the magnetic field, ϵ_B .

For initial prior parameters we use the best fit parameters reported in K20. The assumed prior distributions and bounds for each parameter can be viewed in detail in Table 3 of Ryan et al. (2020). We assume a log-uniform prior distribution for $E_{K,iso}$, n , ϵ_E , ϵ_B , and ξ and a uniform prior distribution for θ_c , θ_w , and p . The prior distribution for the viewing angle, θ_v , is constrained by the posterior probability

distribution reported in [Abbott et al. \(2017a\)](#).

3.3.2.1 Top-Hat Jet Model

We begin by first calculating the simplest model which could describe the outflow geometry, the top-hat. In this scenario, the energy of the jet is independent of angle and there is an instantaneous cutoff in energy at the jet edge:

$$E(\theta) = \begin{cases} E_0 & \theta \leq \theta_c \\ 0 & \theta > \theta_c \end{cases} \quad (3.1)$$

It is unlikely that a top-hat jet could be viewed far off-axis without a significant change in the appearance of the GRB afterglow ([Kathirgamaraju et al., 2016](#); [Zhang et al., 2015](#); [van Eerten et al., 2010](#)). Until recently, the top-hat model was assumed for most GRB analyses. The covariances and posterior probability distributions of the various parameters are shown in [Figure 3.3](#). Our best fit parameters for this model are listed in [Table 3.4](#) and plotted in [Figure 3.4](#). We allow the value of p to vary but restrict $\epsilon_e < 1/3$ and $\epsilon_B < 1/3$ ([Alexander et al., 2017](#); [Laskar et al., 2015](#)). This is done primarily to remove degeneracies within the model fitting; however, we found that if we do not apply the restrictions on these microphysical parameters then the fits tend towards quite unphysical values (ϵ_B approaches 1.0). Therefore, we see this as further evidence that placing these restrictions is valid in this case. The parameters derived here imply a beaming-corrected kinetic energy of $E_K = E_{K,\text{iso}}(1 - \cos \theta_c) = 1.2_{-0.1}^{+0.2} \times 10^{51}$ erg.

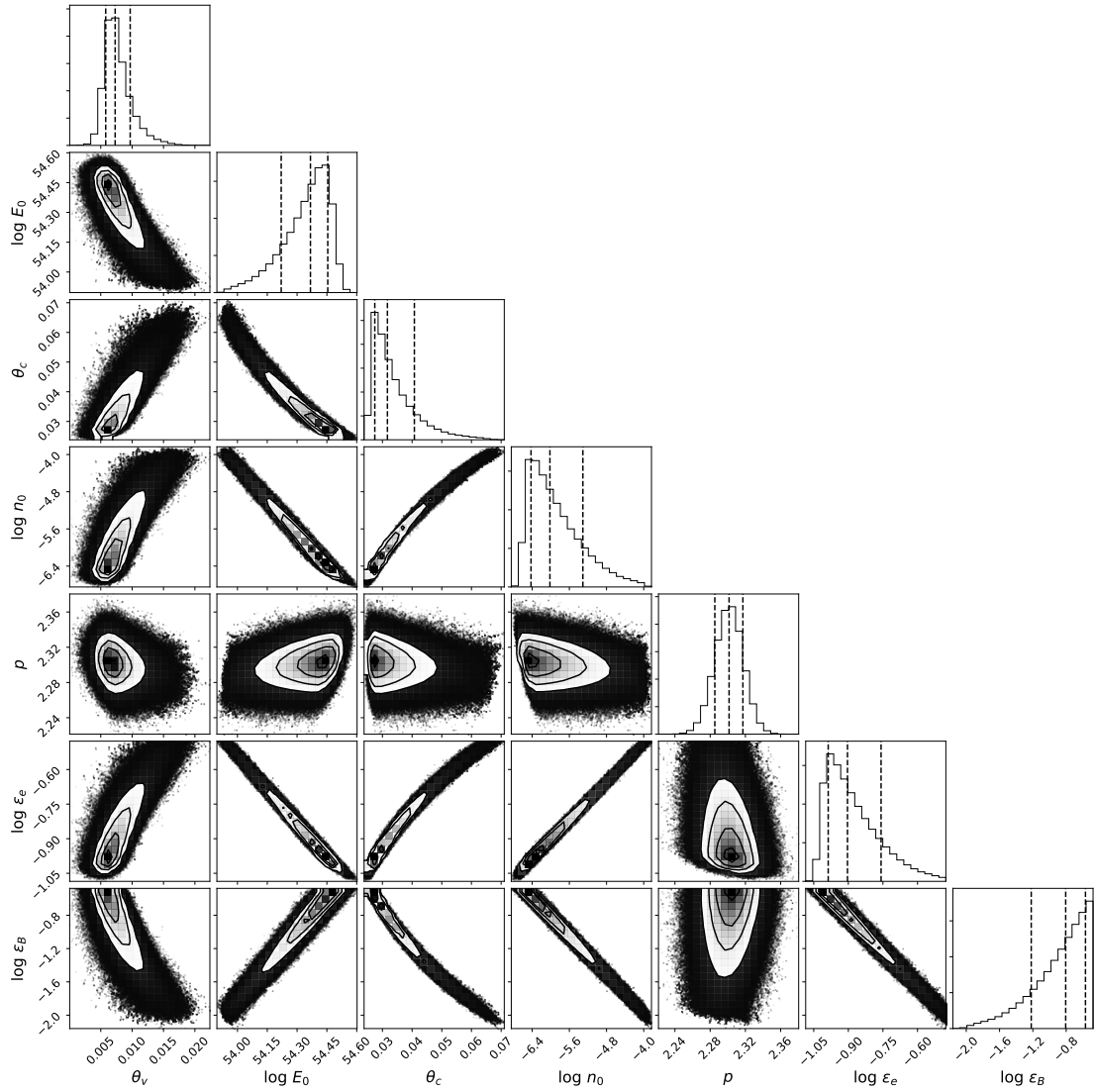


Figure 3.3: The covariances and posterior probability distributions of the parameters for the top-hat model (§3.3.2.1). The histograms denote the 15, 50, and 85 percentiles of the distributions.

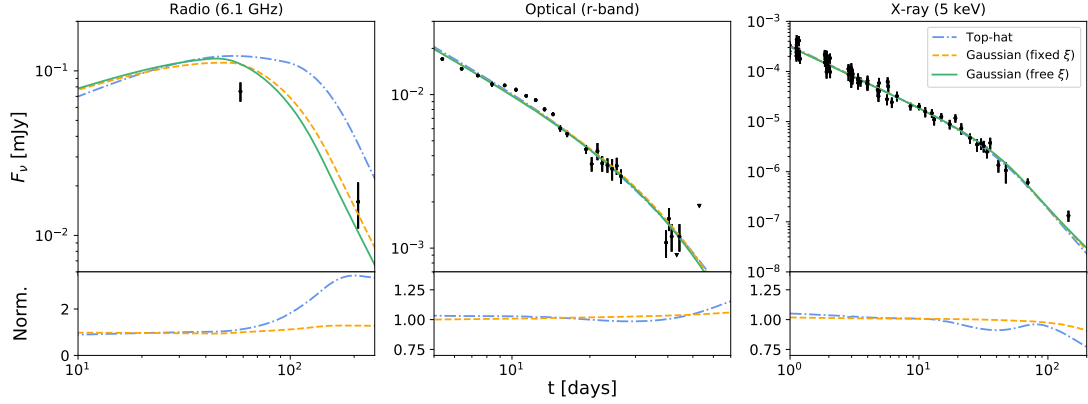


Figure 3.4: Top panel: Comparison between each of the three models described in §3.3.2: a top-hat jet (dash-dotted line), a Gaussian jet with ξ fixed to 1.0 (dashed line), and a Gaussian with ξ free to vary (solid line). Bottom panel: The top-hat and fixed- ξ Gaussian jet models are normalized by the free- ξ Gaussian jet model. The models provide comparable fits to the observed data except at later times in the radio.

3.3.2.2 Gaussian Jet Model

To probe the jet structure we compare the simple top-hat to a more complex Gaussian model:

$$E(\theta) = \begin{cases} E_0 e^{-\frac{\theta^2}{2\theta_w^2}} & \theta \leq \theta_w \\ 0 & \theta > \theta_w \end{cases} \quad (3.2)$$

where θ_w is the truncation angle of the Gaussian wings.

Similarly to the top-hat model we again restrict $\epsilon_e < 1/3$ and $\epsilon_B < 1/3$. In Gaussian models extended emission from the jet could be viewed at angles beyond θ_c and so larger values of θ_v are possible. The best fit parameters are listed in Table 3.4 and plotted in Figure 3.4. The covariances and posterior probability distributions of the parameters are shown in Figure 3.5.

To calculate the beaming-corrected energy we integrate Equation 3.2 over both

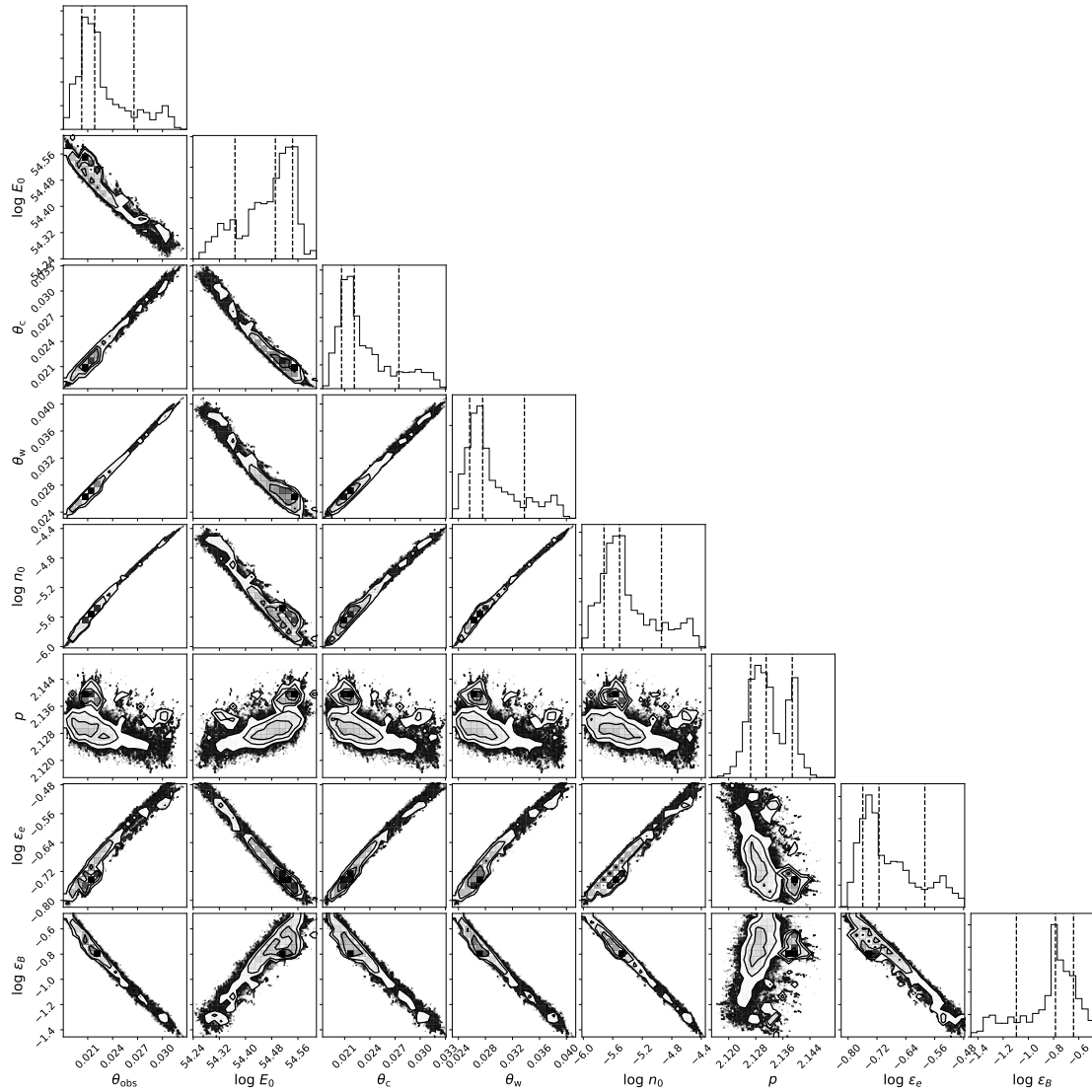


Figure 3.5: The covariances and posterior probability distributions of the parameters for the Gaussian model with ξ fixed to 1.0 (§3.3.2.2). The histograms denote the 15, 50, and 85 percentiles of the distributions.

jets:

$$E = 2 \int_0^{\theta_w} \int_0^{2\pi} d\theta d\phi \sin\theta \frac{E(\theta)}{4\pi}, \quad (3.3)$$

which approximates to:

$$E \sim E_0 \theta_c^2 \left(1 - e^{-\frac{\theta_w^2}{2\theta_c^2}} \right). \quad (3.4)$$

This gives a value for the beaming-corrected kinetic energy of $E_K = 8.4_{-0.7}^{+1.2} \times 10^{50}$ erg, which is slightly less than that found for the top-hat model.

3.3.2.3 Gaussian Jet Model with Free ξ

In the synchrotron afterglow model the emission is driven by a power-law distribution of electrons in the surrounding medium. The participation fraction, ξ , describes the percentage of total electrons which are accelerated by the passing shock wave and contribute to this power-law distribution. 100% participation ($\xi = 1$) is typically assumed in the literature but simulations have shown ξ can be as low as 10^{-2} (Sironi, Spitkovsky, 2011; Sironi et al., 2013) and that lower values tend to be more realistic (Warren et al., 2018).

To test this we expand on our Gaussian model and now allow ξ to vary as a free parameter (Table 3.4). Notably, the beaming-corrected kinetic energy in this scenario is $E_K = 1.1_{-0.9}^{+6.5} \times 10^{53}$ erg, two orders of magnitude higher than in the previous cases. Such a high energy density may lead to concerns over the ability of the afterglow emission to avoid becoming suppressed by processes such as pair-

production opacity. However, at the later times described here the afterglow has had sufficient time to expand and become diffuse. For an X-ray photon the opacity due to pair production is quite low ($\sim 10^{-8}$). This is because the number of high energy (GeV) photons with which the X-ray photon could pair-produce is small and so it is free to travel unhindered through the shock wave. During the prompt emission and possibly for GeV afterglows this could be a bigger concern, but for the later, more diffuse afterglow we do not consider it an issue.

We discuss this case in more detail in §3.4.3. The covariances and posterior probability distributions of the parameters are shown in Figure 3.6. We directly compare the previous top-hat and Gaussian jet models to this case in Figure 3.4 and plot the best fit over the data in Figure 3.7.

3.4 Discussion

3.4.1 Comparison to Past Works

Previous works have completed similar analyses on GRB 160625B (T17, A17, K20). In each instance the jet is modeled with a conical top-hat structure and there is general agreement on the burst parameters (Table 3.4). We begin by simulating the light curves with `afterglowpy` using the model parameters found in A17, T17, and K20. We then compare the results to our own top hat solution in Figure 3.8.

K20 utilize the `BoxFit` package (van Eerten et al., 2012) to model the afterglow while A17 base their results on the synchrotron model described in Laskar et al. (2015, 2014). In Figure 3.8 the differences between the models at radio, opti-

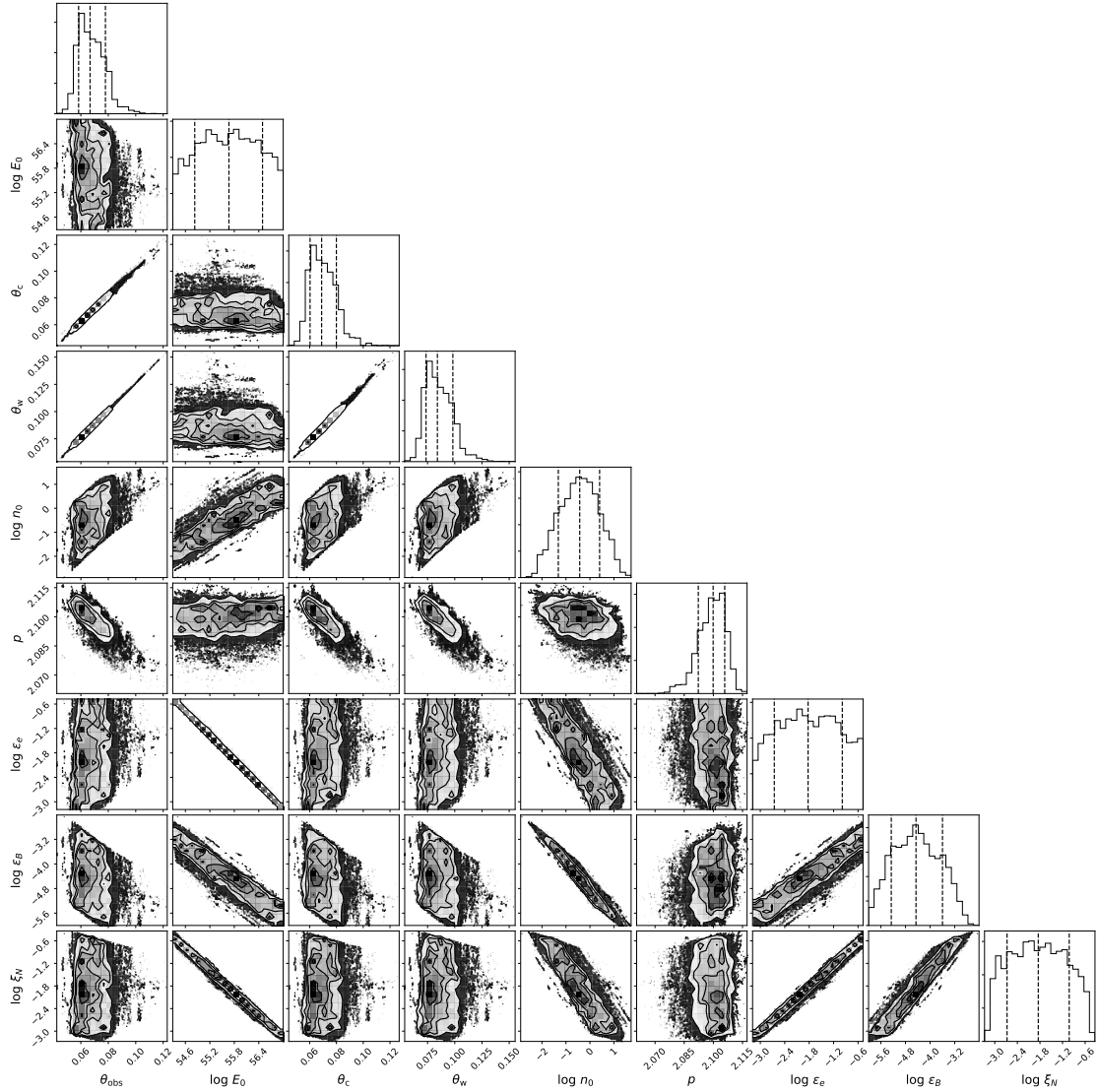


Figure 3.6: The covariances and posterior probability distributions of the parameters for the Gaussian model with ξ left to vary freely (§3.3.2.3). The histograms denote the 15, 50, and 85 percentiles of the distributions.

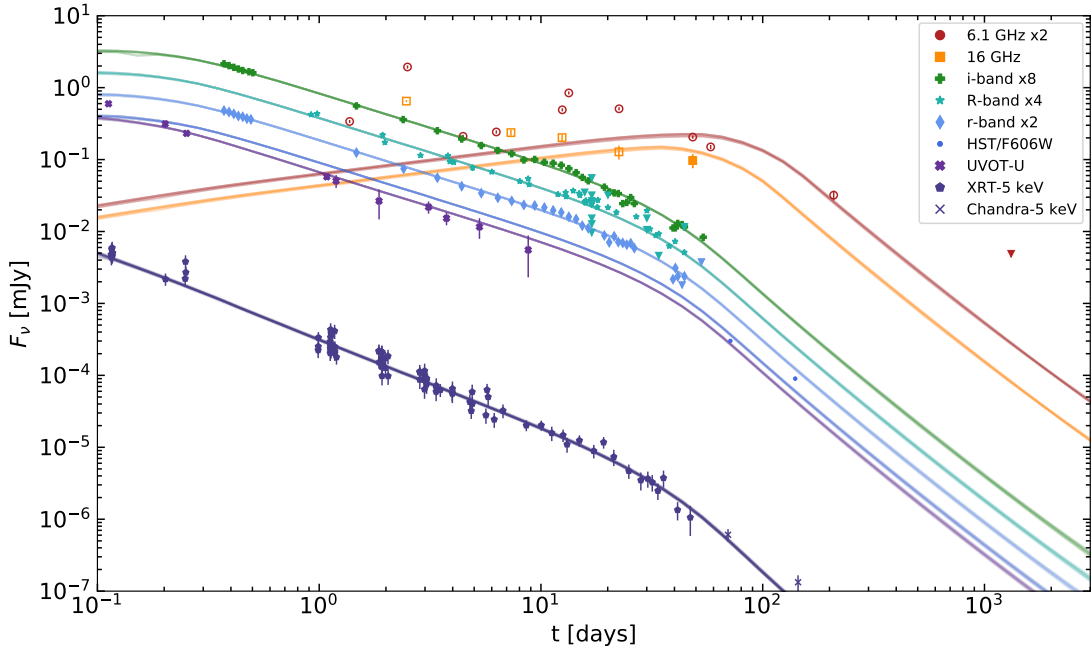


Figure 3.7: The multiwavelength light curve of GRB 160625B overplotted with our best fit model of the afterglow forward shock from §3.3.2.3: a Gaussian jet with ξ free to vary. Times are referenced from the GBM trigger (Jun 25 2016 22:40:16.28 UT). Open points represent radio data which were available but not included in the analysis (See §3.3.1 for more details). Transparent lines represent model uncertainties and are calculated via samples taken from the MCMC posterior distribution.

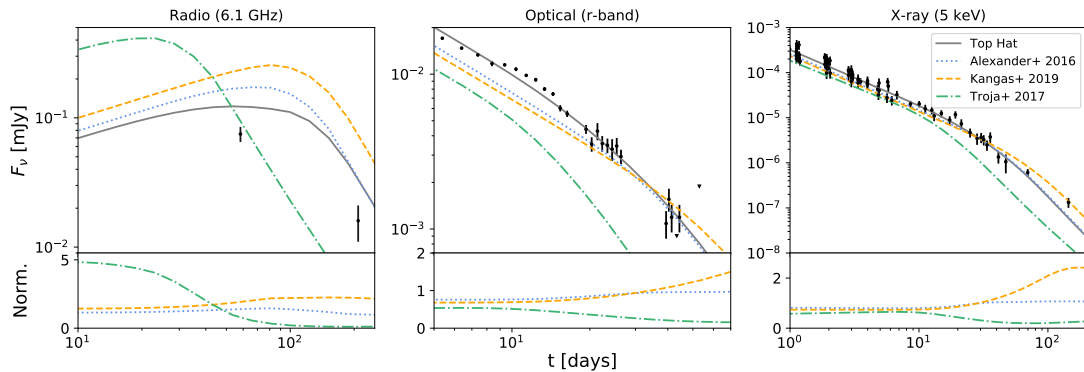


Figure 3.8: Top panel: Comparison between our top-hat jet model (solid line) to previous works from A17 (dotted line), K20 (dashed line), and T17 (dash-dotted line) (Table 3.4). Bottom panel: The A17, K20, and T17 models are normalized by our top hat model (§3.3.2.1). At X-ray wavelengths the models are almost indistinguishable at early times. The discrepancies between models are more apparent at radio and optical frequencies, where fewer observations are available.

cal, and X-ray wavelengths can be primarily explained by systematic offsets between `afterglowpy` and the other models used, differences in the datasets used, and the use of additional late-time data that was not available yet for A17 and T17. The largest discrepancies are seen at radio energies. This is partially due to the fewer number of observations available and the potential contamination of the forward shock by other radio effects. Recently [Kangas, Fruchter \(2019\)](#) have noted inconsistencies in observed jet break times between radio and higher frequencies; thus suggesting that radio afterglow light curves may simply not be well represented by standard afterglow theory. [Jacovich et al. \(2020\)](#) attribute this discrepancy to the lack of proper implementation of Klein-Nishina and effects in most afterglow modeling codes.

3.4.2 Model Comparison with WAIC

To quantify the differences between our own top-hat and Gaussian models described in §3.3.2 we utilize the Widely Applicable Information Criterion (WAIC; [Troja et al. 2020](#); [Watanabe 2010](#)). The WAIC score provides an estimate of the expected log predictive density (elpd), i.e., how likely the model is to provide a good fit for future data ([Gelman et al., 2013](#)). The elpd in general is quite hard to derive without prior knowledge of the true model but the WAIC score can be calculated directly from the MCMC statistical samples. In general, it is the difference between WAIC scores, rather than the raw WAIC score itself, which is most relevant. A model is considered strongly preferred, i.e., has greater predictive power, over another if

the difference between their two WAIC scores is a factor of a few larger than the error on that difference. The uncertainty on the raw WAIC and WAIC difference scores is an estimate of the standard error and can be an underestimate but is usually accurate within a factor of 2 (Bengio, Grandvalet, 2004). Therefore we list a significance range for the confidence level in Table 3.6.

As discussed in §3.3.2 we first began by directly comparing a top-hat and Gaussian style jet and then exploring the effects that varying the participation fraction, ξ , had on the GRB afterglow. Table 3.6 shows the model comparison between each of these three cases. Both Gaussian models show a greater predictive power compared to the simpler top-hat model but there is not a significant difference between the two Gaussian models themselves.

3.4.3 The Participation Fraction, ξ

In §3.3.2.3 we fit the afterglow of GRB 160625B with a Gaussian jet model but allowed the participation fraction, ξ , to vary. In agreement with the findings of Warren et al. (2018) our model prefers a lower value of $\xi \sim 0.01$, rather than total participation. Clearly, decreasing the participation fraction has dramatic effects on the other physical parameters. If all other parameters are kept fixed then the density of the circumburst environment must increase to provide the necessary number of electrons to produce the observed flux. This causes θ_c to increase as the relativistic jet interacts with more material. Increasing the density also results in a faster-evolving shock wave, so $E_{K,\text{iso}}$ must increase to maintain the light curve shape.

Most notably, ϵ_B decreases by four orders of magnitude due to the lack of accelerated electrons.

Figure 3.9 illustrates how varying ξ can have dramatic effects on the predicted afterglow light curve. We begin with the best fit parameter values of the top-hat jet and Gaussian (fixed- ξ) jet models from §3.3.2 but fix ξ to three different values – 1.0, 0.1, and 0.01 – and plot the results. We see the greatest differences at radio energies and at early times in the optical band. Those electrons which pass through the shock wave without being accelerated may increase the opacity to synchrotron self-absorption and also introduce an additional source of emission at very early times at optical wavelengths (\sim few seconds post-burst) that then remains detectable at radio/millimeter wavelengths for several days or more (Ressler, Laskar, 2017). Therefore, constraining the value of ξ is critical for understanding the implications of the total energy budget of the burst (§3.4.7) and the density of the local circumburst environment (§3.4.6), although in practice this can be difficult due to degeneracy issues (Eichler, Waxman, 2005).

3.4.4 Sharp Edge Effects on p

In both Gaussian jet fits the spectral slope of the electron distribution, p , is significantly lower than ~ 2.3 which is the value found both analytically (§3.3.1) and in the top-hat model case (§3.3.2.1). When ξ is allowed to vary p decreases from 2.13 ± 0.01 to 2.10 ± 0.01 . This is explained by the favoured relationship between θ_c and θ_w . In both Gaussian models we find $\theta_c/\theta_w \sim 0.8$ meaning the emission does not

extend greatly off-axis beyond the primary portion of the jet. Therefore, in slightly off-axis viewing angles the effect of a sharp edge may have a significant impact on the resulting light curve. Emission from one side of the jet reaches the viewer before the other side, resulting in slightly less observed flux than expected for a perfectly on-axis viewing angle. This manifests as a steepening of the light curve which can then allow p to instead probe lower values in the parameter distribution.

To investigate this we repeated the fit from 3.3.2.3 but now place a constraint where $\theta_w > 3\theta_c$ so as to force a ‘softer’ edge to the jet. In this scenario we find that p prefers a higher value of $2.23_{-0.03}^{+0.02}$, more consistent with the top-hat jet results, and $\theta_w = 0.59_{-0.16}^{+0.32}$ (Table 3.5). All other parameters remain consistent with those of the free- ξ case in Table 3.4. A softer-edged jet may represent a more physically realistic scenario compared to a sudden drop-off in emission at the jet edge. However, a WAIC analysis between this case (WAIC = 799.0 ± 126.8) and the freely varying ξ case (WAIC = 1782.7 ± 79.1) shows better predictability for the sharp-edged case. This is, in fact, consistent with the results of Beniamini, Nakar (2019) where the authors claim that emission from structured jets cannot be observed far from the core of the jet.

3.4.5 Viewing Angle Effects

Precise predictions for GRB viewing angles have only become possible within the last few years thanks to the advent of various powerful high-resolution hydrodynamic simulations used both directly and indirectly by codes such as

BoxFit (van Eerten et al., 2012), ScaleFit (Ryan et al., 2013), JET (Duffell, MacFadyen, 2013b), and afterglowpy (Ryan et al., 2020). Ryan et al. (2015) show that, in fact, most GRBs are probably observed off-axis and the joint discovery of GW 170817/GRB 170817A highlighted just how significant viewing angle effects could be for a single event (Alexander et al., 2018; Fong et al., 2019; Lamb et al., 2020; Lazzati et al., 2018; Troja et al., 2018, 2019; Wu, MacFadyen, 2018; Xie et al., 2018).

Underestimating the viewing angle of GRBs may introduce biases in the afterglow model fitting, e.g., by overestimating the beaming width of the jet (van Eerten, 2015). To illustrate this we repeat the Gaussian model with the same initial conditions as described in §3.3.2.2 but now we fix θ_v to an almost on-axis angle of 10^{-4} radians (Table 3.5). As a reference we note that *Swift* GRBs are thought to be observed more off-axis than this. Typical values of θ_v range from 0.055 to 0.42 radians (Ryan et al., 2015).

In this case we find that by assuming an on-axis viewing angle we are overestimating θ_c by a factor of ~ 4.1 (compared to the fixed- ξ Gaussian jet model). Utilizing Equation 3.4 the beaming-corrected kinetic energy in this case is $E_K = 2.0_{-0.1}^{+0.4} \times 10^{51}$ erg. Although we have overestimated the beaming angle the slightly lower estimate for $E_{K,\text{iso}}$ means the beaming-corrected kinetic energy remains consistent with the Gaussian case. Interestingly, the fact that $\theta_w/\theta_c < 1$ indicates a strong preference for a sharp jet edge as in the case of a top-hat jet. However, a WAIC comparison between this case (WAIC = 1145.7 ± 197.1) and the Gaussian jet with fixed- ξ (WAIC = 1744.3 ± 78.5) still shows better predictability and preference for a Gaussian-shaped

jet model.

3.4.6 Local Circumburst Environment

Long GRBs are believed to result from the end state of massive stars (Woosley, Bloom, 2006). Due to their short lifespan (tens of Myr), these massive stars live and die in the same dense molecular clouds which birthed them. It would appear to be a reasonable assumption to expect the local circumburst densities of GRBs to reflect that of regions of high star-formation ($> 1 \text{ cm}^{-3}$). Observationally this is not usually the case, at least when assuming a top-hat jet model and $\xi=1$ (Laskar et al., 2015).

The derived value of the local circumburst density, n , for GRB 160625B is exceptionally low for most models in Table 3.4. This parameter can be difficult to constrain as it is highly degenerate with other physical parameters in the system. For most GRBs the value of n tends to be between $\sim 10^{-3}$ and $\sim 10^2 \text{ cm}^{-3}$ when assuming $\xi=1$ (Laskar et al., 2015). Density measurements between *Swift* and *Fermi* GRB populations tend to occupy discrete regions of parameter space, thus leading previous studies (e.g., Racusin et al. 2011) to suggest that these two populations may originate in different host environments, although there was not a large enough sample at the time to definitively confirm this.

The preference for ISM-like, low-density local environments may suggest LAT-detected long GRBs originate from lower-metallicity massive stars. This is motivated by the fact that these types of progenitor stars tend to have lower mass-loss rates

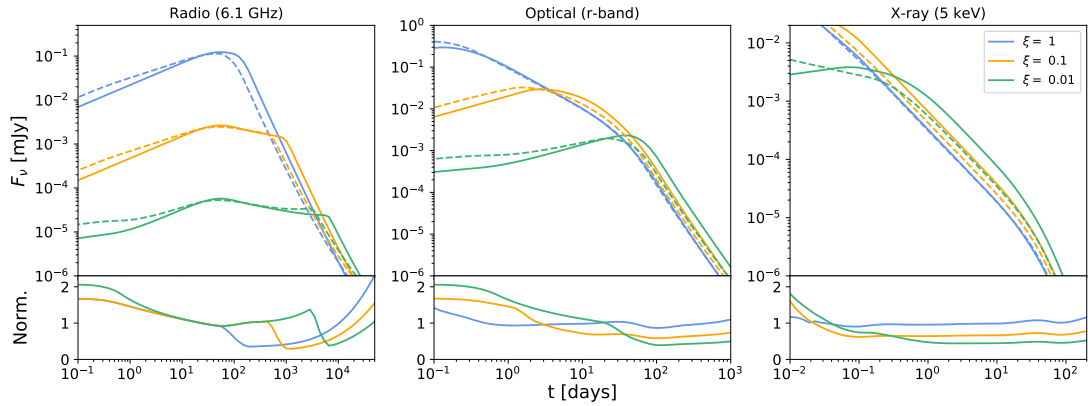


Figure 3.9: Top panel: We present the best fit parameter values of the top-hat (solid line) and Gaussian (dashed line) jet models from §3.3.2 but at three fixed values of ξ . The participation fraction, ξ , plays a pivotal role in the GRB afterglow, especially at radio energies. Lowering the value of ξ can have dramatic effects on the light curve. To account for the lower number of electrons contributing to the emission the total relativistic energy released must be increased and/or the density of the local circumburst environment must increase as well. Bottom panel: The Gaussian fluxes are normalized by the top-hat model for each value of ξ .

(Kudritzki et al., 1987; Vink et al., 2001; Woosley et al., 2002). The ability for the relativistic jet to travel unhindered may also prevent the suppression of several radio components and can allow the reverse shock to propagate freely. GRB 160625B is one of only a few long-duration GRBs with a confirmed reverse shock (e.g., Laskar et al. 2013, 2016b, 2018, 2019; Perley et al. 2014).

In the standard afterglow model the circumburst density is intricately connected to other observed physical parameters. As noted in the case of the Gaussian jet with free- ξ (§3.3.2.3) our estimate of the local circumburst density is highly dependent upon the participation fraction. Decreasing ξ by a factor of 100 can increase n by upwards of five orders of magnitude. Therefore, further work on the impact of the participation fraction, ξ is required before a definitive association can be made between highly energetic long GRBs and massive, metal-poor progenitor stars.

Model	This Work		This Work		This Work		A17		K20		T17	
	Top-Hat	Gaussian (fixed ξ)	Gaussian (free ξ)	Gaussian (free ξ)	Top-Hat	Top-Hat	Top-Hat	Top-Hat	Top-Hat	Top-Hat	Top-Hat	Top-Hat
θ_v	$0.0073^{+0.0024}_{-0.0015}$ [rad]	$0.022^{+0.006}_{-0.001}$	$0.066^{+0.010}_{-0.009}$	$0.066^{+0.010}_{-0.009}$	-	-	-	-	0.012	-	-	-
$E_{k,iso}$	$2.3^{+0.5}_{-0.7} \times 10^{54}$ [erg]	$3.1^{+0.4}_{-0.8} \times 10^{54}$	$4.2^{+24}_{-3.5} \times 10^{55}$	$4.2^{+24}_{-3.5} \times 10^{55}$	$1.1^{+1.0}_{-0.5} \times 10^{54}$	$1.1^{+1.0}_{-0.5} \times 10^{54}$	$1.1^{+1.0}_{-0.5} \times 10^{54}$	$1.1^{+1.0}_{-0.5} \times 10^{54}$	1.8×10^{54}	$2.0^{+1.0}_{-1.4} \times 10^{54}$	$2.0^{+1.0}_{-1.4} \times 10^{54}$	$2.0^{+1.0}_{-1.4} \times 10^{54}$
θ_c	$0.032^{+0.009}_{-0.004}$ [rad]	$0.022^{+0.006}_{-0.001}$	$0.068^{+0.010}_{-0.010}$	$0.068^{+0.010}_{-0.010}$	0.063 ± 0.003	0.063 ± 0.003	0.063 ± 0.003	0.063 ± 0.003	0.059	$0.042^{+0.028}_{-0.012}$	$0.042^{+0.028}_{-0.012}$	$0.042^{+0.028}_{-0.012}$
θ_w	- [rad]	$0.028^{+0.007}_{-0.002}$	$0.083^{+0.014}_{-0.011}$	$0.083^{+0.014}_{-0.011}$	-	-	-	-	-	-	-	-
n	$9.6^{+39.0}_{-5.9} \times 10^{-7}$ [cm ⁻³]	$3.1^{+1.1}_{-1.1} \times 10^{-6}$	$0.352^{+1.71}_{-0.307}$	$0.352^{+1.71}_{-0.307}$	$(5 \pm 3) \times 10^{-5}$	1.1×10^{-5}	$1^{+49}_{-0.9} \times 10^{-4}$	$1^{+49}_{-0.9} \times 10^{-4}$	$1^{+49}_{-0.9} \times 10^{-4}$			
p	2.30 ± 0.02	$2.13^{+0.01}_{-0.01}$	$2.10^{+0.01}_{-0.01}$	$2.10^{+0.01}_{-0.01}$	2.31 ± 0.01	2.31 ± 0.01	2.31 ± 0.01	2.31 ± 0.01	2.30	2.2	2.2	2.2
ϵ_e	$0.12^{+0.05}_{-0.02}$	$0.19^{+0.07}_{-0.02}$	$0.017^{+0.085}_{-0.014}$	$0.017^{+0.085}_{-0.014}$	$0.23^{+0.07}_{-0.08}$	$0.23^{+0.07}_{-0.08}$	$0.23^{+0.07}_{-0.08}$	$0.23^{+0.07}_{-0.08}$	0.13	$0.10^{+0.22}_{-0.09}$	$0.10^{+0.22}_{-0.09}$	$0.10^{+0.22}_{-0.09}$
ϵ_B	$0.16^{+0.11}_{-0.10}$	$0.17^{+0.05}_{-0.09}$	$3.9^{+21.9}_{-3.3} \times 10^{-5}$	$3.9^{+21.9}_{-3.3} \times 10^{-5}$	$0.013^{+0.11}_{-0.01}$	$0.013^{+0.11}_{-0.01}$	$0.013^{+0.11}_{-0.01}$	$0.013^{+0.11}_{-0.01}$	0.030	$0.010^{+0.090}_{-0.009}$	$0.010^{+0.090}_{-0.009}$	$0.010^{+0.090}_{-0.009}$
ξ	1.0	1.0	$0.016^{+0.080}_{-0.013}$	$0.016^{+0.080}_{-0.013}$	1.0	1.0	1.0	1.0	1.0	1.0	1.0	1.0
η ^a	$0.56^{+0.08}_{-0.05}$	$0.49^{+0.08}_{-0.03}$	$0.067^{+0.253}_{-0.057}$	$0.067^{+0.253}_{-0.057}$	$0.73^{+0.10}_{-0.14}$	$0.73^{+0.10}_{-0.14}$	$0.73^{+0.10}_{-0.14}$	$0.73^{+0.10}_{-0.14}$	0.62	$0.75^{+0.16}_{-0.09}$	$0.75^{+0.16}_{-0.09}$	$0.75^{+0.16}_{-0.09}$
E_{rel} ^b	$2.7^{+1.3}_{-0.5} \times 10^{51}$ [erg]	$1.6^{+0.6}_{-0.1} \times 10^{51}$	$1.2^{+6.5}_{-0.9} \times 10^{53}$	$1.2^{+6.5}_{-0.9} \times 10^{53}$	$2.3^{+1.8}_{-1.2} \times 10^{51}$	$2.3^{+1.8}_{-1.2} \times 10^{51}$	$2.3^{+1.8}_{-1.2} \times 10^{51}$	$2.3^{+1.8}_{-1.2} \times 10^{51}$	8.3×10^{51}	$\sim 6 \times 10^{51}$	$\sim 6 \times 10^{51}$	$\sim 6 \times 10^{51}$
χ^2/dof	1.24	0.99	0.86	0.86	1.26	1.26	1.26	1.26	8.6	-	-	-

Uncertainties are given at 1σ confidence levels. The reduced- χ^2 is the minimum over all completed runs.

^a $\eta = \frac{E_{\gamma,iso}}{E_{\gamma,iso} + E_{K,iso}}$, assuming $E_{\gamma,iso} \sim 3 \times 10^{54}$ erg (Zhang et al., 2018)

^b $E_{rel} = E_{\gamma} + E_K$

Table 3.4: Best Fit Model Parameters.

3.4.7 Energetics and Central Engine

One of the main goals of this and future work will be calculating the beaming-corrected energy released by the GRB and especially how that relates to the physics of the central engine. Currently, two popular progenitor models are favored to explain the central engines of long GRBs: magnetars and black hole systems.

The spindown of a newborn millisecond pulsar could potentially power a long GRB via a Poynting-flux dominated relativistic outflow (Thompson et al., 2004; Zhang, Mészáros, 2001). These magnetars are limited by their finite reserve of rotational energy. For a neutron star with a mass limit of $\sim 2 M_{\odot}$, a radius of 10 km, and a spin period of about 1 ms places a cap on the available energy at $\sim 10^{52}$ erg (Metzger et al., 2011, 2007). This energy cap can be increased in the case of ‘supramassive’ neutron stars that have been stabilized by centrifugal forces and therefore could accommodate rotational energies of up to 10^{53} erg (Metzger et al., 2015). However, Beniamini et al. (2017) and Metzger et al. (2018) have recently shown that the true reservoir of available energy is unlikely to reach beyond $\sim \text{few} \times 10^{52}$ erg and so the magnetar model is in strong tension with at least the most energetic long GRBs.

In the second scenario, a black hole is formed in the immediate aftermath of the death of a massive star (MacFadyen, Woosley, 1999; Woosley, 1993; Woosley, Heger, 2012). Stellar material accreting back onto the newly formed black hole may power relativistic jets. The jets burrow through the stellar envelope and provide an outlet for relativistic material to escape (Morsony et al., 2007). The typical 10-100

s durations of long GRBs correspond to the free-fall time of the star’s helium core. Unlike magnetars, these ‘collapsars’ have much less stringent caps on the potential energy which could be extracted. Theoretical predictions can easily produce energy releases greater than 10^{53} erg.

Previous estimates of the total relativistic energy ($E_{\text{rel}} = E_{\gamma} + E_{\text{K}}$) produced by GRB 160625B range from $(2.3\text{-}8.3)\times 10^{51}$ erg when assuming $\xi=1$ (Table 3.4). This is approaching but still within the upper limit of the magnetar model. We found in §3.3.2.2 that modeling the jet as a Gaussian rather than a top-hat leads to an estimate of the total relativistic energy that is below this range. Clearly, based on energetic arguments alone, we cannot rule out either the magnetar or collapsar model as progenitors. However, as noted in §3.3.2.3, assuming the participation fraction of electrons is unity is unlikely to be realistic. In agreement with K20, we find that more reasonable lower values of ξ produce an estimate of the total relativistic energy which is two orders of magnitude higher (Figure 3.9). This value can still be reasonably accommodated by the collapsar model but is in strong tension with the energy cap expected from a magnetar. Regardless, it serves to show that without a better understanding of the participation fraction it will be difficult to draw robust conclusions regarding the progenitor.

3.5 Conclusions

With this work we have performed a case study of GRB 160625B to show the benefits of detailed multiwavelength afterglow modeling as it pertains to under-

		Soft Jet Edge	Fixed θ_v
θ_v	[rad]	$0.134^{+0.042}_{-0.039}$	10^{-4}
$E_{K,\text{iso}}$	[erg]	$1.1^{+1.6}_{-0.7} \times 10^{55}$	$3.9^{+0.3}_{-0.6} \times 10^{54}$
θ_c	[rad]	$0.093^{+0.030}_{-0.026}$	0.09 ± 0.02
θ_w	[rad]	$0.59^{+0.32}_{-0.16}$	$0.024^{+0.003}_{-0.001}$
n	[cm $^{-3}$]	$4.1^{+25.2}_{-3.7}$	$3.4^{+4.6}_{-1.0} \times 10^{-7}$
p		$2.23^{+0.02}_{-0.03}$	$2.301^{+0.003}_{-0.005}$
ϵ_e		$0.076^{+0.113}_{-0.045}$	$0.079^{+0.015}_{-0.006}$
ϵ_B		$7.0^{+18}_{-4.0} \times 10^{-6}$	$0.25^{+0.06}_{-0.10}$
ξ		$0.061^{+0.054}_{-0.029}$	1.0
η ^a		$0.21^{+0.20}_{-0.11}$	$0.44^{+0.05}_{-0.02}$
E_{rel} ^b	[erg]	$1.3^{+0.9}_{-0.6} \times 10^{53}$	$2.0^{+0.4}_{-0.1} \times 10^{51}$
χ^2/dof		6.28	7.24

Uncertainties are given at 1σ confidence levels. The reduced- χ^2 is the minimum over all completed runs.

$$^a \eta = \frac{E_{\gamma,\text{iso}}}{E_{\gamma,\text{iso}} + E_{K,\text{iso}}}, \text{ assuming } E_{\gamma,\text{iso}} \sim 3 \times 10^{54} \text{ erg (Zhang et al., 2018)}$$

$$^b E_{\text{rel}} = E_{\gamma} + E_K$$

Table 3.5: Best Fit Gaussian Model Parameters for §3.4.4 and §3.4.5

standing GRB energetics and environments. We modeled observations from radio to X-ray wavelengths spanning 0.1 to 1319 days post trigger. Using the standard afterglow framework we derived values for several physical parameters pertaining to the burst and performed a comparison between top-hat and Gaussian jet structure models. Our main conclusions can be summarized as follows:

- We fit GRB 160625B with a top-hat jet via the `afterglowpy` modeling package. We find general agreement in the afterglow parameters with previous top-hat jet models.
- Next, we fit the afterglow with a Gaussian-shaped jet. Although the derived density, kinetic energy, and other microphysical parameters remain consistent with the top-hat case we find that this jet shape is strongly preferred.

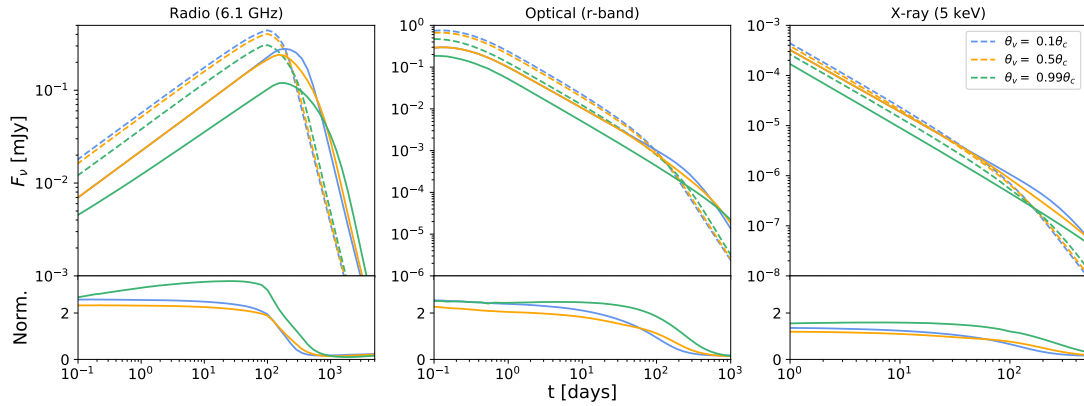


Figure 3.10: Top panel: Here we calculate the afterglow light curves for both a top-hat (solid line) and Gaussian (dashed line) jet structure at various points within the beam. We fix θ_c in the top-hat model so that E_{tot} remains the same in both models. All other parameters besides θ_v and θ_c are the same as listed in Table 3.4. Viewing a GRB off-axis has the greatest affect at early times as this is when edge effects are most noticeable. The differences between Gaussian and top-hat models are most apparent at later times. Bottom panel: The Gaussian fluxes are normalized by the top-hat models for each viewing angle.

- Finally, we considered how allowing more freedom for the participation fraction, ξ , affects the afterglow parameters. This change had the most dramatic effect and resulted in a density which is 5 orders of magnitude higher, a value of ϵ_B which is 4 orders of magnitude lower, and a total relativistic energy which is 2 orders of magnitude higher. This has important implications for constraining the GRB local circumburst environment, central engine, and burst energetics.

Given that our models include several highly degenerate parameters it can be challenging to distinguish between their various subtleties. In Figure 3.10 we show how varying the viewing angle, θ_v , impacts the burst afterglow for both top-hat and Gaussian jet structures. There exists an offset in flux density at late times between the two models that is independent of waveband or viewing angle. Therefore the

	Gaussian (free ξ)	Gaussian (fixed ξ)	Top Hat
WAIC	1782.7 ± 79.1	1744.3 ± 78.5	-3561.8 ± 167.2
Δ WAIC/N	-	0.10 ± 0.09	-14.5 ± 2.7
Confidence Level	-	$(0.58-1.16)\sigma$	$(2.7-5.3)\sigma$

A WAIC analysis is performed for each model considered. A higher WAIC score indicates better predictability for future data based on the model. The Gaussian model with ξ free to vary has a higher likelihood of describing new data well so we use it as the base to compare the others. Each Gaussian model has a higher WAIC score compared to the top-hat case but there is no strong preference for the free- ξ over the fixed- ξ Gaussian model.

Table 3.6: Model Comparison

detection of GRBs viewed substantially off-axis (‘orphan afterglows’) may not be strictly necessary and future multi-wavelength observations at very late times could help further reinforce the preference for a Gaussian-shaped jet over a top-hat jet.

In future work we plan to continue our analysis on the afterglow modeling of bright LAT-detected long GRBs. These events typically have abundant data and also tend to be observed in low-density environments, thus providing an excellent sample for comparing jet structure models. We will use the results to expand on the arguments discussed here and create a comprehensive sample of well-documented LAT long GRBs and their general properties.

Chapter 4: The Afterglows of *Fermi*-LAT GRBs: Jet Structure, Energetics, and Physical Origins

Gamma-ray bursts (GRBs) detected by the Large Area Telescope (LAT) on *Fermi* tend to be extraordinarily bright, making them ideal candidates for testing emission models beyond the traditionally assumed on-axis, top-hat jet model. Here we expand upon the work outlined in Chapter 3 modeling the broadband afterglow of GRB 160625B. We analyze a larger sample of *Fermi*-LAT detected GRBs and test assumptions typically made regarding certain physical parameters of the burst (e.g., jet shape, burst energy, circumburst density, and participation fraction of electrons). We find that the multiwavelength data for most GRBs studied here are better fit by a complex jet structure, similar to that of the short GRB 170817A - implying jet structure is not dependent on progenitor type but is rather a more universal physical process. We also present evidence to suggest that the participation fraction of electrons, ξ , in the GRB jet may be as low as a $\sim \text{few} \times 10^{-2}$ which implies higher isotropic burst kinetic energies, $E_{k,\text{iso}}$, than previously thought ($\sim \text{few} \times 10^{55}$ erg). If so, this could seriously limit magnetar-based progenitor theories and instead suggest a preference for black hole collapsar origins.

4.1 Introduction

Long-duration gamma-ray bursts (GRBs)¹ are amongst the most energetic phenomena in the Universe. The isotropic gamma-ray energy, $E_{\gamma,\text{iso}}$, released by most GRBs ranges between $10^{51} - 10^{53}$ erg (Figure 4.1). GRBs detected by the *Fermi* Large Area Telescope (LAT; Atwood et al. 2009) tend to be extraordinarily bright with measured energies in excess of 10^{53} erg (Ajello et al., 2019a). This is largely due to a combination of the low sensitivity of the LAT (compared to, e.g., the Swift Burst Alert Telescope) and also the Amati relation ($E_{\text{peak}} - E_{\gamma,\text{iso}}$, Amati et al. 2009).

These GRBs, which are produced during the deaths of massive stars, are also known to be highly collimated explosions. Most of their energy is released along a narrow cone of emission with jet opening angle, θ_c , typically between 1–10° (Rhoads, 1999; Sari et al., 1999). GRB emission is often modeled as a uniformly-distributed (top-hat) jet. Due to observational limitations, θ_c can be difficult to measure which leads to uncertainties in the estimate of the intrinsic energy released by the GRB: $E_{\gamma} = E_{\gamma,\text{iso}}(1 - \cos \theta_c) \approx E_{\gamma,\text{iso}} \frac{\theta_c^2}{2}$, where E_{γ} is the beaming-corrected gamma-ray energy of the burst and $E_{\gamma,\text{iso}}$ is the uncorrected isotropic gamma-ray energy (Bloom et al., 2001; Frail et al., 2001).² Measuring the true scale of GRB energetics therefore requires a deep understanding of the jet emission structure and collimation angle.

Motivation for considering non-top-hat jet structures stems from the fact that

¹The primary focus throughout this paper will be on long-duration GRBs, unless otherwise noted.

²This equation is only valid for the simple top-hat jet. See also §1.1.2.

many GRBs exhibit features which cannot be described by purely analytical models (e.g., the methods of [Granot, Sari 2002](#)). [Kangas, Fruchter \(2021\)](#) showed that radio behavior is often inconsistent with that predicted by the standard fireball model. Additionally, in recent years several GRBs detected by the LAT have been detected at very high energies (VHE; >100 GeV) for the first time, leading to new insights into the emission mechanisms of bright GRBs ([Abdalla et al., 2019](#); [MAGIC Collaboration et al., 2019](#); [de Naurois, 2019](#)). The power law temporal and spectral indices of their light curves cannot be explained by standard GRB afterglow theory alone and require an additional component for the VHE emission. Synchrotron self-Compton (SSC) scattering is typically invoked to account for this ([Fraija et al., 2020](#); [Wang et al., 2019](#)).

Recent work has also shown that GRB relativistic jets can take on a variety of shapes and viewing angles beyond the canonical top-hat jet. Some potential jet structure shapes include variations on top-hat, Gaussian, and power law models ([Aloy et al., 2005](#); [Coughlin, Begelman, 2020](#); [Duffell, MacFadyen, 2013a](#); [Margutti et al., 2018](#); [Mészáros et al., 1998](#); [Rossi et al., 2002, 2004](#); [Zhang et al., 2004](#); [Zhang, Mészáros, 2002](#)). Recently, modeling of the joint detection of gravitational waves and a short GRB (GRB 170817A/GW 170817; [Abbott et al. 2017a,c](#)) revealed the burst was viewed not directly on-axis but rather at an angle of $\sim 20^\circ$ and that there was off-axis emission produced by the structured jet ([Fong et al., 2019](#); [Lamb et al., 2020](#); [Lazzati et al., 2018](#); [Troja et al., 2019](#)).

LAT-detected GRBs tend to have bright, multiwavelength afterglows which can be observed for long periods of time (potentially up to 1,000 days; [Perley et al.](#)

2014), making them excellent candidates for testing underlying assumptions historically made in previous GRB modeling. This includes top-hat jet shapes, which are known to be overly simplistic, and assuming the fraction, ξ , of electrons which contribute to the synchrotron emission is 1.0, which is known to be an overestimate. Here, we make use of the ample broadband afterglow data associated with several LAT-detected GRBs to test multiple jet structure models. We use the results to infer the physical conditions of the central engine, the internal structure of the jet, the jet collimation angle, viewing angle, circumburst environment, and microphysics of the most energetic GRBs. In particular, we discuss the implications of varying ξ on various theoretical assumptions.

This paper is organized as follows: for each GRB we describe the available observations and our data reduction methods in §4.2. In §4.3 we outline the details of the GRB afterglow modeling, including an overview of the modeling code used, `afterglowpy`. We discuss the implications of our results in §4.4 and summarize our conclusions in §4.5. All error bars correspond to 1σ uncertainties, unless otherwise noted, and we assume a standard Λ CDM cosmology (Planck Collaboration et al., 2018) throughout the analysis.

4.2 Observations and Data Reduction

Here, we describe the observed broadband afterglow behavior and data reduction methods for our sample of GRB events. The GRBs in our sample are selected based on three criteria: (1) the GRB was detected by the *Fermi*-LAT, (2) the GRB

afterglow is visible from radio to X-rays, and (3) the circumburst environment of the GRB can be described as a constant density medium (i.e., $\rho(r) \propto r^0$).³ These criteria do bias us towards very energetic GRBs and exclude radio-quiet GRBs, orphan afterglows, and those bursts whose circumburst media profile may not be fully represented by analytical methods. For this work, the sample includes GRB 090902B, GRB 160509A, GRB 160625B, and GRB 180720B. We previously published our analysis of GRB 160625B in [Cunningham et al. \(2020\)](#), but include a summary here for completeness. Data observations used in this work are available in their entirety in [Appendix C](#).

These GRBs are amongst the brightest and most energetic events observed to date. Their isotropic gamma-ray energy released, $E_{\gamma,\text{iso}}$, exceeds 10^{53} erg in the 10-1000 keV bandpass ([Figure 4.1](#)). Their redshifts range from $z = 0.654 - 1.822$, placing them at typical distances for GRBs. Their prompt burst durations range from $\sim 100 - 1000$ s, thus classifying each burst as a long GRB. GRB 180720B was one of the first GRBs to be observed at very high energies (VHE; >100 GeV) by the High Energy Stereoscopic System (HESS; [Abdalla et al. 2019](#); [Hoischen et al. 2017](#)).

³The circumburst density profile to be used is determined analytically via the methods of [Granot, Sari \(2002\)](#) prior to modeling. Our modeling software, `Afterglowpy`, can only model constant density media. However, the wind-like option is currently in development and we will expand our sample to include those GRBs in future work.

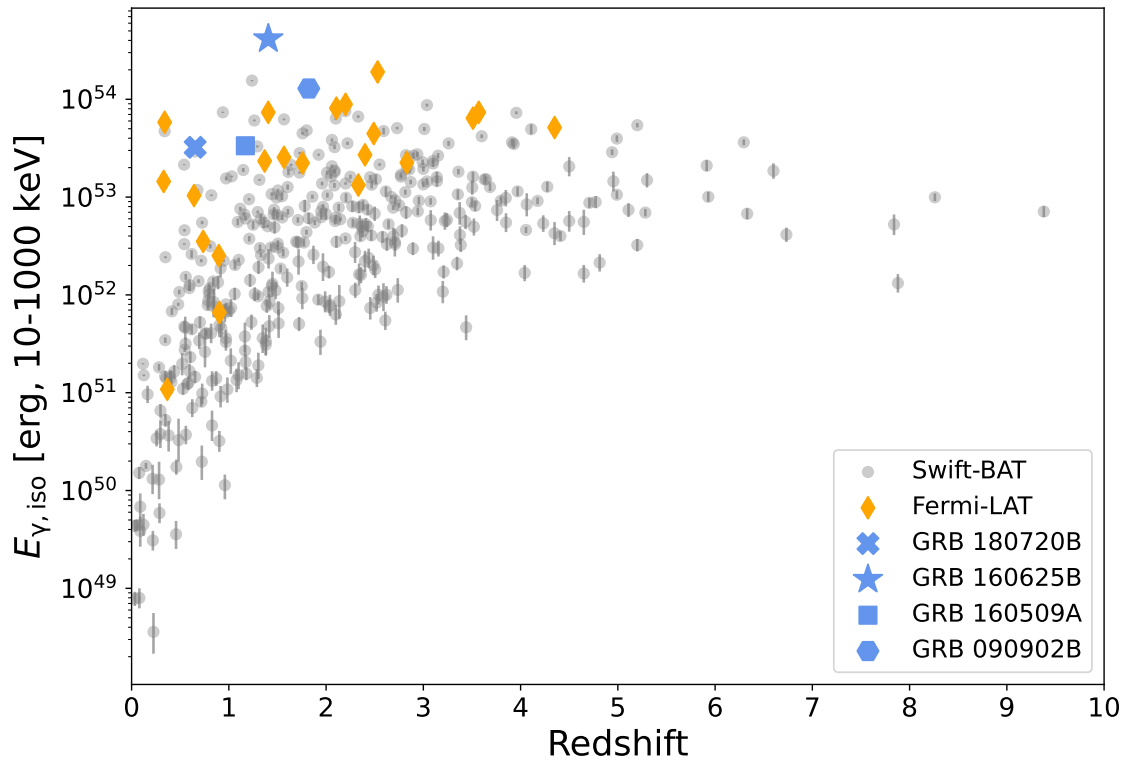


Figure 4.1: Bolometric (10-1000 keV) isotropic energy release vs redshift for the GRBs in our sample (blue symbols) compared between LAT-detected and BAT-detected GRBs. The GRBs in our sample are amongst some of the brightest observed, even by LAT standards. Data are taken from [Lien et al. \(2016b\)](#) and [Ajello et al. \(2019a\)](#).

4.2.1 GRB 090902B

4.2.1.1 Gamma-ray Data

The *Fermi* Gamma-ray Burst Monitor (GBM; Meegan et al. 2009) triggered on GRB 090902B at 11:05:08.31 UT on Sept 2, 2009 (Bissaldi, Connaughton, 2009). The light curve consists of a single bright pulse lasting for 21 seconds. The fluence in the 50 keV - 10 MeV bandpass was $(3.74 \pm 0.03) \times 10^{-4}$ erg cm⁻². We consider the GBM trigger time to be t_0 throughout this work.

The *Fermi* Large Area Telescope (LAT; Atwood et al. 2009) detected GRB 090902B shortly after at 11:05:15 UT just inside its field-of-view (de Palma et al., 2009). Emission lasted for up to 1000 s. The highest energy photon observed in the rest-frame was 33.4 GeV which occurred ~ 82 seconds after the GBM trigger. At the measured redshift of $z = 1.822$ (Cucchiara et al., 2009) the bolometric isotropic gamma-ray energy is $E_{\gamma,\text{iso}} = (1.289 \pm 0.002) \times 10^{54}$ erg (10-1000 keV; Ajello et al. 2019a).

GRB 090902B was also detected by Integral SPI-ACS and the *Suzaku* Wide-band All-sky Monitor (WAM; Terada et al. 2009).

4.2.1.2 X-ray Data

The *Neil Gehrels Swift Observatory* (Gehrels et al., 2004) detected GRB 090902B via a target-of-opportunity (ToO) request ~ 12.5 hours later (Kennea, Stratta, 2009). The observed flux in the 0.3-10 keV bandpass at this time

is 3.2×10^{-12} erg cm⁻² s⁻¹ (Stratta et al., 2009). X-Ray Telescope (XRT; Burrows et al. 2005) observations continued for ~ 23 days and are publicly available via the XRT light curve repository.⁴

Following Pandey et al. (2010) we assume no significant spectral evolution during the XRT observations and that the spectrum is an absorbed power law with galactic neutral hydrogen fixed to $N_{H,gal} = 4.49 \times 10^{20}$ cm⁻² (Willingale et al., 2013). We use $z = 1.822$, a photon index of $\Gamma = 1.76$, an intrinsic absorption column of $N_{H,int} = (2.08 \pm 0.6) \times 10^{22}$ cm⁻², and a counts-to-flux ratio of 5.1×10^{-11} erg cm⁻² ct⁻¹ to convert the XRT count rate light curve to a flux density of 5 keV.

4.2.1.3 Optical/NIR Data

The *Swift* Ultraviolet/Optical Telescope (UVOT; Roming et al. 2005) began observations at $t_0 + 12.5$ hours (concurrent with the XRT) and detected the fading afterglow (Swenson, Stratta, 2009). Gemini-North observed the optical counterpart and measured a redshift of $z = 1.822$ (Cucchiara et al., 2009). The afterglow was also observed by the Nickel 1-meter telescope at Lick Observatory (Perley et al., 2009), Faulkes Telescope North (Guidorzi et al., 2009), and ROTSE-IIIa at the Siding Spring Observatory (Pandey et al., 2009). Additionally, NIR observations were undertaken by GROND (g'r'i'z'JHK, Olivares et al. 2009).

⁴https://www.swift.ac.uk/xrt_curves/ (Evans et al., 2009, 2007)

4.2.1.4 Radio Data

The radio afterglow of GRB 090902B was first detected by the Westerbork Synthesis Radio Telescope (WSRT) at $t_0 + 1.31$ days at 4.8 GHz (van der Horst et al., 2009). The burst was then observed by the Very Large Array (VLA) for a further 200 days at 8.46 GHz (Chandra, Frail, 2009). Cenko et al. (2011) report the available WSRT and VLA data which we use in this work.

4.2.2 GRB 160509A

4.2.2.1 Gamma-ray Data

The *Fermi* Large Area Telescope (LAT; Atwood et al. 2009) triggered on GRB 160509A on May 09, 2016 at 08:59:04.36 UT (Longo et al., 2016a). There are two main components of the LAT light curve: an initial GeV flare lasting for ~ 20 s and long-lived emission beginning ~ 40 s after the trigger and continuing for 1000 s. The highest energy photon observed in the rest-frame was 52 GeV which occurred ~ 77 seconds after the GBM trigger (Longo et al., 2016b). We consider the LAT trigger time to be t_0 throughout this work.

The *Fermi* Gamma-ray Burst Monitor (GBM; Meegan et al. 2009) also triggered on the burst at the same time (08:59:04.36 UT; Roberts et al. 2016). The GBM emission lasts for ~ 371 s and the light curve is complex with multiple peaks. At the measured redshift of $z = 1.17$ (Tanvir et al., 2016) the bolometric isotropic gamma-ray energy is $E_{\gamma,\text{iso}} = (3.348 \pm 0.003) \times 10^{53}$ erg (10-1000 keV; Ajello et al.

2019a).

The burst was also observed by *Konus-Wind* with a fluence of $(2.90 \pm 0.35) \times 10^{-4}$ erg cm $^{-2}$ (20 keV - 10 MeV; Frederiks et al. 2016) and the CALET gamma-ray burst Monitor (Yoshida et al., 2016).

4.2.2.2 X-ray Data

The *Neil Gehrels Swift Observatory* detected GRB 160509A via a target-of-opportunity (ToO) request (Kennea et al., 2016). XRT observations continued for ~ 20 days before the flux dropped below detector sensitivity levels. To convert the XRT count rates to a flux density we follow the methods of both Laskar et al. (2016a) and Kangas et al. (2020) and assume $\Gamma = 2.07 \pm 0.04$ across the light curve and that the spectrum is an absorbed power law with galactic neutral hydrogen fixed to $N_{H,gal} = 2.12 \times 10^{21}$ cm $^{-2}$ (Willingale et al., 2013). We use an intrinsic absorption column of $N_{H,int} = 1.52 \times 10^{22}$ cm $^{-2}$ and a counts-to-flux ratio of 6.5×10^{-11} erg cm $^{-2}$ ct $^{-1}$ to convert the XRT count rate light curve to a flux density of 5 keV.

GRB 160509A was observed by the *Chandra* X-ray Observatory on June 20, 2016 (42.1 days post trigger; Kangas et al. 2020). We use the reduced 5 keV observation reported by Kangas et al. (2020) in our analysis here.

4.2.2.3 Optical/NIR Data

Gemini-North discovered an optical counterpart consistent with the *Swift*-XRT position at $t_0 + 5.75$ hours (Levan et al., 2016). At $t_0 + 1.03$ days Cenko et al.

(2016) observed the fading afterglow with the Lowell Discovery Telescope (LDT) and provide the first evidence for significant host extinction. Further Gemini-North observations with the GMOS-N spectrograph at ~ 1.2 days measured a redshift of $z = 1.17$ (Tanvir et al., 2016). The source was also visible in J- and K-bands. Laskar et al. (2016a) report g- and r-band observations with Keck-I/LRIS at ~ 28.2 days. Finally, Kangas et al. (2020) report multiband observations of GRB 160509A with GTC/CIRCE and HST/WFC3 between 5 and 35 days post trigger. The *Swift* UVOT only reported upper limits (Marshall, Roegiers, 2016).

We correct the optical observations for galactic reddening ($E_{B-V} = 0.25$ mag; Schlafly, Finkbeiner 2011) along the line of sight. Like Kangas et al. (2020), we follow the Pei (1992) extinction law for the Small Magellanic Cloud (SMC) model to correct for host extinction and assume $A_V = 2.8 \pm 0.1$ mag.

4.2.2.4 Radio Data

The radio afterglow was observed by the VLA from $\sim 0.35 - 20$ days at 1.2-37 GHz (PI Berger; Laskar et al. 2016a). Additional late-time VLA observations were carried out by Kangas et al. (2020) (PI Fruchter) at 6 and 9 GHz between ~ 24 and 80 days after the LAT trigger. Mooley et al. (2016) did not detect GRB 160509A with AMI-LA and report only upper limits.

4.2.2.5 VHE Data

GRB 160509A was within the FOV of HAWC but no excess VHE emission was detected (Lennarz, Taboada, 2016). Observing conditions were not conducive for detection since the sensitivity of HAWC at the burst elevation ($\sim 33^\circ$) is two orders of magnitude lower than at zenith.

4.2.3 GRB 160625B

We described the available broadband data in detail for the afterglow of GRB 160625B in Section 2.2. For convenience, we summarize the relevant information below.

The *Fermi*-GBM first triggered on GRB 160625B at 22:40:16.28 UT on 25 June, 2016 and again at 22:51:16.03. The fluence in the 10-1000 keV bandpass was $(6.4256 \pm 0.0019) \times 10^{-4}$ erg cm $^{-2}$ (von Kienlin et al., 2020). The *Fermi*-LAT triggered on the second pulse at 22:43:24.82 (Dirirsa et al., 2016). At the measured redshift of $z = 1.406$ (Xu et al., 2016) the bolometric isotropic gamma-ray energy is $E_{\gamma,\text{iso}} = (4.148 \pm 0.002) \times 10^{54}$ erg (10-1000 keV; Ajello et al. 2019a). For the analysis presented here we choose t_0 to be that corresponding to the first GBM trigger.

Swift began observing GRB 160625B 2.5 hours after the initial GBM trigger (Evans, 2016). The XRT on board *Swift* observed GRB 160625B for 47 days. We convert the 0.3-10 keV flux count rate light curves to a flux density at an energy of 5 keV. In addition to the XRT data we include the late-time *Chandra* observations taken by Kangas et al. (2020) at 69.8 and 144 days after the burst.

GRB160625B is one of the better observed GRBs in the optical. This includes observations taken by the 2 m Faulkes Telescope North (FTN) operated by Las Cumbres Observatory (LCO; [Brown et al. 2013](#)), the 2m Liverpool Telescope (LT; [Steele et al. 2004](#)) at Roque de los Muchachos Observatory (ORM), the Low Dispersion Survey Spectrograph 3 (LDSS3) at Magellan, the Reionization And Transients InfraRed camera (RATIR; [Butler et al. 2012](#)), the Ultraviolet/Optical Telescope (UVOT; [Roming et al. 2005](#)), the Hubble Space Telescope (HST), as well as several observations compiled from the Gamma-ray Burst Coordinates Network (GCN) Circulars ([Zhang et al., 2018](#)). The observations range from a few hours to 140 days post trigger ([Alexander et al., 2017](#); [Kangas et al., 2020](#); [Troja et al., 2017](#)).

In the radio we consolidate previous observations from the VLA (Program IDs 15A-235 and S81171, PIs Berger and Cenko, respectively), our own late-time observations (Program ID SC1031, PI Cenko), as well as observations from the Australian Telescope Compact Array (ATCA). The radio data span 1.4 to 1319 days post trigger.

4.2.4 GRB 180720B

4.2.4.1 Gamma-ray Data

GRB180720B was first detected by the *Fermi* Gamma-ray Burst Monitor (GBM; [Meegan et al. 2009](#)) on July 20, 2018 at 14:21:39.65 UT ([Roberts, Meegan, 2018](#)). The GBM light curve consists of a bright initial pulse with peak flux of

2.74×10^{-5} erg cm $^{-2}$ s $^{-1}$ at ~ 15 seconds followed by two more pulses at ~ 26 and ~ 50 seconds. The fluence in the 10-1000 keV bandpass was $(2.985 \pm 0.001) \times 10^{-4}$ erg cm $^{-2}$ (Roberts, Meegan, 2018). For the analysis presented here we choose t_0 to be that corresponding to the GBM trigger.

The *Fermi* Large Area Telescope (LAT; Atwood et al. 2009) detected high-energy emission from GRB 180720B at 14:21:44.55 UT. The burst was within the LAT field of view for up to 1000 seconds post-trigger. The highest energy photon observed in the rest-frame was 5 GeV which occurred ~ 137 seconds after the GBM trigger (Bissaldi, Racusin, 2018). At the measured redshift of $z = 0.654$ (Vreeswijk et al., 2018) the bolometric isotropic gamma-ray energy is $E_{\gamma,\text{iso}} = (3.229 \pm 0.001) \times 10^{53}$ erg (10-1000 keV; Ajello et al. 2019a).

GRB 180720B was detected by the *Swift* Burst Alert Telescope (BAT; Barthelmy et al. 2005) at 14:21:44 UT on July 20, 2018 (Siegel et al., 2018). The BAT emission is variable and multi-peaked. The fluence in the 15-150 keV bandpass was $(8.6 \pm 0.1) \times 10^{-5}$ erg cm $^{-2}$ (Barthelmy et al., 2018).

Detections were also reported by *Konus-Wind* (Frederiks et al., 2018), CALET (Cherry et al., 2018), and MAXI/GSC (Negoro et al., 2018).

4.2.4.2 X-ray Data

The *Swift*-XRT began observations 86.5 seconds after the BAT detection at 14:23:11.0 UT (Siegel et al., 2018). XRT observations lasted for 34.3 days before flux levels dropped below instrument sensitivities. The hardness ratio appears relatively

constant over time so we assume a single spectrum that can be described as an absorbed power law with the Galactic neutral hydrogen column fixed to 3.92×10^{20} cm^{-2} (Willingale et al., 2013). Using a photon index of $\Gamma_x = 1.79_{-0.06}^{+0.06}$, assuming an intrinsic host absorption of $n_{\text{H,int}} = 3.4 \times 10^{21}$ cm^{-2} , an unabsorbed counts-to-flux conversion factor of 4.49×10^{-11} $\text{erg cm}^{-2} \text{ct}^{-1}$, and a redshift of 0.654 (Vreeswijk et al., 2018) we convert the 0.3-10 keV count rate light curves to a flux density at an energy of 1 keV. We choose only to include data taken during photon counting mode, which begins 0.1 days after the burst.

4.2.4.3 Optical/NIR Data

Optical observations of GRB 180720B began 73 seconds after the trigger (Sasada et al., 2018) and include coverage by several different ground-based optical instruments. Fraija et al. (2019b) compiled this data reported via the GCN circulars and converted them to flux densities, correcting for galactic extinction. They report a temporal decay of $\alpha_o = 1.22 \pm 0.02$ and spectral index $\beta_o = 0.80 \pm 0.04$. Vreeswijk et al. (2018) observed the burst with the X-shooter spectrograph on the Very Large Telescope (VLT) and measured the redshift to be 0.654.

4.2.4.4 Radio Data

The burst was observed by the Arcminute Microkelvin Imager Large Array (AMI-LA; Hickish et al. 2018; Zwart et al. 2008) on 2018-07-22.21 for 3.9 hours at 15.5 GHz (Sfaradi et al., 2018). They found an initial flux density of ~ 1 mJy.

Rhodes et al. (2020) further reported five observation epochs which resulted in three detections and two 3σ upper limits.

GRB180720B was also observed by the Giant Metrewave Radio Telescope (GMRT) on 2018 Jul 29.99 UT at 1.4 GHz (Chandra et al., 2018). They report a flux density of $\sim 370 \pm 59 \mu\text{Jy}$.

4.2.4.5 VHE Data

The High Energy Stereoscopic System (HESS) began observing the GRB location ten hours after initial detection by *Fermi*-GBM and continued for another two hours (Abdalla et al., 2019). Observations in the sub-TeV band (100 to 440 GeV) revealed a new gamma-ray point source with a statistical significance of 5.3σ . Baseline observations were carried out 18 days later to rule out the possibility of a previously unidentified source producing the observed emission. The energy flux observed by HESS ($\sim 10^{-10} \text{ erg cm}^{-2} \text{ s}^{-1}$) is similar to that of the X-ray observed by the XRT (0.3 to 10 KeV).

4.3 Analysis and Broadband Modeling

Throughout this work we assume the standard fireball model for a relativistic blast wave expanding into the surrounding medium and accelerating electrons via synchrotron radiation (Granot, Sari, 2002; Sari et al., 1998). Emitting electrons are accelerated to a power-law distribution of energies with a minimum Lorentz factor of γ_m and index $-p$. The resulting spectral energy distribution (SED) is

typically described by a series of power law segments smoothly broken at three characteristic frequencies – ν_{sa} , the self-absorption frequency, ν_m , the frequency of the lowest energy electron in the distribution, and ν_c , the cooling frequency. The values of these frequencies depend on the structure of the surrounding medium of the explosion as well as the jet shape, jet microphysics, initial energy produced, and viewing angle.

We use the `Afterglowpy` code to describe the forward shock synchrotron emission emanating from the GRB afterglow (Ryan et al., 2020). `Afterglowpy` uses a combination of numerical and analytical methods to model the blast wave propagating into the surrounding medium. A useful feature of the code is its ability to model the emission as a function of the observer’s viewing angle, θ_v , and of the jet structure type. `Afterglowpy` is currently capable of modeling top-hat, power law, and Gaussian-shaped structured jets. Here, we follow the methods of Chapter 3 and focus on three GRB jet models: a top-hat jet and two Gaussian jet models - one where the participation fraction, ξ , is fixed to 1.0 and one where it is free to vary.

We employ the statistical sampling techniques of the EMCEE Python package for Markov-Chain Monte Carlo (MCMC; Foreman-Mackey et al. 2013) analysis with the `afterglowpy` models; for details, see Troja et al. (2018) and Cunningham et al. (2020). For each of our models `Afterglowpy` generates samples from the entire posterior distribution. As input, the code takes broadband fluxes, observation times, and instrument frequencies. As output, it produces samples from the posterior distribution for the viewing angle, θ_v , the isotropic kinetic energy released by the blast wave, $E_{k,iso}$, jet core opening angle, θ_c , circumburst density, n , the spectral slope of

Parameter	Unit	Distribution	Bounds
θ_v	rad	$\sin \theta$	[0.0, 0.8]
$E_{k,iso}$	erg	log-uniform	[10^{45} , 10^{57}]
θ_c	rad	uniform	[0.01, $\pi/2$]
θ_w	rad	uniform	[0.01, $12\theta_c$]
n	cm^{-3}	log-uniform	[10^{-10} , 10^4]
p		uniform	[2.0, 5.0]
ϵ_e		log-uniform	[10^{-4} , $1/3$]
ϵ_B		log-uniform	[10^{-6} , $1/3$]
ξ		log-uniform	[10^{-4} , 1]

Table 4.1: The parameter estimation prior distributions and bounds used in the MCMC fitting.

the electron distribution, p , the fraction of shock energy imparted to electrons, ϵ_e , and to the magnetic field, ϵ_B , and the fraction of electrons which are accelerated by the passing shock wave, ξ . `Afterglowpy` does not currently account for possible reverse shocks, interstellar scintillation (ISS), self-absorption, SSC scattering, or Klein-Nishina effects so we remove any data which may be affected before beginning modelling and focus only on the forward shock emission. We also bin data within similar epochs, where appropriate.

The assumed prior distributions and bounds for each parameter can be viewed in Table 4.1. In general, we assume a log-uniform prior distribution for $E_{k,iso}$, n , ϵ_e , ϵ_B , and ξ and a uniform prior distribution for θ_c , θ_w , and p . Assuming an isotropic distribution of sources, the prior distribution for the viewing angle, θ_v , is uniform in $\sin \theta_v$, as also utilized by [Abbott et al. \(2017c\)](#). We restrict $\epsilon_e < 1/3$ and $\epsilon_B < 1/3$ ([Laskar et al., 2015](#)) as well as $n < 10^4 \text{ cm}^{-3}$. This is done primarily to remove degeneracies and spurious solutions within the model fitting.

Since each of the GRB afterglows in our sample are unusually bright and long-lasting it follows that many previous works have already published relevant analysis in the literature before this work was completed. Several groups have already performed in-depth analyses on both the prompt and afterglow emission of each GRB and in some cases perform similar modeling. Therefore, for each GRB we begin by first summarizing these previous works. Then, we use their findings as a guiding point in combination with our own analytical considerations to begin our modeling analysis with `Afterglowpy`.

4.3.1 GRB 090902B

4.3.1.1 Previous Works

[Cenko et al. \(2011\)](#) model GRB 090902B as a forward shock expanding into a constant density medium. Their model predicts a slightly shallower X-ray decay than observed but the authors attribute this discrepancy to synchrotron radiative losses at late times. They also find that the radio light curve is strongly affected by ISS. Their best-fit model results in a large isotropic energy (5×10^{53} erg) and low circumburst density ($n \approx 10^{-4} \text{ cm}^{-3}$), and they find a jet break at about 20 days.

[Pandey et al. \(2010\)](#) also fit the afterglow with an ISM-like environment, but account for a moderate amount of host extinction ($A_v = 0.2$). They do not find evidence of a jet break. The authors came to their conclusions via the analytical methods of closure relations, rather than a full MCMC-based exploration of parameter space. In [McBreen et al. \(2010\)](#), the authors analyzed the afterglow of

GRB 090902B as part of a larger investigation of *Fermi*-LAT GRBs. They find similar results as Pandey et al. (2010).

4.3.1.2 Analytical Constraints

The entirety of the XRT observations can be well approximated by a single power law with index $\alpha_{XRT} = -1.31 \pm 0.03$. Both Pandey et al. (2010) and Cenko et al. (2011) attribute the steep optical light curve at $t < 1$ day to the presence of a reverse shock. The later optical data declines with $\alpha_r = -1.02 \pm 0.03$, $\alpha_g = -1.02 \pm 0.03$, and $\alpha_i = -0.99 \pm 0.04$. The difference between α_X and α_{opt} implies the X-ray and optical data originate from separate regions of the synchrotron spectrum (i.e., $\nu_{opt} < \nu_c < \nu_X$). The relative flatness of the optical light curve also suggests an ISM, rather than wind-like, medium. In this case, $p = 2.44 \pm 0.07$ ($\alpha_X = \frac{2-3p}{4}$), which is marginally consistent with that found from the optical decline: $p = 2.32 \pm 0.05$ ($\alpha_{opt} = \frac{3(1-p)}{4}$).⁵ The X-ray spectral index used here is slightly lower ($\beta_x = 0.76 \pm 0.14$) than in previous works (Cenko et al., 2011; Pandey et al., 2010) and produces an estimate of $p = 1.52 \pm 0.28$, much lower than that found from the temporal relations. For consistency with previous works we proceed following the estimates of p from the optical and X-ray temporal slopes.

The 8.46 GHz VLA data decline at a rate of $\alpha_{8.46} = -0.47 \pm 0.06$. Pandey et al. (2010) determined that $\nu_a < \nu_m$ in the slow-cooling regime and that the radio data at 4.8 and 8.46 GHz are not self-absorbed, although the reverse shock is thought to

⁵The closure relations for structured jets derived in Ryan et al. (2020) reduce to those of Granot, Sari (2002) for on-axis ($\theta_v < \theta_c$) cases.

Model	This Work		This Work		Cenko et al.
	Top-Hat	Top-Hat	Gaussian (fixed ξ)	Gaussian (free ξ)	Top-Hat
θ_v [rad]	$0.035^{+0.018}_{-0.011}$	$0.062^{+0.011}_{-0.017}$	$0.104^{+0.045}_{-0.035}$	—	—
$E_{k,\text{iso}}$ [erg]	$6.5^{+7.1}_{-2.7} \times 10^{53}$	$7.7^{+3.8}_{-1.9} \times 10^{53}$	$8.8^{+86.5}_{-7.4} \times 10^{54}$	$5.6^{+0.7}_{-0.3} \times 10^{53}$	$5.6^{+0.7}_{-0.3} \times 10^{53}$
θ_c [rad]	$0.044^{+0.016}_{-0.017}$	$0.042^{+0.007}_{-0.011}$	$0.068^{+0.028}_{-0.023}$	0.068 ± 0.003	0.068 ± 0.003
θ_w [rad]	—	$0.272^{+0.168}_{-0.137}$	$0.455^{+0.338}_{-0.234}$	—	—
n [cm^{-3}]	$1.5^{+12.9}_{-1.3} \times 10^{-4}$	$2.4^{+4.4}_{-2.1} \times 10^{-3}$	$2.0^{+20.7}_{-1.9}$	$5.6^{+0.9}_{-0.7} \times 10^{-4}$	$5.6^{+0.9}_{-0.7} \times 10^{-4}$
p	$2.14^{+0.05}_{-0.06}$	$2.24^{+0.04}_{-0.04}$	$2.23^{+0.04}_{-0.04}$	2.21 ± 0.02	2.21 ± 0.02
ϵ_e	$0.19^{+0.10}_{-0.10}$	$0.25^{+0.06}_{-0.09}$	$0.02^{+0.12}_{-0.02}$	0.13 ± 0.01	0.13 ± 0.01
ϵ_B	$0.030^{+0.097}_{-0.024}$	$3.83^{+9.20}_{-1.96} \times 10^{-3}$	$1.85^{+21.71}_{-1.60} \times 10^{-5}$	0.33	0.33
ξ	1.0	1.0	$0.041^{+0.219}_{-0.036}$	1.0	1.0
$E_{\text{rel}}^{\text{a}}$ [erg]	$1.9^{+1.2}_{-0.9} \times 10^{51}$	$3.6^{+1.0}_{-1.3} \times 10^{51}$	$5.6^{+29.1}_{-4.3} \times 10^{52}$	$(7.4 \pm 0.8) \times 10^{51}$	$(7.4 \pm 0.8) \times 10^{51}$
η^{b}	$0.66^{+0.11}_{-0.18}$	$0.63^{+0.06}_{-0.10}$	$0.13^{+0.35}_{-0.11}$	0.70 ± 0.03	0.70 ± 0.03
χ^2/dof	3.17	2.96	3.02	1.11	1.11

$$^{\text{a}} E_{\text{rel}} = E_{\gamma} + E_{\text{K}}$$

$$^{\text{b}} \eta = \frac{E_{\gamma,\text{iso}}}{E_{\gamma,\text{iso}} + E_{\text{K,iso}}}, \text{ assuming } E_{\gamma,\text{iso}} = 1.3 \times 10^{54} \text{ erg [10-1000 keV]}$$

Table 4.2: Best Fit Model Parameters for GRB 090902B

contribute to the radio emission at $t < 5$ days.

4.3.1.3 Afterglowpy Modeling

Optical data points at $t < 1$ days and radio points at $t < 5$ days are excluded from the analysis to prevent contamination from the reverse shock. We bin the VLA data by similar epochs and treat the last point as an upper limit. We also introduce a 10% uncertainty in the radio points due to ISS effects.

Our best fit parameters for each of our three models are listed in Table 4.2. The free- ξ Gaussian model is plotted in Figure 4.2. The covariances and posterior probability distributions of the various parameters are shown in Figures B.1, B.2, and B.3.

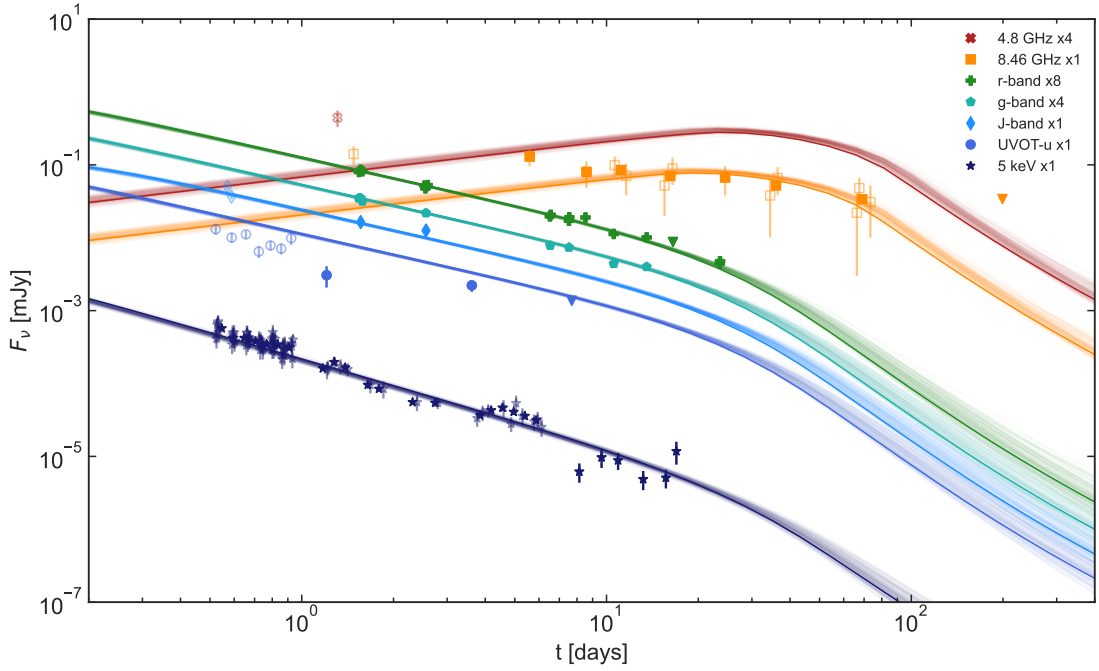


Figure 4.2: The multiwavelength light curve of GRB 090902B overplotted with our best fit model of the afterglow forward shock as a Gaussian jet with ξ free to vary. Times are referenced from the GBM trigger (Sept 02 2009 11:05:08.31 UT). Open points represent data which were available but not included in the analysis (See §4.3.1.3 for more details). Transparent lines represent model uncertainties and are calculated via samples taken from the MCMC posterior distribution.

The top-hat jet afterglow presents a multimodal solution representing two possible physical scenarios. The first solution is one where $\theta_v \sim \theta_c$, $p \sim 2.16$, and $E_{k,iso} \sim 6 \times 10^{53}$ erg. In the second, $\theta_v < \theta_c$, $p \sim 2.08$, and $E_{k,iso} \sim 3 \times 10^{53}$ erg. The first solution is consistent with that of the Gaussian jet with fixed- ξ model. In the Gaussian jet with free- ξ model the isotropic energy, $E_{k,iso}$ increases by an order of magnitude, the circumburst density, n , increases by several orders of magnitude, and ϵ_B decreases by several orders of magnitude.

4.3.2 GRB 160509A

4.3.2.1 Previous Works

[Laskar et al. \(2016a\)](#) model GRB 160509A as a combination of a reverse and forward shock. They find a low circumburst density ($\sim 10^{-3} \text{ cm}^{-3}$), high X-ray absorption column ($N_H = 1.5 \times 10^{22} \text{ cm}^{-2}$), and large host extinction ($A_V \approx 3.4$ mag).

In [Fraija et al. \(2020\)](#), the authors present an overview of LAT GRB afterglows based on the second *Fermi*-LAT catalog and in particular model the SSC components of the light curves to explain GeV flares and late-time steepening of the LAT emission. The authors model the afterglow of GRB 160509A as an example. They argue the early ($t < 40$ s) LAT observations are produced via SSC emission from a reverse shock in an ISM-like environment. The late-time LAT and XRT are consistent with a forward shock in an ISM with $p \approx 2.4$ and very low circumburst density ($\sim 4 \times 10^{-4} \text{ cm}^{-3}$).

[Kangas et al. \(2020\)](#) present late-time observations of GRB 160509A with *Chandra*, HST, and the VLA. They also find that the afterglow is consistent with an ISM-like environment of very low density ($n \sim 10^{-5} \text{ cm}^{-3}$). They use their multiwavelength modeling results to compare to magnetar origin models and find an extreme millisecond magnetar is consistent with the data. They also include the participation fraction, ξ , as an additional parameter in the analysis.

4.3.2.2 Analytical Constraints

Before calculating detailed models we begin by estimating some fundamental properties of the event via the observational temporal decline rate of the data. From $t \sim 0.6$ days to $t \sim 4.5$ days the X-ray data can be well approximated by a single power law. Then at around 5 days the decay steepens, signifying the jet-break. Kangas et al. (2020) and Laskar et al. (2016a) put the jet break (t_{jet}) at ~ 3.5 and 5.7 days, respectively.⁶ At earlier times ($t < 0.6$ days) the XRT light curve appears flatter. Laskar et al. (2016a) suggest this is a plateau phase, which is commonly seen in GRB X-ray afterglows, therefore we exclude those early points from our analysis. We also ignore a majority of the early ($t < 10$ days, $\nu < 5$ GHz) radio data due to the contribution from the known reverse shock component.

The pre-jet break X-ray data declines as a simple power law with temporal index $\alpha_{X,\text{early}} = -1.23 \pm 0.04$. Assuming $\nu_X > \nu_m$, then $F_\nu \sim t^{-3/2}$ and $\alpha = \frac{(2-3p)}{4}$ giving an estimate of $p = 2.3 \pm 0.06$. This is true for both ISM and wind-like mediums. After the jet break the emission steepens to $\alpha_{X,\text{late}} = -1.86 \pm 0.16$. For $\nu_X > \nu_m$, $F_\nu \sim t^{-p}$ for the post-jet break decline, which would imply a lower $p \sim 1.9$ (Ryan et al., 2020). In the X-rays $\beta_X = 1 - \Gamma = -1.07$. For $\nu_m < \nu_c < \nu_X$, $\beta = -p/2$; therefore, $p \sim 2.14$. For $\nu_m < \nu_X < \nu_c$, $\beta = \frac{(1-p)}{2}$ and $p \sim 3.14$. Therefore, we conclude $\nu_m < \nu_c < \nu_X$ and $p \sim 2.2$ for our initial guess. We are unable to determine the circumburst density profile based on the closure relations alone but both Laskar et al. (2016a) and Kangas et al. (2020) find a preference for an ISM-like

⁶The estimate of t_{jet} found by Kangas et al. (2020) depends upon the smoothing parameter value, w , used.

environment so we proceed under the same assumption.

4.3.2.3 Afterglow Modeling

In the optical, we fit the g-band and HST (F160W and F110W) data. We choose to ignore the r'-band, z'-band, J-band, and K-band observations in the fitting due to the heavy extinction at those wavelengths. We also ignore radio emission below 5 GHz and earlier than 10.03 days due to the presence of the reverse shock. We also ignore X-ray points earlier than 0.6 days as the afterglow appears to be in a plateau phase.

Our best fit parameters for each of our three models are listed in Table 4.3. The free- ξ Gaussian model is plotted in Figure 4.3. The covariances and posterior probability distributions of the various parameters are shown in Figures B.4, B.5, and B.6.

The Gaussian jet with fixed- ξ afterglow presents a multimodal solution representing two possible physical scenarios. In one, $E_{k,iso} \sim 6 \times 10^{53}$ erg and in the other, $E_{k,iso} \sim 2 \times 10^{54}$ erg. Only the lower energy solution is consistent with that found for the top-hat jet. Similarly to that of GRB 090902B, the Gaussian jet model with free- ξ increases by two orders of magnitude in terms of $E_{k,iso}$ and n . ϵ_B also decreases by four orders of magnitude when ξ is free to vary.

Model	This Work		This Work		This Work		Laskar et al.	Kangas et al.	Frajia et al.
	Top-Hat	Gaussian	(fixed ξ)	Gaussian	(free ξ)	Gaussian	Top-Hat	Top-Hat	Top-Hat
θ_v [rad]	$0.013^{+0.003}_{-0.003}$	$0.011^{+0.003}_{-0.003}$	$0.011^{+0.003}_{-0.003}$	$0.022^{+0.017}_{-0.010}$	$0.022^{+0.017}_{-0.010}$	—	0.026	—	—
$E_{k,iso}$ [erg]	$6.3^{+1.9}_{-1.1} \times 10^{53}$	$1.3^{+1.0}_{-0.6} \times 10^{54}$	$1.3^{+1.0}_{-0.6} \times 10^{54}$	$3.8^{+24.4}_{-3.2} \times 10^{55}$	$3.8^{+24.4}_{-3.2} \times 10^{55}$	$1.87^{+0.54}_{-0.26} \times 10^{53}$	8.50×10^{53}	$7.0^{+0.8}_{-0.8} \times 10^{53}$	—
θ_c [rad]	$0.029^{+0.006}_{-0.004}$	$0.039^{+0.007}_{-0.006}$	$0.039^{+0.007}_{-0.006}$	$0.150^{+0.102}_{-0.071}$	$0.150^{+0.102}_{-0.071}$	$0.068^{+0.002}_{-0.003}$	0.046	~ 0.145	—
θ_w [rad]	—	$0.017^{+0.008}_{-0.005}$	$0.017^{+0.008}_{-0.005}$	$0.046^{+0.027}_{-0.020}$	$0.046^{+0.027}_{-0.020}$	—	—	—	—
η [cm^{-3}]	$6.7^{+11.7}_{-4.2} \times 10^{-6}$	$4.5^{+6.7}_{-2.2} \times 10^{-6}$	$4.5^{+6.7}_{-2.2} \times 10^{-6}$	$0.422^{+9.62}_{-0.416}$	$0.422^{+9.62}_{-0.416}$	$(8.6 \pm 2.2) \times 10^{-4}$	2.10×10^{-5}	$4.5^{+1.1}_{-1.1} \times 10^{-4}$	—
p	$2.17^{+0.05}_{-0.04}$	$2.10^{+0.03}_{-0.02}$	$2.10^{+0.03}_{-0.02}$	$2.03^{+0.03}_{-0.02}$	$2.03^{+0.03}_{-0.02}$	2.39 ± 0.03	2.29	$2.40^{+0.08}_{-0.08}$	—
ϵ_e	$0.26^{+0.05}_{-0.06}$	$0.29^{+0.03}_{-0.05}$	$0.29^{+0.03}_{-0.05}$	$0.025^{+0.130}_{-0.023}$	$0.025^{+0.130}_{-0.023}$	$0.84^{+0.06}_{-0.08}$	0.19	$3.1^{+0.3}_{-0.3} \times 10^{-2}$	—
ϵ_B	$0.132^{+0.120}_{-0.074}$	$0.178^{+0.102}_{-0.091}$	$0.178^{+0.102}_{-0.091}$	$4.14^{+75.40}_{-3.76} \times 10^{-5}$	$4.14^{+75.40}_{-3.76} \times 10^{-5}$	$0.11^{+0.07}_{-0.05}$	0.015	$4.1^{+0.9}_{-0.9} \times 10^{-5}$	—
ξ	1.0	1.0	1.0	$0.006^{+0.036}_{-0.005}$	$0.006^{+0.036}_{-0.005}$	1.0	1.0	1.0	—
E_{rel}^a [erg]	$4.2^{+1.2}_{-0.7} \times 10^{50}$	$2.3^{+0.7}_{-0.5} \times 10^{50}$	$2.3^{+0.7}_{-0.5} \times 10^{50}$	$4.0^{+22.7}_{-3.4} \times 10^{52}$	$4.0^{+22.7}_{-3.4} \times 10^{52}$	$(1.74 \pm 0.32) \times 10^{51}$	1.70×10^{51}	—	—
η^b	$0.35^{+0.05}_{-0.06}$	$0.20^{+0.13}_{-0.07}$	$0.20^{+0.13}_{-0.07}$	$0.01^{+0.05}_{-0.01}$	$0.01^{+0.05}_{-0.01}$	0.64 ± 0.07	0.5	0.15 ± 0.02	—
χ^2/dof	2.67	2.46	2.46	2.53	2.53	1.34	1.8	—	—

^a $E_{rel} = E_\gamma + E_K$

^b $\eta = \frac{E_{\gamma,iso}}{E_{\gamma,iso} + E_{k,iso}}$, assuming $E_{\gamma,iso} \sim 3.3 \times 10^{53}$ erg [10-1000 keV]

Table 4.3: Best Fit Model Parameters for GRB 160509A

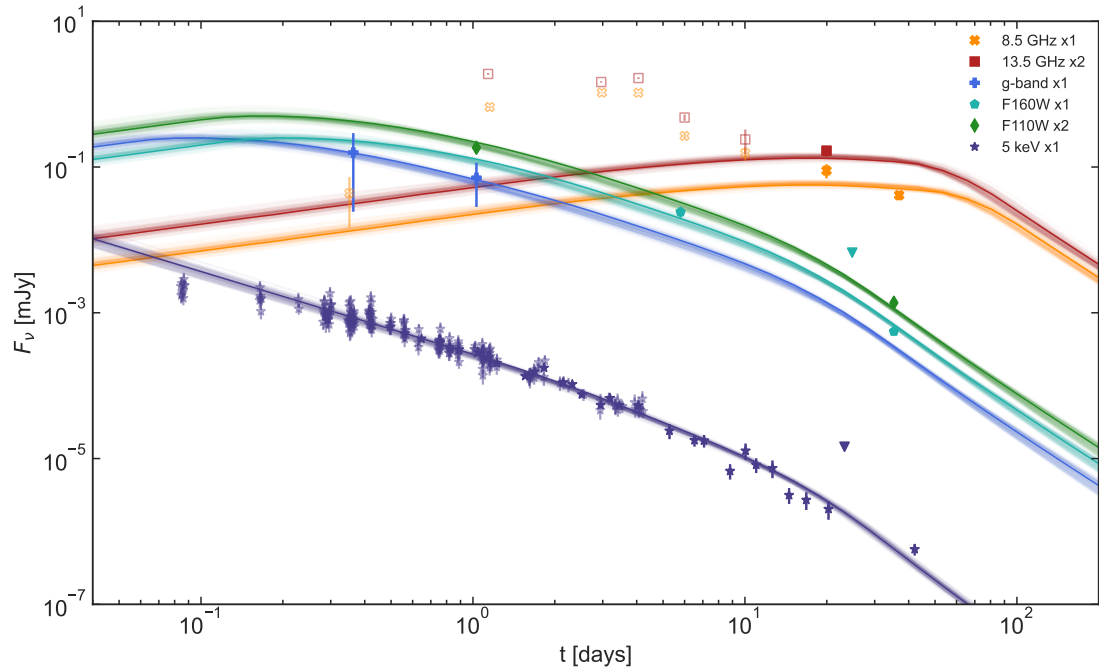


Figure 4.3: The multiwavelength light curve of GRB 160509A overplotted with our best fit model of the afterglow forward shock as a Gaussian jet with ξ free to vary. Times are referenced from the LAT trigger (May 09 2016 08:59:04.36 UT). Open points represent data which were available but not included in the analysis (See §4.3.2.3 for more details). Transparent lines represent model uncertainties and are calculated via samples taken from the MCMC posterior distribution.

4.3.3 GRB 160625B

4.3.3.1 Previous Works

[Alexander et al. \(2017\)](#) model the afterglow of GRB 160626B as a combination of a reverse shock and forward shock propagating into a uniform ISM-like medium of very low density ($n \sim 5 \times 10^{-5} \text{ cm}^{-3}$). They find the radio emission is dominated by the reverse shock as well as scattering due to interstellar scintillation from the Milky Way galaxy.

In [Troja et al. \(2017\)](#) the authors measure the polarization of the early afterglow to probe the configuration of the surrounding magnetic field. Their broadband modeling also results in a low circumburst density ($\sim 10^{-4} \text{ cm}^{-3}$) and high isotropic kinetic energy ($E_{k,\text{iso}} \sim 10^{54} \text{ erg}$).

[Kangas et al. \(2020\)](#) also model GRB 160625B in addition to GRB 160509A. They report modeling parameters consistent with [Troja et al. \(2017\)](#) and [Alexander et al. \(2017\)](#) but again examine how lowering the participation fraction, ξ , impacts the modeling and limits on the progenitor.

4.3.3.2 Analytical Constraints

In Chapter 3 we examined the early and late-time temporal and spectral evolution of the afterglow to determine that the burst was most probably expanding into an ISM-like environment with $p \sim 2.3$, a jet-break occurs at around 20 days, and that the cooling break occurred between the X-ray and optical observations.

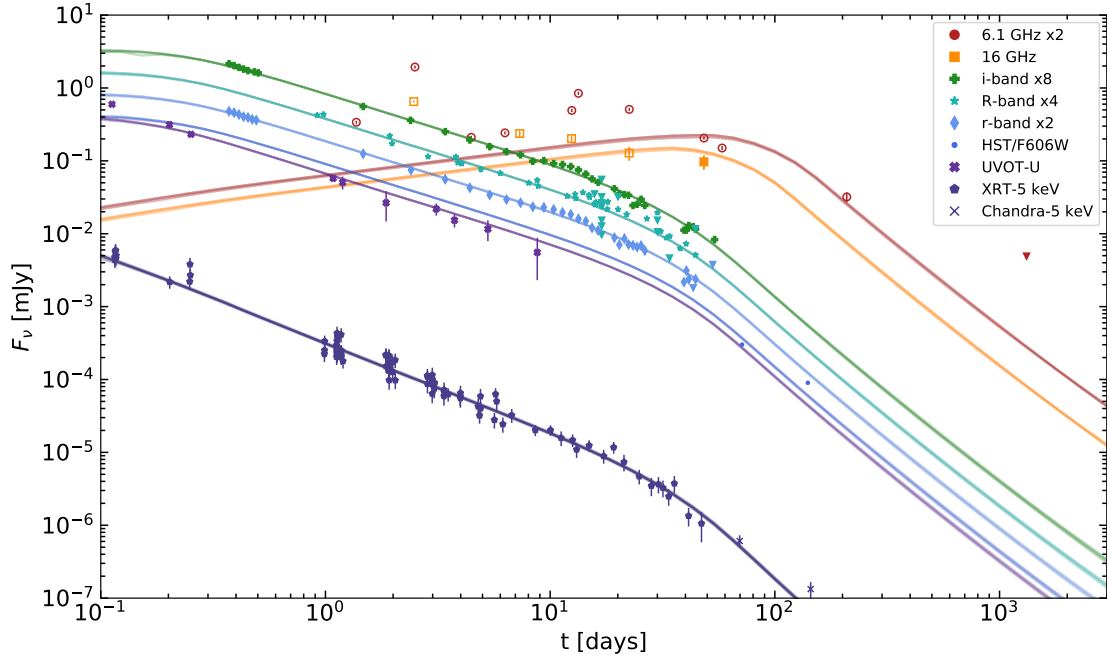


Figure 4.4: The multiwavelength light curve of GRB 160625B overplotted with our best fit model of the afterglow forward shock as a Gaussian jet with ξ free to vary. Times are referenced from the GBM trigger (Jun 25 2016 22:40:16.28 UT). Open points represent data which were available but not included in the analysis (See §4.3.3.3 for more details). Transparent lines represent model uncertainties and are calculated via samples taken from the MCMC posterior distribution.

For more details, see §3.3.1.

4.3.3.3 Afterglowpy Modeling

Details on our MCMC analysis and modeling setup for GRB 160625B can be found in §3.3.2. We ignore any radio emission influenced by the reverse shock or the interstellar scintillation ($\nu < 10$ GHz and $t < 20$ days) to model only the forward shock component. The current model parameters are listed in Table 4.4. The resulting light curve is shown in Figure 4.4.

Model	This Work		This Work		This Work		Alexander et al.	Kangas et al.	Troja et al.
	Top-Hat	Gaussian (fixed ξ)	Gaussian (fixed ξ)	Gaussian (free ξ)	Top-Hat	Top-Hat	Top-Hat	Top-Hat	Top-Hat
θ_v [rad]	$0.0073^{+0.0024}_{-0.0015}$	$0.022^{+0.006}_{-0.001}$	$0.022^{+0.006}_{-0.001}$	$0.066^{+0.010}_{-0.009}$	-	0.012	-	-	
$E_{k,iso}$ [erg]	$2.3^{+0.5}_{-0.7} \times 10^{54}$	$3.1^{+0.4}_{-0.8} \times 10^{54}$	$3.1^{+0.4}_{-0.8} \times 10^{54}$	$4.2^{+24}_{-3.5} \times 10^{55}$	$1.1^{+1.0}_{-0.5} \times 10^{54}$	1.8×10^{54}	$1.1^{+1.0}_{-0.5} \times 10^{54}$	$2.0^{+1.0}_{-1.4} \times 10^{54}$	
θ_c [rad]	$0.032^{+0.009}_{-0.004}$	$0.022^{+0.006}_{-0.001}$	$0.022^{+0.006}_{-0.001}$	$0.068^{+0.010}_{-0.010}$	0.063 ± 0.003	0.059	0.063 ± 0.003	$0.042^{+0.028}_{-0.012}$	
θ_w [rad]	-	$0.028^{+0.007}_{-0.002}$	$0.028^{+0.007}_{-0.002}$	$0.083^{+0.014}_{-0.011}$	-	-	-	-	
η [cm^{-3}]	$9.6^{+39.0}_{-5.9} \times 10^{-7}$	$3.1^{+11}_{-1.1} \times 10^{-6}$	$3.1^{+11}_{-1.1} \times 10^{-6}$	$0.352^{+1.71}_{-0.307}$	$(5 \pm 3) \times 10^{-5}$	1.1×10^{-5}	$(5 \pm 3) \times 10^{-5}$	$1^{+49}_{-0.9} \times 10^{-4}$	
p	2.30 ± 0.02	$2.13^{+0.01}_{-0.01}$	$2.13^{+0.01}_{-0.01}$	$2.10^{+0.01}_{-0.01}$	2.31 ± 0.01	2.30	2.31 ± 0.01	2.2	
ϵ_e	$0.12^{+0.05}_{-0.02}$	$0.19^{+0.07}_{-0.02}$	$0.19^{+0.07}_{-0.02}$	$0.017^{+0.085}_{-0.014}$	$0.23^{+0.07}_{-0.08}$	0.13	$0.23^{+0.07}_{-0.08}$	$0.10^{+0.22}_{-0.09}$	
ϵ_B	$0.16^{+0.11}_{-0.10}$	$0.17^{+0.05}_{-0.09}$	$0.17^{+0.05}_{-0.09}$	$3.9^{+21.9}_{-3.3} \times 10^{-5}$	$0.013^{+0.11}_{-0.01}$	0.030	$0.013^{+0.11}_{-0.01}$	$0.010^{+0.090}_{-0.009}$	
ξ	1.0	1.0	1.0	$0.016^{+0.080}_{-0.013}$	1.0	1.0	1.0	1.0	
E_{rel}^a [erg]	$2.7^{+1.3}_{-0.5} \times 10^{51}$	$1.6^{+0.6}_{-0.1} \times 10^{51}$	$1.6^{+0.6}_{-0.1} \times 10^{51}$	$1.2^{+6.5}_{-0.9} \times 10^{53}$	$2.3^{+1.8}_{-1.2} \times 10^{51}$	8.3×10^{51}	$2.3^{+1.8}_{-1.2} \times 10^{51}$	$\sim 6 \times 10^{51}$	
η^b	$0.56^{+0.08}_{-0.05}$	$0.49^{+0.08}_{-0.03}$	$0.49^{+0.08}_{-0.03}$	$0.067^{+0.253}_{-0.057}$	$0.73^{+0.10}_{-0.14}$	0.62	$0.73^{+0.10}_{-0.14}$	$0.75^{+0.16}_{-0.09}$	
χ^2/dof	1.24	0.99	0.99	0.86	1.26	8.6	1.26	-	

^a $E_{rel} = E_\gamma + E_K$

^b $\eta = \frac{E_{\gamma,iso}}{E_{\gamma,iso} + E_{k,iso}}$, assuming $E_{\gamma,iso} \sim 4.15 \times 10^{54}$ erg [10-1000 keV]

Table 4.4: Best Fit Model Parameters for GRB 160625B

4.3.4 GRB 180720B

4.3.4.1 Previous Works

[Fraija et al. \(2019b\)](#) modeled the radio to sub-TeV emission of GRB 180720B as an external shock wave propagating through an ISM-like medium. Their multi-wavelength analysis covers up to 30 days after the initial trigger. They find that early (<200 s) X-ray and LAT data are consistent with synchrotron self-compton emission and that the radio emission is in the self-absorption regime.

[Rhodes et al. \(2020\)](#) interpret the AMI-LA data of GRB 180720B as forward shock emission. The radio afterglow is visible for ~ 6 days before fading and only upper limits are available. They find a power law decay of $\alpha_r = 1.2 \pm 0.1$. Given the similar temporal slopes between the radio and optical light curves [Rhodes et al. \(2020\)](#) find that to be consistent with an ISM-like homogeneous medium. They make arguments supporting the hypothesis that GRBs with VHE emission (including 190114C and 190829A) are drawn from the same population as other radio-bright GRBs; i.e., GRB 180720B is not coming from a special class of GRBs.

In [Abdalla et al. \(2019\)](#) the authors report a detailed analysis of the late time (>10 hours) VHE emission observed by HESS. At such late times the bulk Lorentz factor is expected to have decreased significantly as it is dependent upon the radius, R , that the blast wave has traveled:

$$\Gamma = \sqrt{\frac{E_{\text{iso}}}{\frac{4\pi}{3}R^3 n m_p c^2}} \approx 10^{-4} \left(E_{\text{iso}} n^{-1} t^{-3} (1+z)^3 \right)^{1/8} \quad (4.1)$$

where E_{iso} is the isotropic energy released, n is the density of the circumburst medium, m_p is the proton mass, and c is the speed of light (Blandford, McKee, 1976). The radius for a homogeneous medium is given as $R \approx 8\Gamma^2 tc \frac{1}{(1+z)}$ where t is the time since the initial blast and z is the redshift. In GRB modeling the ratio of the isotropic energy and density (E_{iso}/n) is often degenerate. For GRB 180720B ($z=0.654$ and $t=10$ hr), even assuming a generous ratio of $E_{\text{iso}}/n \approx 10^{55}$ erg cm³ leads to a maximum bulk Lorentz factor of $\Gamma \lesssim 20$ at the time of the VHE emission and cannot explain such high energy photons ($E_{\text{max}}^{\text{syn}} = 9 \Gamma mc^2 / 4\alpha_F \approx 100 \Gamma$ MeV where α_F is the fine structure constant; Aharonian 2000). Therefore, the presence of a second source of emission, such as SSC, is necessary.

Duan, Wang (2019) analyzed the prompt spectral evolution and high-energy emission during the early X-ray flare. They conclude that the prompt emission is produced via synchrotron emission and the 100 MeV to GeV emission is produced via synchrotron self-Compton radiation. Wang et al. (2019) also interpret the sub-TeV emission of GRB 180720B as SSC emission from afterglow shocks expanding in a constant-density circumburst medium. Ronchi et al. (2020) assume a wind-like circumburst medium to model the very early high-energy afterglow emission as synchrotron dominated radiation.

4.3.4.2 Analytical Constraints

Prior to performing the MCMC analysis we gather insight on some of the physical parameters by analytically fitting the temporal decay of the broadband

light curves. [Fraija et al. \(2019b\)](#) and [Rhodes et al. \(2020\)](#) both ascribe the decrease in X-ray emission at ~ 3 days to the cooling break passing through the X-ray band, rather than to a jet break. No previous works seem to find a jet break for this burst.

For $t < 3$ days the XRT data show a power law decay of $\alpha_{X,\text{early}} = -1.29 \pm 0.01$. In the case of a slow-cooling constant-density (ISM-like) profile $\alpha_{\text{ISM}} = \frac{3(1-p)}{4}$ ($\nu < \nu_c$) which yields an estimate for p of 2.73 ± 0.02 ([Granot, Sari, 2002](#)). In the slow-cooling wind-like scenario $\alpha_{\text{wind}} = \frac{(1-3p)}{4}$ which yields $p = 2.06 \pm 0.02$. For the late-time XRT data ($t > 3$ days) we find $\alpha_{X,\text{late}} = -1.69 \pm 0.07$.

Using the r'-band data we find $\alpha_r = -1.1 \pm 0.1$. This produces a p of 2.47 ± 0.19 for the ISM scenario and $p = 1.81 \pm 0.19$ for the wind. [Rhodes et al. \(2020\)](#) report $\alpha_{15.5} = -1.2 \pm 0.1$ for their 15.5 GHz AMI-LA radio data. This is only consistent for observations below the self-absorption frequency ($\alpha \sim -5/4$, $\nu < \nu_{SA}$) in ISM-like environments.

The early XRT data and r'-band data should exist within the same power law segment of the SED ($\nu_{SA} < \nu < \nu_c$). At $t = 1.9$ days the spectral index between the optical and X-ray data is $\beta = -0.68 \pm 0.03$. In this regime $\beta = \frac{(1-p)}{2}$ which produces $p = 2.36 \pm 0.07$. Likewise, based on the X-ray spectral evolution ($\beta_x = 1 - \Gamma = -0.79 \pm 0.06$) we find an estimate of $p = 2.58 \pm 0.12$. Thus, we proceed assuming a slow-cooling, ISM-like environment with an initial guess of $p \sim 2.6$, $\nu_c \gtrsim 1$ keV, and $\nu_{SA} > 15.5$ GHz.

Model		This Work	This Work	This Work	Fraija et al.
		Top-Hat	Gaussian (fixed ξ)	Gaussian (free ξ)	Top-Hat
θ_v	[rad]	$0.13^{+0.06}_{-0.05}$	$0.11^{+0.04}_{-0.04}$	$0.11^{+0.04}_{-0.04}$	—
$E_{k,\text{iso}}$	[erg]	$1.6^{+6.8}_{-0.8} \times 10^{54}$	$1.6^{+4.0}_{-0.8} \times 10^{54}$	$1.6^{+6.4}_{-1.0} \times 10^{54}$	$4.7^{+0.3}_{-0.1} \times 10^{54}$
θ_c	[rad]	$0.18^{+0.07}_{-0.07}$	$0.52^{+0.28}_{-0.22}$	$0.54^{+0.31}_{-0.23}$	—
θ_w	[rad]	—	$0.16^{+0.05}_{-0.06}$	$0.16^{+0.06}_{-0.06}$	—
n	[cm ⁻³]	$15.4^{+64.0}_{-14.6}$	$21.0^{+63.6}_{-19.2}$	$21.9^{+71.6}_{-20.2}$	$1.0^{+0.1}_{-0.1}$
p		$2.26^{+0.05}_{-0.04}$	$2.25^{+0.04}_{-0.03}$	$2.25^{+0.04}_{-0.03}$	$2.4^{+0.1}_{-0.1}$
ϵ_e		$0.16^{+0.13}_{-0.12}$	$0.18^{+0.12}_{-0.11}$	$0.13^{+0.14}_{-0.10}$	$1.0^{+0.1}_{-0.1} \times 10^{-2}$
ϵ_B		$2.5^{+10.0}_{-1.3} \times 10^{-6}$	$2.2^{+5.7}_{-1.0} \times 10^{-6}$	$2.1^{+5.0}_{-0.9} \times 10^{-6}$	$5.6^{+0.5}_{-0.5} \times 10^{-5}$
ξ		1.0	1.0	$0.21^{+0.40}_{-0.14}$	1.0
$E_{\text{rel}}^{\text{a}}$	[erg]	$3.3^{+7.8}_{-1.6} \times 10^{52}$	$2.5^{+2.6}_{-1.1} \times 10^{52}$	$2.6^{+3.7}_{-1.2} \times 10^{52}$	—
η^{b}		$0.17^{+0.13}_{-0.13}$	$0.17^{+0.12}_{-0.12}$	$0.17^{+0.16}_{-0.13}$	—
χ^2/dof		18.50	23.20	23.36	—

$$^{\text{a}} E_{\text{rel}} = E_{\gamma} + E_{\text{K}}$$

$$^{\text{b}} \eta = \frac{E_{\gamma,\text{iso}}}{E_{\gamma,\text{iso}} + E_{\text{K,iso}}}, \text{ assuming } E_{\gamma,\text{iso}} \sim 3.3 \times 10^{53} \text{ erg [10-1000 keV]}$$

Table 4.5: Best Fit Model Parameters for GRB 180720B

4.3.4.3 Afterglowpy Modeling

Given that `Afterglowpy` does not currently account for self-absorption, we exclude the radio (AMI-LA and GMRT) points from our MCMC analysis. Due to the presence of VHE emission at $t = 0.5$ days, we choose to exclude the optical and radio points prior to this. This is to prevent any possible contamination from SSC effects.

Our best fit parameters for each of our three models are listed in Table 4.5. The free- ξ Gaussian model is plotted in Figure 4.5. The covariances and posterior probability distributions of the various parameters are shown in Figures B.7, B.8, and B.9.

Interestingly, all three cases find similar solutions independent of model type. The biggest difference is seen between the Gaussian models and the top-hat in terms of the collimation angle, θ_c . The Gaussian models prefer a θ_c that is more than twice as large as seen in the top-hat model. Also, each Gaussian model prefers $\theta_w < \theta_c$, which suggests a more top-hat-like jet shape.

Since we exclude the radio emission from the analysis, we perform a manual estimate of the 1.4 and 15.5 GHz self-absorbed light curves. We follow the frequency scaling relations of [Granot, Sari \(2002\)](#) and assume that $\nu_{radio} < \nu_{sa} < \nu_m$. Our results manage to recreate the approximate order of magnitude flux of the radio points at 15.5 GHz but not the shape of the light curve at early times ([Figure 4.5](#)). This is likely because the radio points occur around the time of a spectral break and our simple analysis does not account for that.

4.4 Discussion

4.4.1 Model Comparison with WAIC

In [Chapter 3](#) we described how the Widely Applicable Information Criterion (WAIC; [Watanabe 2010](#)) can be used to discriminate between different jet structure models. A WAIC score is an estimate of the expected log predictive density (elpd) and provides a measure of model predictability for future observations ([Gelman et al., 2013](#)). Higher WAIC scores indicate better predictive power over new, unseen data. To determine whether one model predicts the observations better than another we compute an uncertainty on the difference between their individual WAIC scores.

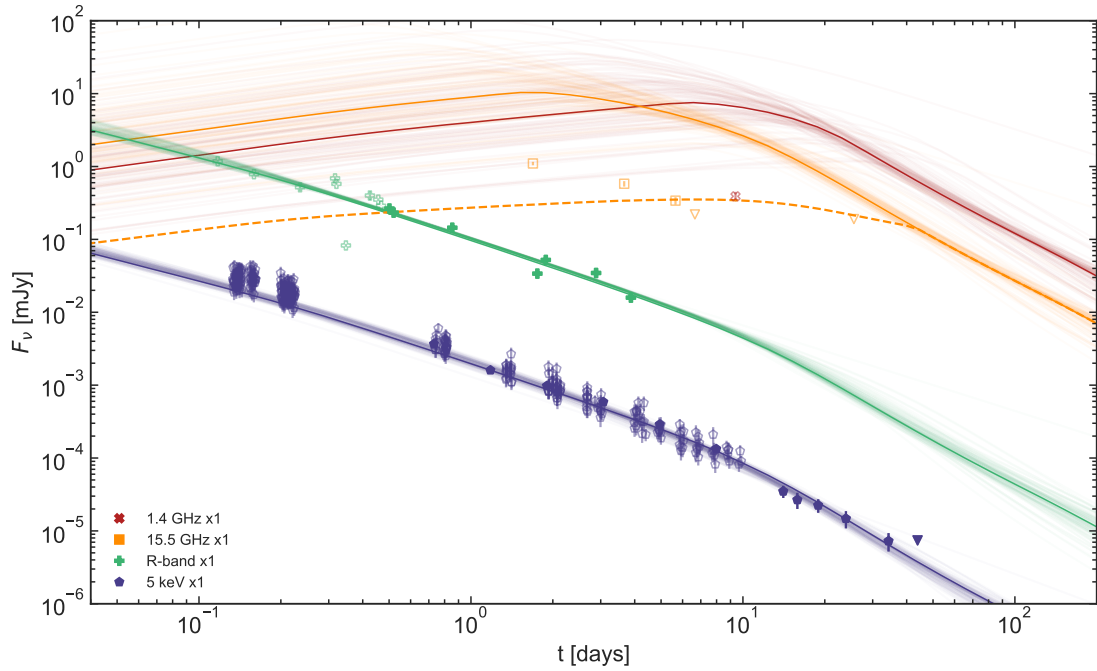


Figure 4.5: The multiwavelength light curve of GRB 180720B overplotted with our best fit model of the afterglow forward shock as a Gaussian jet with ξ free to vary. Times are referenced from the GBM trigger (July 20 2018 14:21:39.65 UT). Open points represent data which were available but not included in the analysis (See §4.3.4.3 for more details). The dashed line represent a manual estimate of the 15.5 GHz self-absorbed light curve, assuming $\nu_{radio} < \nu_{sa} < \nu_m$. Transparent lines represent model uncertainties and are calculated via samples taken from the MCMC posterior distribution.

	Gaussian (free- ξ)	Gaussian (fixed- ξ)	Top-Hat
WAIC	128.8 ± 37.2	121.6 ± 36.8	-3.0 ± 37.2
Δ WAIC/N	-	0.09 ± 0.09	1.6 ± 0.6
Confidence Level	-	0.96σ	2.8σ

Table 4.6: Model Comparison for GRB 090902B

	Gaussian (free- ξ)	Gaussian (fixed- ξ)	Top-Hat
WAIC	141.4 ± 31.6	175.2 ± 31.2	185.7 ± 31.3
Δ WAIC/N	-	-0.7 ± 0.5	-0.9 ± 1.4
Confidence Level	-	1.38σ	0.68σ

Table 4.7: Model Comparison for GRB 160509A

If the uncertainty on the difference is less than the difference itself then the model with the higher WAIC score is robustly favored. To evaluate the significance of the difference between two models we use the standard error (SE) of the difference in WAIC scores, which has been shown to be an accurate and unbiased estimator (Sivula et al., 2020; Vehtari et al., 2015).

Tables 4.6, 4.7, 4.8, and 4.9 show the WAIC score analysis for each GRB. GRB 090902B and GRB 160625B both favor the free- ξ Gaussian model over the top-hat case, but the the difference is not significant when compared to the fixed- ξ case. In the case of GRB 180720B the fixed- ξ Gaussian model is only mildly favored over the free- ξ Gaussian and top-hat models. Given the errors on the WAIC scores we cannot distinguish between models for GRB 160509A and so we consider them approximately equally likely.

	Gaussian (free- ξ)	Gaussian (fixed- ξ)	Top-Hat
WAIC	1782.7 ± 79.1	1744.3 ± 78.5	-3561.8 ± 167.2
Δ WAIC/N	-	0.10 ± 0.09	-14.5 ± 2.7
Confidence Level	-	1.16σ	5.3σ

Table 4.8: Model Comparison for GRB 160625B

	Gaussian (free- ξ)	Gaussian (fixed- ξ)	Top-Hat
WAIC	-336.4 ± 46.9	-221.7 ± 68.7	-555.0 ± 44.7
Δ WAIC/N	-	-6.0 ± 2.6	11.5 ± 4.3
Confidence Level	-	2.34σ	2.70σ

Table 4.9: Model Comparison for GRB 180720B

4.4.2 Participation Fraction, ξ

GRB afterglow modeling is plagued by several degeneracies between parameters although sufficient broadband observations can help constrain models in many cases. For example, $E_{k,\text{iso}}$, n , ϵ_e , and ϵ_B may be constrained given observations of ν_m , ν_c , ν_{sa} , and F_m (the flux at ν_m) from the SED. The electron distribution index, p , can be estimated via the methods of [Granot, Sari \(2002\)](#), as demonstrated in §4.3, and the jet collimation angle, θ_c , is directly related to the timing of a jet break within an afterglow light curve. [Eichler, Waxman \(2005\)](#) show that ξ is subject to a simple degeneracy that is independent of the synchrotron spectral regime: $E'_{k,\text{iso}} = E_{k,\text{iso}}/\xi$, $n' = n/\xi$, $\epsilon'_B = \xi\epsilon_B$, $\epsilon'_e = \xi\epsilon_e$. Therefore, introducing this additional degenerate free parameter naturally compounds the difficulties in constraining our afterglow models here.

For simplicity most authors typically assume $\xi = 1$ and that virtually all of the ambient electrons undergo acceleration. However, simulations show that lower

values of ξ may be more realistic and could potentially be as low as 0.01 (Sironi, Spitkovsky, 2011; Sironi et al., 2013; Warren et al., 2018). Therefore, arbitrarily fixing ξ to 1.0 may be introducing unintended biases within the modeling process. For our third model presented here we left ξ as a free parameter and found results which covered a wide range of values, though none were consistent with 1.0 (Figure 4.6).

In Figure 3.9 we showed how varying the value of ξ could have dramatic effects on interpretations of the resulting light curve. In most cases, a lower estimate of ξ leads to significantly higher predictions for $E_{k,\text{iso}}$ and n . Clearly, a better understanding of ξ is needed to fully constrain the model parameter space. A combination of better observational constraints on the other physical parameters with more precise theoretical simulations will be needed to help determine better priors for ξ .

4.4.3 Jet Structure Shape

In 3 out of 4 cases a Gaussian jet structure is found to have higher predictive power over a top-hat jet. In the fourth case (GRB 160509A) a strong preference cannot be determined as the WAIC scores are all roughly consistent with each other, given the relative uncertainties. However, for the Gaussian models of GRB 160509A $\theta_w < \theta_c$, suggesting a single core of emission without wings, which is more reminiscent of a top-hat jet shape. Interestingly, for GRB 180720B, similar physical parameters are found independent of the jet structure model used and again $\theta_w < \theta_c$ for

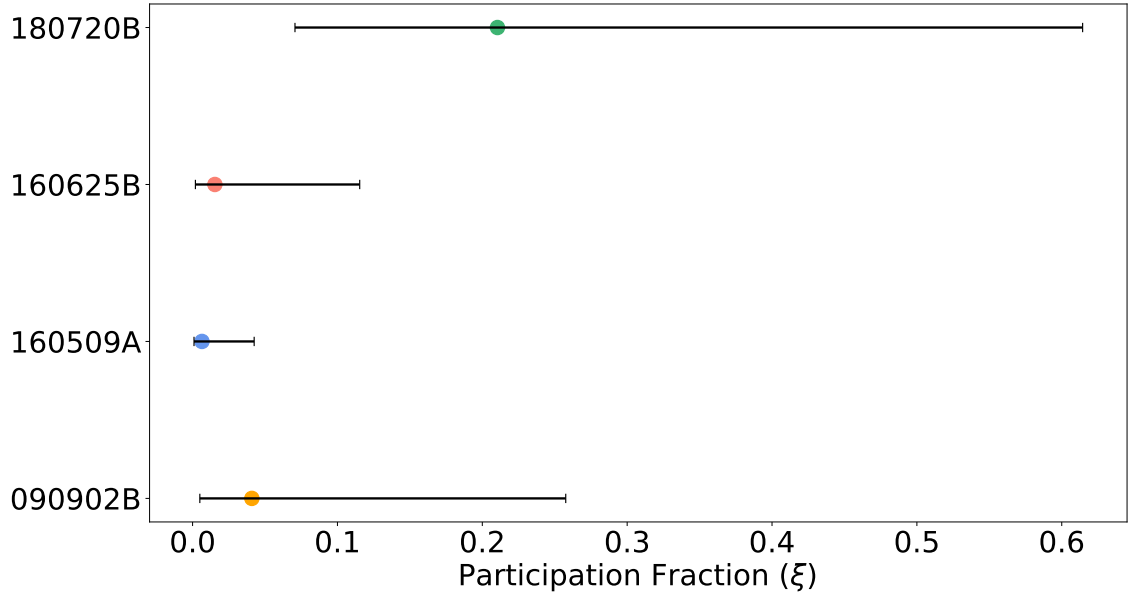


Figure 4.6: ξ parameter ranges for the four GRBs in our sample. ξ is highly degenerate with several other parameters such as $E_{k,\text{iso}}$, n , ϵ_e , and ϵ_B and is difficult to constrain. Most authors assume $\xi = 1.0$ but our results here are consistent with simulations that show lower values are likely more physically realistic.

the Gaussian models.

In Chapter 3 we found that the off-axis emission of GRB 160625B did not extend greatly beyond the primary core of the jet emission ($\theta_c/\theta_w \sim 0.8$). We showed how this is likely due to sharp edge effects creating a degeneracy with p . We see a similar pattern of behavior in p for GRB 160509A, suggesting it may be difficult to constrain p and θ_c/θ_w for some structured jets. This is consistent with the findings of [Lamb et al. \(2021\)](#). They find that the sharpness of a jet edge can vary from GRB to GRB and that it is intricately connected to the relationship between observer viewing angle, jet collimation angle, and other effects such as the lateral spreading of the jet.

4.4.4 Energetics and Central Engine

In §4.4.2 we discussed how the degeneracy of ξ with several other parameters make it difficult to constrain. Assuming $\xi = 1.0$ acts to place a bound on the other parameters in the model. When ξ is allowed to explore lower fractions the other model parameters must compensate for the change. If a smaller portion of electrons are producing synchrotron emission then the overall population density must increase to recreate the observed flux. Likewise, the total energy of the burst must increase as well. In this way, energy and circumburst density estimates from models where ξ has been fixed to 1.0 then act as strict lower bounds on the parameter space.

As noted in §4.1, the total energy released is dependent upon the jet collimation angle, θ_c : $E = E_{\text{iso}}(1 - \cos \theta_c) \approx E_{\text{iso}} \frac{\theta_c^2}{2}$. Berger et al. (2003) report a strong correlation between $L_{X,\text{iso}}$ and the beaming factor $f_b = [1 - \cos \theta_c]$ resulting in a true X-ray luminosity, $L_X = f_b L_{X,\text{iso}}$, that is a constant for all GRBs. This suggests that brighter X-ray GRBs are more highly collimated. As the four GRBs analyzed here are amongst the brightest observed (Figure 4.7), they provide the best opportunity to both precisely measure θ_c and to distinguish between collapsar and magnetar progenitor scenarios.

Assuming lower values of ξ are more physically likely (Warren et al., 2018), the E_{rel} lower bounds on each of the free- ξ Gaussian cases range from $(0.6 - 3) \times 10^{52}$ erg. These conservative lower limits are in potential tension with the maximum available energy which could be released by a rapidly rotating newborn magnetar ($\sim 10^{52}$ erg;

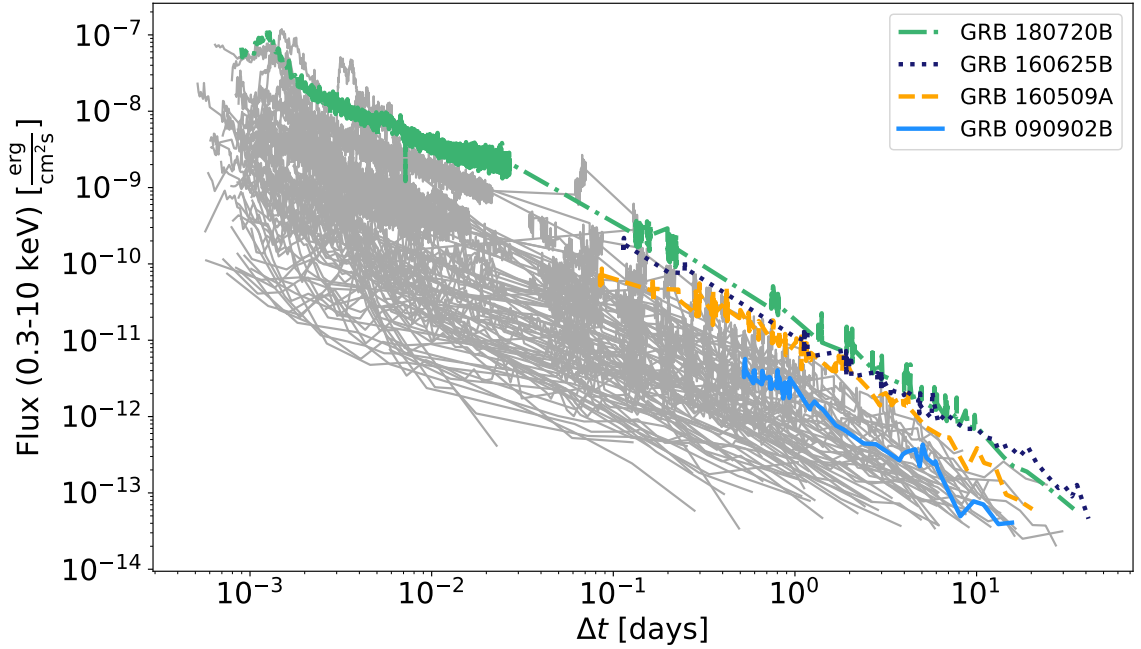


Figure 4.7: The 0.3-10 keV *Swift*-XRT light curves for the 4 GRBs in our sample. A comparison sample of other XRT-detected GRBs are shown in gray. Data are taken from the *Swift* repository. We limit the comparison sample to those detected within the last ten years and with $0.5 < z < 2.0$ for clarity. GRB 090902B, GRB 160509A, GRB 160625B, and GRB 180720B have some of the brightest afterglows observed to date.

(Beniamini et al. 2017; Metzger et al. 2018). An alternative progenitor scenario of a collapsar black hole origin could easily accommodate this and even higher energies. Here, stellar material accretes onto a newborn black hole and produces a relativistic jet (MacFadyen, Woosley, 1999; Woosley, 1993; Woosley, Heger, 2012).

4.4.5 Circumburst Densities and Birth Environments

In the cases of GRB 090902B, GRB 160509A and GRB 160509A, when ξ is fixed to 1.0 we find unusually low estimates for the circumburst densities ($n \sim 10^{-4} - 10^{-6} \text{ cm}^{-3}$). We discussed in §3.4.6 how the extremely low values of n for bright GRBs are usually interpreted as deriving from low-metallicity massive stars

progenitors. However, in the models where ξ is free to vary we see n increase by 4-5 orders of magnitude, relative to the models where ξ has been fixed to 1.0. Such a large difference will undoubtedly influence current theoretical considerations regarding their birth environments. The higher values of n in the free- ξ case are more consistent with that expected for the regions of high star-formation where long GRBs are produced. Interestingly, in the case of GRB 180720B a high density ($n \sim 20 \text{ cm}^{-3}$) is found regardless of the model used, although this is also the case which found the highest estimate of ξ (~ 0.2). Although our sample presented here is small, we interpret these results as preliminary evidence that lower values of ξ do in general produce more reasonable values for other physical parameters regarding GRB modeling.

4.4.6 Comparison to Other Populations of GRBs

An initial goal for undertaking this work was to understand why only certain GRBs are detectable by the *Fermi*-LAT. Are LAT-detected GRBs truly more energetic events or are their jets simply more narrowly collimated? A smaller collimation angle may give the impression of higher energies before accounting for beaming correction effects. To investigate this we compare our sample of 4 LAT-detected GRBs to a general population of long GRBs which were not necessarily detected by the *Fermi*-LAT.

In [Laskar et al. \(2014\)](#), the authors present an overview of 68 long GRBs at low redshifts ($z \sim 1$) which represent a combination of pre-*Swift*, *Swift*, and *Fermi*

populations. The jet collimation angles, θ_c , of this sample range from about 2° to 50° , with a median value of $\sim 7^\circ$. When the participation fraction, ξ is fixed to 1.0 we find relatively small ($\theta_c \lesssim 4^\circ$) collimation angles for three of the GRBs - GRB 090902B, GRB 160509A, and GRB 160625B - that we investigate here, placing them within the ~ 25 th percentile for opening angles. When ξ is free to vary for these same three GRBs we see θ_c increase to between 4 - 8° , which are more typical values.

Using our derived estimates for θ_c and θ_w we can calculate the beaming-corrected γ -ray energy for each GRB (Table 4.10). For top-hat models $E_\gamma = E_{\gamma,\text{iso}}(1 - \cos \theta_c)$ and for Gaussian models $E_\gamma = E_{\gamma,\text{iso}} \theta_c^2 \left(e^{-\frac{\theta_w^2}{2\theta_c^2}} - 1 \right)$. For GRB 090902B, GRB 160625B, and GRB 180720B, regardless of the model used, E_γ is greater than 1.0×10^{51} erg, placing them at above-average energies. Several cases in particular - the free- ξ Gaussian models for GRB 160625B and GRB 090902B and each of the models for GRB 180720B - are approaching the highest E_γ estimates known to date for long GRBs, suggesting that LAT-detected long GRBs may indeed be amongst the most energetic types of GRBs. The case of GRB 160509A is unusual in that the estimates for the total energy are lower than the others, this is most likely due to the fact that θ_w is much smaller than θ_c , limited the total energy released at larger angles.

	Top-Hat	Gaussian (fixed- ξ)	Gaussian (free- ξ)
GRB 090902B	$1.3_{-0.8}^{+1.0} \times 10^{51}$	$2.2_{-1.0}^{+0.8} \times 10^{51}$	$6.0_{-3.3}^{+6.0} \times 10^{51}$
GRB 160509A	$1.5_{-0.4}^{+0.6} \times 10^{50}$	$4.5_{-2.2}^{+5.1} \times 10^{49}$	$3.5_{-2.3}^{+5.3} \times 10^{50}$
GRB 160625B	$2.1_{-0.5}^{+1.5} \times 10^{51}$	$1.1_{-0.2}^{+0.8} \times 10^{51}$	$9.7_{-2.2}^{+4.0} \times 10^{51}$
GRB 180720B	$5.4_{-3.3}^{+5.2} \times 10^{51}$	$3.9_{-2.3}^{+3.1} \times 10^{51}$	$4.1_{-2.5}^{+3.7} \times 10^{51}$

Table 4.10: Beaming-corrected γ -ray energies in units of ergs (E_γ)

4.5 Conclusions

In this work we have performed multiwavelength analysis of 4 bright, long GRBs detected by the *Fermi*-LAT. We modeled the radio to X-ray forward shock synchrotron emission of each GRB with three different jet structure types - a top-hat, a Gaussian, and a Gaussian with freely-varying participation fraction, ξ . We derived several physical parameters pertaining to the bursts and discuss the implications of the various jet models used. Our main conclusions can be summarized as follows:

- We first begin by modeling each GRB as a top-hat jet with $\xi = 1.0$, which are assumptions typically made previously in the literature.
- Then, we expand our analysis to include two variations of a Gaussian jet - one with $\xi = 1.0$ and one with ξ free to vary.
- In both cases where ξ is fixed the derived physical parameters are roughly consistent with each other. However when free to vary, we find lower values of ξ between $0.006_{-0.005}^{+0.036}$ and $0.21_{-0.14}^{+0.40}$. This has a significant effect on the other model parameters and results in a total energy, E_{rel} , that is 1-2 orders of magnitude larger, a circumburst density, n , that is 4-5 orders of magnitude

larger, and a ϵ_B that is 4 orders of magnitude smaller than those of fixed- ξ cases.

- Lower values of ξ may suggest a preference for a collapsar, rather than magnetar, origin (for at least the most energetic of long GRBs) since the lower limits found here - $E_{\text{rel}} > (0.6 - 3) \times 10^{52}$ erg - are in tension with the maximum available energy from a newborn magnetar ($\sim \text{few} \times 10^{52}$ erg).
- We find that GRB 090902B, GRB 160625B, and GRB 180720B are all mildly-to-moderately better described by a Gaussian-shaped jet compared to a top-hat jet, although the model comparisons between the fixed and free- ξ Gaussian cases do not distinguish between the two. The preferred jet shape is not clear in the case of GRB 160509A.

In future work we plan to continue expanding on the sample reported here to include more GRBs detected by the *Fermi*-LAT. As this paper was being completed, an additional feature was developed for `afterglowpy` to model wind type circumburst density profiles. This will allow us to expand our sample to include these types of GRBs and allow us to generalize our results to be independent of the GRB density profile.

In this work we note how assuming a fixed value of ξ introduces biases in the other derived model parameters. For example, the typically assumed value of $\xi = 1.0$ may be underestimating $E_{\text{k,iso}}$ by a factor of 10 to 100. Due to the lack of observational constraints and noted degeneracies, theoretical simulations will provide the best opportunity to constrain the parameter space of ξ ; therefore,

we highly encourage research in this area in future work.

Chapter 5: Summary and Future Directions

5.1 Summary of Results

For FRBs, which are primarily observed at radio energies, the main objective was to explore the potential of high-energy observations towards understanding their progenitors and emission processes. The work presented here in Chapter 2 was completed prior to the joint detection of X-ray and FRB-like emission from the Galactic magnetar SGR 1935-2154. Today, we understand that high-energy emission does originate from some FRBs and thus the conclusions drawn from our work still remain relevant today. The main conclusions and results from Chapter 2 can be summarized as follows:

- We searched for high-energy counterparts to FRBs with the *Fermi*-GBM, *Fermi*-LAT, and *Swift* BAT and found no detectable high-energy emission on timescales of ~ 0.1 , 1, 10, and 100 s.
- Given our non-detections, we report upper limits to the FRB high-energy emission for each of the above timescales in the following energy ranges: 15-350 keV, 300-40,000 keV, and 60-100,000 MeV (Table 5.1).

Timescale [s]	f_γ [$\times 10^6$ erg cm $^{-2}$]		
	300-40,000 keV	60-100,000 MeV	15-350 keV
0.1	<0.24-0.30	–	–
0.064	–	–	<0.0048-0.0092
1	<0.69-0.89	–	<0.021-0.027
10	<2.1-2.7	–	<0.055-0.080
100	<6.5-8.5	<0.31-1.50	<0.065-0.170
300	–	–	<1.6-4.8

Table 5.1: High-energy upper limits to the fluence, f_γ

- We also report lower limits on the ratio of radio to high-energy fluence, $f_r/f_\gamma > 10^5 - 10^{10}$ Jy ms erg $^{-1}$ cm 2 , for timescales of 0.1 and 100 s.
- We consider the implications of non-detections in the context of several theoretical models. The neutron star coalescence model and cosmic comb model are deemed unlikely, but two of the more promising theories - magnetically or rotationally powered neutron stars - remain viable. Observed FRB DMs and the distance of FRB 121102 are consistent with the distance lower limits derived in this work from the magnetar hyperflare model, and high-energy non-detections are also consistent with the pulsar analog model.

Our primary intentions for Chapters 3 and 4 were to determine the true scale of GRB energetics, their birth environments, jet collimation angles, and jet emission structure. We accomplished this by performing an in-depth study of the GRB jet shape via broadband observations of their afterglows. We focused on *Fermi*-LAT detected GRBs due to their highly energetic nature and bright multiwavelength

afterglows. The main conclusions and results from Chapters 3 and 4 can be jointly summarized as follows:

- We fit the multiwavelength afterglows of several bright *Fermi*-LAT detected GRBs with top-hat and Gaussian jet structure models via the `afterglowpy` modeling package.
- We explore the role that the participation fraction, ξ , has on the broadband modeling and parameter fitting. We find lower estimates for ξ between $0.006_{-0.005}^{+0.036}$ and $0.21_{-0.14}^{+0.40}$. None of our results are consistent with the typically assumed value of 1.0.
- Model parameters are highly dependent upon the value of ξ assumed. Lower, and possibly more realistic, values of ξ lead to 2 times higher estimates of the total burst energy, E_{rel} , and 4-5 times higher estimates of the circumburst density, n , as compared to an assumption of $\xi = 1.0$.
- We find in most cases presented here that a structured jet is a better fit compared to the simple top-hat model, but that the exact shape can vary between GRBs. In at least one case, that of GRB 160509A, it was not possible to determine the preferred jet structure model.
- We discuss the implications of these results on two progenitor scenarios - black hole collapsar and new-born magnetar origins. Our conservative lower limits on E_{rel} - $(0.6 - 3) \times 10^{52}$ erg - are in tension with the maximum available energy from a newborn magnetar ($\sim \text{few} \times 10^{52}$ erg). Assuming lower values of ξ , in

the case of extremely energetic GRBs ($E_{\gamma,\text{iso}} \gtrsim 10^{54}$ erg) only the collapsar origin can comfortably produce the requisite observed energy.

5.2 Publication Plans for Chapter 4

Chapters 2 and 3 have been previously published in the *Astrophysical Journal* (ApJ). The eventual goal is to publish the results of Chapter 4 in ApJ as well. Prior to that, some further analysis is required - mainly, adding to the current sample of *Fermi*-LAT detected GRBs. The goal is not to have a fully exhaustive list of all long GRBs detected by the LAT, but rather a large enough sample from which to infer the general properties of the population, ideally around 6-10.

For the analysis presented in Chapter 4 of this thesis we were limited to only evaluate those GRBs whose environments could be described by a constant density medium. This was due to computational limitations within `afterglowpy`. However, as this thesis was being finalized a wind-like circumburst profile has been implemented within the modeling software. At the time of writing, the option is not fully complete, but we expect a fully functional wind-like type medium available in the very near future. This will allow us to expand our sample of potential GRBs to model and allow us to generalize our results to be independent of CBM type.

5.3 Future Directions

5.3.1 High-Energy and Optical Observations of FRBs

The field of FRB follow-up has changed dramatically since the completion of Chapter 2. Known FRBs now number in the hundreds, and since the reported FRB/magnetar connection the drive to identify non-radio counterparts is stronger than ever. The coincident detection of an FRB and a short, hard X-ray flare from the soft gamma-ray repeater (SGR) 1935-2154 (The Chime/FRB Collaboration et al., 2020) constituted the first definitive connection between an FRB and a magnetar (Figure 1.9) and has naturally reignited interest in the question of whether previous FRBs may have produced higher-energy signals that were simply undetected. The ratio of radio to high-energy emission for this event was $f_r/f_\gamma \sim 10^{12}$ Jy ms erg⁻¹ cm², which is consistent with the results we report in Chapter 2 ($f_r/f_\gamma > 10^5 - 10^{10}$ Jy ms erg⁻¹ cm²). However, SGR 1935-2154 is a local magnetar within the Milky Way, meaning it was observationally relatively much brighter than the distant, extragalactic FRBs in our own sample (Figure 5.1). Given the sensitivity limit of the *Swift* BAT (10^{-8} erg cm⁻² s⁻¹; Lien et al. 2016a), it could only detect a similar event to that of SGR 1935-2154 ($E_\gamma \sim 10^{39}$ erg; Mereghetti et al. 2020) at distances of ~ 30 kpc or less. Future detections of Galactic FRBs or more sensitive X-ray instruments are therefore necessary to fully constrain the high-energy properties of FRBs.

The field of FRBs is also primed for advancement due to the development of

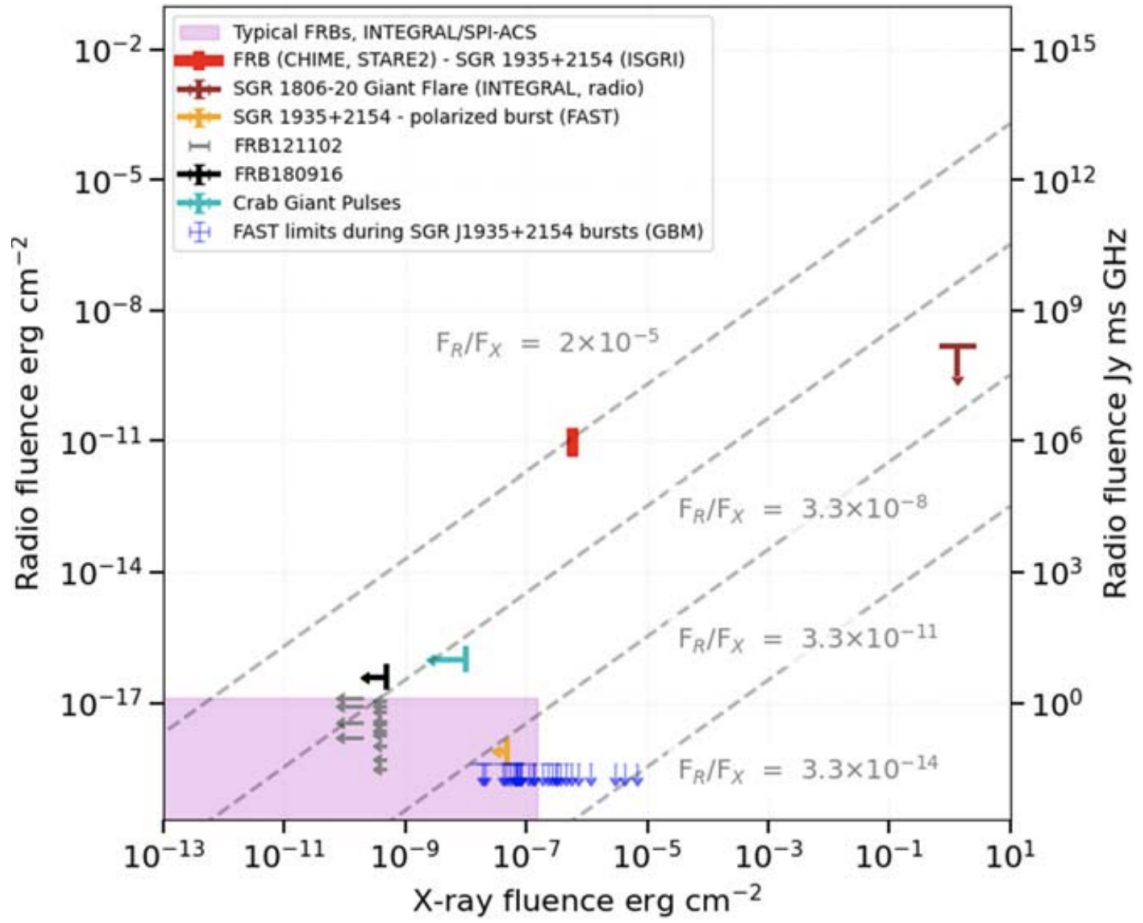


Figure 5.1: Radio versus X-ray fluences for known FRBs and magnetars (Mereghetti et al., 2020). Our reported f_r/f_γ limits in Cunningham et al. (2019) are consistent with the sample of INTEGRAL-detected FRBs shown here (purple shaded region). The SGR 1935-2154 event (bright red region) is noticeably brighter in both X-rays and radio than previously detected FRBs.

several wide-field radio instruments which will greatly improve FRB identification and follow-up, including the Square Kilometer Array (SKA; [Schilizzi et al. 2010](#)), the Australian Square Kilometer Array Pathfinder (ASKAP; [Johnston et al. 2008](#)) Telescope, and the Deep Synoptic Array (DSA-2000; [Hallinan et al. 2019](#)). The sub-arcsecond localization capabilities and quick survey times of these instruments will allow the multiwavelength follow-up necessary to help answer some key questions.

The rate of FRBs detected by these next generation radio interferometers could potentially reach up to 10^4 per day ([Hashimoto et al., 2020](#)). FRBs detected by ASKAP are localized within an arcsecond uncertainty, sufficient to identify the likely host galaxy and perform follow up with optical instruments. Previously localized FRBs come from a range of host galaxies but most hosts can generally be described as bright, slightly massive, and in several cases the FRB is located on the outskirts of the galaxy. Identifying FRB hosts reveals clues about their progenitors - the fact that most non-repeating FRBs are associated with older stellar populations and are not typically nuclear rules out several progenitor theories. Although ~ 10 FRBs have now been localized the sample is still small, and it is difficult to draw robust conclusions regarding their overall properties; therefore, it is necessary to continue following up new FRBs as they are discovered. Identifying non-radio counterparts will be critical for understanding these FRBs, so in future work I plan on expanding upon the work completed in [Chapter 2](#) and continuing to search for counterparts and hosts in the optical as well as high-energy. Several popular models for FRBs do predict counterparts at higher energies so the detection (or non-detection) for FRBs will provide valuable constraints on their progenitors.

5.3.2 VHE Emission from GRBs

Recently, several long GRBs have been observed at very high energies (VHE; \sim TeV emission). The Major Atmospheric Gamma Imaging Cherenkov (MAGIC; [Aleksić et al. 2016](#)) Telescope detected >0.2 TeV photons from GRB 190114C and the High Energy Stereoscopic System (HESS; [Hoischen et al. 2017](#)) observed both GRB 180720B and GRB 190829A at energies above 0.1 TeV ([Abdalla et al., 2019](#); [MAGIC Collaboration et al., 2019](#); [de Naurois, 2019](#)). The detected photons are associated with the afterglow, rather than the prompt, emission but they likely have a separate origin from the rest of the synchrotron-powered afterglow. These TeV photons are thought to originate from synchrotron self-Compton (SSC) radiation which occurs when the synchrotron photons Compton scatter with the same shock-accelerated electrons that produced them (Figure 5.2).

All three events were relatively nearby at low redshifts ($z=0.079-0.654$) suggesting that the presence of TeV emission might be more prevalent than originally believed, rather than produced amongst only the most extreme events. This hints that all GRBs, not just the highly energetic ones, may produce some level of VHE emission and the lack of detection is more likely due to the insensitivity of current instruments. Therefore, these events would be an excellent test to expand on our current afterglow modeling methods to understand how SSC effects influence GRB afterglows and what that may reveal about the GRB emission mechanism.

Several of these long GRBs also display unusual properties in the radio. The radio afterglow of a typical GRB is expected to follow the standard fireball model in

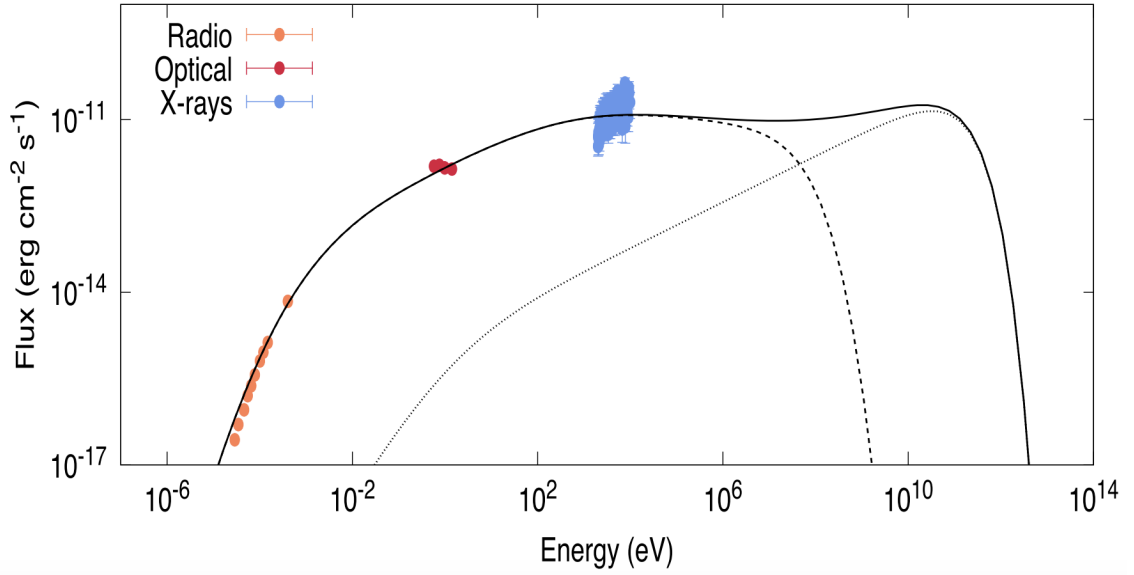


Figure 5.2: The SED of GRB 190114C highlighting the synchrotron (dashed line) and SSC (dotted line) components (Fraija et al., 2019a). The combined SSC and synchrotron emission is shown as a solid line. The radio, optical, and X-ray observations are dominated by synchrotron emission. The SSC component is expected to peak at TeV energies.

which the electrons in the shock wave are accelerated via synchrotron emission due to the interaction of the jet with the circumburst media. However, there are several examples of GRBs whose radio emission cannot be described solely via synchrotron forward shock emission, including GRB 160625B, as we showed in Chapter 3. In these cases the radio afterglow can be complicated by the inclusion of reverse shocks, scintillation effects, ‘refreshed shocks’, etc. The three GRBs with VHE emission described above all notably display unusual radio properties.

Dedicated, fast, multiwavelength follow-up campaigns are required to complete this work. The Cherenkov Telescope Array (CTA; Cherenkov Telescope Array Consortium et al. 2019) plans to begin operations in 2022. The CTA’s wide field-of-view, high sensitivity, rapid slew capabilities, and one arcminute resolution make

it an ideal instrument for identifying new GRBs for further follow-up. Using broadband observations and building on the work done in Chapters 3 and 4, I can use the `Afterglowpy` modeling package to explore these sources of VHE and excess radio emission. This will allow me to infer what portion of the afterglow cannot be explained by standard synchrotron forward shock modelling, thus allowing us to separate and focus on any extraneous emission. Then, I can draw and make connections between the VHE/radio emission and other properties of the afterglow.

5.4 Facilities and Software

The analysis in chapters 3 and 4 was performed on the YORP cluster administered by the Center for Theory and Computation, part of the Department of Astronomy at the University of Maryland. We acknowledge the use of public data from the *Swift* and *Fermi* data archives. The National Radio Astronomy Observatory is a facility of the National Science Foundation operated under cooperative agreement by Associated Universities, Inc.

Facilities: FERMI (GBM, LAT), SWIFT (BAT, XRT, UVOT), CXO, HST, RATIR, LCOGT (FTN), Liverpool:2m, Magellan, Maidanak:1.5m, ROTSE-IIIa, Nickel, NOT, CrAO:1.25m, VLA, ATCA, WSRT, AMI-LA, GMRT

Software: `afterglowpy`, XSPEC, Python, CASA

Appendix A: FRB Observational Supplementary Material

A.1 FRB Observations by Instrument

Table [A.1](#) summarizes which FRBs were observable within the FOV of the *Fermi*-GBM, *Fermi*-LAT, and *Swift*-BAT at the time of radio detection. Here Y denotes the FRB was observed by the instrument and N denotes it was not observed. The subsequent repeating bursts from FRB 121102 have been combined for brevity. FRB 131104 was detected on the edge of the BAT FOV but is excluded due to its low partial coding fraction.

FRB Name	<i>Fermi</i> -GBM	<i>Fermi</i> -LAT	<i>Swift</i> -BAT
010125	N	N	N
010621	N	N	N
010724	N	N	N
090625	Y	Y	N
110220	N	N	N
110523	Y	N	N
110626	Y	N	N
110703	Y	N	N
120127	N	N	N
121002	N	N	N
121102	Y	Y	N
130626	N	N	N
130628	Y	Y	N
130729	Y	N	N
131104	Y	N	N
140514	N	N	N
150215	Y	Y	Y
150418	Y	Y	N
150807	Y	N	N
160317	Y	Y	N
160410	N	N	Y
160608	Y	Y	N
170107	N	N	N

Table A.1: Summary of observations available per FRB.

A.2 Summary of Extraneous Signals Detected with the *Fermi*-GBM Targeted Search

We follow a similar approach in our *Fermi*-GBM analysis to that of electromagnetic followup of gravitational wave compact binary sources. [Blackburn et al. \(2015\)](#) develop a Bayesian method to search GBM continuous data for coincident signals around LIGO triggers. The analysis only requires an event time for the LIGO trigger and a localization probability map. Therefore it is convenient to adapt the method to our purposes for candidates temporally coincident with FRBs. A log likelihood ratio (logLR) parameter is calculated for each FRB in the *Fermi*-GBM data to determine the probability of the presence of a signal compared to the null hypothesis of a constant background (see [Goldstein et al. 2016a](#) for more details about this analysis). LogLR values greater than 10.0 are likely indicative of a real signal. We find six candidate signals coincident in time with the FRB detections (t_{FRB}) however we determine them all to be unrelated for the reasons outlined below:

A.2.1 Local Particle Activity

Fermi is sensitive to increased levels of local particle activity in the magnetosphere along its orbit (even when outside the South Atlantic Anomaly). These events are characterized by long (several tens to hundreds of seconds), smooth, and hard signals observed as a slow rise against the normal background emission. Three of the candidate signals (FRB131104 and bursts 19 and 20 from FRB121102)

discovered by the targeted search are likely caused by this local magnetospheric activity. All three were identified within the 100 second timescale searches with logLR values greater than 10.0. None of the signals are temporally coincident with the FRBs. The signal around burst 19 occurred 90 seconds before t_{FRB} , the signal around burst 20 occurred 450 seconds before t_{FRB} , and third signal occurred 331 seconds after the t_{FRB} of FRB 131104. We considered all three candidate signals to be unrelated.

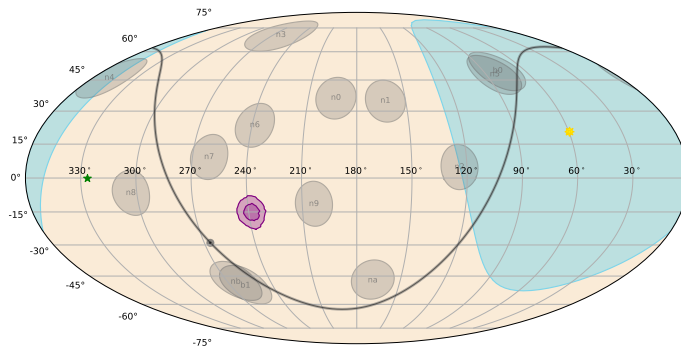
A.2.2 Other Unrelated Signals

FRB 110523: Only CTIME data are available for the analysis of FRB 110523. A candidate signal is seen ~ 80 seconds before t_{FRB} with a duration of 8 seconds and a logLR of 22. The signal is soft and localizes near, but not on, the Galactic plane (Figure [A.1\(a\)](#)). The signal is not localized near the FRB. We assume this to be unrelated particle activity.

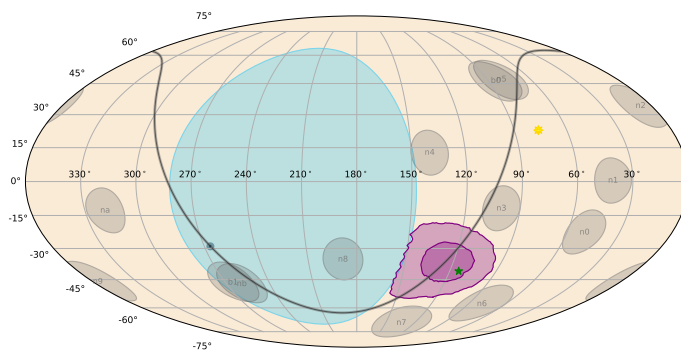
FRB 160608: A candidate signal is seen ~ 10 seconds before t_{FRB} with a logLR of 10.8. The signal properties are consistent with that of a Galactic transient (i.e., a soft, 10 second long burst that localizes to the Galactic plane). Although the localization is consistent with the FRB (Figure [A.1\(b\)](#)) based on further analysis with the BAT we suspect it is likely a flare from the nearby high-mass X-ray binary system Vela X-1.

FRB 121102 Burst 19: A second candidate signal is seen in addition to the

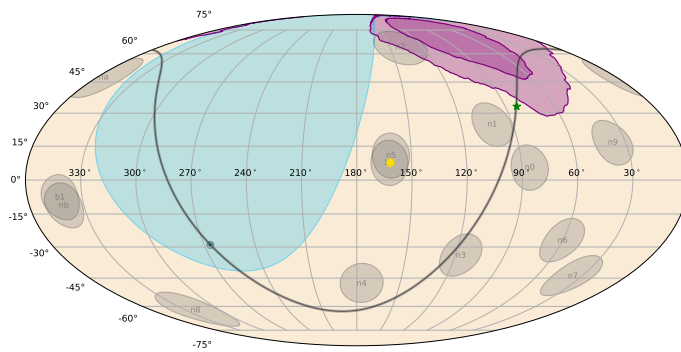
local particle activity described above. A shorter event occurs 109 seconds before t_{FRB} for a duration of 10 seconds with a logLR of 13.6. However, given the disagreement with the FRB location (Figure [A.1\(c\)](#)) and the number of trials, we consider this signal both insignificant and unrelated.



(a)



(b)



(c)

Figure A.1: A localization map of the candidate signal for a.) FRB 110523, b.) FRB 160608, and c.) FRB 121102 Burst 19. The blue shaded region represents the area occulted by the Earth, the gray stripe is the Galactic plane, the gray circles represent the positions of each of the detectors, and the yellow and green stars are the locations of the Sun and FRB, respectively. The purple region shows the 50% and 90% confidence regions for the GBM localization of the candidate signal.

Appendix B: MCMC Corner Plots

The following are the MCMC covariances and posterior probability distributions of the parameters for each GRB and model described in §4.3. The histograms denote the 15, 50, and 85 percentiles of the distributions. The blue points mark the best-fit solution. Each model was run for 40,000 steps with 100 walkers. The parameter bounds used are shown in Table 4.1.

B.1 GRB 090902B

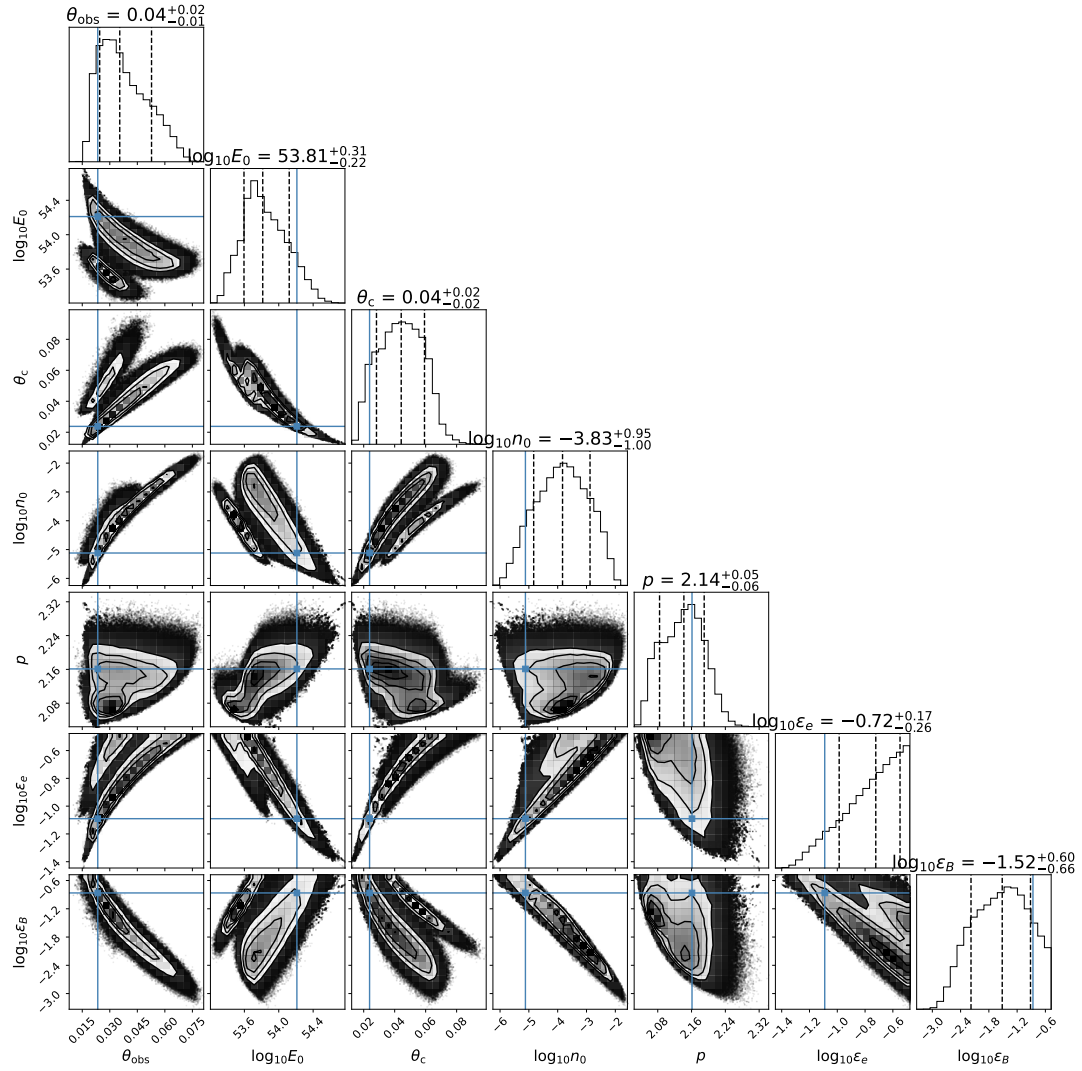


Figure B.1: GRB 090902B: Top-hat

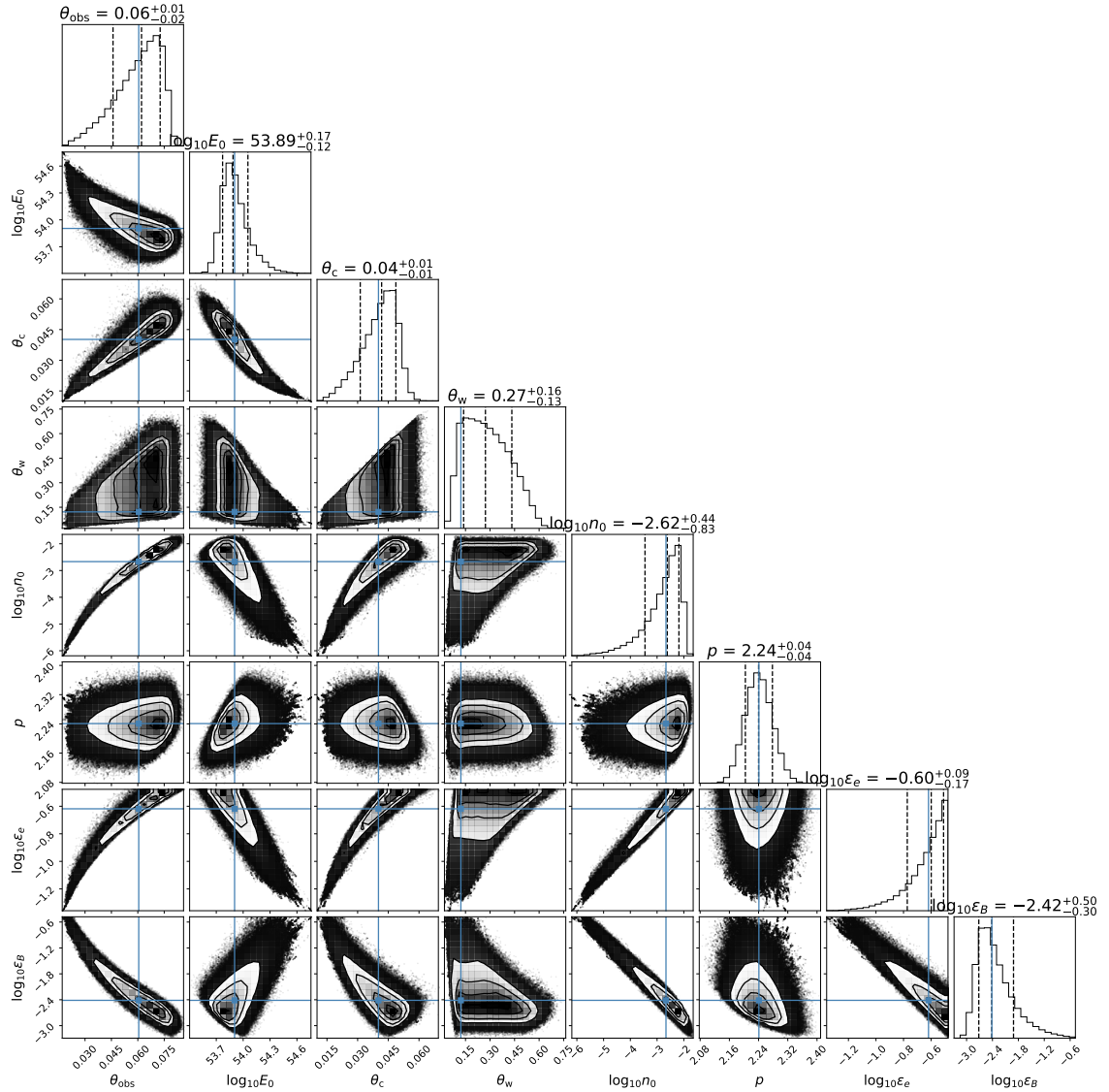


Figure B.2: GRB 090902B: Gaussian with fixed ξ

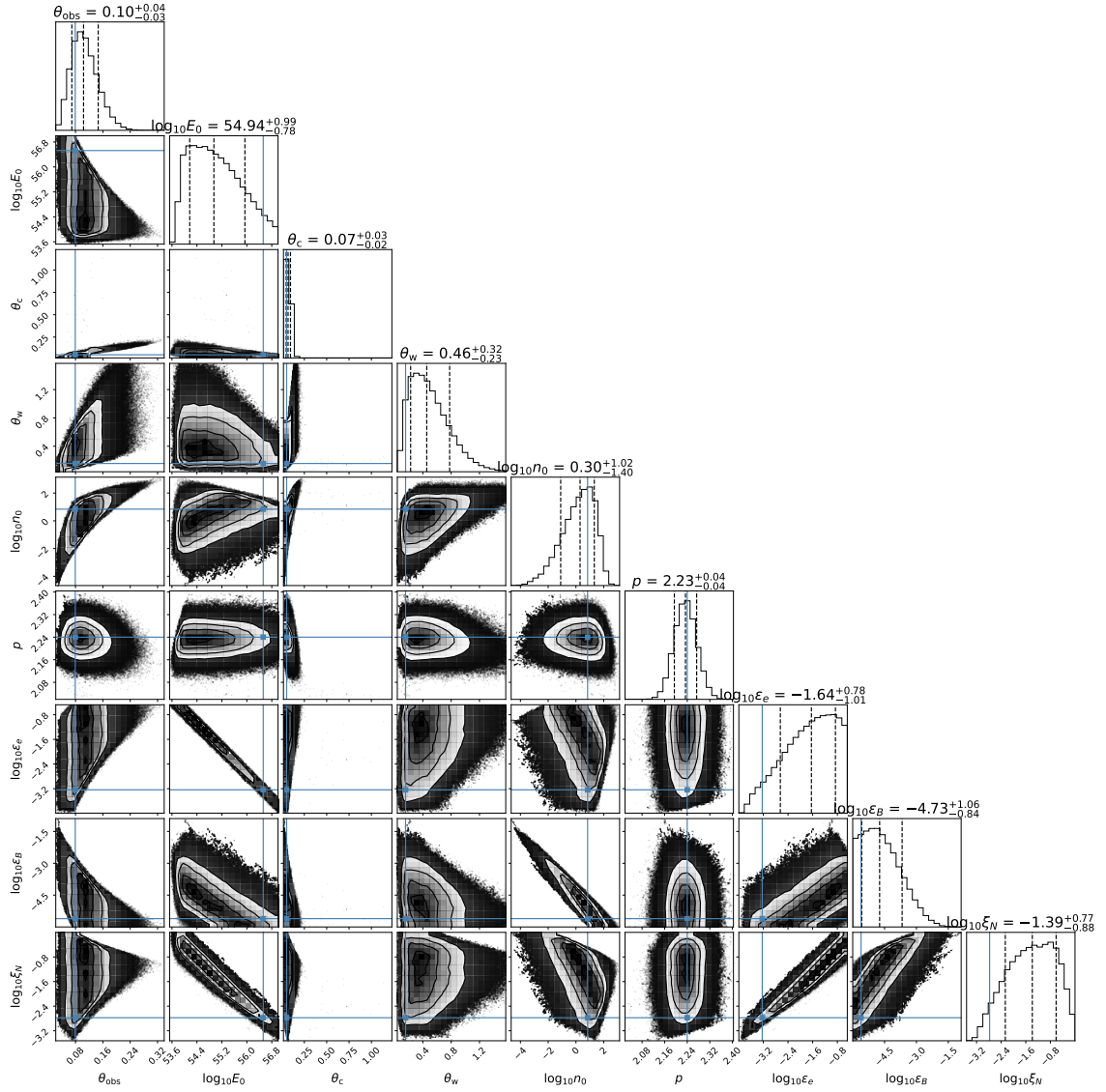


Figure B.3: GRB 090902B: Gaussian with free ξ

B.2 GRB 160509A

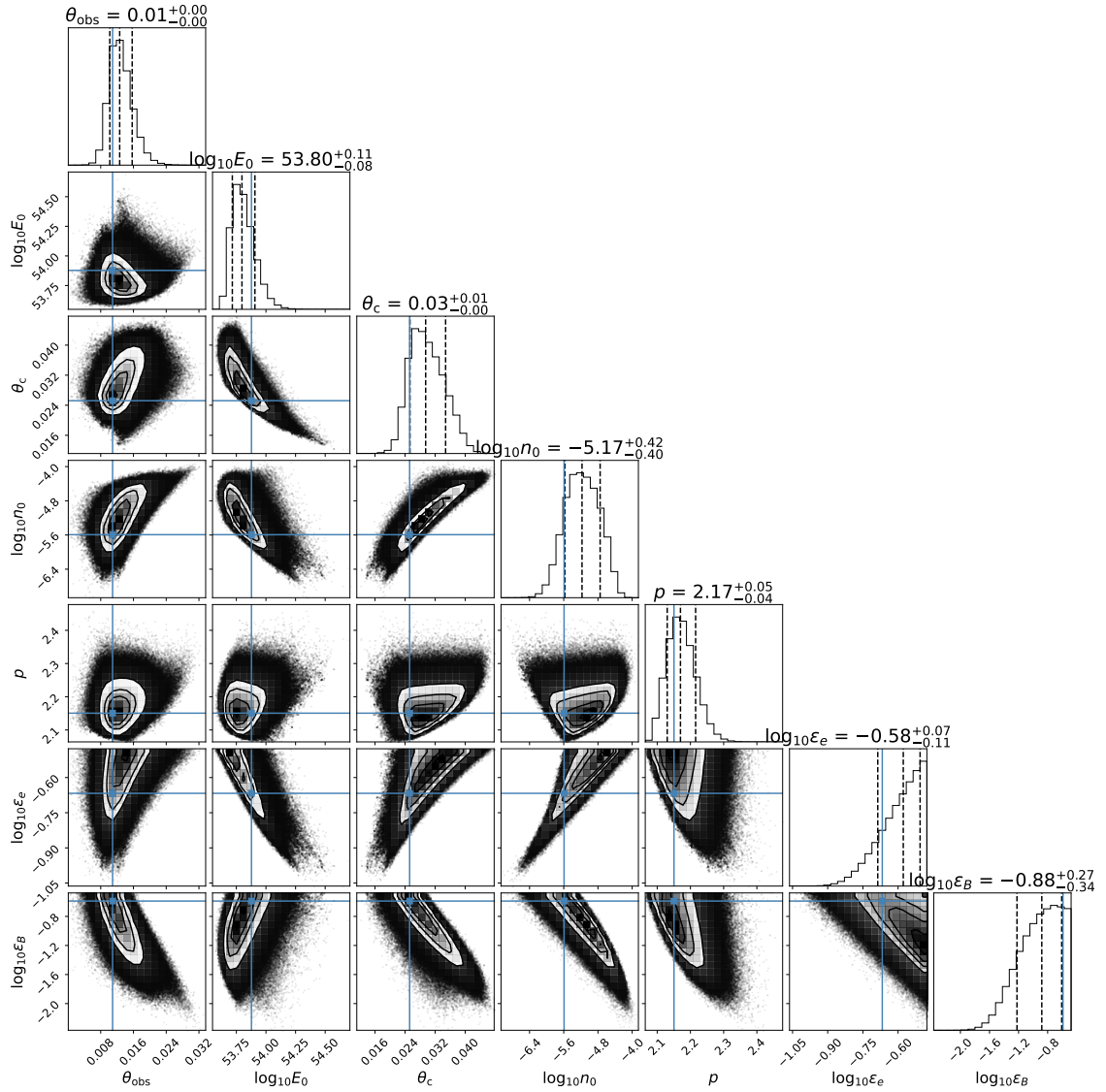


Figure B.4: GRB 160509A: Top-hat

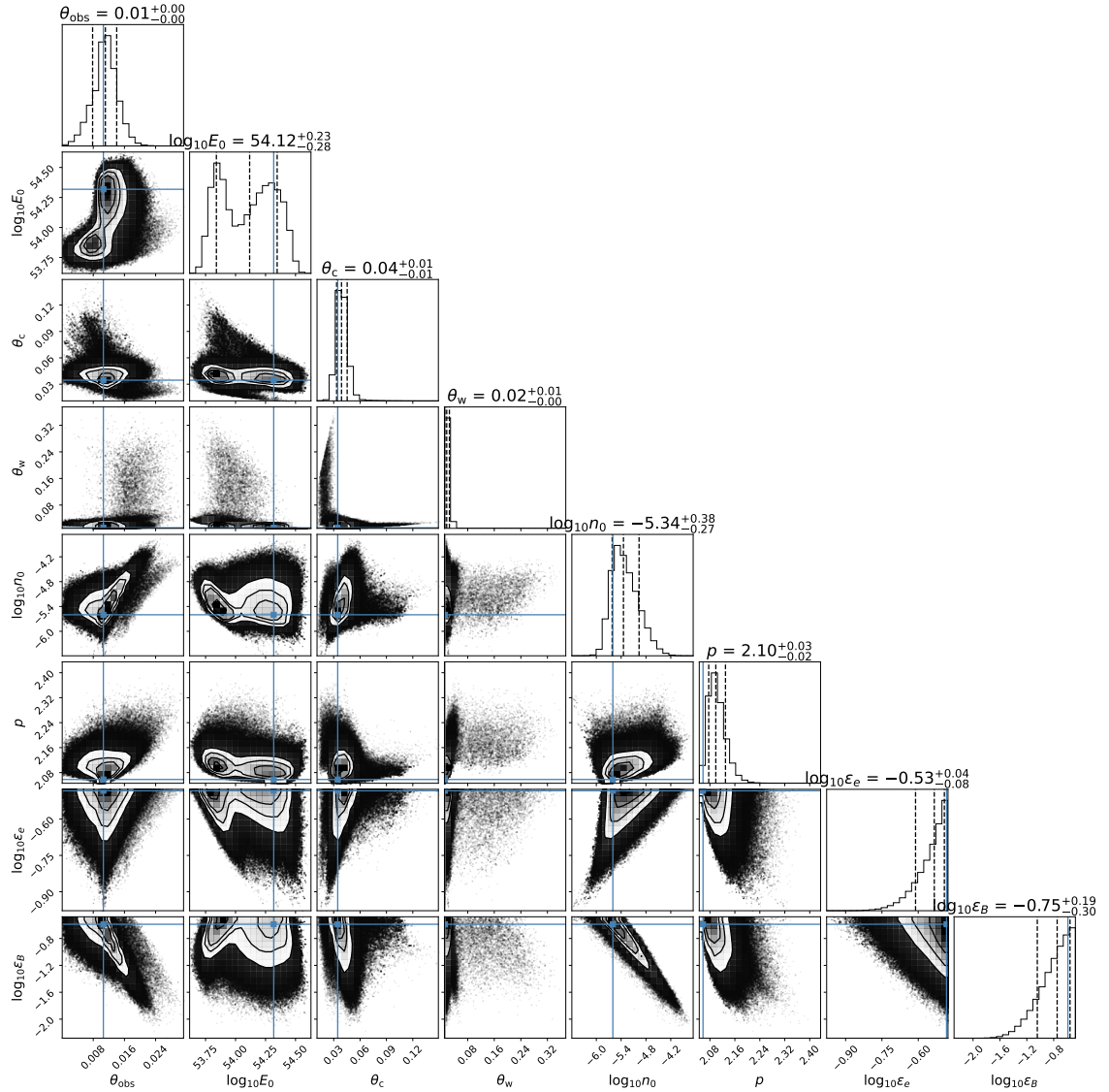


Figure B.5: GRB 160509A: Gaussian with fixed ξ

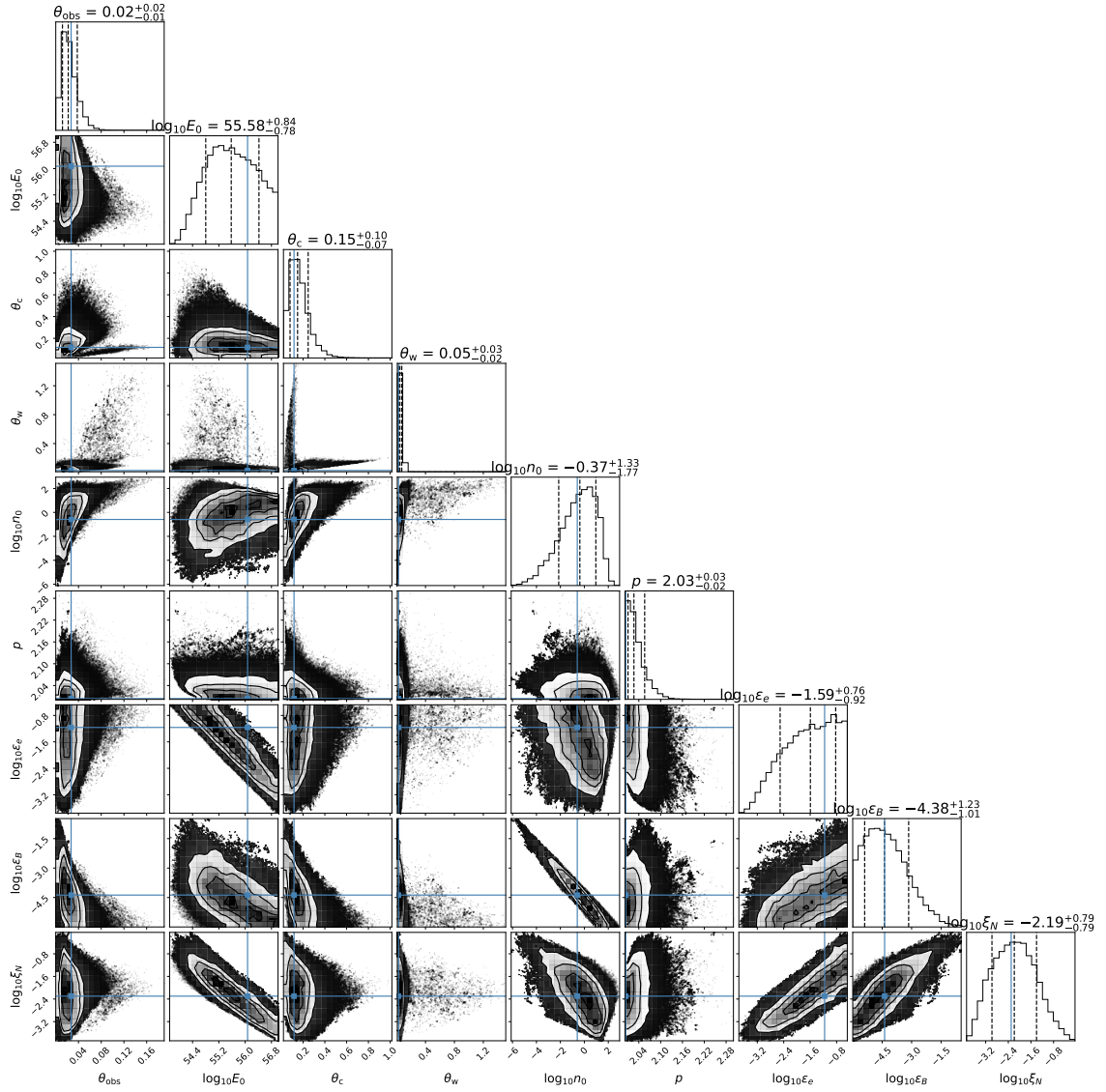


Figure B.6: GRB 160509A: Gaussian with free ξ

B.3 GRB 180720B

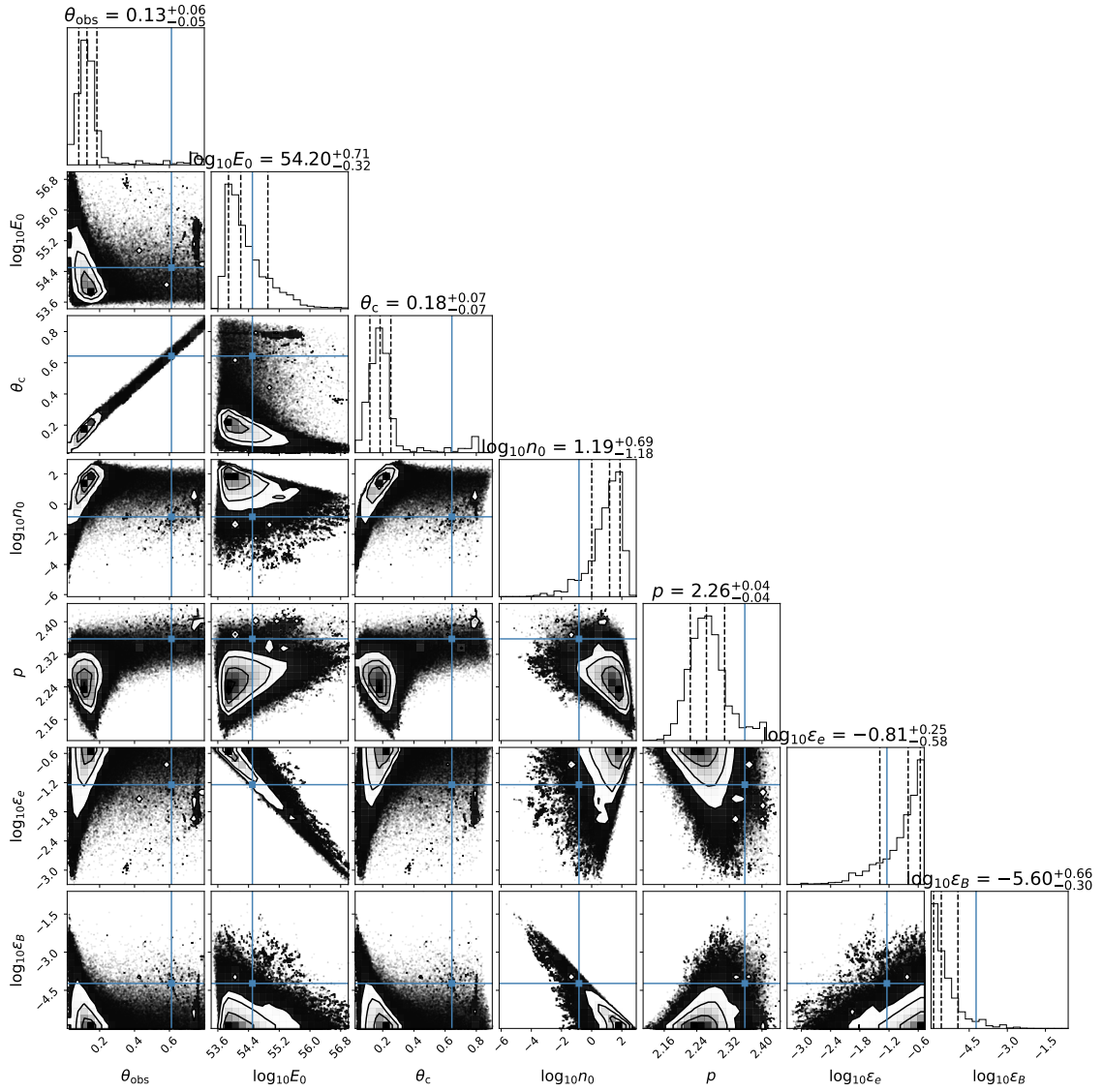


Figure B.7: GRB 180720B: Top-hat

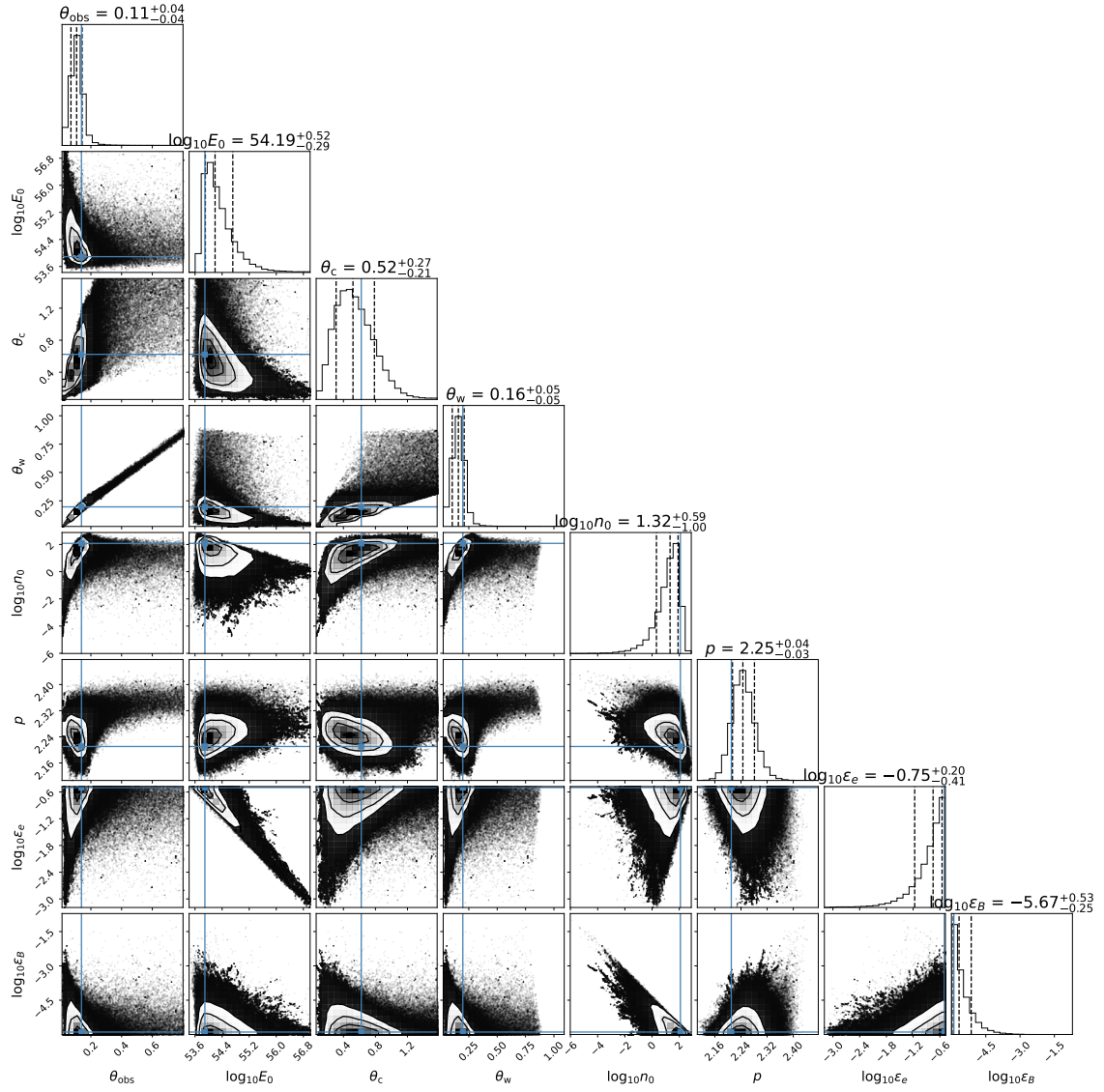


Figure B.8: GRB 180720B: Gaussian with fixed ξ

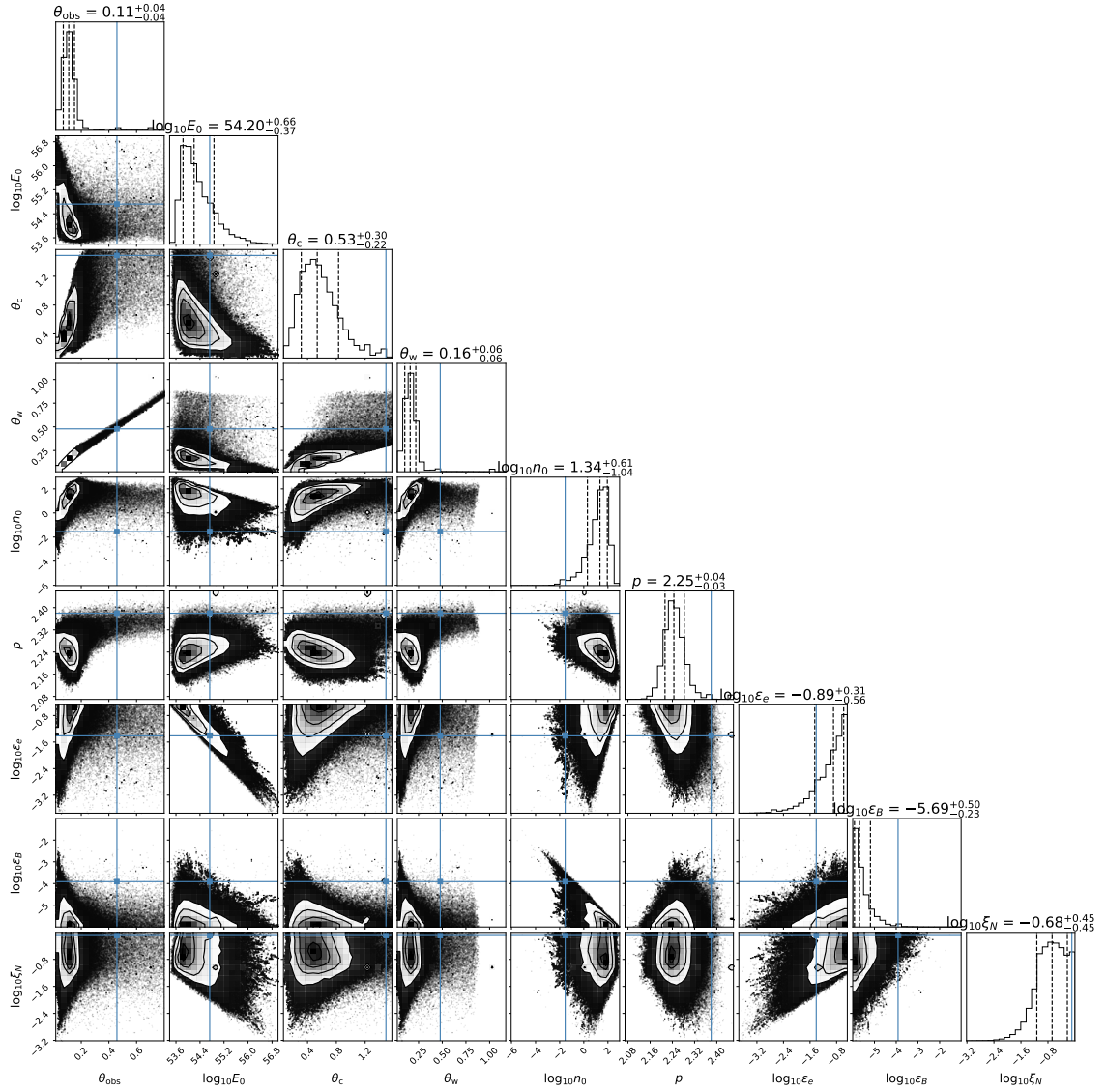


Figure B.9: GRB 180720B: Gaussian with free ξ

Appendix C: GRB Data Tables

C.1 GRB 090902B

Table C.1: X-ray data for GRB 090902B. Times are in reference to the GBM trigger (Sept 2, 2009 at 11:05:08.31 UTC).

Δt [s]	Energy [keV]	Flux Density [nJy]	Instrument
45207.75	5	140.80 ± 36.89	<i>Swift</i> /XRT
45368.54	5	120.71 ± 31.78	<i>Swift</i> /XRT
45569.01	5	188.06 ± 42.41	<i>Swift</i> /XRT
45767.09	5	199.88 ± 45.46	<i>Swift</i> /XRT
45932.21	5	208.90 ± 47.22	<i>Swift</i> /XRT
46103.25	5	150.03 ± 37.18	<i>Swift</i> /XRT
51028.51	5	100.54 ± 26.29	<i>Swift</i> /XRT
51246.66	5	145.77 ± 38.04	<i>Swift</i> /XRT
51402.61	5	135.86 ± 35.38	<i>Swift</i> /XRT
51631.94	5	123.49 ± 32.36	<i>Swift</i> /XRT
51811.65	5	148.15 ± 38.66	<i>Swift</i> /XRT
51983.45	5	108.76 ± 28.38	<i>Swift</i> /XRT
52334.07	5	113.08 ± 22.13	<i>Swift</i> /XRT
56828.46	5	97.40 ± 25.47	<i>Swift</i> /XRT
57023.32	5	145.76 ± 35.78	<i>Swift</i> /XRT
57212.78	5	145.82 ± 37.93	<i>Swift</i> /XRT
57459.18	5	106.45 ± 26.93	<i>Swift</i> /XRT
57675.95	5	124.77 ± 32.55	<i>Swift</i> /XRT
57870.36	5	122.04 ± 31.77	<i>Swift</i> /XRT
58052.23	5	127.39 ± 33.30	<i>Swift</i> /XRT
58329.04	5	120.85 ± 31.66	<i>Swift</i> /XRT

continued ...

... continued

Δt [s]	Energy [keV]	Flux Density [nJy]	Instrument
58533.91	5	114.96 \pm 25.75	<i>Swift</i> /XRT
62583.75	5	121.72 \pm 31.79	<i>Swift</i> /XRT
62833.21	5	111.06 \pm 29.13	<i>Swift</i> /XRT
63099.63	5	85.02 \pm 22.44	<i>Swift</i> /XRT
63344.38	5	116.63 \pm 30.40	<i>Swift</i> /XRT
63583.40	5	105.98 \pm 27.62	<i>Swift</i> /XRT
63824.44	5	107.86 \pm 28.26	<i>Swift</i> /XRT
64052.43	5	100.88 \pm 26.49	<i>Swift</i> /XRT
64340.41	5	85.07 \pm 22.41	<i>Swift</i> /XRT
64695.80	5	91.49 \pm 20.39	<i>Swift</i> /XRT
68420.57	5	99.50 \pm 25.91	<i>Swift</i> /XRT
68682.43	5	106.56 \pm 27.74	<i>Swift</i> /XRT
68931.21	5	120.82 \pm 30.56	<i>Swift</i> /XRT
69223.50	5	86.48 \pm 22.61	<i>Swift</i> /XRT
69431.63	5	148.57 \pm 38.60	<i>Swift</i> /XRT
69613.65	5	125.36 \pm 32.53	<i>Swift</i> /XRT
69846.97	5	87.04 \pm 22.73	<i>Swift</i> /XRT
70095.72	5	111.87 \pm 29.37	<i>Swift</i> /XRT
70365.65	5	96.27 \pm 25.17	<i>Swift</i> /XRT
70663.68	5	120.83 \pm 27.27	<i>Swift</i> /XRT
74144.89	5	72.07 \pm 18.99	<i>Swift</i> /XRT
74541.87	5	63.39 \pm 16.72	<i>Swift</i> /XRT
74910.86	5	99.10 \pm 25.80	<i>Swift</i> /XRT
75150.71	5	89.76 \pm 23.52	<i>Swift</i> /XRT
75462.98	5	97.43 \pm 25.56	<i>Swift</i> /XRT
75733.89	5	70.78 \pm 18.59	<i>Swift</i> /XRT
76022.94	5	102.68 \pm 26.85	<i>Swift</i> /XRT
76362.75	5	82.97 \pm 18.39	<i>Swift</i> /XRT
79933.40	5	104.65 \pm 26.58	<i>Swift</i> /XRT
80174.65	5	94.87 \pm 24.96	<i>Swift</i> /XRT
80473.96	5	64.42 \pm 16.91	<i>Swift</i> /XRT
80910.21	5	117.37 \pm 22.81	<i>Swift</i> /XRT
104534.61	5	45.55 \pm 11.96	<i>Swift</i> /XRT
105147.73	5	49.39 \pm 11.23	<i>Swift</i> /XRT
110705.55	5	57.86 \pm 10.88	<i>Swift</i> /XRT
115788.77	5	51.14 \pm 11.94	<i>Swift</i> /XRT
122290.20	5	46.28 \pm 9.26	<i>Swift</i> /XRT
145116.43	5	28.15 \pm 6.64	<i>Swift</i> /XRT
160135.67	5	24.86 \pm 6.61	<i>Swift</i> /XRT
206337.02	5	16.34 \pm 4.03	<i>Swift</i> /XRT
241332.65	5	15.97 \pm 2.87	<i>Swift</i> /XRT

continued ...

... continued

Δt [s]	Energy [keV]	Flux Density [nJy]	Instrument
325123.61	5	9.85 ± 2.38	<i>Swift</i> /XRT
338770.66	5	11.75 ± 2.80	<i>Swift</i> /XRT
353414.85	5	12.60 ± 2.63	<i>Swift</i> /XRT
396783.02	5	13.70 ± 3.68	<i>Swift</i> /XRT
420466.63	5	8.23 ± 1.87	<i>Swift</i> /XRT
436259.21	5	15.78 ± 4.28	<i>Swift</i> /XRT
457661.86	5	10.57 ± 2.87	<i>Swift</i> /XRT
499932.21	5	8.85 ± 2.25	<i>Swift</i> /XRT
513563.68	5	9.53 ± 2.47	<i>Swift</i> /XRT
529034.39	5	7.45 ± 2.01	<i>Swift</i> /XRT
703452.43	5	1.82 ± 0.53	<i>Swift</i> /XRT
832327.31	5	2.85 ± 0.81	<i>Swift</i> /XRT
942669.15	5	2.59 ± 0.68	<i>Swift</i> /XRT
1139416.59	5	1.43 ± 0.42	<i>Swift</i> /XRT
1353318.85	5	1.50 ± 0.43	<i>Swift</i> /XRT
1464247.00	5	3.47 ± 1.19	<i>Swift</i> /XRT

Table C.2: Optical data for GRB 090902B. Magnitudes

are not corrected for extinction, while flux densities are.

Times are in reference to the GBM trigger (Sept 2, 2009

at 11:05:08.31 UTC).

Δt [day]	Filter	AB Mag	Frequency [$\times 10^{14}$ Hz]	Flux Density [μJy]	Instrument
0.522	u	20.34 ± 0.18	8.33	13.1362 ± 2.2005	<i>Swift</i> /UVOT
0.589	u	20.63 ± 0.17	8.33	10.0571 ± 1.5930	<i>Swift</i> /UVOT
0.656	u	20.52 ± 0.14	8.33	11.1294 ± 1.4597	<i>Swift</i> /UVOT
0.723	u	21.11 ± 0.2	8.33	6.4636 ± 1.2007	<i>Swift</i> /UVOT
0.790	u	20.9 ± 0.16	8.33	7.8428 ± 1.1709	<i>Swift</i> /UVOT
0.856	u	21.01 ± 0.18	8.33	7.0871 ± 1.1872	<i>Swift</i> /UVOT
0.923	u	20.65 ± 0.21	8.33	9.8735 ± 1.9243	<i>Swift</i> /UVOT
1.206	u	21.92 ± 0.35	8.33	3.0653 ± 0.9909	<i>Swift</i> /UVOT
3.614	u	22.27 ± 0.2	8.33	2.2206 ± 0.4125	<i>Swift</i> /UVOT
7.693	u	>22.8	8.33	<1.3629	<i>Swift</i> /UVOT
0.056	R	16.4 ± 0.5	4.68	0.9168 ± 0.5362	ROTSE-IIIa
0.269	R	>18.7	4.68	<0.1102	ROTSE-III d
0.294	R	>18.6	4.68	<0.1209	ROTSE-III c
0.721	R	20.6 ± 0.1	4.68	0.0192 ± 0.0018	Nickel
0.865	R	21.04 ± 0.11	4.68	0.0128 ± 0.0014	Liverpool
1.431	R	21.4 ± 0.1	4.68	0.0092 ± 0.0009	Liverpool
3.467	R	22.6 ± 0.25	4.68	0.0030 ± 0.0008	Liverpool
3.797	R	>22.1	4.68	<0.0048	Liverpool
1.557	R	21.4 ± 0.11	4.68	0.0092 ± 0.0010	NOT
1.537	g	—	6.38	8.72 ± 0.55	GROND
1.561	g	—	6.38	8.72 ± 0.75	GROND
1.581	g	—	6.38	7.92 ± 0.68	GROND
2.556	g	—	6.38	5.47 ± 0.39	GROND
6.533	g	—	6.38	1.96 ± 0.14	GROND
7.529	g	—	6.38	1.84 ± 0.12	GROND
10.560	g	—	6.38	1.10 ± 0.09	GROND
13.544	g	—	6.38	1.00 ± 0.09	GROND
1.540	r	—	4.84	10.00 ± 0.42	GROND
1.561	r	—	4.84	10.71 ± 0.45	GROND
1.581	r	—	4.84	10.21 ± 0.50	GROND
2.528	r	—	4.84	6.49 ± 0.37	GROND
2.545	r	—	4.84	5.94 ± 0.38	GROND
2.567	r	—	4.84	6.36 ± 0.50	GROND

continued ...

... continued

Δt [day]	Filter	AB Mag	Frequency [$\times 10^{14}$ Hz]	Flux Density [μJy]	Instrument
2.590	r	—	4.84	6.58 ± 0.32	GROND
6.519	r	—	4.84	2.45 ± 0.27	GROND
6.562	r	—	4.84	2.57 ± 0.24	GROND
7.529	r	—	4.84	2.14 ± 0.20	GROND
7.546	r	—	4.84	2.39 ± 0.22	GROND
8.527	r	—	4.84	2.37 ± 0.17	GROND
10.560	r	—	4.84	1.41 ± 0.18	GROND
13.544	r	—	4.84	1.26 ± 0.11	GROND
16.519	r	—	4.84	<1.0932	GROND
23.526	r	—	4.84	0.55 ± 0.04	VLT
23.577	r	—	4.84	0.59 ± 0.05	VLT
1.540	i	—	4.00	11.16 ± 0.71	GROND
1.561	i	—	4.00	11.31 ± 0.56	GROND
1.581	i	—	4.00	11.71 ± 0.66	GROND
2.523	i	—	4.00	7.92 ± 0.56	GROND
2.567	i	—	4.00	7.20 ± 0.62	GROND
2.545	i	—	4.00	7.60 ± 0.48	GROND
2.590	i	—	4.00	7.60 ± 0.54	GROND
6.533	i	—	4.00	2.91 ± 0.21	GROND
7.529	i	—	4.00	2.34 ± 0.42	GROND
1.561	z	—	3.37	12.45 ± 0.61	GROND
2.556	z	—	3.37	8.90 ± 0.44	GROND
6.533	z	—	3.37	2.66 ± 0.70	GROND
0.571	J	—	2.40	50.05 ± 4.29	GROND
0.588	J	—	2.40	36.52 ± 2.86	GROND
1.561	J	—	2.40	16.38 ± 1.04	GROND
2.556	J	—	2.40	12.54 ± 1.26	GROND
1.561	H	—	1.81	22.45 ± 1.76	GROND
2.556	H	—	1.81	15.51 ± 1.44	GROND
1.561	K	—	1.37	31.84 ± 3.69	GROND
2.556	K	—	1.37	16.95 ± 2.23	GROND

Table C.3: Radio data for GRB 090902B. Times are in reference to the GBM trigger (Sept 2, 2009 at 11:05:08.31 UTC).

Δt [day]	Frequency [GHz]	Flux Density [μJy]	Instrument
1.31	4.80	111 ± 28	WSRT
1.48	8.46	141 ± 39	VLA
4.59	8.46	13 ± 31	VLA
5.59	8.46	130 ± 34	VLA
7.69	8.46	10 ± 32	VLA
8.59	8.46	80 ± 32	VLA
10.64	8.46	99 ± 31	VLA
11.60	8.46	71 ± 33	VLA
15.50	8.46	52 ± 32	VLA
16.46	8.46	89 ± 36	VLA
22.51	8.46	26 ± 29	VLA
24.50	8.46	67 ± 29	VLA
34.43	8.46	38 ± 28	VLA
36.43	8.46	66 ± 27	VLA
39.23	8.46	21 ± 31	VLA
65.44	8.46	9 ± 20	VLA
66.31	8.46	22 ± 19	VLA
67.54	8.46	48 ± 19	VLA
73.42	8.46	31 ± 21	VLA
199.16	8.46	18 ± 16	VLA

C.2 GRB 160509A

Table C.4: X-ray data for GRB 160509A. Times are in reference to the LAT trigger (May 09, 2016 at 08:59:04.36 UTC).

Δt [s]	Energy [keV]	Flux Density [nJy]	Instrument
7287.09	5	2317.68 \pm 506.54	<i>Swift</i> /XRT
7311.50	5	1727.80 \pm 389.49	<i>Swift</i> /XRT
7341.47	5	2537.33 \pm 569.20	<i>Swift</i> /XRT
7367.08	5	1810.94 \pm 397.01	<i>Swift</i> /XRT
7400.62	5	1938.21 \pm 415.67	<i>Swift</i> /XRT
7443.03	5	1585.16 \pm 318.27	<i>Swift</i> /XRT
7471.22	5	2882.78 \pm 648.80	<i>Swift</i> /XRT
7496.03	5	2401.88 \pm 524.94	<i>Swift</i> /XRT
7525.48	5	2358.86 \pm 419.53	<i>Swift</i> /XRT
14208.51	5	1480.40 \pm 333.18	<i>Swift</i> /XRT
14242.24	5	2222.85 \pm 501.91	<i>Swift</i> /XRT
14280.57	5	1691.68 \pm 362.26	<i>Swift</i> /XRT
14313.30	5	1575.19 \pm 345.86	<i>Swift</i> /XRT
14355.31	5	1049.12 \pm 236.50	<i>Swift</i> /XRT
14410.41	5	1562.14 \pm 308.66	<i>Swift</i> /XRT
19705.32	5	1528.92 \pm 342.99	<i>Swift</i> /XRT
19771.29	5	1130.89 \pm 190.02	<i>Swift</i> /XRT
24291.14	5	749.58 \pm 170.79	<i>Swift</i> /XRT
24372.00	5	1089.07 \pm 246.20	<i>Swift</i> /XRT
24457.88	5	994.94 \pm 224.92	<i>Swift</i> /XRT
24529.97	5	1404.50 \pm 316.02	<i>Swift</i> /XRT
24588.39	5	1449.72 \pm 326.71	<i>Swift</i> /XRT
24672.13	5	912.25 \pm 208.52	<i>Swift</i> /XRT
24760.01	5	1055.12 \pm 239.28	<i>Swift</i> /XRT
24858.65	5	683.64 \pm 155.28	<i>Swift</i> /XRT
24964.23	5	965.41 \pm 219.62	<i>Swift</i> /XRT
25064.90	5	899.13 \pm 204.55	<i>Swift</i> /XRT
25165.82	5	910.67 \pm 206.52	<i>Swift</i> /XRT
25256.36	5	802.27 \pm 179.04	<i>Swift</i> /XRT
25371.79	5	820.69 \pm 187.89	<i>Swift</i> /XRT
25476.10	5	948.31 \pm 213.37	<i>Swift</i> /XRT

continued ...

... continued

Δt [s]	Energy [keV]	Flux Density [nJy]	Instrument
25582.27	5	693.79 \pm 157.58	<i>Swift</i> /XRT
25700.38	5	917.33 \pm 207.38	<i>Swift</i> /XRT
25762.32	5	1847.32 \pm 415.01	<i>Swift</i> /XRT
25833.27	5	1060.84 \pm 239.44	<i>Swift</i> /XRT
25909.12	5	1254.27 \pm 283.55	<i>Swift</i> /XRT
25973.56	5	1304.22 \pm 295.30	<i>Swift</i> /XRT
26040.63	5	1291.02 \pm 277.99	<i>Swift</i> /XRT
29992.31	5	801.31 \pm 180.75	<i>Swift</i> /XRT
30070.29	5	713.02 \pm 160.84	<i>Swift</i> /XRT
30137.98	5	771.48 \pm 174.28	<i>Swift</i> /XRT
30205.06	5	879.00 \pm 197.41	<i>Swift</i> /XRT
30264.98	5	754.45 \pm 171.94	<i>Swift</i> /XRT
30330.99	5	1222.27 \pm 262.32	<i>Swift</i> /XRT
30373.23	5	1384.05 \pm 303.28	<i>Swift</i> /XRT
30429.09	5	793.66 \pm 179.03	<i>Swift</i> /XRT
30507.56	5	525.47 \pm 118.19	<i>Swift</i> /XRT
30622.27	5	553.35 \pm 126.11	<i>Swift</i> /XRT
30686.58	5	1445.31 \pm 308.14	<i>Swift</i> /XRT
30726.46	5	1006.68 \pm 226.41	<i>Swift</i> /XRT
30800.67	5	615.67 \pm 139.69	<i>Swift</i> /XRT
30878.39	5	792.92 \pm 174.48	<i>Swift</i> /XRT
30937.37	5	1013.24 \pm 222.65	<i>Swift</i> /XRT
31006.14	5	781.66 \pm 176.84	<i>Swift</i> /XRT
31072.41	5	796.49 \pm 175.51	<i>Swift</i> /XRT
31135.02	5	768.36 \pm 173.83	<i>Swift</i> /XRT
31216.76	5	696.40 \pm 156.63	<i>Swift</i> /XRT
31280.45	5	929.04 \pm 208.65	<i>Swift</i> /XRT
31340.64	5	840.48 \pm 180.38	<i>Swift</i> /XRT
31412.58	5	789.02 \pm 177.46	<i>Swift</i> /XRT
31479.12	5	974.03 \pm 208.77	<i>Swift</i> /XRT
31535.88	5	1050.90 \pm 225.84	<i>Swift</i> /XRT
31590.22	5	726.52 \pm 164.36	<i>Swift</i> /XRT
31675.24	5	648.51 \pm 142.90	<i>Swift</i> /XRT
31758.23	5	783.09 \pm 164.95	<i>Swift</i> /XRT
35753.28	5	1042.04 \pm 234.60	<i>Swift</i> /XRT
35810.69	5	696.15 \pm 157.16	<i>Swift</i> /XRT
35885.74	5	958.22 \pm 205.31	<i>Swift</i> /XRT
35942.95	5	936.67 \pm 210.02	<i>Swift</i> /XRT
36002.88	5	1021.43 \pm 229.97	<i>Swift</i> /XRT
36062.93	5	1082.24 \pm 245.00	<i>Swift</i> /XRT
36120.72	5	684.83 \pm 155.03	<i>Swift</i> /XRT

continued ...

... continued

Δt [s]	Energy [keV]	Flux Density [nJy]	Instrument
36196.82	5	1008.88 \pm 228.71	<i>Swift</i> /XRT
36252.61	5	928.08 \pm 208.38	<i>Swift</i> /XRT
36326.07	5	765.94 \pm 173.16	<i>Swift</i> /XRT
36374.97	5	1618.54 \pm 362.41	<i>Swift</i> /XRT
36438.38	5	657.57 \pm 144.24	<i>Swift</i> /XRT
36505.22	5	1382.09 \pm 310.31	<i>Swift</i> /XRT
36557.62	5	839.51 \pm 190.05	<i>Swift</i> /XRT
36658.19	5	588.52 \pm 129.77	<i>Swift</i> /XRT
36723.51	5	1023.11 \pm 224.43	<i>Swift</i> /XRT
36790.05	5	680.36 \pm 153.81	<i>Swift</i> /XRT
36883.07	5	672.76 \pm 152.09	<i>Swift</i> /XRT
36954.46	5	823.55 \pm 162.71	<i>Swift</i> /XRT
42744.08	5	646.07 \pm 145.11	<i>Swift</i> /XRT
42825.94	5	718.92 \pm 162.74	<i>Swift</i> /XRT
42915.71	5	642.89 \pm 144.56	<i>Swift</i> /XRT
42983.65	5	636.43 \pm 143.58	<i>Swift</i> /XRT
43077.17	5	647.93 \pm 146.67	<i>Swift</i> /XRT
43157.32	5	720.88 \pm 158.65	<i>Swift</i> /XRT
43234.45	5	825.45 \pm 181.08	<i>Swift</i> /XRT
47989.01	5	525.43 \pm 118.00	<i>Swift</i> /XRT
48076.15	5	769.47 \pm 173.38	<i>Swift</i> /XRT
48135.20	5	720.19 \pm 162.27	<i>Swift</i> /XRT
48228.06	5	793.85 \pm 173.95	<i>Swift</i> /XRT
48320.11	5	509.19 \pm 112.28	<i>Swift</i> /XRT
48452.49	5	436.35 \pm 98.64	<i>Swift</i> /XRT
48550.65	5	574.56 \pm 129.74	<i>Swift</i> /XRT
48659.35	5	528.13 \pm 119.39	<i>Swift</i> /XRT
48759.14	5	523.20 \pm 118.40	<i>Swift</i> /XRT
48909.85	5	581.62 \pm 97.70	<i>Swift</i> /XRT
54302.93	5	393.41 \pm 88.14	<i>Swift</i> /XRT
54488.32	5	336.81 \pm 76.45	<i>Swift</i> /XRT
54647.85	5	592.77 \pm 112.62	<i>Swift</i> /XRT
64515.39	5	323.05 \pm 72.64	<i>Swift</i> /XRT
64632.23	5	304.66 \pm 68.97	<i>Swift</i> /XRT
64720.62	5	406.14 \pm 91.02	<i>Swift</i> /XRT
64797.22	5	403.15 \pm 90.76	<i>Swift</i> /XRT
64875.82	5	348.18 \pm 78.47	<i>Swift</i> /XRT
64963.39	5	421.33 \pm 92.93	<i>Swift</i> /XRT
65042.31	5	303.28 \pm 68.58	<i>Swift</i> /XRT
65130.57	5	429.43 \pm 97.11	<i>Swift</i> /XRT
65213.43	5	403.39 \pm 90.91	<i>Swift</i> /XRT

continued ...

... continued

Δt [s]	Energy [keV]	Flux Density [nJy]	Instrument
65291.78	5	377.04 \pm 85.07	<i>Swift</i> /XRT
65387.69	5	319.64 \pm 72.04	<i>Swift</i> /XRT
65493.12	5	401.17 \pm 90.80	<i>Swift</i> /XRT
65591.66	5	601.99 \pm 135.95	<i>Swift</i> /XRT
65744.38	5	417.16 \pm 81.40	<i>Swift</i> /XRT
70541.08	5	282.62 \pm 63.51	<i>Swift</i> /XRT
70662.07	5	359.44 \pm 81.01	<i>Swift</i> /XRT
70774.21	5	279.25 \pm 61.87	<i>Swift</i> /XRT
70878.95	5	447.26 \pm 100.21	<i>Swift</i> /XRT
70987.77	5	309.46 \pm 69.68	<i>Swift</i> /XRT
71078.65	5	319.14 \pm 71.79	<i>Swift</i> /XRT
71251.28	5	343.90 \pm 56.96	<i>Swift</i> /XRT
75977.24	5	296.62 \pm 67.24	<i>Swift</i> /XRT
76072.39	5	263.90 \pm 59.63	<i>Swift</i> /XRT
76205.29	5	370.23 \pm 81.91	<i>Swift</i> /XRT
76333.91	5	401.67 \pm 90.29	<i>Swift</i> /XRT
76445.22	5	312.99 \pm 67.43	<i>Swift</i> /XRT
76598.46	5	337.97 \pm 74.85	<i>Swift</i> /XRT
76751.04	5	211.25 \pm 41.17	<i>Swift</i> /XRT
87496.03	5	315.68 \pm 71.29	<i>Swift</i> /XRT
87729.20	5	314.13 \pm 71.03	<i>Swift</i> /XRT
88102.18	5	350.80 \pm 57.41	<i>Swift</i> /XRT
93160.21	5	280.37 \pm 62.89	<i>Swift</i> /XRT
93284.32	5	219.87 \pm 49.48	<i>Swift</i> /XRT
93413.33	5	293.41 \pm 66.03	<i>Swift</i> /XRT
93567.87	5	370.97 \pm 83.64	<i>Swift</i> /XRT
93799.19	5	169.62 \pm 38.17	<i>Swift</i> /XRT
93968.62	5	138.45 \pm 35.08	<i>Swift</i> /XRT
94115.74	5	306.96 \pm 65.76	<i>Swift</i> /XRT
94237.98	5	237.33 \pm 53.64	<i>Swift</i> /XRT
94380.15	5	227.39 \pm 51.56	<i>Swift</i> /XRT
94501.26	5	307.97 \pm 69.16	<i>Swift</i> /XRT
94594.65	5	286.64 \pm 64.44	<i>Swift</i> /XRT
94735.86	5	235.49 \pm 49.70	<i>Swift</i> /XRT
98950.79	5	244.96 \pm 54.94	<i>Swift</i> /XRT
99073.65	5	305.97 \pm 68.96	<i>Swift</i> /XRT
99204.49	5	246.98 \pm 54.15	<i>Swift</i> /XRT
99334.28	5	237.08 \pm 53.28	<i>Swift</i> /XRT
99497.76	5	177.94 \pm 40.34	<i>Swift</i> /XRT
99644.69	5	281.61 \pm 63.59	<i>Swift</i> /XRT
99788.73	5	193.55 \pm 43.67	<i>Swift</i> /XRT

continued ...

... continued

Δt [s]	Energy [keV]	Flux Density [nJy]	Instrument
99972.26	5	321.03 \pm 72.14	<i>Swift</i> /XRT
100140.51	5	255.89 \pm 57.90	<i>Swift</i> /XRT
100268.88	5	203.72 \pm 45.73	<i>Swift</i> /XRT
100430.85	5	216.52 \pm 43.68	<i>Swift</i> /XRT
105679.94	5	181.68 \pm 40.90	<i>Swift</i> /XRT
105846.32	5	226.77 \pm 48.54	<i>Swift</i> /XRT
139146.80	5	131.06 \pm 32.30	<i>Swift</i> /XRT
139419.91	5	139.68 \pm 35.30	<i>Swift</i> /XRT
139703.03	5	135.45 \pm 35.38	<i>Swift</i> /XRT
140014.62	5	123.75 \pm 32.22	<i>Swift</i> /XRT
140318.74	5	143.51 \pm 31.67	<i>Swift</i> /XRT
144884.41	5	165.64 \pm 37.38	<i>Swift</i> /XRT
145134.24	5	128.77 \pm 25.51	<i>Swift</i> /XRT
150419.50	5	168.88 \pm 38.49	<i>Swift</i> /XRT
150632.47	5	208.63 \pm 37.46	<i>Swift</i> /XRT
157471.88	5	131.44 \pm 32.28	<i>Swift</i> /XRT
158833.98	5	220.03 \pm 41.05	<i>Swift</i> /XRT
180491.71	5	109.18 \pm 24.84	<i>Swift</i> /XRT
186221.84	5	112.03 \pm 23.58	<i>Swift</i> /XRT
193963.29	5	104.62 \pm 23.66	<i>Swift</i> /XRT
220331.40	5	75.83 \pm 14.20	<i>Swift</i> /XRT
253851.23	5	46.24 \pm 12.12	<i>Swift</i> /XRT
254356.10	5	62.19 \pm 15.23	<i>Swift</i> /XRT
273320.35	5	67.46 \pm 13.09	<i>Swift</i> /XRT
288252.51	5	54.84 \pm 14.40	<i>Swift</i> /XRT
288700.56	5	52.30 \pm 12.86	<i>Swift</i> /XRT
293929.80	5	61.85 \pm 16.24	<i>Swift</i> /XRT
294592.27	5	46.62 \pm 9.07	<i>Swift</i> /XRT
305921.53	5	52.46 \pm 10.27	<i>Swift</i> /XRT
339713.78	5	59.02 \pm 16.62	<i>Swift</i> /XRT
341372.92	5	47.43 \pm 10.99	<i>Swift</i> /XRT
351247.62	5	54.12 \pm 16.55	<i>Swift</i> /XRT
351860.87	5	46.09 \pm 10.17	<i>Swift</i> /XRT
357407.46	5	46.57 \pm 9.25	<i>Swift</i> /XRT
362673.06	5	66.27 \pm 17.85	<i>Swift</i> /XRT
364511.34	5	44.47 \pm 8.55	<i>Swift</i> /XRT
456218.96	5	24.07 \pm 5.61	<i>Swift</i> /XRT
563726.28	5	17.88 \pm 3.25	<i>Swift</i> /XRT
611257.59	5	17.63 \pm 3.42	<i>Swift</i> /XRT
761863.90	5	6.76 \pm 1.60	<i>Swift</i> /XRT
868575.89	5	12.80 \pm 3.24	<i>Swift</i> /XRT

continued ...

... continued

Δt [s]	Energy [keV]	Flux Density [nJy]	Instrument
950140.18	5	8.20 ± 1.87	<i>Swift</i> /XRT
1090830.26	5	7.39 ± 2.00	<i>Swift</i> /XRT
1255447.00	5	3.16 ± 0.78	<i>Swift</i> /XRT
1452339.88	5	2.71 ± 0.74	<i>Swift</i> /XRT
1753101.64	5	2.03 ± 0.58	<i>Swift</i> /XRT
2007949.41	5	<14.50	<i>Swift</i> /XRT
3637440.00	5	0.57 ± 0.10	<i>Chandra</i> /ACIS-S

Table C.5: Optical data for GRB 160509A. Magnitudes are not corrected for extinction, while flux densities are. Times are in reference to the LAT trigger (May 09, 2016 at 08:59:04.36 UTC).

Δt [day]	Filter	AB Mag	Frequency [$\times 10^{14}$ Hz]	Flux Density [μJy]	Instrument
0.36	g	—	6.38	157.9 ± 133.5	DCT
1.03	g	25.03 ± 0.15	6.38	71.2 ± 42.9	DCT
1.03	F110W	—	2.68	91.88 ± 7.33	HST/WFC3
5.80	F160W	—	1.96	24.20 ± 4.00	HST/WFC3
24.80	F160W	—	1.96	< 6.68	HST/WFC3
35.30	F160W	26.07 ± 0.07	1.96	0.55 ± 0.04	HST/WFC3
35.30	F110W	27.11 ± 0.10	2.68	0.69 ± 0.04	HST/WFC3

Table C.6: Radio data for GRB160509A. Times are in reference to the LAT trigger (May 09, 2016 at 08:59:04.36 UTC).

Δt [day]	Frequency [GHz]	Flux Density [μJy]	Instrument
0.3632	5.0	78.2 ± 23.9	VLA
0.3632	7.4	90.8 ± 18.6	VLA
0.3514	8.5	43.8 ± 29.1	VLA
0.3514	11.0	50.6 ± 27.4	VLA
1.1682	5.0	204.7 ± 22.3	VLA
1.1682	7.4	437.1 ± 18.5	VLA
1.1528	8.5	664.7 ± 22.9	VLA
1.1528	11.0	963.4 ± 17.2	VLA
1.1369	13.5	946.0 ± 27.2	VLA
1.1369	16.0	1025.9 ± 31.7	VLA
1.1163	19.2	1341.7 ± 33.7	VLA
1.1163	24.5	1891.8 ± 56.3	VLA
1.0911	30.0	2117.8 ± 47.9	VLA
1.0911	37.0	2410.9 ± 61.5	VLA
2.1479	5.0	509.1 ± 18.9	VLA
2.1479	7.4	754.1 ± 14.9	VLA
2.1259	19.2	1140.0 ± 16.0	VLA
2.1259	24.5	1171.0 ± 21.0	VLA
2.9937	5.0	447.6 ± 18.0	VLA
2.9937	7.4	1049.6 ± 15.7	VLA
2.9781	8.5	1049.0 ± 17.1	VLA
2.9781	11.0	757.5 ± 19.4	VLA
2.9623	13.5	733.3 ± 17.6	VLA
2.9623	16.0	704.8 ± 23.6	VLA
2.9417	19.2	696.7 ± 28.3	VLA
2.9417	24.5	680.5 ± 50.7	VLA
2.9165	30.0	576.1 ± 48.8	VLA
2.9165	37.0	626.0 ± 70.8	VLA
4.0600	1.6	250.9 ± 103.9	VLA
4.0600	2.7	222.2 ± 35.4	VLA
4.0600	3.5	384.4 ± 27.1	VLA
4.0600	5.0	430.4 ± 14.7	VLA
4.0600	7.4	1389.1 ± 20.2	VLA
4.0600	8.5	1044.9 ± 18.6	VLA
4.0600	11.0	1261.0 ± 17.9	VLA

continued ...

... continued

Δt [day]	Frequency [GHz]	Flux Density [μJy]	Instrument
4.0600	13.5	830.8 ± 25.4	VLA
4.0600	16.0	692.0 ± 27.5	VLA
4.0600	19.2	603.3 ± 18.6	VLA
4.0600	24.5	536.5 ± 26.9	VLA
4.0600	30.0	408.1 ± 40.4	VLA
4.0600	37.0	408.1 ± 41.1	VLA
5.3100	1.3	432.0 ± 144.0	VLA
5.3100	1.6	249.5 ± 74.6	VLA
5.3100	2.7	207.3 ± 44.8	VLA
5.3100	3.5	337.2 ± 25.3	VLA
6.0000	1.3	942.6 ± 314.2	VLA
6.0000	1.6	172.7 ± 69.5	VLA
6.0000	2.7	334.8 ± 40.1	VLA
6.0000	3.5	300.1 ± 23.1	VLA
6.0000	5.0	324.3 ± 25.5	VLA
6.0000	7.4	274.9 ± 14.8	VLA
6.0000	8.5	267.4 ± 18.0	VLA
6.0000	11.0	208.2 ± 19.2	VLA
6.0000	13.5	238.9 ± 24.1	VLA
6.0000	16.0	214.0 ± 22.7	VLA
6.0000	19.2	213.4 ± 30.3	VLA
6.0000	24.5	225.8 ± 56.4	VLA
6.0000	30.0	132.7 ± 47.0	VLA
6.0000	37.0	154.2 ± 71.1	VLA
10.0300	1.3	264.0 ± 88.0	VLA
10.0300	1.6	270.2 ± 102.6	VLA
10.0300	2.7	161.0 ± 45.9	VLA
10.0300	3.5	148.3 ± 25.2	VLA
10.0300	5.0	167.9 ± 17.5	VLA
10.0300	7.4	167.9 ± 19.3	VLA
10.0300	8.5	155.2 ± 32.0	VLA
10.0300	11.0	140.2 ± 22.8	VLA
10.0300	13.5	119.5 ± 44.0	VLA
10.0300	16.0	142.0 ± 47.6	VLA
10.0300	19.2	147.8 ± 39.6	VLA
10.0300	24.5	135.0 ± 45.0	VLA
10.0300	30.0	78.2 ± 60.4	VLA
10.0300	37.0	99.8 ± 68.0	VLA
19.9500	2.7	75.7 ± 21.8	VLA
19.9500	3.5	51.2 ± 16.3	VLA
19.9500	5.0	137.2 ± 18.9	VLA

continued ...

... continued

Δt [day]	Frequency [GHz]	Flux Density [μJy]	Instrument
19.9500	7.4	109.9 ± 16.2	VLA
19.9500	8.5	89.4 ± 19.3	VLA
19.9500	11.0	65.9 ± 18.5	VLA
19.9500	13.5	83.6 ± 13.7	VLA
19.9500	16.0	69.2 ± 11.9	VLA
23.90	6.0	80 ± 8	VLA
23.90	9.0	71 ± 7	VLA
36.90	5.0	50 ± 7	VLA
36.90	6.9	52 ± 7	VLA
36.90	8.5	41 ± 6	VLA
36.90	9.5	29 ± 6	VLA
79.90	6.0	27 ± 6	VLA
79.90	9.0	25 ± 5	VLA

C.3 GRB 160625B

Table C.7: X-ray data for GRB 160625B. Times are in reference to the first GBM trigger (June 25, 2016 at 22:40:16.28 UTC).

Δt [s]	Energy [keV]	Flux Density [nJy]	Instrument
9968.86	5	4786.94 ± 1076.10	<i>Swift</i> /XRT
9991.55	5	4358.44 ± 980.82	<i>Swift</i> /XRT
10017.81	5	5670.52 ± 1243.70	<i>Swift</i> /XRT
10042.20	5	4771.93 ± 1072.73	<i>Swift</i> /XRT
10066.52	5	5932.79 ± 1267.32	<i>Swift</i> /XRT
10092.31	5	4582.16 ± 1008.06	<i>Swift</i> /XRT
10125.11	5	5040.12 ± 822.67	<i>Swift</i> /XRT
17515.77	5	2180.07 ± 422.44	<i>Swift</i> /XRT
21499.74	5	2205.68 ± 497.27	<i>Swift</i> /XRT
21564.44	5	3807.24 ± 858.33	<i>Swift</i> /XRT
21638.05	5	2698.46 ± 553.17	<i>Swift</i> /XRT
85485.79	5	224.58 ± 51.05	<i>Swift</i> /XRT
85599.37	5	252.16 ± 56.93	<i>Swift</i> /XRT
85707.30	5	334.84 ± 64.83	<i>Swift</i> /XRT
96795.67	5	295.68 ± 66.38	<i>Swift</i> /XRT
96892.94	5	204.32 ± 46.00	<i>Swift</i> /XRT
97023.70	5	238.12 ± 53.82	<i>Swift</i> /XRT
97128.51	5	254.81 ± 57.75	<i>Swift</i> /XRT
97223.42	5	338.85 ± 76.18	<i>Swift</i> /XRT
97289.48	5	432.14 ± 97.41	<i>Swift</i> /XRT
97376.74	5	222.66 ± 50.40	<i>Swift</i> /XRT
97507.87	5	220.11 ± 49.55	<i>Swift</i> /XRT
97633.93	5	267.18 ± 59.13	<i>Swift</i> /XRT
97719.86	5	277.14 ± 62.22	<i>Swift</i> /XRT
97803.36	5	388.21 ± 87.16	<i>Swift</i> /XRT
97899.64	5	250.82 ± 56.39	<i>Swift</i> /XRT
98023.80	5	367.81 ± 60.86	<i>Swift</i> /XRT
101411.35	5	412.77 ± 92.72	<i>Swift</i> /XRT
101498.60	5	217.60 ± 49.22	<i>Swift</i> /XRT
101636.25	5	204.76 ± 46.32	<i>Swift</i> /XRT
101768.21	5	249.07 ± 47.50	<i>Swift</i> /XRT

continued ...

... continued

Δt [s]	Energy [keV]	Flux Density [nJy]	Instrument
103410.56	5	178.99 \pm 37.72	<i>Swift</i> /XRT
160543.39	5	214.33 \pm 47.00	<i>Swift</i> /XRT
160697.90	5	219.17 \pm 49.32	<i>Swift</i> /XRT
160894.71	5	151.84 \pm 28.50	<i>Swift</i> /XRT
165223.22	5	131.72 \pm 29.79	<i>Swift</i> /XRT
165415.54	5	148.16 \pm 33.43	<i>Swift</i> /XRT
165591.07	5	212.54 \pm 46.83	<i>Swift</i> /XRT
165735.23	5	209.86 \pm 47.22	<i>Swift</i> /XRT
165934.10	5	98.00 \pm 25.56	<i>Swift</i> /XRT
166111.07	5	176.30 \pm 39.78	<i>Swift</i> /XRT
166303.26	5	143.97 \pm 31.80	<i>Swift</i> /XRT
166550.54	5	137.78 \pm 25.52	<i>Swift</i> /XRT
171789.87	5	172.90 \pm 38.92	<i>Swift</i> /XRT
172009.82	5	126.78 \pm 24.64	<i>Swift</i> /XRT
176554.97	5	184.77 \pm 41.86	<i>Swift</i> /XRT
176761.79	5	97.60 \pm 23.97	<i>Swift</i> /XRT
245418.17	5	112.81 \pm 26.79	<i>Swift</i> /XRT
245658.54	5	87.11 \pm 22.65	<i>Swift</i> /XRT
245980.06	5	109.55 \pm 20.47	<i>Swift</i> /XRT
257473.45	5	100.48 \pm 26.18	<i>Swift</i> /XRT
257691.92	5	86.47 \pm 22.63	<i>Swift</i> /XRT
257973.57	5	63.99 \pm 16.81	<i>Swift</i> /XRT
258220.30	5	115.41 \pm 30.07	<i>Swift</i> /XRT
258402.99	5	90.71 \pm 23.82	<i>Swift</i> /XRT
258669.60	5	98.20 \pm 22.16	<i>Swift</i> /XRT
262667.10	5	87.34 \pm 22.74	<i>Swift</i> /XRT
262963.97	5	88.01 \pm 22.89	<i>Swift</i> /XRT
263196.98	5	84.96 \pm 22.10	<i>Swift</i> /XRT
263497.52	5	74.80 \pm 19.60	<i>Swift</i> /XRT
263795.70	5	90.35 \pm 21.50	<i>Swift</i> /XRT
291004.60	5	59.31 \pm 15.53	<i>Swift</i> /XRT
291364.99	5	72.08 \pm 18.86	<i>Swift</i> /XRT
291705.20	5	67.05 \pm 14.48	<i>Swift</i> /XRT
303929.87	5	62.75 \pm 12.92	<i>Swift</i> /XRT
343961.97	5	58.66 \pm 15.37	<i>Swift</i> /XRT
344381.87	5	55.72 \pm 14.63	<i>Swift</i> /XRT
344757.97	5	65.17 \pm 16.97	<i>Swift</i> /XRT
413126.35	5	42.74 \pm 11.22	<i>Swift</i> /XRT
419080.35	5	32.05 \pm 7.30	<i>Swift</i> /XRT
423144.69	5	58.82 \pm 15.44	<i>Swift</i> /XRT
423927.38	5	40.31 \pm 8.98	<i>Swift</i> /XRT

continued ...

... continued

Δt [s]	Energy [keV]	Flux Density [nJy]	Instrument
487992.15	5	27.93 ± 6.73	<i>Swift</i> /XRT
493826.27	5	62.83 ± 13.25	<i>Swift</i> /XRT
499395.37	5	50.06 ± 13.15	<i>Swift</i> /XRT
531957.37	5	24.36 ± 5.73	<i>Swift</i> /XRT
582608.74	5	32.35 ± 7.01	<i>Swift</i> /XRT
742311.56	5	20.20 ± 3.49	<i>Swift</i> /XRT
867243.77	5	20.19 ± 3.32	<i>Swift</i> /XRT
966716.47	5	15.79 ± 3.59	<i>Swift</i> /XRT
1087278.76	5	14.71 ± 2.89	<i>Swift</i> /XRT
1133202.42	5	10.96 ± 2.57	<i>Swift</i> /XRT
1288190.39	5	12.41 ± 2.25	<i>Swift</i> /XRT
1495179.19	5	8.90 ± 1.90	<i>Swift</i> /XRT
1656197.43	5	11.73 ± 2.15	<i>Swift</i> /XRT
1840984.37	5	7.35 ± 1.88	<i>Swift</i> /XRT
2152212.70	5	4.69 ± 1.06	<i>Swift</i> /XRT
2437915.60	5	3.48 ± 0.98	<i>Swift</i> /XRT
2621204.82	5	3.66 ± 0.93	<i>Swift</i> /XRT
2744691.16	5	3.27 ± 0.84	<i>Swift</i> /XRT
2910473.56	5	2.49 ± 0.64	<i>Swift</i> /XRT
3084905.21	5	3.75 ± 1.00	<i>Swift</i> /XRT
3569514.78	5	1.34 ± 0.38	<i>Swift</i> /XRT
4074274.13	5	1.06 ± 0.47	<i>Swift</i> /XRT
6026863.72	5	0.608 ± 0.120	<i>Chandra</i> /ACIS-S
12472303.72	5	0.133 ± 0.033	<i>Chandra</i> /ACIS-S

Table C.8: Optical data for GRB 160625B. Magnitudes

are not corrected for extinction, while flux densities are.

Times are in reference to the first GBM trigger (June 25,

2016 at 22:40:16.28 UTC).

Δt [day]	Filter	AB Mag	Frequency [$\times 10^{14}$ Hz]	Flux Density [μJy]	Instrument
0.37	r	18.24 ± 0.01	4.82	240 ± 2	RATIR
0.39	r	18.29 ± 0.01	4.82	229 ± 2	RATIR
0.41	r	18.35 ± 0.01	4.82	216 ± 2	RATIR
0.43	r	18.43 ± 0.01	4.82	202 ± 2	RATIR
0.45	r	18.45 ± 0.01	4.82	197 ± 2	RATIR
0.47	r	18.52 ± 0.01	4.82	186 ± 2	RATIR
0.49	r	18.55 ± 0.01	4.82	181 ± 2	RATIR
0.56	r	18.49 ± 0.12	4.82	191 ± 22	LCOGT/FTN
1.40	r	19.51 ± 0.20	4.82	74.5 ± 15.0	LCOGT/FTN
1.42	r	19.60 ± 0.04	4.82	68.6 ± 2.6	LCOGT/FTN
1.47	r	19.70 ± 0.01	4.82	62.5 ± 0.8	RATIR
2.40	r	20.26 ± 0.03	4.82	37.3 ± 1.0	RATIR
2.49	r	20.09 ± 0.06	4.82	43.7 ± 2.5	LCOGT/FTN
3.41	r	20.57 ± 0.01	4.82	27.9 ± 0.3	RATIR
3.47	r	20.48 ± 0.04	4.82	30.5 ± 1.1	LCOGT/FTN
4.39	r	20.87 ± 0.01	4.82	21.3 ± 0.3	RATIR
4.54	r	20.75 ± 0.11	4.82	23.8 ± 2.5	LCOGT/FTN
5.38	r	21.11 ± 0.02	4.82	17.1 ± 0.3	RATIR
5.52	r	21.00 ± 0.13	4.82	18.9 ± 2.4	LCOGT/FTN
6.39	r	21.27 ± 0.02	4.82	14.7 ± 0.3	RATIR
7.18	r	21.26 ± 0.03	4.82	14.9 ± 0.4	ORM/LT
7.38	r	21.38 ± 0.02	4.82	13.3 ± 0.3	RATIR
8.37	r	21.52 ± 0.04	4.82	11.7 ± 0.4	RATIR
9.37	r	21.54 ± 0.02	4.82	11.5 ± 0.2	RATIR
10.13	r	21.57 ± 0.03	4.82	11.2 ± 0.3	ORM/LT
10.36	r	21.61 ± 0.03	4.82	10.8 ± 0.3	RATIR
11.35	r	21.71 ± 0.02	4.82	9.82 ± 0.18	RATIR
12.35	r	21.78 ± 0.03	4.82	9.21 ± 0.26	RATIR
13.36	r	21.93 ± 0.03	4.82	8.02 ± 0.22	RATIR
14.41	r	22.01 ± 0.03	4.82	7.45 ± 0.21	RATIR
15.14	r	22.06 ± 0.05	4.82	7.11 ± 0.34	ORM/LT
15.36	r	22.24 ± 0.05	4.82	6.03 ± 0.28	RATIR
16.34	r	22.33 ± 0.05	4.82	5.55 ± 0.26	RATIR

continued ...

... continued

Δt [day]	Filter	AB Mag	Frequency [$\times 10^{14}$ Hz]	Flux Density [μJy]	Instrument
19.32	r	22.58 ± 0.07	4.82	4.41 ± 0.29	RATIR
21.10	r	22.64 ± 0.12	4.82	4.17 ± 0.49	ORM/LT
20.32	r	22.82 ± 0.11	4.82	3.53 ± 0.38	RATIR
21.39	r	22.61 ± 0.13	4.82	4.29 ± 0.55	RATIR
22.32	r	22.81 ± 0.12	4.82	3.56 ± 0.42	RATIR
23.38	r	22.84 ± 0.11	4.82	3.47 ± 0.37	RATIR
24.38	r	22.90 ± 0.16	4.82	3.28 ± 0.52	RATIR
25.39	r	22.85 ± 0.13	4.82	3.44 ± 0.44	RATIR
26.37	r	23.02 ± 0.11	4.82	2.94 ± 0.31	RATIR
37.12	r	24.05 ± 0.28	4.82	1.14 ± 0.33	ORM/LT
39.40	r	24.10 ± 0.20	4.82	1.09 ± 0.22	RATIR
40.39	r	23.71 ± 0.17	4.82	1.56 ± 0.26	RATIR
41.39	r	24.00 ± 0.20	4.82	1.19 ± 0.24	RATIR
43.31	r	<24.30	4.82	<0.904	RATIR
44.36	r	24.00 ± 0.20	4.82	1.19 ± 0.24	RATIR
48.15	r	24.23 ± 0.15	4.82	0.96 ± 0.14	Magellan/LDSS3
52.92	r	<23.50	4.82	<1.89	RATIR
0.37	i	18.05 ± 0.01	3.96	269 ± 3	RATIR
0.39	i	18.11 ± 0.01	3.96	253 ± 2	RATIR
0.41	i	18.17 ± 0.01	3.96	239 ± 2	RATIR
0.43	i	18.23 ± 0.01	3.96	227 ± 2	RATIR
0.45	i	18.28 ± 0.01	3.96	216 ± 2	RATIR
0.48	i	18.33 ± 0.01	3.96	208 ± 2	RATIR
0.50	i	18.36 ± 0.01	3.96	202 ± 2	RATIR
0.57	i	18.47 ± 0.14	3.96	182 ± 25	LCOGT/FTN
1.19	i	19.56 ± 0.04	3.96	66.7 ± 2.5	LCOGT/FTN
1.41	i	19.46 ± 0.05	3.96	73.1 ± 3.4	LCOGT/FTN
1.46	i	19.48 ± 0.03	3.96	71.8 ± 2	LCOGT/FTN
1.47	i	19.51 ± 0.01	3.96	69.6 ± 0.7	RATIR
2.39	i	19.99 ± 0.01	3.96	45.0 ± 0.5	RATIR
2.50	i	20.04 ± 0.10	3.96	42.9 ± 4.1	LCOGT/FTN
3.41	i	20.38 ± 0.01	3.96	31.5 ± 0.3	RATIR
3.49	i	20.32 ± 0.09	3.96	33.1 ± 2.9	LCOGT/FTN
4.39	i	20.66 ± 0.01	3.96	24.1 ± 0.3	RATIR
5.38	i	20.89 ± 0.02	3.96	19.6 ± 0.3	RATIR
6.39	i	21.06 ± 0.02	3.96	16.7 ± 0.3	RATIR
7.17	i	21.09 ± 0.03	3.96	16.3 ± 0.5	ORM/LT
7.38	i	21.17 ± 0.02	3.96	15.1 ± 0.3	RATIR
8.37	i	21.39 ± 0.04	3.96	12.3 ± 0.4	RATIR
9.37	i	21.37 ± 0.02	3.96	12.5 ± 0.2	RATIR
10.12	i	21.35 ± 0.03	3.96	12.8 ± 0.4	ORM/LT

continued ...

... continued

Δt [day]	Filter	AB Mag	Frequency [$\times 10^{14}$ Hz]	Flux Density [μJy]	Instrument
10.36	i	21.47 \pm 0.03	3.96	11.5 \pm 0.3	RATIR
11.35	i	21.50 \pm 0.02	3.96	11.1 \pm 0.2	RATIR
12.35	i	21.57 \pm 0.03	3.96	10.4 \pm 0.3	RATIR
13.36	i	21.69 \pm 0.02	3.96	9.37 \pm 0.20	RATIR
14.41	i	21.83 \pm 0.02	3.96	8.23 \pm 0.18	RATIR
15.13	i	21.90 \pm 0.08	3.96	7.73 \pm 0.59	ORM/LT
15.36	i	22.00 \pm 0.04	3.96	7.06 \pm 0.26	RATIR
16.34	i	22.11 \pm 0.04	3.96	6.34 \pm 0.26	RATIR
19.32	i	22.34 \pm 0.07	3.96	5.17 \pm 0.33	RATIR
20.32	i	22.51 \pm 0.09	3.96	4.40 \pm 0.38	RATIR
21.09	i	22.36 \pm 0.10	3.96	5.06 \pm 0.49	ORM/LT
21.39	i	22.54 \pm 0.14	3.96	4.30 \pm 0.59	RATIR
22.32	i	22.56 \pm 0.11	3.96	4.21 \pm 0.44	RATIR
23.38	i	22.91 \pm 0.13	3.96	3.05 \pm 0.38	RATIR
24.38	i	22.87 \pm 0.17	3.96	3.17 \pm 0.54	RATIR
25.39	i	22.70 \pm 0.13	3.96	3.71 \pm 0.47	RATIR
26.37	i	22.91 \pm 0.12	3.96	3.06 \pm 0.34	RATIR
37.10	i	23.56 \pm 0.26	3.96	1.68 \pm 0.45	ORM/LT
39.40	i	23.75 \pm 0.19	3.96	1.40 \pm 0.26	RATIR
40.39	i	23.75 \pm 0.20	3.96	1.40 \pm 0.29	RATIR
41.39	i	23.60 \pm 0.17	3.96	1.62 \pm 0.28	RATIR
43.31	i	23.64 \pm 0.21	3.96	1.56 \pm 0.34	RATIR
44.36	i	23.72 \pm 0.18	3.96	1.45 \pm 0.27	RATIR
48.13	i	23.90 \pm 0.30	3.96	1.22 \pm 0.39	Magellan/LDSS3
53.92	i	24.08 \pm 0.27	3.96	1.04 \pm 0.29	RATIR
0.37	H	17.65 \pm 0.02	1.83	332 \pm 6	RATIR
0.39	H	17.69 \pm 0.02	1.83	320 \pm 5	RATIR
0.41	H	17.71 \pm 0.02	1.83	313 \pm 5	RATIR
0.43	H	17.82 \pm 0.01	1.83	282 \pm 4	RATIR
0.46	H	17.83 \pm 0.01	1.83	281 \pm 3	RATIR
0.48	H	17.85 \pm 0.01	1.83	276 \pm 3	RATIR
0.50	H	17.92 \pm 0.01	1.83	258 \pm 3	RATIR
1.47	H	18.96 \pm 0.03	1.83	99.3 \pm 2.5	RATIR
2.40	H	19.45 \pm 0.02	1.83	63.0 \pm 1.3	RATIR
3.41	H	19.80 \pm 0.04	1.83	45.5 \pm 1.6	RATIR
4.39	H	20.00 \pm 0.04	1.83	38.0 \pm 1.4	RATIR
5.38	H	20.12 \pm 0.06	1.83	34.1 \pm 1.8	RATIR
6.39	H	20.35 \pm 0.09	1.83	27.5 \pm 2.5	RATIR
7.38	H	20.50 \pm 0.07	1.83	24.1 \pm 1.6	RATIR
8.37	H	20.41 \pm 0.11	1.83	26.1 \pm 2.8	RATIR
9.37	H	20.55 \pm 0.08	1.83	22.9 \pm 1.8	RATIR

continued ...

... continued

Δt [day]	Filter	AB Mag	Frequency [$\times 10^{14}$ Hz]	Flux Density [μJy]	Instrument
10.36	H	20.64 ± 0.11	1.83	21.1 ± 2.3	RATIR
11.35	H	20.91 ± 0.12	1.83	16.4 ± 1.9	RATIR
12.35	H	20.91 ± 0.15	1.83	16.4 ± 2.5	RATIR
13.36	H	21.02 ± 0.10	1.83	14.9 ± 1.4	RATIR
14.41	H	21.10 ± 0.12	1.83	13.8 ± 1.6	RATIR
15.36	H	21.11 ± 0.14	1.83	13.7 ± 1.9	RATIR
16.34	H	21.33 ± 0.19	1.83	11.2 ± 2.1	RATIR
19.34	H	21.05 ± 0.23	1.83	14.5 ± 3.4	RATIR
20.32	H	21.77 ± 0.24	1.83	7.47 ± 1.9	RATIR
21.39	H	21.05 ± 0.28	1.83	14.4 ± 4.2	RATIR
22.32	H	22.05 ± 0.34	1.83	5.75 ± 2.1	RATIR
41.89	H	<22.50	1.83	<3.8	RATIR
0.37	J	17.79 ± 0.01	2.40	302 ± 4	RATIR
0.39	J	17.85 ± 0.01	2.40	286 ± 4	RATIR
0.41	J	17.87 ± 0.01	2.40	280 ± 3	RATIR
0.43	J	17.92 ± 0.01	2.40	268 ± 3	RATIR
0.46	J	17.99 ± 0.01	2.40	250 ± 3	RATIR
0.48	J	17.97 ± 0.01	2.40	255 ± 3	RATIR
0.50	J	18.04 ± 0.01	2.40	241 ± 3	RATIR
1.47	J	19.11 ± 0.02	2.40	89.6 ± 1.9	RATIR
2.40	J	19.62 ± 0.02	2.40	56.0 ± 1.0	RATIR
3.41	J	19.95 ± 0.03	2.40	41.3 ± 1.2	RATIR
4.39	J	20.32 ± 0.04	2.40	29.4 ± 1.0	RATIR
5.38	J	20.39 ± 0.05	2.40	27.6 ± 1.4	RATIR
6.39	J	20.50 ± 0.07	2.40	24.9 ± 1.7	RATIR
7.38	J	20.73 ± 0.06	2.40	20.2 ± 1.2	RATIR
8.37	J	20.75 ± 0.12	2.40	19.8 ± 2.2	RATIR
9.37	J	20.89 ± 0.08	2.40	17.4 ± 1.3	RATIR
10.36	J	20.83 ± 0.09	2.40	18.3 ± 1.5	RATIR
11.35	J	20.92 ± 0.08	2.40	17.0 ± 1.2	RATIR
12.35	J	21.38 ± 0.16	2.40	11.1 ± 1.8	RATIR
13.36	J	21.16 ± 0.08	2.40	13.6 ± 1.0	RATIR
14.41	J	21.40 ± 0.10	2.40	10.9 ± 1.1	RATIR
15.36	J	21.85 ± 0.18	2.40	7.19 ± 1.30	RATIR
16.34	J	21.39 ± 0.14	2.40	11.0 ± 1.5	RATIR
19.34	J	21.50 ± 0.22	2.40	9.92 ± 2.20	RATIR
20.32	J	22.03 ± 0.23	2.40	6.08 ± 1.40	RATIR
21.39	J	<21.80	2.40	<7.52	RATIR
22.32	J	22.34 ± 0.31	2.40	4.58 ± 1.49	RATIR
23.38	J	21.87 ± 0.10	2.40	7.07 ± 0.71	RATIR
24.38	J	21.98 ± 0.12	2.40	6.36 ± 0.78	RATIR

continued ...

... continued

Δt [day]	Filter	AB Mag	Frequency [$\times 10^{14}$ Hz]	Flux Density [μJy]	Instrument
25.39	J	22.43 ± 0.18	2.40	4.22 ± 0.75	RATIR
26.37	J	22.43 ± 0.17	2.40	4.24 ± 0.74	RATIR
41.89	J	<22.90	2.40	<2.73	RATIR
53.92	J	<23.40	2.40	<1.72	RATIR
0.37	Y	17.90 ± 0.01	2.94	284 ± 4	RATIR
0.39	Y	17.95 ± 0.01	2.94	269 ± 4	RATIR
0.41	Y	18.01 ± 0.01	2.94	256 ± 4	RATIR
0.43	Y	18.07 ± 0.01	2.94	242 ± 3	RATIR
0.46	Y	18.14 ± 0.01	2.94	227 ± 3	RATIR
0.48	Y	18.14 ± 0.01	2.94	226 ± 3	RATIR
0.50	Y	18.22 ± 0.01	2.94	211 ± 3	RATIR
1.47	Y	19.27 ± 0.02	2.94	79.8 ± 1.5	RATIR
2.40	Y	19.80 ± 0.02	2.94	49.4 ± 0.8	RATIR
3.41	Y	20.15 ± 0.03	2.94	35.6 ± 0.9	RATIR
4.39	Y	20.44 ± 0.03	2.94	27.4 ± 0.7	RATIR
5.38	Y	20.59 ± 0.04	2.94	23.7 ± 0.9	RATIR
6.39	Y	20.72 ± 0.06	2.94	21.1 ± 1.2	RATIR
7.38	Y	20.96 ± 0.05	2.94	16.9 ± 0.9	RATIR
8.37	Y	20.95 ± 0.08	2.94	17.1 ± 1.3	RATIR
9.37	Y	21.10 ± 0.06	2.94	14.8 ± 0.9	RATIR
10.36	Y	21.23 ± 0.09	2.94	13.2 ± 1.1	RATIR
11.35	Y	21.15 ± 0.07	2.94	14.1 ± 0.9	RATIR
12.35	Y	21.35 ± 0.10	2.94	11.8 ± 1.2	RATIR
13.36	Y	21.49 ± 0.08	2.94	10.4 ± 0.8	RATIR
14.41	Y	21.62 ± 0.09	2.94	9.16 ± 0.75	RATIR
15.36	Y	21.91 ± 0.14	2.94	7.01 ± 0.95	RATIR
16.34	Y	21.78 ± 0.14	2.94	7.93 ± 1.05	RATIR
19.32	Y	22.51 ± 0.35	2.94	4.06 ± 1.57	RATIR
20.32	Y	22.14 ± 0.18	2.94	5.72 ± 1.03	RATIR
21.39	Y	<22.20	2.94	<5.4	RATIR
22.32	Y	22.39 ± 0.24	2.94	4.52 ± 1.11	RATIR
41.89	Y	<23.10	2.94	<2.36	RATIR
0.37	Z	17.99 ± 0.01	3.42	271 ± 3	RATIR
0.39	Z	18.03 ± 0.01	3.42	260 ± 3	RATIR
0.41	Z	18.08 ± 0.01	3.42	249 ± 3	RATIR
0.43	Z	18.16 ± 0.01	3.42	230 ± 3	RATIR
0.46	Z	18.20 ± 0.01	3.42	223 ± 3	RATIR
0.48	Z	18.23 ± 0.01	3.42	216 ± 3	RATIR
0.50	Z	18.30 ± 0.01	3.42	204 ± 3	RATIR
1.47	Z	19.41 ± 0.02	3.42	73.1 ± 1.2	RATIR
2.39	Z	19.91 ± 0.01	3.42	46.1 ± 0.6	RATIR

continued ...

... continued

Δt [day]	Filter	AB Mag	Frequency [$\times 10^{14}$ Hz]	Flux Density [μJy]	Instrument
3.41	Z	20.28 ± 0.02	3.42	32.9 ± 0.7	RATIR
4.39	Z	20.56 ± 0.02	3.42	25.3 ± 0.5	RATIR
5.38	Z	20.81 ± 0.04	3.42	20.1 ± 0.8	RATIR
6.39	Z	20.95 ± 0.05	3.42	17.8 ± 0.8	RATIR
7.38	Z	21.08 ± 0.04	3.42	15.7 ± 0.7	RATIR
8.37	Z	21.43 ± 0.11	3.42	11.4 ± 1.2	RATIR
9.37	Z	21.22 ± 0.05	3.42	13.8 ± 0.6	RATIR
10.36	Z	21.42 ± 0.07	3.42	11.5 ± 0.7	RATIR
11.35	Z	21.32 ± 0.05	3.42	12.6 ± 0.6	RATIR
12.35	Z	21.48 ± 0.07	3.42	10.9 ± 0.8	RATIR
13.36	Z	21.60 ± 0.06	3.42	9.72 ± 0.54	RATIR
14.41	Z	21.81 ± 0.07	3.42	8.02 ± 0.51	RATIR
15.36	Z	21.76 ± 0.09	3.42	8.36 ± 0.71	RATIR
16.34	Z	21.83 ± 0.09	3.42	7.87 ± 0.69	RATIR
19.32	Z	22.18 ± 0.15	3.42	5.71 ± 0.86	RATIR
20.32	Z	22.41 ± 0.18	3.42	4.59 ± 0.83	RATIR
21.39	Z	<22.50	3.42	<4.25	RATIR
22.32	Z	22.61 ± 0.22	3.42	3.85 ± 0.88	RATIR
23.38	Z	22.48 ± 0.11	3.42	4.34 ± 0.48	RATIR
24.38	Z	23.14 ± 0.27	3.42	2.36 ± 0.67	RATIR
25.39	Z	22.66 ± 0.15	3.42	3.67 ± 0.56	RATIR
26.37	Z	22.86 ± 0.15	3.42	3.05 ± 0.46	RATIR
41.89	Z	23.57 ± 0.32	3.42	1.59 ± 0.55	RATIR
53.92	Z	23.86 ± 0.33	3.42	1.21 ± 0.42	RATIR
48.18	g	24.33 ± 0.15	6.38	1.00 ± 0.15	Magellan/LDSS3
71.46	F606W	25.22 ± 0.03	5.04	0.301 ± 0.011	HST/WFC3
140.16	F606W	26.60 ± 0.06	5.04	0.090 ± 0.006	HST/WFC3
0.11	u	17.52 ± 0.08	8.65	597 ± 46	<i>Swift</i> /UVOT
0.20	u	18.22 ± 0.12	8.65	313 ± 37	<i>Swift</i> /UVOT
0.25	u	18.55 ± 0.09	8.65	231 ± 20	<i>Swift</i> /UVOT
1.08	u	20.06 ± 0.10	8.65	57.5 ± 5.6	<i>Swift</i> /UVOT
1.19	u	20.20 ± 0.20	8.65	50.6 ± 10.2	<i>Swift</i> /UVOT
1.86	u	20.90 ± 0.40	8.65	26.5 ± 11.8	<i>Swift</i> /UVOT
3.11	u	21.11 ± 0.19	8.65	21.9 ± 4.2	<i>Swift</i> /UVOT
3.75	u	21.50 ± 0.20	8.65	15.3 ± 3.1	<i>Swift</i> /UVOT
5.28	u	21.80 ± 0.30	8.65	11.6 ± 3.7	<i>Swift</i> /UVOT
8.76	u	22.60 ± 0.50	8.65	5.55 ± 3.24	<i>Swift</i> /UVOT
0.92	R	19.11 ± 0.05	4.68	106 ± 5	TSHAO/Zeiss-1000
0.98	R	19.08 ± 0.10	4.68	109 ± 10	CrAo/AZT-11
1.93	R	19.82 ± 0.06	4.68	55 ± 3	AbAo/AS-32
1.98	R	20.08 ± 0.07	4.68	43.3 ± 2.9	SAORAS/BTA

continued ...

... continued

Δt [day]	Filter	AB Mag	Frequency [$\times 10^{14}$ Hz]	Flux Density [μJy]	Instrument
2.86	R	20.53 ± 0.06	4.68	28.6 ± 1.6	TSHAO/Zeiss-1000
3.81	R	20.54 ± 0.10	4.68	28.3 ± 2.7	Mondy/AZT-33IK
3.88	R	20.74 ± 0.07	4.68	23.6 ± 1.6	SAORAS/BTA
4.04	R	20.77 ± 0.20	4.68	22.9 ± 4.6	SAORAS/BTA
4.92	R	20.96 ± 0.37	4.68	19.2 ± 7.8	AbAo/AS-32
6.00	R	21.10 ± 0.17	4.68	16.9 ± 2.9	AbAo/AS-32
8.03	R	21.43 ± 0.18	4.68	12.5 ± 2.2	AbAo/AS-32
8.76	R	21.34 ± 0.09	4.68	13.6 ± 1.2	Mondy/AZT-33IK
8.85	R	21.54 ± 0.18	4.68	11.3 ± 2.0	TSHAO/Zeiss-1000
11.92	R	21.88 ± 0.29	4.68	8.24 ± 2.52	TSHAO/Zeiss-1000
12.92	R	21.82 ± 0.16	4.68	8.71 ± 1.38	TSHAO/Zeiss-1000
12.99	R	21.96 ± 0.11	4.68	7.66 ± 0.82	Maidanak/AZT-22
13.99	R	21.76 ± 0.08	4.68	9.21 ± 0.70	Maidanak/AZT-22
14.87	R	21.85 ± 0.09	4.68	8.47 ± 0.732	TSHAO/Zeiss-1000
14.99	R	21.92 ± 0.09	4.68	7.94 ± 0.69	Maidanak/AZT-22
15.75	R	22.14 ± 0.11	4.68	6.49 ± 0.69	Mondy/AZT-33IK
15.75	R	<21.81	4.68	<8.79	Mondy/AZT-33IK
15.90	R	22.18 ± 0.11	4.68	6.25 ± 0.67	Maidanak/AZT-22
15.96	R	22.10 ± 0.34	4.68	6.73 ± 2.48	TSHAO/Zeiss-1000
16.93	R	22.23 ± 0.10	4.68	5.97 ± 0.58	Maidanak/AZT-22
16.95	R	22.13 ± 0.28	4.68	6.55 ± 1.93	TSHAO/Zeiss-1000
16.95	R	<21.91	4.68	<8.02	TSHAO/Zeiss-1000
16.95	R	<22.21	4.68	<6.08	TSHAO/Zeiss-1000
16.95	R	<22.11	4.68	<6.67	TSHAO/Zeiss-1000
16.95	R	<22.91	4.68	<3.19	TSHAO/Zeiss-1000
16.95	R	<22.71	4.68	<3.84	TSHAO/Zeiss-1000
16.95	R	<23.21	4.68	<2.42	TSHAO/Zeiss-1000
16.95	R	<22.21	4.68	<6.08	TSHAO/Zeiss-1000
16.95	R	<21.31	4.68	<13.9	TSHAO/Zeiss-1000
17.97	R	22.33 ± 0.17	4.68	5.45 ± 0.92	Maidanak/AZT-22
18.05	R	22.08 ± 0.35	4.68	6.86 ± 2.61	AbAo/AS-32
20.04	R	22.34 ± 0.21	4.68	5.40 ± 1.15	AbAo/AS-32
20.04	R	j21.91	4.68	<8.02	AbAo/AS-32
21.89	R	22.51 ± 0.34	4.68	4.61 ± 1.70	Maidanak/AZT-22
26.93	R	22.66 ± 0.26	4.68	4.02 ± 1.10	Maidanak/AZT-22
30.04	R	22.45 ± 0.26	4.68	4.88 ± 1.32	AbAo/AS-32
30.04	R	<22.71	4.68	<3.84	AbAo/AS-32
30.04	R	<23.11	4.68	<2.65	AbAo/AS-32
31.03	R	23.09 ± 0.09	4.68	2.7 ± 0.2	CrAo/AZT-11
32.96	R	23.31 ± 0.07	4.68	2.21 ± 0.15	CrAo/AZT-11
33.98	R	23.26 ± 0.08	4.68	2.31 ± 0.18	CrAo/AZT-11

continued ...

...continued

Δt [day]	Filter	AB Mag	Frequency [$\times 10^{14}$ Hz]	Flux Density [μJy]	Instrument
33.98	R	<24.01	4.68	<1.16	CrAo/AZT-11
37.92	R	23.68 ± 0.10	4.68	1.57 ± 0.15	SAORAS/BTA
40.29	R	23.52 ± 0.10	4.68	1.82 ± 0.18	Maidanak/AZT-22
44.34	R	23.90 ± 0.11	4.68	1.28 ± 0.14	Maidanak/AZT-22
44.34	R	<23.01	4.68	<2.91	Maidanak/AZT-22

Table C.9: Radio data for GRB 160625B. Times are in reference to the first GBM trigger (June 25, 2016 at 22:40:16.28 UTC).

Δt [day]	Frequency [GHz]	Flux Density [μJy]	Instrument
1.37	5.00	163 ± 34	VLA
1.37	7.10	232 ± 22	VLA
1.35	8.50	288 ± 23	VLA
1.35	11.00	507 ± 35	VLA
2.50	5.00	932 ± 24	VLA
2.50	7.10	1310 ± 20	VLA
2.49	8.50	1135 ± 28	VLA
2.49	11.00	946 ± 25	VLA
2.47	13.50	646 ± 25	VLA
2.47	16.00	650 ± 19	VLA
2.45	19.20	553 ± 34	VLA
2.45	24.50	530 ± 47	VLA
4.45	4.80	104 ± 15	VLA
4.45	7.40	454 ± 14	VLA
4.45	19.00	278 ± 21	VLA
4.45	25.00	204 ± 29	VLA
4.54	5.50	116 ± 28	ATCA
4.54	6.50	275 ± 27	ATCA
4.54	7.50	401 ± 32	ATCA
4.54	39.00	243 ± 59	ATCA
6.31	1.45	300 ± 90	VLA
6.31	1.77	200 ± 90	VLA
6.30	2.68	164 ± 33	VLA
6.30	3.52	165 ± 43	VLA
6.29	5.00	117 ± 21	VLA
6.29	7.10	180 ± 24	VLA
6.28	8.50	262 ± 41	VLA
6.28	11.00	209 ± 32	VLA
7.32	13.50	270 ± 18	VLA
7.32	16.00	237 ± 23	VLA
7.30	19.20	119 ± 40	VLA
7.30	24.50	80 ± 27	VLA
12.50	1.45	297 ± 74	VLA
12.50	1.77	307 ± 50	VLA
12.49	2.68	621 ± 31	VLA

continued ...

... continued

Δt [day]	Frequency [GHz]	Flux Density [μJy]	Instrument
12.49	3.52	475 ± 40	VLA
12.48	5.00	219 ± 21	VLA
12.48	7.10	185 ± 21	VLA
12.47	8.50	176 ± 23	VLA
12.47	11.00	193 ± 21	VLA
12.45	13.50	176 ± 23	VLA
12.45	16.00	202 ± 21	VLA
12.43	19.20	218 ± 26	VLA
12.43	24.50	147 ± 38	VLA
13.35	4.80	377 ± 15	VLA
13.35	7.40	310 ± 13	VLA
13.35	22.00	163 ± 11	VLA
15.73	19.00	157 ± 17	ATCA
15.73	39.00	<270	ATCA
22.52	1.45	265 ± 75	VLA
22.52	1.77	346 ± 62	VLA
22.51	2.68	512 ± 57	VLA
22.51	3.52	300 ± 27	VLA
22.50	5.00	229 ± 31	VLA
22.50	7.10	201 ± 25	VLA
22.49	8.50	183 ± 24	VLA
22.49	11.00	132 ± 30	VLA
22.47	13.50	134 ± 22	VLA
22.47	16.00	128 ± 28	VLA
22.45	19.20	159 ± 38	VLA
22.45	24.50	85 ± 30	VLA
28.59	9.00	105 ± 16	ATCA
28.59	19.00	<90	ATCA
31.25	7.40	113 ± 14	VLA
31.25	22.00	88 ± 16	VLA
48.38	1.45	142 ± 47	VLA
48.38	1.77	120 ± 61	VLA
48.37	2.68	109 ± 35	VLA
48.37	3.52	72 ± 24	VLA
48.36	5.00	96 ± 31	VLA
48.36	7.10	101 ± 21	VLA
48.35	8.50	84 ± 25	VLA
48.35	11.00	95 ± 23	VLA
48.33	13.50	78 ± 16	VLA
48.33	16.00	97 ± 21	VLA
48.31	19.20	81 ± 33	VLA

continued ...

... continued

Δt [day]	Frequency [GHz]	Flux Density [μJy]	Instrument
48.31	24.50	82 ± 27	VLA
58.25	6.10	75 ± 10	VLA
58.25	22.00	52 ± 12	VLA
208.95	6.10	16 ± 5	VLA
1319	6.10	<2.46	VLA

C.4 GRB 180720B

Table C.10: X-ray data for GRB 180720B. Times are in reference to the GBM trigger (July 20, 2018 at 14:21:39.65 UTC).

Δt [s]	Energy [keV]	Flux Density [nJy]	Instrument
11519.93	5	8013.56 ± 1716.80	<i>Swift</i> /XRT
11535.18	5	7600.71 ± 1684.20	<i>Swift</i> /XRT
11550.71	5	11465.36 ± 2404.60	<i>Swift</i> /XRT
11570.26	5	6333.37 ± 1418.07	<i>Swift</i> /XRT
11587.44	5	7211.18 ± 1512.38	<i>Swift</i> /XRT
11608.26	5	7496.52 ± 1644.20	<i>Swift</i> /XRT
11628.67	5	5274.99 ± 1164.37	<i>Swift</i> /XRT
11648.97	5	7531.60 ± 1658.23	<i>Swift</i> /XRT
11662.28	5	12109.34 ± 2480.05	<i>Swift</i> /XRT
11678.92	5	7884.59 ± 1691.22	<i>Swift</i> /XRT
11696.73	5	8963.88 ± 1800.44	<i>Swift</i> /XRT
11716.08	5	6407.27 ± 1351.64	<i>Swift</i> /XRT
11736.49	5	8904.86 ± 1955.58	<i>Swift</i> /XRT
11751.89	5	6583.59 ± 1447.66	<i>Swift</i> /XRT
11770.04	5	9668.49 ± 2027.74	<i>Swift</i> /XRT
11785.27	5	8566.64 ± 1920.67	<i>Swift</i> /XRT
11800.72	5	6572.07 ± 1443.28	<i>Swift</i> /XRT
11823.32	5	6093.10 ± 1299.05	<i>Swift</i> /XRT
11848.39	5	5473.26 ± 1182.63	<i>Swift</i> /XRT
11870.21	5	8909.29 ± 1954.06	<i>Swift</i> /XRT
11886.18	5	9154.91 ± 1834.89	<i>Swift</i> /XRT
11902.46	5	9791.97 ± 2016.66	<i>Swift</i> /XRT
11915.70	5	8697.47 ± 1907.61	<i>Swift</i> /XRT
11928.99	5	11392.44 ± 2383.76	<i>Swift</i> /XRT
11944.98	5	6282.41 ± 1416.09	<i>Swift</i> /XRT
11963.87	5	9531.28 ± 1996.65	<i>Swift</i> /XRT
11979.93	5	7467.40 ± 1639.90	<i>Swift</i> /XRT
11996.90	5	7806.13 ± 1678.48	<i>Swift</i> /XRT
12014.87	5	8710.66 ± 1782.01	<i>Swift</i> /XRT
12033.36	5	7273.16 ± 1637.21	<i>Swift</i> /XRT
12051.17	5	6344.43 ± 1426.24	<i>Swift</i> /XRT

continued ...

... continued

Δt [s]	Energy [keV]	Flux Density [nJy]	Instrument
12067.09	5	10291.28 \pm 2310.42	<i>Swift</i> /XRT
12082.57	5	10084.53 \pm 2063.07	<i>Swift</i> /XRT
12098.43	5	7220.38 \pm 1623.16	<i>Swift</i> /XRT
12114.40	5	9076.13 \pm 1942.08	<i>Swift</i> /XRT
12130.47	5	7997.02 \pm 1713.25	<i>Swift</i> /XRT
12143.46	5	11201.21 \pm 2396.80	<i>Swift</i> /XRT
12159.71	5	11426.32 \pm 2207.70	<i>Swift</i> /XRT
12177.79	5	5643.01 \pm 1270.26	<i>Swift</i> /XRT
12196.09	5	7231.52 \pm 1623.49	<i>Swift</i> /XRT
12216.52	5	6237.00 \pm 1403.97	<i>Swift</i> /XRT
12238.79	5	6691.98 \pm 1471.49	<i>Swift</i> /XRT
12254.32	5	10169.49 \pm 2085.08	<i>Swift</i> /XRT
12270.53	5	9145.91 \pm 1959.39	<i>Swift</i> /XRT
12286.95	5	7982.39 \pm 1705.98	<i>Swift</i> /XRT
12302.33	5	7962.91 \pm 1710.10	<i>Swift</i> /XRT
12322.08	5	7185.57 \pm 1617.50	<i>Swift</i> /XRT
12336.88	5	8337.74 \pm 1874.35	<i>Swift</i> /XRT
12352.69	5	10481.84 \pm 2293.13	<i>Swift</i> /XRT
12363.45	5	11279.24 \pm 2177.12	<i>Swift</i> /XRT
12381.46	5	7451.92 \pm 1644.89	<i>Swift</i> /XRT
12395.32	5	10658.17 \pm 2343.61	<i>Swift</i> /XRT
12412.63	5	5761.92 \pm 1278.40	<i>Swift</i> /XRT
12435.47	5	9777.99 \pm 1765.27	<i>Swift</i> /XRT
13287.90	5	10173.50 \pm 2171.97	<i>Swift</i> /XRT
13307.80	5	7986.31 \pm 1802.08	<i>Swift</i> /XRT
13331.79	5	6116.26 \pm 1290.54	<i>Swift</i> /XRT
13351.38	5	11986.91 \pm 2562.64	<i>Swift</i> /XRT
13374.20	5	8266.63 \pm 1737.37	<i>Swift</i> /XRT
13397.19	5	6817.45 \pm 1494.12	<i>Swift</i> /XRT
13419.40	5	8556.57 \pm 1880.69	<i>Swift</i> /XRT
13437.05	5	10879.49 \pm 2440.08	<i>Swift</i> /XRT
13451.67	5	10250.39 \pm 2191.39	<i>Swift</i> /XRT
13470.15	5	7242.42 \pm 1631.75	<i>Swift</i> /XRT
13494.14	5	7586.56 \pm 1665.08	<i>Swift</i> /XRT
13515.28	5	9313.24 \pm 2095.13	<i>Swift</i> /XRT
13542.38	5	5215.10 \pm 1154.59	<i>Swift</i> /XRT
13567.18	5	6524.59 \pm 1467.79	<i>Swift</i> /XRT
13592.54	5	7051.87 \pm 1524.34	<i>Swift</i> /XRT
13621.19	5	8578.82 \pm 1762.20	<i>Swift</i> /XRT
13642.02	5	7234.56 \pm 1625.04	<i>Swift</i> /XRT
13659.90	5	12098.59 \pm 2386.56	<i>Swift</i> /XRT

continued ...

... continued

Δt [s]	Energy [keV]	Flux Density [nJy]	Instrument
13676.88	5	8104.96 \pm 1820.55	<i>Swift</i> /XRT
13701.27	5	8935.33 \pm 1918.15	<i>Swift</i> /XRT
13717.87	5	8188.48 \pm 1847.70	<i>Swift</i> /XRT
13746.78	5	4906.20 \pm 1075.25	<i>Swift</i> /XRT
13775.29	5	8056.72 \pm 1817.97	<i>Swift</i> /XRT
13794.18	5	9718.45 \pm 2139.15	<i>Swift</i> /XRT
13812.11	5	9401.05 \pm 1970.58	<i>Swift</i> /XRT
13832.20	5	7249.67 \pm 1635.86	<i>Swift</i> /XRT
13854.27	5	8177.81 \pm 1834.14	<i>Swift</i> /XRT
13879.85	5	7123.08 \pm 1535.47	<i>Swift</i> /XRT
13901.51	5	7929.88 \pm 1702.31	<i>Swift</i> /XRT
13919.71	5	10845.13 \pm 2436.05	<i>Swift</i> /XRT
13938.55	5	7971.75 \pm 1708.94	<i>Swift</i> /XRT
13965.33	5	7932.48 \pm 1707.58	<i>Swift</i> /XRT
17259.00	5	9687.49 \pm 2123.07	<i>Swift</i> /XRT
17276.78	5	6383.98 \pm 1364.79	<i>Swift</i> /XRT
17294.35	5	7738.23 \pm 1735.52	<i>Swift</i> /XRT
17309.80	5	6638.39 \pm 1386.01	<i>Swift</i> /XRT
17332.59	5	4555.95 \pm 1023.34	<i>Swift</i> /XRT
17358.22	5	5341.69 \pm 1175.72	<i>Swift</i> /XRT
17381.48	5	4453.84 \pm 1006.47	<i>Swift</i> /XRT
17403.94	5	5977.66 \pm 1310.04	<i>Swift</i> /XRT
17427.23	5	5311.01 \pm 1167.29	<i>Swift</i> /XRT
17445.29	5	6678.41 \pm 1497.83	<i>Swift</i> /XRT
17469.51	5	5477.18 \pm 1120.82	<i>Swift</i> /XRT
17491.30	5	4472.09 \pm 1004.51	<i>Swift</i> /XRT
17512.24	5	6422.22 \pm 1442.54	<i>Swift</i> /XRT
17537.07	5	3651.49 \pm 800.25	<i>Swift</i> /XRT
17568.23	5	4371.03 \pm 960.69	<i>Swift</i> /XRT
17597.83	5	3878.78 \pm 828.09	<i>Swift</i> /XRT
17627.07	5	4485.08 \pm 1011.99	<i>Swift</i> /XRT
17650.39	5	4510.85 \pm 1017.81	<i>Swift</i> /XRT
17673.78	5	8124.05 \pm 1782.99	<i>Swift</i> /XRT
17694.52	5	3835.40 \pm 864.10	<i>Swift</i> /XRT
17723.21	5	4342.29 \pm 953.01	<i>Swift</i> /XRT
17744.29	5	6443.97 \pm 1443.08	<i>Swift</i> /XRT
17765.10	5	5097.63 \pm 1143.29	<i>Swift</i> /XRT
17794.56	5	3487.20 \pm 785.65	<i>Swift</i> /XRT
17820.86	5	6144.95 \pm 1317.28	<i>Swift</i> /XRT
17846.46	5	3723.99 \pm 840.26	<i>Swift</i> /XRT
17872.54	5	5052.71 \pm 1133.22	<i>Swift</i> /XRT

continued ...

... continued

Δt [s]	Energy [keV]	Flux Density [nJy]	Instrument
17891.84	5	6614.35 \pm 1485.69	<i>Swift</i> /XRT
17909.53	5	7229.28 \pm 1545.50	<i>Swift</i> /XRT
17927.77	5	5506.61 \pm 1182.06	<i>Swift</i> /XRT
17954.09	5	4183.24 \pm 897.99	<i>Swift</i> /XRT
17982.36	5	5115.87 \pm 1156.07	<i>Swift</i> /XRT
18003.07	5	6052.02 \pm 1328.24	<i>Swift</i> /XRT
18024.11	5	5749.65 \pm 1297.32	<i>Swift</i> /XRT
18042.41	5	5710.94 \pm 1282.77	<i>Swift</i> /XRT
18060.59	5	6412.66 \pm 1451.31	<i>Swift</i> /XRT
18081.08	5	6140.27 \pm 1258.09	<i>Swift</i> /XRT
18108.73	5	4586.84 \pm 1034.95	<i>Swift</i> /XRT
18133.55	5	4179.17 \pm 935.89	<i>Swift</i> /XRT
18159.81	5	4237.59 \pm 905.92	<i>Swift</i> /XRT
18192.72	5	4147.63 \pm 930.23	<i>Swift</i> /XRT
18214.79	5	5731.29 \pm 1283.48	<i>Swift</i> /XRT
18238.23	5	4052.66 \pm 917.20	<i>Swift</i> /XRT
18265.06	5	4996.57 \pm 1124.00	<i>Swift</i> /XRT
18281.73	5	7565.63 \pm 1691.73	<i>Swift</i> /XRT
18300.79	5	5976.79 \pm 1230.76	<i>Swift</i> /XRT
18324.06	5	5906.96 \pm 1236.52	<i>Swift</i> /XRT
18346.38	5	4984.34 \pm 1069.95	<i>Swift</i> /XRT
18367.61	5	5763.62 \pm 1290.72	<i>Swift</i> /XRT
18386.91	5	7663.02 \pm 1718.65	<i>Swift</i> /XRT
18410.77	5	3858.09 \pm 828.19	<i>Swift</i> /XRT
18442.69	5	3978.98 \pm 877.05	<i>Swift</i> /XRT
18463.01	5	6584.79 \pm 1472.40	<i>Swift</i> /XRT
18485.19	5	7118.47 \pm 1525.98	<i>Swift</i> /XRT
18502.63	5	6027.12 \pm 1320.88	<i>Swift</i> /XRT
18525.19	5	4159.92 \pm 941.47	<i>Swift</i> /XRT
18549.19	5	5968.93 \pm 1308.13	<i>Swift</i> /XRT
18568.19	5	6379.36 \pm 1435.07	<i>Swift</i> /XRT
18584.74	5	5651.15 \pm 1273.17	<i>Swift</i> /XRT
18610.56	5	3978.43 \pm 871.90	<i>Swift</i> /XRT
18637.65	5	5081.70 \pm 1141.43	<i>Swift</i> /XRT
18661.09	5	4542.60 \pm 1020.34	<i>Swift</i> /XRT
18685.66	5	5315.77 \pm 1166.66	<i>Swift</i> /XRT
18709.66	5	4769.03 \pm 1045.16	<i>Swift</i> /XRT
18735.07	5	5426.74 \pm 1117.50	<i>Swift</i> /XRT
18755.54	5	7552.70 \pm 1578.96	<i>Swift</i> /XRT
18774.29	5	5082.24 \pm 1139.84	<i>Swift</i> /XRT
18803.16	5	4052.92 \pm 874.81	<i>Swift</i> /XRT

continued ...

... continued

Δt [s]	Energy [keV]	Flux Density [nJy]	Instrument
18828.33	5	4069.50 \pm 922.41	<i>Swift</i> /XRT
18857.83	5	4023.58 \pm 881.79	<i>Swift</i> /XRT
18884.36	5	5765.59 \pm 1295.05	<i>Swift</i> /XRT
18907.74	5	5216.93 \pm 1148.26	<i>Swift</i> /XRT
18931.38	5	4513.82 \pm 966.30	<i>Swift</i> /XRT
18959.08	5	4269.88 \pm 938.46	<i>Swift</i> /XRT
18984.16	5	5022.78 \pm 1133.32	<i>Swift</i> /XRT
19006.24	5	5991.81 \pm 1307.52	<i>Swift</i> /XRT
19025.24	5	7401.18 \pm 1555.41	<i>Swift</i> /XRT
19047.31	5	3625.63 \pm 798.01	<i>Swift</i> /XRT
19087.08	5	3020.72 \pm 683.65	<i>Swift</i> /XRT
19118.47	5	3937.25 \pm 874.15	<i>Swift</i> /XRT
19142.24	5	5029.16 \pm 1133.04	<i>Swift</i> /XRT
19165.68	5	4491.87 \pm 1013.52	<i>Swift</i> /XRT
19192.14	5	5211.54 \pm 1143.78	<i>Swift</i> /XRT
19214.94	5	4812.14 \pm 1051.60	<i>Swift</i> /XRT
19237.39	5	5697.96 \pm 1277.93	<i>Swift</i> /XRT
19256.73	5	7961.20 \pm 1749.76	<i>Swift</i> /XRT
19272.50	5	5638.36 \pm 1272.21	<i>Swift</i> /XRT
19293.93	5	5579.74 \pm 1251.42	<i>Swift</i> /XRT
19322.14	5	3230.47 \pm 728.91	<i>Swift</i> /XRT
19349.97	5	4566.75 \pm 1027.31	<i>Swift</i> /XRT
19370.51	5	5921.77 \pm 1295.94	<i>Swift</i> /XRT
19399.15	5	4700.46 \pm 986.54	<i>Swift</i> /XRT
19424.36	5	5378.20 \pm 1180.36	<i>Swift</i> /XRT
19447.64	5	4745.39 \pm 1042.97	<i>Swift</i> /XRT
19475.18	5	5151.66 \pm 999.20	<i>Swift</i> /XRT
63952.95	5	860.52 \pm 194.54	<i>Swift</i> /XRT
64050.11	5	1205.11 \pm 271.63	<i>Swift</i> /XRT
64174.21	5	858.40 \pm 194.26	<i>Swift</i> /XRT
64307.10	5	986.47 \pm 223.91	<i>Swift</i> /XRT
64420.69	5	1103.82 \pm 248.05	<i>Swift</i> /XRT
64518.22	5	1358.75 \pm 305.34	<i>Swift</i> /XRT
64631.67	5	1034.72 \pm 208.10	<i>Swift</i> /XRT
65545.07	5	1693.28 \pm 276.58	<i>Swift</i> /XRT
68969.52	5	757.65 \pm 170.43	<i>Swift</i> /XRT
69043.36	5	1181.81 \pm 265.44	<i>Swift</i> /XRT
69101.65	5	848.46 \pm 191.14	<i>Swift</i> /XRT
69172.24	5	820.53 \pm 185.40	<i>Swift</i> /XRT
69233.35	5	1180.94 \pm 258.80	<i>Swift</i> /XRT
69295.91	5	960.17 \pm 211.92	<i>Swift</i> /XRT

continued ...

... continued

Δt [s]	Energy [keV]	Flux Density [nJy]	Instrument
69346.75	5	1112.56 \pm 249.15	<i>Swift</i> /XRT
69405.29	5	767.24 \pm 174.40	<i>Swift</i> /XRT
69478.13	5	1116.50 \pm 250.03	<i>Swift</i> /XRT
69542.56	5	799.77 \pm 180.71	<i>Swift</i> /XRT
69602.04	5	1168.37 \pm 255.68	<i>Swift</i> /XRT
69651.13	5	1054.54 \pm 237.56	<i>Swift</i> /XRT
69703.17	5	1343.94 \pm 295.36	<i>Swift</i> /XRT
69770.73	5	706.83 \pm 158.52	<i>Swift</i> /XRT
69843.69	5	889.36 \pm 199.75	<i>Swift</i> /XRT
69900.86	5	894.90 \pm 201.60	<i>Swift</i> /XRT
69978.09	5	922.25 \pm 208.07	<i>Swift</i> /XRT
70047.99	5	927.13 \pm 203.47	<i>Swift</i> /XRT
70090.79	5	1319.58 \pm 296.38	<i>Swift</i> /XRT
70146.45	5	864.86 \pm 196.30	<i>Swift</i> /XRT
70206.00	5	1172.24 \pm 263.68	<i>Swift</i> /XRT
70258.03	5	929.44 \pm 208.14	<i>Swift</i> /XRT
70325.35	5	1001.97 \pm 225.38	<i>Swift</i> /XRT
70381.01	5	1090.34 \pm 244.53	<i>Swift</i> /XRT
70438.68	5	1064.93 \pm 238.48	<i>Swift</i> /XRT
70491.90	5	942.47 \pm 207.12	<i>Swift</i> /XRT
116210.71	5	336.62 \pm 75.79	<i>Swift</i> /XRT
116353.13	5	411.23 \pm 92.38	<i>Swift</i> /XRT
116452.17	5	525.08 \pm 117.82	<i>Swift</i> /XRT
116545.98	5	530.76 \pm 116.33	<i>Swift</i> /XRT
116644.98	5	436.17 \pm 98.09	<i>Swift</i> /XRT
116780.25	5	347.57 \pm 78.62	<i>Swift</i> /XRT
116906.55	5	463.68 \pm 101.63	<i>Swift</i> /XRT
117017.57	5	445.86 \pm 100.39	<i>Swift</i> /XRT
117159.95	5	492.46 \pm 79.18	<i>Swift</i> /XRT
120633.16	5	405.37 \pm 91.94	<i>Swift</i> /XRT
120710.13	5	443.52 \pm 99.17	<i>Swift</i> /XRT
120826.72	5	485.44 \pm 109.43	<i>Swift</i> /XRT
120966.67	5	391.75 \pm 86.06	<i>Swift</i> /XRT
121098.46	5	522.40 \pm 87.35	<i>Swift</i> /XRT
121398.46	5	749.13 \pm 167.90	<i>Swift</i> /XRT
121537.01	5	458.00 \pm 103.13	<i>Swift</i> /XRT
121643.33	5	484.16 \pm 108.64	<i>Swift</i> /XRT
121740.86	5	309.26 \pm 69.48	<i>Swift</i> /XRT
121872.53	5	309.02 \pm 56.01	<i>Swift</i> /XRT
166457.09	5	230.14 \pm 51.56	<i>Swift</i> /XRT
166558.26	5	499.24 \pm 112.08	<i>Swift</i> /XRT

continued ...

... continued

Δt [s]	Energy [keV]	Flux Density [nJy]	Instrument
166671.34	5	234.35 \pm 52.82	<i>Swift</i> /XRT
166778.53	5	231.42 \pm 51.90	<i>Swift</i> /XRT
166913.04	5	272.85 \pm 61.32	<i>Swift</i> /XRT
167009.33	5	402.86 \pm 90.35	<i>Swift</i> /XRT
167116.76	5	231.14 \pm 52.05	<i>Swift</i> /XRT
167254.87	5	281.14 \pm 60.10	<i>Swift</i> /XRT
172200.31	5	303.34 \pm 68.07	<i>Swift</i> /XRT
172312.26	5	259.13 \pm 58.35	<i>Swift</i> /XRT
172395.50	5	408.06 \pm 91.46	<i>Swift</i> /XRT
172489.02	5	307.88 \pm 69.01	<i>Swift</i> /XRT
172713.79	5	321.67 \pm 73.25	<i>Swift</i> /XRT
172919.35	5	313.39 \pm 52.83	<i>Swift</i> /XRT
177994.28	5	253.50 \pm 56.81	<i>Swift</i> /XRT
178105.86	5	233.91 \pm 52.36	<i>Swift</i> /XRT
178222.07	5	251.77 \pm 56.67	<i>Swift</i> /XRT
178329.76	5	340.57 \pm 76.66	<i>Swift</i> /XRT
178411.40	5	470.47 \pm 102.77	<i>Swift</i> /XRT
178490.23	5	264.70 \pm 59.32	<i>Swift</i> /XRT
178600.05	5	265.00 \pm 59.32	<i>Swift</i> /XRT
178776.80	5	297.49 \pm 67.14	<i>Swift</i> /XRT
179031.56	5	186.95 \pm 42.08	<i>Swift</i> /XRT
179135.24	5	305.64 \pm 68.72	<i>Swift</i> /XRT
179265.11	5	187.21 \pm 42.09	<i>Swift</i> /XRT
179399.88	5	262.44 \pm 59.34	<i>Swift</i> /XRT
179507.57	5	227.11 \pm 51.18	<i>Swift</i> /XRT
179685.59	5	169.62 \pm 38.35	<i>Swift</i> /XRT
179814.97	5	206.62 \pm 46.56	<i>Swift</i> /XRT
179966.41	5	237.93 \pm 52.36	<i>Swift</i> /XRT
180084.75	5	222.65 \pm 50.12	<i>Swift</i> /XRT
180262.13	5	227.51 \pm 37.76	<i>Swift</i> /XRT
183820.01	5	232.69 \pm 52.38	<i>Swift</i> /XRT
183955.03	5	233.14 \pm 52.59	<i>Swift</i> /XRT
184083.41	5	268.62 \pm 60.46	<i>Swift</i> /XRT
184201.25	5	281.84 \pm 63.58	<i>Swift</i> /XRT
184337.49	5	243.67 \pm 42.06	<i>Swift</i> /XRT
230173.32	5	141.56 \pm 32.32	<i>Swift</i> /XRT
230381.31	5	161.31 \pm 36.50	<i>Swift</i> /XRT
230572.36	5	127.86 \pm 28.85	<i>Swift</i> /XRT
230765.93	5	231.07 \pm 52.03	<i>Swift</i> /XRT
230895.31	5	186.21 \pm 41.93	<i>Swift</i> /XRT
231082.61	5	196.39 \pm 44.22	<i>Swift</i> /XRT

continued ...

... continued

Δt [s]	Energy [keV]	Flux Density [nJy]	Instrument
231206.47	5	195.26 \pm 43.96	<i>Swift</i> /XRT
231350.39	5	259.01 \pm 58.03	<i>Swift</i> /XRT
231463.72	5	227.73 \pm 51.12	<i>Swift</i> /XRT
231632.58	5	193.94 \pm 43.54	<i>Swift</i> /XRT
231812.18	5	122.12 \pm 23.36	<i>Swift</i> /XRT
246886.67	5	169.03 \pm 33.64	<i>Swift</i> /XRT
252655.14	5	137.29 \pm 23.37	<i>Swift</i> /XRT
258467.01	5	134.04 \pm 30.20	<i>Swift</i> /XRT
258749.50	5	100.73 \pm 26.30	<i>Swift</i> /XRT
259011.10	5	124.33 \pm 32.52	<i>Swift</i> /XRT
259226.23	5	167.47 \pm 37.76	<i>Swift</i> /XRT
259519.84	5	124.05 \pm 27.99	<i>Swift</i> /XRT
259787.61	5	143.19 \pm 32.22	<i>Swift</i> /XRT
260029.58	5	208.19 \pm 46.78	<i>Swift</i> /XRT
261888.27	5	114.47 \pm 21.53	<i>Swift</i> /XRT
344635.89	5	85.73 \pm 21.70	<i>Swift</i> /XRT
344903.56	5	121.28 \pm 30.67	<i>Swift</i> /XRT
345159.97	5	71.41 \pm 16.65	<i>Swift</i> /XRT
350266.70	5	77.39 \pm 20.22	<i>Swift</i> /XRT
350493.53	5	123.36 \pm 32.14	<i>Swift</i> /XRT
350661.69	5	118.60 \pm 30.84	<i>Swift</i> /XRT
350949.47	5	124.39 \pm 21.86	<i>Swift</i> /XRT
356436.10	5	160.93 \pm 35.35	<i>Swift</i> /XRT
356721.08	5	107.56 \pm 20.87	<i>Swift</i> /XRT
362025.87	5	124.07 \pm 31.22	<i>Swift</i> /XRT
362392.70	5	90.37 \pm 16.90	<i>Swift</i> /XRT
367750.58	5	88.32 \pm 22.94	<i>Swift</i> /XRT
368105.39	5	60.47 \pm 15.28	<i>Swift</i> /XRT
373366.49	5	160.03 \pm 36.00	<i>Swift</i> /XRT
373575.77	5	88.98 \pm 23.21	<i>Swift</i> /XRT
379334.86	5	58.89 \pm 11.23	<i>Swift</i> /XRT
419736.48	5	63.16 \pm 12.35	<i>Swift</i> /XRT
425014.50	5	68.36 \pm 17.75	<i>Swift</i> /XRT
425377.56	5	65.73 \pm 17.14	<i>Swift</i> /XRT
425713.38	5	80.10 \pm 20.86	<i>Swift</i> /XRT
426123.85	5	68.49 \pm 14.10	<i>Swift</i> /XRT
430634.82	5	62.81 \pm 16.41	<i>Swift</i> /XRT
430969.79	5	81.09 \pm 21.06	<i>Swift</i> /XRT
431479.99	5	52.57 \pm 9.86	<i>Swift</i> /XRT
505296.41	5	42.47 \pm 11.10	<i>Swift</i> /XRT
505732.69	5	59.87 \pm 15.58	<i>Swift</i> /XRT

continued ...

... continued

Δt [s]	Energy [keV]	Flux Density [nJy]	Instrument
506213.73	5	80.79 ± 15.44	<i>Swift</i> /XRT
511271.20	5	35.25 ± 9.31	<i>Swift</i> /XRT
511910.72	5	39.96 ± 10.45	<i>Swift</i> /XRT
512331.18	5	64.83 ± 15.88	<i>Swift</i> /XRT
518459.68	5	38.96 ± 10.21	<i>Swift</i> /XRT
522678.09	5	64.95 ± 16.87	<i>Swift</i> /XRT
523273.23	5	49.29 ± 9.42	<i>Swift</i> /XRT
579959.44	5	33.26 ± 8.76	<i>Swift</i> /XRT
580397.90	5	62.94 ± 15.95	<i>Swift</i> /XRT
585625.86	5	39.18 ± 10.28	<i>Swift</i> /XRT
586113.15	5	37.13 ± 9.40	<i>Swift</i> /XRT
591251.30	5	55.03 ± 14.31	<i>Swift</i> /XRT
591892.78	5	28.93 ± 6.78	<i>Swift</i> /XRT
597082.74	5	45.32 ± 11.85	<i>Swift</i> /XRT
597609.60	5	40.43 ± 9.65	<i>Swift</i> /XRT
666160.81	5	32.62 ± 7.47	<i>Swift</i> /XRT
671553.81	5	58.94 ± 15.46	<i>Swift</i> /XRT
672121.31	5	35.27 ± 8.21	<i>Swift</i> /XRT
677429.22	5	35.91 ± 9.42	<i>Swift</i> /XRT
678017.39	5	30.51 ± 7.82	<i>Swift</i> /XRT
683542.55	5	23.04 ± 5.56	<i>Swift</i> /XRT
752124.10	5	39.80 ± 8.66	<i>Swift</i> /XRT
758005.34	5	30.76 ± 6.69	<i>Swift</i> /XRT
763492.49	5	36.45 ± 9.63	<i>Swift</i> /XRT
764266.74	5	36.41 ± 8.72	<i>Swift</i> /XRT
769539.57	5	25.36 ± 5.43	<i>Swift</i> /XRT
835330.48	5	23.00 ± 4.88	<i>Swift</i> /XRT
844041.00	5	34.93 ± 7.11	<i>Swift</i> /XRT
851367.75	5	25.42 ± 4.39	<i>Swift</i> /XRT
1215630.44	5	9.80 ± 1.86	<i>Swift</i> /XRT
1369725.51	5	7.48 ± 1.88	<i>Swift</i> /XRT
1634070.81	5	6.30 ± 1.32	<i>Swift</i> /XRT
2066547.30	5	4.14 ± 1.09	<i>Swift</i> /XRT
2964219.69	5	2.04 ± 0.58	<i>Swift</i> /XRT
3790131.92	5	<2.08	<i>Swift</i> /XRT

Table C.11: Optical data for GRB 180720B. Flux Densities are corrected for host extinction. Times are in reference to the GBM trigger (July 20, 2018 at 14:21:39.65 UTC). Data were collected from the GCN circulars and converted to flux densities by [Fraija et al. \(2019b\)](#).

Δt [day]	Filter	Frequency [$\times 10^{14}$ Hz]	Flux Density [μJy]
0.001	R	4.68	645916.74 ± 28542.68
0.117	R	4.68	1182.41 ± 52.25
0.159	R	4.68	783.52 ± 52.53
0.235	R	4.68	519.10 ± 59.26
0.316	R	4.68	687.09 ± 46.04
0.320	R	4.68	577.94 ± 25.56
0.347	R	4.68	82.55 ± 3.65
0.425	R	4.68	399.92 ± 55.39
0.456	R	4.68	351.21 ± 15.51
0.467	R	4.68	289.09 ± 1.00
0.502	R	4.68	265.09 ± 23.95
0.520	R	4.68	232.82 ± 5.09
0.854	R	4.68	144.53 ± 6.39
1.754	R	4.68	33.89 ± 1.50
1.885	R	4.68	52.22 ± 2.31
2.884	R	4.68	34.59 ± 0.76
3.874	R	4.68	15.87 ± 0.70

Table C.12: Radio data for GRB180720B. Times are in reference to the GBM trigger (July 20, 2018 at 14:21:39.65 UTC).

Δt [day]	Frequency [GHz]	Flux Density [μJy]	Instrument
1.69	15.5	1100 ± 60	AMI-LA
3.66	15.5	580 ± 50	AMI-LA
5.65	15.5	340 ± 40	AMI-LA
6.66	15.5	<220	AMI-LA
9.39	1.4	390 ± 59	GMRT
25.59	15.5	<190	AMI-LA

Bibliography

- Abbott B. P., Abbott R., Abbott T. D., Acernese F., Ackley K., Adams C., Adams T., Addesso P., Adhikari R. X., Adya V. B., et al.* . GW170817: Observation of Gravitational Waves from a Binary Neutron Star Inspiral // . X 2017a. 119, 16. 161101.
- Abbott B. P., Abbott R., Abbott T. D., Acernese F., Ackley K., Adams C., Adams T., Addesso P., Adhikari R. X., Adya V. B., et al.* . Gravitational Waves and Gamma-Rays from a Binary Neutron Star Merger: GW170817 and GRB 170817A // . X 2017b. 848. L13.
- Abbott B. P., Abbott R., Abbott T. D., Acernese F., Ackley K., Adams C., Adams T., Addesso P., Adhikari R. X., Adya V. B., et al.* . Multi-messenger Observations of a Binary Neutron Star Merger // . X 2017c. 848, 2. L12.
- Abdalla H., Adam R., Aharonian F., Ait Benkhali F., Angüner E. O., Arakawa M., Arcaro C., Armand C., Ashkar H., Backes M. et al.* A very-high-energy component deep in the γ -ray burst afterglow // . XI 2019. 575, 7783. 464–467.
- Abramowicz Marek A., Bejger Michał, Wielgus Maciek.* Collisions of Neutron Stars with Primordial Black Holes as Fast Radio Bursts Engines // . Nov 2018. 868. 17.
- Acero F., Ackermann M., Ajello M., Albert A., Atwood W. B., Axelsson M., Baldini L., Ballet J., Barbiellini G., Bastieri D., Belfiore A., Bellazzini R., Bissaldi E., Blandford R. D., Fermi-LAT Collaboration* . Fermi Large Area Telescope Third Source Catalog // . VI 2015. 218. 23.
- Ackermann M., Ajello M., Albert A., Allafort A., Atwood W. B., Axelsson M., Baldini L., Ballet J., Barbiellini G., Bastieri D., Bechtol K., Bellazzini R., Bissaldi E., Blandford R. D., Bloom E. D., et al.* . The Fermi Large Area Telescope on Orbit: Event Classification, Instrument Response Functions, and Calibration // . XI 2012. 203. 4.
- Ackermann M., Ajello M., Albert A., Anderson B., Arimoto M., Atwood W. B., Axelsson M., Baldini L., Ballet J., Barbiellini G., Baring M. G., Bastieri D.,*

Becerra Gonzalez J., Bellazzini R., Bissaldi E., Blandford R. D., Bloom E. D., et al. . Fermi-LAT Observations of the LIGO Event GW150914 // . V 2016. 823. L2.

Aharonian F. A. TeV gamma rays from BL Lac objects due to synchrotron radiation of extremely high energy protons // . XI 2000. 5, 7. 377–395.

Ajello M., Arimoto M., Axelsson M., Baldini L., Barbiellini G., Bastieri D., Bellazzini R., Bhat P. N., Bissaldi E., Blandford R. D., Bonino R., Bonnell J., Bottacini E., Bregeon J., Bruel P., Buehler R., Cameron R. A., Caputo R., Caraveo P. A., Cavazzuti E., Chen S., Cheung C. C., Chiaro G., Ciprini S., Costantin D., Crnogorcevic M., Cutini S., Dainotti M., D’Ammando F., de la Torre Luque P., de Palma F., Desai A., Desiante R., Di Lalla N., Di Venere L., Fana Dirirsa F., Fegan S. J., Franckowiak A., Fukazawa Y., Funk S., Fusco P., Gargano F., Gasparrini D., Giglietto N., Giordano F., Giroletti M., Green D., Grenier I. A., Grove J. E., Guiriec S., Hays E., Hewitt J. W., Horan D., Jóhannesson G., Kocevski D., Kuss M., Latronico L., Li J., Longo F., Loparco F., Lovellette M. N., Lubrano P., Maldera S., Manfreda A., Martí-Devesa G., Mazziotta M. N., Mereu I., Meyer M., Michelson P. F., Mirabal N., Mitthumsiri W., Mizuno T., Monzani M. E., Moretti E., Morselli A., Moskalenko I. V., Negro M., Nuss E., Ohno M., Omodei N., Orienti M., Orlando E., Palatiello M., Paliya V. S., Paneque D., Persic M., Pesce-Rollins M., Petrosian V., Piron F., Poolakkil S., Poon H., Porter T. A., Principe G., Racusin J. L., Rainò S., Rando R., Razzano M., Razaque S., Reimer A., Reimer O., Reposeur T., Ryde F., Serini D., Sgrò C., Siskind E. J., Sonbas E., Spandre G., Spinelli P., Suson D. J., Tajima H., Takahashi M., Tak D., Thayer J. B., Torres D. F., Troja E., Valverde J., Veres P., Vianello G., von Kienlin A., Wood K., Yassine M., Zhu S., Zimmer S. A Decade of Gamma-Ray Bursts Observed by Fermi-LAT: The Second GRB Catalog // . VI 2019a. 878, 1. 52.

Ajello M., Arimoto M., Axelsson M., Baldini L., Barbiellini G., Bastieri D., Bellazzini R., Bhat P. N., Bissaldi E., Blandford R. D., Bonino R., Bonnell J., Bottacini E., Bregeon J., Bruel P., et al. . A Decade of Gamma-Ray Bursts Observed by Fermi-LAT: The Second GRB Catalog // . VI 2019b. 878, 1. 52.

Aleksić J., Ansoldi S., Antonelli L. A., Antoranz P., Babic A., Bangale P., Barceló M., Barrio J. A., Becerra González J., Bednarek W., Bernardini E., Biasuzzi B., Biland A., Bitossi M., Blanch O., Bonnefoy S., Bonnoli G., Borracci F., Bretz T., Carmona E., Carosi A., Cecchi R., Colin P., Colombo E., Contreras J. L., Corti D., Cortina J., Covino S., Da Vela P., Dazzi F., DeAngelis A., De Caneva G., De Lotto B., de Oña Wilhelmi E., Delgado Mendez C., Dettlaff A., Dominis Prester D., Dorner D., Doro M., Einecke S., Eisenacher D., Elsaesser D., Fidalgo D., Fink D., Fonseca M. V., Font L., Frantzen K., Fruck C., Galindo D., García López R. J., Garczarczyk M., Garrido Terrats D., Gaug M., Giavitto G., Godinović N., González Muñoz A., Gozzini S. R., Haberer W., Hadasch D., Hanabata Y., Hayashida M., Herrera J., Hildebrand D., Hose J., Hrupec D., Idec W., Illa

J. M., Kadenius V., Kellermann H., Knoetig M. L., Kodani K., Konno Y., Krause J., Kubo H., Kushida J., La Barbera A., Lelas D., Lemus J. L., Lewandowska N., Lindfors E., Lombardi S., Longo F., López M., López-Coto R., López-Oramas A., Lorca A., Lorenz E., Lozano I., Makariev M., Mallot K., Maneva G., Mankuzhiyil N., Mannheim K., Maraschi L., Marcote B., Mariotti M., Martínez M., Mazin D., Menzel U., Miranda J. M., Mirzoyan R., Moralejo A., Munar-Adrover P., Nakajima D., Negrello M., Neustroev V., Niedzwiecki A., Nilsson K., Nishijima K., Noda K., Orito R., Overkemping A., Paiano S., Palatiello M., Paneque D., Paoletti R., Paredes J. M., Paredes-Fortuny X., Persic M., Poutanen J., Prada Moroni P. G., Prandini E., Puljak I., Reinthal R., Rhode W., Ribó M., Rico J., Rodriguez Garcia J., Rügamer S., Saito T., Saito K., Satalecka K., Scalzotto V., Scapin V., Schultz C., Schlammer J., Schmidl S., Schweizer T., Sillanpää A., Sitarek J., Snidaric I., Sobczynska D., Spanier F., Stamerra A., Steinbring T., Storz J., Strzys M., Takalo L., Takami H., Tavecchio F., Tejedor L. A., Temnikov P., Terzić T., Tescaro D., Teshima M., Thaele J., Tibolla O., Torres D. F., Toyama T., Treves A., Vogler P., Wetteskind H., Will M., Zanin R. The major upgrade of the MAGIC telescopes, Part I: The hardware improvements and the commissioning of the system // *Astroparticle Physics. I* 2016. 72. 61–75.

Alexander K. D., Laskar T., Berger E., Guidorzi C., Dichiara S., Fong W., Gomboc A., Kobayashi S., Kopac D., Mundell C. G., Tanvir N. R., Williams P. K. G. A Reverse Shock and Unusual Radio Properties in GRB 160625B // . Oct 2017. 848, 1. 69.

Alexander K. D., Margutti R., Blanchard P. K., Fong W., Berger E., Hajela A., Eftekhari T., Chornock R., Cowperthwaite P. S., Giannios D., Guidorzi C., Kathirgamaraju A., MacFadyen A., Metzger B. D., Nicholl M., Sironi L., Villar V. A., Williams P. K. G., Xie X., Zrake J. A Decline in the X-Ray through Radio Emission from GW170817 Continues to Support an Off-axis Structured Jet // . VIII 2018. 863, 2. L18.

Aloy M. A., Janka H. T., Müller E. Relativistic outflows from remnants of compact object mergers and their viability for short gamma-ray bursts // . VI 2005. 436, 1. 273–311.

Amati L., Frontera F., Guidorzi C. Extremely energetic Fermi gamma-ray bursts obey spectral energy correlations // . Dec 2009. 508, 1. 173–180.

Arnaud K. A. XSPEC: The First Ten Years // *Astronomical Data Analysis Software and Systems V*. 101. 1996. 17. (Astronomical Society of the Pacific Conference Series).

Atwood W. B., Abdo A. A., Ackermann M., Althouse W., Anderson B., Axelsson M., Baldini L., Ballet J., Band D. L., Barbiellini G., al. et. The Large Area Telescope on the Fermi Gamma-Ray Space Telescope Mission // . VI 2009. 697. 1071–1102.

- Band D., Matteson J., Ford L., Schaefer B., Palmer D., Teegarden B., Cline T., Briggs M., Paciesas W., Pendleton G., Fishman G., Kouveliotou C., Meegan C., Wilson R., Lestrade P.* BATSE Observations of Gamma-Ray Burst Spectra. I. Spectral Diversity // . VIII 1993. 413. 281.
- Barthelmy S. D., Barbier L. M., Cummings J. R., Fenimore E. E., Gehrels N., Hullinger D., Krimm H. A., Markwardt C. B., Palmer D. M., Parsons A., Sato G., Suzuki M., Takahashi T., Tashiro M., Tueller J.* The Burst Alert Telescope (BAT) on the SWIFT Midex Mission // . X 2005. 120. 143–164.
- Barthelmy S. D., Cummings J. R., Krimm H. A., Lien A. Y., Markwardt C. B., Palmer D. M., Sakamoto T., Siegel M. H., Stamatikos M., Ukwatta T. N.* GRB 180720B: Swift-BAT refined analysis. // GRB Coordinates Network. I 2018. 22998. 1.
- Beloborodov Andrei M.* A Flaring Magnetar in FRB 121102? // . VII 2017. 843, 2. L26.
- Beloborodov Andrei M., Hascoët Romain, Vurm Indrek.* On the Origin of GeV Emission in Gamma-Ray Bursts // . VI 2014. 788, 1. 36.
- Bengio Yoshua, Grandvalet Yves.* No Unbiased Estimator of the Variance of K-Fold Cross-Validation // J. Mach. Learn. Res. XII 2004. 5. 1089–1105.
- Beniamini Paz, Giannios Dimitrios, Metzger Brian D.* Constraints on millisecond magnetars as the engines of prompt emission in gamma-ray bursts // . XII 2017. 472, 3. 3058–3073.
- Beniamini Paz, Nakar Ehud.* Observational constraints on the structure of gamma-ray burst jets // . II 2019. 482, 4. 5430–5440.
- Berger E.* Short-Duration Gamma-Ray Bursts // . VIII 2014. 52. 43–105.
- Berger E., Kulkarni S. R., Frail D. A.* A Standard Kinetic Energy Reservoir in Gamma-Ray Burst Afterglows // . VI 2003. 590, 1. 379–385.
- Berger E., Kulkarni S. R., Frail D. A.* The Nonrelativistic Evolution of GRBs 980703 and 970508: Beaming-independent Calorimetry // . IX 2004. 612, 2. 966–973.
- Bhandari Shivani, Sadler Elaine M., Prochaska J. Xavier, Simha Sunil, Ryder Stuart D., Marnoch Lachlan, Bannister Keith W., Macquart Jean-Pierre, Flynn Chris, Shannon Ryan M., Tejos Nicolas, Corro-Guerra Felipe, Day Cherie K., Deller Adam T., Ekers Ron, Lopez Sebastian, Mahony Elizabeth K., Nuñez Consuelo, Phillips Chris.* The Host Galaxies and Progenitors of Fast Radio Bursts Localized with the Australian Square Kilometre Array Pathfinder // . VI 2020. 895, 2. L37.

- Bhattacharya Dipankar.* Flat Spectrum Gamma Ray Burst Afterglows // Bulletin of the Astronomical Society of India. VI 2001. 29. 107–114.
- Bhattacharyya Sudip.* Fast Radio Bursts from neutron stars plunging into black holes // arXiv e-prints. Nov 2017. arXiv:1711.09083.
- Bissaldi E., Connaughton V.* GRB 090902B: Fermi GBM detection of a bright burst. // GRB Coordinates Network. I 2009. 9866. 1.
- Bissaldi E., Racusin J. L.* GRB 180720B : Fermi-LAT detection. // GRB Coordinates Network. I 2018. 22980. 1.
- Blackburn Lindy, Briggs Michael S, Camp Jordan, Christensen Nelson, Connaughton Valerie, Jenke Peter, Remillard Ronald A, Veitch John.* High-energy electromagnetic offline follow-up of LIGO-Virgo gravitational-wave binary coalescence candidate events // The Astrophysical Journal Supplement Series. 2015. 217, 1. 8.
- Blandford R. D., McKee C. F.* Fluid dynamics of relativistic blast waves // Physics of Fluids. VIII 1976. 19. 1130–1138.
- Blandford R. D., Znajek R. L.* Electromagnetic extraction of energy from Kerr black holes. // . V 1977. 179. 433–456.
- Bloom Joshua S., Frail Dale A., Sari Re'em.* The Prompt Energy Release of Gamma-Ray Bursts using a Cosmological k-Correction // . VI 2001. 121, 6. 2879–2888.
- Bochenek Christopher D., Ravi Vikram, Dong Dillon.* Localized Fast Radio Bursts Are Consistent with Magnetar Progenitors Formed in Core-collapse Supernovae // . II 2021. 907, 2. L31.
- Boella G., Butler R. C., Perola G. C., Piro L., Scarsi L., Blecker J. A. M.* BeppoSAX, the wide band mission for X-ray astronomy // . IV 1997. 122. 299–307.
- Bregman J. N.* The Search for the Missing Baryons at Low Redshift // . IX 2007. 45. 221–259.
- Brown T. M., Baliber N., Bianco F. B., Bowman M., Burlson B., Conway P., Crellin M., Depagne É., De Vera J., Dilday B., Dragomir D., Dubberley M., Eastman J. D., Elphick M., Falarski M., Foale S., Ford M., Fulton B. J., Garza J., Gomez E. L., Graham M., Greene R., Haldeman B., Hawkins E., Haworth B., Haynes R., Hidas M., Hjellstrom A. E., Howell D. A., Hygelund J., Lister T. A., Lobdill R., Martinez J., Mullins D. S., Norbury M., Parrent J., Paulson R., Petry D. L., Pickles A., Posner V., Rosing W. E., Ross R., Sand D. J., Saunders E. S., Shobbrook J., Shporer A., Street R. A., Thomas D., Tsapras Y., Tufts J. R., Valenti S., Vander Horst K., Walker Z., White G., Willis M.* Las Cumbres Observatory Global Telescope Network // . IX 2013. 125, 931. 1031.

- Buehler R., Scargle J. D., Blandford R. D., Baldini L., Baring M. G., Belfiore A., Charles E., Chiang J., D'Ammando F., Dermer C. D., Funk S., Grove J. E., Harding A. K., Hays E., Kerr M., Massaro F., Mazziotta M. N., Romani R. W., Saz Parkinson P. M., Tennant A. F., Weisskopf M. C.* Gamma-Ray Activity in the Crab Nebula: The Exceptional Flare of 2011 April // . IV 2012. 749. 26.
- Bühler R., Blandford R.* The surprising Crab pulsar and its nebula: a review // Reports on Progress in Physics. VI 2014. 77, 6. 066901.
- Burns E.* GRB 160625B: Fermi GBM refined analysis. // GRB Coordinates Network. I 2016. 19587. 1.
- Burrows David N., Hill J. E., Nousek J. A., Kennea J. A., Wells A., Osborne J. P., Abbey A. F., Beardmore A., Mukerjee K., Short A. D. T., Chincarini G., Campana S., Citterio O., Moretti A., Pagani C., Tagliaferri G., Giommi P., Capalbi M., Tamburelli F., Angelini L., Cusumano G., Bräuningner H. W., Burkert W., Hartner G. D.* The Swift X-Ray Telescope // . X 2005. 120, 3-4. 165–195.
- Butler Nat, Klein Chris, Fox Ori, Lotkin Gennadiy, Bloom Josh, Prochaska J. Xavier, Ramirez-Ruiz Enrico, de Diego José A., Georgiev Leonid, González Jesús, Lee William H., Richer Michael G., Román Carlos, Watson Alan M., Gehrels Neil, Kuttyrev Alexander, Bernstein Rebecca, Alvarez Luis Carlos, Ceseña Urania, Clark David, Colorado Enrique, Córdova Antolín., Farah Alejandro, García Benjamín., Guisa Gerardo, Herrera Joel, Lazo Francisco, López Eduardo, Luna Esteban, Martínez Benjamín., Murillo Francisco, Murillo José Manuel, Núñez Juan Manuel, Pedrayes M. Herlinda, Quirós Fernando, Ochoa José Luis, Sierra Gerardo, Moseley Harvey, Rapchun David, Robinson Frederick D., Samuel Mathew V., Sparr Leroy M.* First Light with RATIR: An Automated 6-band Optical/NIR Imaging Camera // Ground-based and Airborne Instrumentation for Astronomy IV. 8446. IX 2012. 844610. (Society of Photo-Optical Instrumentation Engineers (SPIE) Conference Series).
- Callister Thomas, Kanner Jonah, Weinstein Alan.* Gravitational-wave Constraints on the Progenitors of Fast Radio Bursts // . VII 2016. 825. L12.
- Cenko S. B., Frail D. A., Harrison F. A., Haislip J. B., Reichart D. E., Butler N. R., Cobb B. E., Cucchiara A., Berger E., Bloom J. S., Chandra P., Fox D. B., Perley D. A., Prochaska J. X., Filippenko A. V., Glazebrook K., Ivarsen K. M., Kasliwal M. M., Kulkarni S. R., LaCluyze A. P., Lopez S., Morgan A. N., Pettini M., Rana V. R.* Afterglow Observations of Fermi Large Area Telescope Gamma-ray Bursts and the Emerging Class of Hyper-energetic Events // . V 2011. 732, 1. 29.
- Cenko S. B., Frail D. A., Harrison F. A., Kulkarni S. R., Nakar E., Chandra P. C., Butler N. R., Fox D. B., Gal-Yam A., Kasliwal M. M., Kelemen J., Moon D. S., Ofek E. O., Price P. A., Rau A., Soderberg A. M., Teplitz H. I., Werner*

- M. W., Bock D. C. J., Bloom J. S., Starr D. A., Filippenko A. V., Chevalier R. A., Gehrels N., Nousek J. N., Piran T.* The Collimation and Energetics of the Brightest Swift Gamma-ray Bursts // . III 2010. 711, 2. 641–654.
- Cenko S. B., Troja E., Tegler S.* GRB 160509A: DCT Imaging / Afterglow Confirmation. // GRB Coordinates Network. I 2016. 19416. 1.
- Champion D. J., Petroff E., Kramer M., Keith M. J., Bailes M., Barr E. D., Bates S. D., Bhat N. D. R., Burgay M., Burke-Spolaor S., Flynn C. M. L., Jameson A., Johnston S., Ng C., Levin L., Possenti A., Stappers B. W., van Straten W., Thornton D., Tiburzi C., Lyne A. G.* Five new fast radio bursts from the HTRU high-latitude survey at Parkes: first evidence for two-component bursts // . VII 2016. 460. L30–L34.
- Chandra P., Frail D. A.* GRB 090902B: VLA radio detection. // GRB Coordinates Network. I 2009. 9889. 1.
- Chandra P., Nayana A. J., Bhattacharya D., Cenko S. B., Corsi A.* GMRT radio detection of GRB 180720B. // GRB Coordinates Network. I 2018. 23073. 1.
- Chatterjee S., Law C. J., Wharton R. S., Burke-Spolaor S., Hessels J. W. T., Bower G. C., Cordes J. M., Tendulkar S. P., Bassa C. G., Demorest P., Butler B. J., Seymour A., Scholz P., Abruzzo M. W., Bogdanov S., Kaspi V. M., Keimpema A., Lazio T. J. W., Marcote B., McLaughlin M. A., Paragi Z., Ransom S. M., Rupen M., Spitler L. G., van Langevelde H. J.* A direct localization of a fast radio burst and its host // . I 2017. 541. 58–61.
- Chatterjee Shami.* Fast radio bursts // Astronomy and Geophysics. II 2021. 62, 1. 1.29–1.35.
- Chawla P., Andersen B. C., Bhardwaj M., Fonseca E., Josephy A., Kaspi V. M., Michilli D., Pleunis Z., Bandura K. M., Bassa C. G., Boyle P. J., Brar C., Cassanelli T., Cubranic D., Dobbs M., Dong F. Q., Gaensler B. M., Good D. C., Hessels J. W. T., Landecker T. L., Leung C., Li D. Z., Lin H. . H., Masui K., Mckinven R., Mena-Parra J., Merryfield M., Meyers B. W., Naidu A., Ng C., Patel C., Rafiei-Ravandi M., Rahman M., Sanghavi P., Scholz P., Shin K., Smith K. M., Stairs I. H., Tendulkar S. P., Vanderlinde K.* Detection of Repeating FRB 180916.J0158+65 Down to Frequencies of 300 MHz // . VI 2020. 896, 2. L41.
- Cherenkov Telescope Array Consortium , Acharya B. S., Agudo I., Al Samarai I., Alfaro R., Alfaro J., Alispach C., Alves Batista R., Amans J. P., Amato E., Ambrosi G., Antolini E., Antonelli L. A., et al. .* Science with the Cherenkov Telescope Array. 2019.
- Cherry M. L., Yoshida A., Sakamoto T., Sugita S., Kawakubo Y., Tezuka A., Matsukawa S., Onozawa H., Ito T., Morita H., Sone Y., Yamaoka K., Nakahira S., Takahashi I., Asaoka Y., Ozawa S., Torii S., Shimizu Y., Tamura T., Ishizaki W., Ricciarini S., Penacchioni A. V., Marrocchesi P. S.* GRB 180720B: CALET

- Gamma-Ray Burst Monitor detection. // GRB Coordinates Network. I 2018. 23042. 1.
- Connaughton V., Briggs M. S., Goldstein A., Meegan C. A., Paciesas W. S., Preece R. D., Wilson-Hodge C. A., Gibby M. H., Greiner J., Gruber D., Jenke P., Kippen R. M., Pelassa V., Xiong S., Yu H.-F., Bhat P. N., Burgess J. M., Byrne D., Fitzpatrick G., Foley S., Giles M. M., Guiriec S., van der Horst A. J., von Kienlin A., McBreen S., McGlynn S., Tierney D., Zhang B.-B.* Localization of Gamma-Ray Bursts Using the Fermi Gamma-Ray Burst Monitor // . II 2015. 216. 32.
- Cordes J. M., Lazio T. J. W.* NE2001.I. A New Model for the Galactic Distribution of Free Electrons and its Fluctuations // ArXiv Astrophysics e-prints. VII 2002.
- Cordes J. M., Wasserman I.* Supergiant pulses from extragalactic neutron stars // . III 2016. 457. 232–257.
- Costa E., Frontera F., Heise J., Feroci M., in't Zand J., Fiore F., Cinti M. N., Dal Fiume D., Nicastro L., Orlandini M., Palazzi E., Rapisarda# M., Zavattini G., Jager R., Parmar A., Owens A., Molendi S., Cusumano G., Maccarone M. C., Giarrusso S., Coletta A., Antonelli L. A., Giommi P., Muller J. M., Piro L., Butler R. C.* Discovery of an X-ray afterglow associated with the γ -ray burst of 28 February 1997 // . VI 1997. 387, 6635. 783–785.
- Coughlin Eric R., Begelman Mitchell C.* Structured, relativistic jets driven by radiation // . XII 2020. 499, 3. 3158–3177.
- Cucchiara A., Fox D. B., Tanvir N., Berger E.* GRB 090902B: Gemini-N absorption redshift. // GRB Coordinates Network. I 2009. 9873. 1.
- Cunningham Virginia, Cenko S. Bradley, Burns Eric, Goldstein Adam, Lien Amy, Kocevski Daniel, Briggs Michael, Connaughton Valerie, Miller M. Coleman, Racusin Judith, Stanbro Matthew.* A Search for High-energy Counterparts to Fast Radio Bursts // . VII 2019. 879, 1. 40.
- Cunningham Virginia, Cenko S. Bradley, Ryan Geoffrey, Vogel Stuart N., Corsi Alessandra, Cucchiara Antonino, Fruchter Andrew S., Horesh Assaf, Kangas Thomas, Kocevski Daniel, Perley Daniel A., Racusin Judith.* GRB 160625B: Evidence for a Gaussian-shaped Jet // . XII 2020. 904, 2. 166.
- D'Avanzo P.* Short gamma-ray bursts: A review // Journal of High Energy Astrophysics. IX 2015. 7. 73–80.
- DeLaunay J. J., Fox D. B., Murase K., Mészáros P., Keivani A., Messick C., Mostafá M. A., Oikonomou F., Tešić G., Turley C. F.* Discovery of a Transient Gamma-Ray Counterpart to FRB 131104 // . XI 2016. 832. L1.
- Dirrsa F., Vianello G., Racusin J., Axelsson M.* GRB 160625B: Fermi-LAT refined analysis. // GRB Coordinates Network. I 2016. 19586. 1.

- Dokuchaev V. I., Eroshenko Y. N.* Recurrent fast radio bursts from collisions of neutron stars in the evolved stellar clusters // ArXiv e-prints. I 2017.
- Duan Ming-Ya, Wang Xiang-Gao.* Origin for the Prompt Spectral Evolution Characteristics and High Energy Emission during the X-Ray Flare in GRB 180720B // . X 2019. 884, 1. 61.
- Duffell Paul C., MacFadyen Andrew I.* A “Boosted Fireball” Model for Structured Relativistic Jets // . X 2013a. 776, 1. L9.
- Duffell Paul C., MacFadyen Andrew I.* Rayleigh-Taylor Instability in a Relativistic Fireball on a Moving Computational Grid // . X 2013b. 775, 2. 87.
- Duncan Robert C., Thompson Christopher.* Formation of Very Strongly Magnetized Neutron Stars: Implications for Gamma-Ray Bursts // . VI 1992. 392. L9.
- Eichler David, Waxman Eli.* The Efficiency of Electron Acceleration in Collisionless Shocks and Gamma-Ray Burst Energetics // . VII 2005. 627, 2. 861–867.
- Evans P. A.* GRB 160625B: Tiled Swift observations. // GRB Coordinates Network. I 2016. 19582. 1.
- Evans P. A., Beardmore A. P., Page K. L., Osborne J. P., O’Brien P. T., Willingale R., Starling R. L. C., Burrows D. N., Godet O., Vetere L., Racusin J., Goad M. R., Wiersema K., Angelini L., Capalbi M., Chincarini G., Gehrels N., Kennea J. A., Margutti R., Morris D. C., Mountford C. J., Pagani C., Perri M., Romano P., Tanvir N.* Methods and results of an automatic analysis of a complete sample of Swift-XRT observations of GRBs // . VIII 2009. 397, 3. 1177–1201.
- Evans P. A., Beardmore A. P., Page K. L., Tyler L. G., Osborne J. P., Goad M. R., O’Brien P. T., Vetere L., Racusin J., Morris D., Burrows D. N., Capalbi M., Perri M., Gehrels N., Romano P.* An online repository of Swift/XRT light curves of γ -ray bursts // . VII 2007. 469, 1. 379–385.
- Falcke Heino, Rezzolla Luciano.* Fast radio bursts: the last sign of supramassive neutron stars // . Feb 2014. 562. A137.
- Fenimore E. E., Ramirez-Ruiz E.* Redshifts For 220 BATSE Gamma-Ray Bursts Determined by Variability and the Cosmological Consequences // arXiv e-prints. IV 2000. astro-ph/0004176.
- Fitzpatrick Edward L.* Correcting for the Effects of Interstellar Extinction // . I 1999. 111, 755. 63–75.
- Fong W., Blanchard P. K., Alexander K. D., Strader J., Margutti R., Hajela A., Villar V. A., Wu Y., Ye C. S., Berger E., Chornock R., Coppejans D., Cowperthwaite P. S., Eftekhari T., Giannios D., Guidorzi C., Kathirgamaraju A., Laskar T., Macfadyen A., Metzger B. D., Nicholl M., Paterson K., Terreran G., Sand D. J., Sironi L., Williams P. K. G., Xie X., Zrake J.* The Optical Afterglow

of GW170817: An Off-axis Structured Jet and Deep Constraints on a Globular Cluster Origin // . IX 2019. 883, 1. L1.

Fonseca E., Andersen B. C., Bhardwaj M., Chawla P., Good D. C., Josephy A., Kaspi V. M., Masui K. W., Mckinven R., Michilli D., Pleunis Z., Shin K., Tendulkar S. P., Bandura K. M., Boyle P. J., Brar C., Cassanelli T., Cubranic D., Dobbs M., Dong F. Q., Gaensler B. M., Hinshaw G., Landecker T. L., Leung C., Li D. Z., Lin H. H., Mena-Parra J., Merryfield M., Naidu A., Ng C., Patel C., Pen U., Rafiei-Ravandi M., Rahman M., Ransom S. M., Scholz P., Smith K. M., Stairs I. H., Vanderlinde K., Yadav P., Zwaniga A. V. Nine New Repeating Fast Radio Burst Sources from CHIME/FRB // . III 2020. 891, 1. L6.

Foreman-Mackey Daniel, Hogg David W., Lang Dustin, Goodman Jonathan. emcee: The MCMC Hammer // . III 2013. 125, 925. 306.

Fraija N., Barniol Duran R., Dichiara S., Beniamini P. Synchrotron Self-Compton as a Likely Mechanism of Photons beyond the Synchrotron Limit in GRB 190114C // . X 2019a. 883, 2. 162.

Fraija N., Dichiara S., Pedreira A. C. Caligula do E. S., Galvan-Gamez A., Becerra R. L., Montalvo A., Montero J., Betancourt Kamenetskaia B., Zhang B. B. Modeling the Observations of GRB 180720B: from Radio to Sub-TeV Gamma-Rays // . XI 2019b. 885, 1. 29.

Fraija N., Laskar T., Dichiara S., Beniamini P., Duran R. Barniol, Dainotti M. G., Becerra R. L. GRB Fermi-LAT Afterglows: Explaining Flares, Breaks, and Energetic Photons // . XII 2020. 905, 2. 112.

Frail D. A., Kulkarni S. R., Sari R., Djorgovski S. G., Bloom J. S., Galama T. J., Reichart D. E., Berger E., Harrison F. A., Price P. A., Yost S. A., Diercks A., Goodrich R. W., Chaffee F. Beaming in Gamma-Ray Bursts: Evidence for a Standard Energy Reservoir // . Nov 2001. 562, 1. L55–L58.

Frail D. A., Waxman E., Kulkarni S. R. A 450 Day Light Curve of the Radio Afterglow of GRB 970508: Fireball Calorimetry // . VII 2000. 537, 1. 191–204.

Frederiks D., Golenetskii S., Aptekar R., Kozlova A., Lysenko A., Svinkin D., Tsvetkova A., Ulanov M., Cline T. Konus-Wind observation of GRB 180720B. // GRB Coordinates Network. I 2018. 23011. 1.

Frederiks D., Golenetskii S., Aptekar R., Oleynik P., Ulanov M., Svinkin D., Tsvetkova A., Lysenko A., Kozlova A., Cline T. Konus-Wind observation of GRB 160509A. // GRB Coordinates Network. I 2016. 19417. 1.

Frontera Filippo. The key role of BeppoSAX in the GRB history // Rendiconti Lincei. Scienze Fisiche e Naturali. II 2019.

Gajjar V., Siemion A. P. V., Price D. C., Law C. J., Michilli D., Hessels J. W. T., Chatterjee S., Archibald A. M., Bower G. C., Brinkman C., Burke-Spolaor S., Cordes J. M., Croft S., Enriquez J. Emilio, Foster G., Gizani N., Hellbourg G., Isaacson H., Kaspi V. M., Lazio T. J. W., Lebofsky M., Lynch R. S., MacMahon D., McLaughlin M. A., Ransom S. M., Scholz P., Seymour A., Spitler L. G., Tendulkar S. P., Werthimer D., Zhang Y. G. Highest Frequency Detection of FRB 121102 at 4-8 GHz Using the Breakthrough Listen Digital Backend at the Green Bank Telescope // . VIII 2018. 863, 1. 2.

Galama T. J., Vreeswijk P. M., van Paradijs J., Kouveliotou C., Augusteijn T., Böhnhardt H., Brewer J. P., Doublie V., Gonzalez J. F., Leibundgut B., Lidman C., Hainaut O. R., Patat F., Heise J., in't Zand J., Hurley K., Groot P. J., Strom R. G., Mazzali P. A., Iwamoto K., Nomoto K., Umeda H., Nakamura T., Young T. R., Suzuki T., Shigeyama T., Koshut T., Kippen M., Robinson C., de Wildt P., Wijers R. A. M. J., Tanvir N., Greiner J., Pian E., Palazzi E., Frontera F., Masetti N., Nicastro L., Feroci M., Costa E., Piro L., Peterson B. A., Tinney C., Boyle B., Cannon R., Stathakis R., Sadler E., Begam M. C., Ianna P. An unusual supernova in the error box of the γ -ray burst of 25 April 1998 // . X 1998. 395, 6703. 670–672.

Gao He, Mészáros Peter. Reverse Shock Emission in Gamma-Ray Bursts Revisited // Advances in Astronomy. I 2015. 2015. 192383.

Gardner Jonathan P., Mather John C., Clampin Mark, Doyon Rene, Greenhouse Matthew A., Hammel Heidi B., Hutchings John B., Jakobsen Peter, Lilly Simon J., Long Knox S., Lunine Jonathan I., McCaughrean Mark J., Mountain Matt, Nella John, Rieke George H., Rieke Marcia J., Rix Hans-Walter, Smith Eric P., Sonneborn George, Stiavelli Massimo, Stockman H. S., Windhorst Rogier A., Wright Gillian S. The James Webb Space Telescope // . IV 2006. 123, 4. 485–606.

Gehrels N., Chincarini G., Giommi P., Mason K. O., Nousek J. A., Wells A. A., White N. E., Barthelmy S. D., Burrows D. N., Cominsky L. R., Hurley K. C., Marshall F. E., Mészáros P., Roming P. W. A., Angelini L., Barbier L. M., Belloni T., Campana S., Caraveo P. A., Chester M. M., Citterio O., Cline T. L., Cropper M. S., Cummings J. R., Dean A. J., Feigelson E. D., Fenimore E. E., Frail D. A., Fruchter A. S., Garmire G. P., Gendreau K., Ghisellini G., Greiner J., Hill J. E., Hunsberger S. D., Krimm H. A., Kulkarni S. R., Kumar P., Lebrun F., Lloyd-Ronning N. M., Markwardt C. B., Mattson B. J., Mushotzky R. F., Norris J. P., Osborne J., Paczynski B., Palmer D. M., Park H. S., Parsons A. M., Paul J., Rees M. J., Reynolds C. S., Rhoads J. E., Sasseen T. P., Schaefer B. E., Short A. T., Smale A. P., Smith I. A., Stella L., Tagliaferri G., Takahashi T., Tashiro M., Townsley L. K., Tueller J., Turner M. J. L., Vietri M., Voges W., Ward M. J., Willingale R., Zerbi F. M., Zhang W. W. The Swift Gamma-Ray Burst Mission // . VIII 2004. 611. 1005–1020.

- Gelman Andrew, Hwang Jessica, Vehtari Aki.* Understanding predictive information criteria for Bayesian models // arXiv e-prints. VII 2013. arXiv:1307.5928.
- Goldstein A., Burns E., Hamburg R., Connaughton V., Veres P., Briggs M. S., Hui C. M., The GBM-LIGO Collaboration .* Updates to the Fermi-GBM Short GRB Targeted Offline Search in Preparation for LIGO’s Second Observing Run // ArXiv e-prints. XII 2016a.
- Goldstein Adam, Connaughton Valerie, Briggs Michael S., Burns Eric.* Estimating Long GRB Jet Opening Angles and Rest-frame Energetics // . II 2016b. 818, 1. 18.
- Goodman J.* Are gamma-ray bursts optically thick? // . IX 1986. 308. L47.
- Goodman Jonathan, Weare Jonathan.* Ensemble samplers with affine invariance // Communications in Applied Mathematics and Computational Science. I 2010. 5, 1. 65–80.
- Granot Jonathan, Sari Re’em.* The Shape of Spectral Breaks in Gamma-Ray Burst Afterglows // . IV 2002. 568, 2. 820–829.
- Gu Wei-Min, Dong Yi-Ze, Liu Tong, Ma Renyi, Wang Junfeng.* A Neutron Star-White Dwarf Binary Model for Repeating Fast Radio Burst 121102 // . Jun 2016. 823. L28.
- Guidorzi C., Tanvir N. R., Cano Z., Steele I. A., Melandri A., Bersier D., Kobayashi S., Mottram C. J., Mundell C. G., Smith R. J., Gomboc A., O’Brien P.* GRB 090902B: Faulkes telescope north observations. // GRB Coordinates Network. I 2009. 9875. 1.
- Guiriec S., Kouveliotou C., Daigne F., Zhang B., Hascoët R., Nemmen R. S., Thompson D. J., Bhat P. N., Gehrels N., Gonzalez M. M., Kaneko Y., McEnery J., Mochkovitch R., Racusin J. L., Ryde F., Sacahui J. R., Ünsal A. M.* Toward a Better Understanding of the GRB Phenomenon: a New Model for GRB Prompt Emission and its Effects on the New L_i^{NT} - $E_{peak,i}^{rest,NT}$ Relation // . VII 2015. 807, 2. 148.
- Hallinan Gregg, Ravi V., Weinreb S., Kocz J., Huang Y., Woody D. P., Lamb J., D’Addario L., Catha M., Law C., Kulkarni S. R., Phinney E. S., Eastwood M. W., Bouman K., McLaughlin M., Ransom S., Siemens X., Cordes J., Lynch R., Kaplan D., Brazier A., Bhatnagar S., Myers S., Walter F., Gaensler B.* The DSA-2000 — A Radio Survey Camera // Bulletin of the American Astronomical Society. 51. IX 2019. 255.
- Hankins T. H., Eilek J. A.* Radio Emission Signatures in the Crab Pulsar // . XI 2007. 670. 693–701.

- Hashimoto Tetsuya, Goto Tomotsugu, On Alvina Y. L., Lu Ting-Yi, Santos Daryl Joe D., Ho Simon C. C., Wang Ting-Wen, Kim Seong Jin, Hsiao Tiger Y. Y. Fast radio bursts to be detected with the Square Kilometre Array // . VIII 2020. 497, 4. 4107–4116.
- Heintz Kasper E., Prochaska J. Xavier, Simha Sunil, Platts Emma, Fong Wen-fai, Tejos Nicolas, Ryder Stuart D., Aggerwal Kshitij, Bhandari Shivani, Day Cherie K., Deller Adam T., Kilpatrick Charles D., Law Casey J., Macquart Jean-Pierre, Mannings Alexandra, Marnoch Lachlan J., Sadler Elaine M., Shannon Ryan M. Host Galaxy Properties and Offset Distributions of Fast Radio Bursts: Implications for Their Progenitors // . XI 2020. 903, 2. 152.
- Hickish Jack, Razavi-Ghods Nima, Perrott Yvette C., Titterington David J., Carey Steve H., Scott Paul F., Grainge Keith J. B., Scaife Anna M. M., Alexander Paul, Saunders Richard D. E., Crofts Mike, Javid Kamran, Rumsey Clare, Jin Terry Z., Ely John A., Shaw Clive, Northrop Ian G., Pooley Guy, D’Alessandro Robert, Doherty Peter, Willatt Greg P. A digital correlator upgrade for the Arcminute MicroKelvin Imager // . IV 2018. 475, 4. 5677–5687.
- Hoischen C., Balzer A., Bissaldi E., Füßling M., Garrigoux T., Gottschall D., Holler M., Mitchell A., O’Brien P., Parsons R., Pühlhofer G., Rowell G., Schüssler F., Tam P. H. T., Wagner S., H. E. S. S. Collaboration . GRB Observations with H.E.S.S. II // 35th International Cosmic Ray Conference (ICRC2017). 301. I 2017. 636. (International Cosmic Ray Conference).
- Hurley K., Boggs S. E., Smith D. M., Duncan R. C., Lin R., Zoglauer A., Krucker S., Hurford G., Hudson H., Wigger C., Hajdas W., Thompson C., Mitrofanov I., Sanin A., Boynton W., Fellows C., von Kienlin A., Lichti G., Rau A., Cline T. An exceptionally bright flare from SGR 1806-20 and the origins of short-duration γ -ray bursts // . IV 2005. 434. 1098–1103.
- Hurley K., Cline T., Mazets E., Barthelmy S., Butterworth P., Marshall F., Palmer D., Aptekar R., Golenetskii S., Il’Inskii V., Frederiks D., McTiernan J., Gold R., Trombka J. A giant periodic flare from the soft γ -ray repeater SGR1900+14 // . I 1999. 397. 41–43.
- Ivezić Željko, Kahn Steven M., Tyson J. Anthony, Abel Bob, Acosta Emily, Allsman Robyn, Alonso David, AlSayyad Yusra, Anderson Scott F., Andrew John, Angel James Roger P., Angeli George Z., Ansari Reza, Antilogus Pierre, Araujo Constanza, Armstrong Robert, Arndt Kirk T., Astier Pierre, Aubourg Éric, Auza Nicole, Axelrod Tim S., Bard Deborah J., Barr Jeff D., Barrau Aurelian, Bartlett James G., Bauer Amanda E., Bauman Brian J., Baumont Sylvain, Bechtol Ellen, Bechtol Keith, Becker Andrew C., Becla Jacek, Beldica Cristina, Bellavia Steve, Bianco Federica B., Biswas Rahul, Blanc Guillaume, Blazek Jonathan, Blandford Roger D., Bloom Josh S., Bogart Joanne, Bond Tim W., Booth Michael T., Borgland Anders W., Borne Kirk, Bosch James F., Boutigny Dominique, Brackett

Craig A., Bradshaw Andrew, Brandt William Nielsen, Brown Michael E., Bullock James S., Burchat Patricia, Burke David L., Cagnoli Gianpietro, Calabrese Daniel, Callahan Shawn, Callen Alice L., Carlin Jeffrey L., Carlson Erin L., Chandrasekharan Srinivasan, Charles-Emerson Glenaver, Chesley Steve, Cheu Elliott C., Chiang Hsin-Fang, Chiang James, Chirino Carol, Chow Derek, Ciardi David R., Claver Charles F., Cohen-Tanugi Johann, Cockrum Joseph J., Coles Rebecca, Connolly Andrew J., Cook Kem H., Cooray Asantha, Covey Kevin R., Cribbs Chris, Cui Wei, Cutri Roc, Daly Philip N., Daniel Scott F., Daruich Felipe, Daubard Guillaume, Daues Greg, Dawson William, Delgado Francisco, Dellapenna Alfred, de Peyster Robert, de Val-Borro Miguel, Digel Seth W., Doherty Peter, Dubois Richard, Dubois-Felsmann Gregory P., Durech Josef, Economou Frossie, Eifler Tim, Eracleous Michael, Emmons Benjamin L., Fausti Neto Angelo, Ferguson Henry, Figueroa Enrique, Fisher-Levine Merlin, Focke Warren, Foss Michael D., Frank James, Freemon Michael D., Gangler Emmanuel, Gawiser Eric, Geary John C., Gee Perry, Geha Marla, Gessner Charles J. B., Gibson Robert R., Gilmore D. Kirk, Glanzman Thomas, Glick William, Goldina Tatiana, Goldstein Daniel A., Goodenow Iain, Graham Melissa L., Gressler William J., Gris Philippe, Guy Leanne P., Guyonnet Augustin, Haller Gunther, Harris Ron, Hascall Patrick A., Haupt Justine, Hernandez Fabio, Herrmann Sven, Hileman Edward, Hoblitt Joshua, Hodgson John A., Hogan Craig, Howard James D., Huang Dajun, Huffer Michael E., Ingraham Patrick, Innes Walter R., Jacoby Suzanne H., Jain Bhuvnesh, Jammes Fabrice, Jee M. James, Jenness Tim, Jernigan Garrett, Jevremović Darko, Johns Kenneth, Johnson Anthony S., Johnson Margaret W. G., Jones R. Lynne, Juramy-Gilles Claire, Jurić Mario, Kalirai Jason S., Kallivayalil Nitya J., Kalmbach Bryce, Kantor Jeffrey P., Karst Pierre, Kasliwal Mansi M., Kelly Heather, Kessler Richard, Kinnison Veronica, Kirkby David, Knox Lloyd, Kotov Ivan V., Krabbendam Victor L., Krughoff K. Simon, Kubánek Petr, Kuczewski John, Kulkarni Shri, Ku John, Kurita Nadine R., Lage Craig S., Lambert Ron, Lange Travis, Langton J. Brian, Le Guillou Laurent, Levine Deborah, Liang Ming, Lim Kian-Tat, Lintott Chris J., Long Kevin E., Lopez Margaux, Lotz Paul J., Lupton Robert H., Lust Nate B., MacArthur Lauren A., Mahabal Ashish, Mandelbaum Rachel, Markiewicz Thomas W., Marsh Darren S., Marshall Philip J., Marshall Stuart, May Morgan, McKercher Robert, McQueen Michelle, Meyers Joshua, Migliore Myriam, Miller Michelle, Mills David J., Miraval Connor, Moeyens Joachim, Moolekamp Fred E., Monet David G., Moniez Marc, Monkewitz Serge, Montgomery Christopher, Morrison Christopher B., Mueller Fritz, Muller Gary P., Muñoz Arancibia Freddy, Neill Douglas R., Newbry Scott P., Nief Jean-Yves, Nomerotski Andrei, Nordby Martin, O'Connor Paul, Oliver John, Olivier Scot S., Olsen Knut, O'Mullane William, Ortiz Sandra, Osier Shawn, Owen Russell E., Pain Reynald, Palecek Paul E., Parejko John K., Parsons James B., Pease Nathan M., Peterson J. Matt, Peterson John R., Petravick Donald L., Libby Petrick M. E., Petry Cathy E., Pierfederici Francesco, Pietrowicz Stephen, Pike Rob, Pinto Philip A., Plante Raymond, Plate Stephen, Plutchak Joel P., Price Paul A., Prouza Michael, Radeka Veljko, Rajagopal Jayadev, Rasmussen Andrew P., Regnault Nicolas,

Reil Kevin A., Reiss David J., Reuter Michael A., Ridgway Stephen T., Riot Vincent J., Ritz Steve, Robinson Sean, Roby William, Roodman Aaron, Rosing Wayne, Roucelle Cecille, Rumore Matthew R., Russo Stefano, Saha Abhijit, Sassolas Benoit, Schalk Terry L., Schellart Pim, Schindler Rafe H., Schmidt Samuel, Schneider Donald P., Schneider Michael D., Schoening William, Schumacher German, Schwamb Megan E., Sebag Jacques, Selvy Brian, Sembroski Glenn H., Seppala Lynn G., Serio Andrew, Serrano Eduardo, Shaw Richard A., Shipsey Ian, Sick Jonathan, Silvestri Nicole, Slater Colin T., Smith J. Allyn, Smith R. Chris, Sobhani Shahram, Soldahl Christine, Storrie-Lombardi Lisa, Stover Edward, Strauss Michael A., Street Rachel A., Stubbs Christopher W., Sullivan Ian S., Sweeney Donald, Swinbank John D., Szalay Alexander, Takacs Peter, Tether Stephen A., Thaler Jon J., Thayer John Gregg, Thomas Sandrine, Thornton Adam J., Thukral Vaikunth, Tice Jeffrey, Trilling David E., Turri Max, Van Berg Richard, Vanden Berk Daniel, Vetter Kurt, Virieux Françoise, Vucina Tomislav, Wahl William, Walkowicz Lucianne, Walsh Brian, Walter Christopher W., Wang Daniel L., Wang Shin-Yawn, Warner Michael, Wiecha Oliver, Willman Beth, Winters Scott E., Wittman David, Wolff Sidney C., Wood-Vasey W. Michael, Wu Xiuqin, Xin Bo, Yoachim Peter, Zhan Hu. LSST: From Science Drivers to Reference Design and Anticipated Data Products // . III 2019. 873, 2. 111.

Iwamoto K., Mazzali P. A., Nomoto K., Umeda H., Nakamura T., Patat F., Danziger I. J., Young T. R., Suzuki T., Shigeyama T., Augsteijn T., Doublier V., Gonzalez J. F., Boehnhardt H., Brewer J., Hainaut O. R., Lidman C., Leibundgut B., Cappellaro E., Turatto M., Galama T. J., Vreeswijk P. M., Kouveliotou C., van Paradijs J., Pian E., Palazzi E., Frontera F. A hypernova model for the supernova associated with the γ -ray burst of 25 April 1998 // . X 1998. 395, 6703. 672–674.

Jacovich Taylor, Beniamini Paz, van der Horst Alexander. Modeling Synchrotron Self-Compton and Klein-Nishina Effects in Gamma-Ray Burst Afterglows // arXiv e-prints. VII 2020. arXiv:2007.04418.

Johnston S., Taylor R., Bailes M., Bartel N., Baugh C., Bietenholz M., Blake C., Braun R., Brown J., Chatterjee S., Darling J., Deller A., Dodson R., Edwards P., Ekers R., Ellingsen S., Feain I., Gaensler B., Haverkorn M., Hobbs G., Hopkins A., Jackson C., James C., Joncas G., Kaspi V., Kilborn V., Koribalski B., Kothes R., Landecker T., Lenc E., Lovell J., Macquart J. P., Manchester R., Matthews D., McClure-Griffiths N., Norris R., Pen U. L., Phillips C., Power C., Protheroe R., Sadler E., Schmidt B., Stairs I., Staveley-Smith L., Stil J., Tingay S., Tzioumis A., Walker M., Wall J., Wolleben M. Science with ASKAP. The Australian square-kilometre-array pathfinder // Experimental Astronomy. XII 2008. 22, 3. 151–273.

Kangas Tuomas, Fruchter Andrew. A sample of GRB radio afterglows inconsistent with the standard jet model // arXiv e-prints. XI 2019. arXiv:1911.01938.

- Kangas Tuomas, Fruchter Andrew S.* The Late-time Radio Behavior of Gamma-ray Burst Afterglows: Testing the Standard Model // . IV 2021. 911, 1. 14.
- Kangas Tuomas, Fruchter Andrew S., Cenko S. Bradley, Corsi Alessandra, de Ugarte Postigo Antonio, Pe'er Asaf, Vogel Stuart N., Cucchiara Antonino, Gompertz Benjamin, Graham John, Levan Andrew, Misra Kuntal, Perley Daniel A., Racusin Judith, Tanvir Nial.* The Late-time Afterglow Evolution of Long Gamma-Ray Bursts GRB 160625B and GRB 160509A // . V 2020. 894, 1. 43.
- Kann D. A.* GRB 160625A - two different events? // GRB Coordinates Network. I 2016. 19579. 1.
- Kathirgamaraju Adithan, Barniol Duran Rodolfo, Giannios Dimitrios.* GRB off-axis afterglows and the emission from the accompanying supernovae // . IX 2016. 461, 2. 1568–1575.
- Katz J. I.* Fast radio bursts // Progress in Particle and Nuclear Physics. Nov 2018. 103. 1–18.
- Keane E. F., Johnston S., Bhandari S., Barr E., Bhat N. D. R., Burgay M., Caleb M., Flynn C., Jameson A., Kramer M., Petroff E., Possenti A., van Straten W., Bailes M., Burke-Spolaor S., Eatough R. P., Stappers B. W., Totani T., Honma M., Furusawa H., Hattori T., Morokuma T., Niino Y., Sugai H., Terai T., Tominaga N., Yamasaki S., Yasuda N., Allen R., Cooke J., Jencson J., Kasliwal M. M., Kaplan D. L., Tingay S. J., Williams A., Wayth R., Chandra P., Perrodin D., Berezhina M., Mickaliger M., Bassa C.* The host galaxy of a fast radio burst // . II 2016. 530. 453–456.
- Keane E. F., Petroff E.* Fast radio bursts: search sensitivities and completeness // . III 2015. 447. 2852–2856.
- Kennea J. A., Roegiers T. G. R., Osborne J. P., Page K. L., Melandri A., D'Avanzo P., D'Elia V., Burrows D. N., McCauley L. M., Pagani C., Evans P. A.* GRB 160509A: Swift-XRT afterglow detection. // GRB Coordinates Network. I 2016. 19408. 1.
- Kennea J. A., Stratta G.* GRB 090902B: Swift/XRT afterglow candidate. // GRB Coordinates Network. I 2009. 9868. 1.
- Kirsten F., Snelders M. P., Jenkins M., Nimmo K., van den Eijnden J., Hessels J. W. T., Gawroński M. P., Yang J.* Detection of two bright radio bursts from magnetar SGR 1935 + 2154 // Nature Astronomy. XI 2020.
- Klebesadel Ray W., Strong Ian B., Olson Roy A.* Observations of Gamma-Ray Bursts of Cosmic Origin // . VI 1973. 182. L85.
- Kobayashi Shiho, Sari Re'em.* Optical Flashes and Radio Flares in Gamma-Ray Burst Afterglow: Numerical Study // . X 2000. 542, 2. 819–828.

- Kocevski Daniel, Butler Nathaniel.* Gamma-Ray Burst Energetics in the Swift Era // . VI 2008. 680, 1. 531–538.
- Koshut T. M., Paciesas W. S., Kouveliotou C., van Paradijs J., Pendleton G. N., Fishman G. J., Meegan C. A.* T_{90} as a Measurement of the Duration of GRBs // American Astronomical Society Meeting Abstracts #186. 186. V 1995. 53.01. (American Astronomical Society Meeting Abstracts).
- Kouveliotou C., Dieters S., Strohmayer T., van Paradijs J., Fishman G. J., Meegan C. A., Hurley K., Kommers J., Smith I., Frail D., Murakami T.* An X-ray pulsar with a superstrong magnetic field in the soft γ -ray repeater SGR1806 - 20 // . V 1998. 393. 235–237.
- Kouveliotou C., Meegan C. A., Fishman G. J., Bhat N. P., Briggs M. S., Koshut T. M., Paciesas W. S., Pendleton G. N.* Identification of two classes of gamma-ray bursts // . VIII 1993. 413. L101–L104.
- Krimm H. A., Holland S. T., Corbet R. H. D., Pearlman A. B., Romano P., Kennea J. A., Bloom J. S., Barthelmy S. D., Baumgartner W. H., Cummings J. R., Gehrels N., Lien A. Y., Markwardt C. B., Palmer D. M., Sakamoto T., Stamatikos M., Ukwatta T. N.* The Swift/BAT Hard X-Ray Transient Monitor // . XI 2013. 209. 14.
- Kudritzki R. P., Pauldrach A., Puls J.* Radiation driven winds of hot luminous stars. II. Wind models for O-stars in the Magellanic clouds. // . II 1987. 173. 293–298.
- Kulkarni S. R.* From gamma-ray bursts to fast radio bursts // Nature Astronomy. X 2018. 2. 832–835.
- Kulkarni S. R., Ofek E. O., Neill J. D.* The Arecibo Fast Radio Burst: Dense Circum-burst Medium // ArXiv e-prints. XI 2015.
- Kumar Pawan, Lu Wenbin, Bhattacharya Mukul.* Fast radio burst source properties and curvature radiation model // . VII 2017. 468, 3. 2726–2739.
- Lamb Gavin P, Kann D. Alexander, Fernández Joseph John, Mandel Ilya, Levan Andrew J., Tanvir Nial R.* GRB jet structure and the jet break // arXiv e-prints. IV 2021. arXiv:2104.11099.
- Lamb Gavin P., Levan Andrew J., Tanvir Nial R.* GRB 170817A as a Refreshed Shock Afterglow viewed off-axis // arXiv e-prints. V 2020. arXiv:2005.12426.
- Laskar T., Berger E., Zauderer B. A., Margutti R., Soderberg A. M., Chakraborti S., Lunnan R., Chornock R., Chandra P., Ray A.* A Reverse Shock in GRB 130427A // . X 2013. 776, 2. 119.

- Laskar Tanmoy, Alexander Kate D., Berger Edo, Fong Wen-fai, Margutti Raffaella, Shivers Isaac, Williams Peter K. G., Kopač Drejc, Kobayashi Shiho, Mundell Carole, Gomboc Andreja, Zheng WeiKang, Menten Karl M., Graham Melissa L., Filippenko Alexei V.* A Reverse Shock in GRB 160509A // . XII 2016a. 833, 1. 88.
- Laskar Tanmoy, Alexander Kate D., Berger Edo, Fong Wen-fai, Margutti Raffaella, Shivers Isaac, Williams Peter K. G., Kopač Drejc, Kobayashi Shiho, Mundell Carole, Gomboc Andreja, Zheng WeiKang, Menten Karl M., Graham Melissa L., Filippenko Alexei V.* A Reverse Shock in GRB 160509A // . XII 2016b. 833, 1. 88.
- Laskar Tanmoy, Berger Edo, Margutti Raffaella, Perley Daniel, Zauderer B. Ashley, Sari Re'em, Fong Wen-fai.* Energy Injection in Gamma-Ray Burst Afterglows // . XI 2015. 814, 1. 1.
- Laskar Tanmoy, Berger Edo, Margutti Raffaella, Zauderer B. Ashley, Williams Peter K. G., Fong Wen-fai, Sari Re'em, Alexander Kate D., Kamble Atish.* A VLA Study of High-redshift GRBs. II. The Complex Radio Afterglow of GRB 140304A: Shell Collisions and Two Reverse Shocks // . VI 2018. 859, 2. 134.
- Laskar Tanmoy, Berger Edo, Tanvir Nial, Zauderer B. Ashley, Margutti Raffaella, Levan Andrew, Perley Daniel, Fong Wen-fai, Wiersema Klaas, Menten Karl, Hrudkova Marie.* GRB 120521C at $z \sim 6$ and the Properties of High-redshift γ -Ray Bursts // . I 2014. 781, 1. 1.
- Laskar Tanmoy, van Eerten Hendrik, Schady Patricia, Mundell C. G., Alexander Kate D., Barniol Duran Rodolfo, Berger Edo, Bolmer J., Chornock Ryan, Coppejans Deanne L., Fong Wen-fai, Gomboc Andreja, Jordana-Mitjans Núria, Kobayashi Shiho, Margutti Raffaella, Menten Karl M., Sari Re'em, Yamazaki Ryo, Lipunov V. M., Gorbousov E., Kornilov V. G., Tyurina N., Zimnukhov D., Podesta R., Levato H., Buckley D. A. H., Tlatov A., Rebolo R., Serra-Ricart M.* A Reverse Shock in GRB 181201A // . X 2019. 884, 2. 121.
- Lazzati Davide, Perna Rosalba, Morsony Brian J., Lopez-Camara Diego, Cantiello Matteo, Ciolfi Riccardo, Giacomazzo Bruno, Workman Jared C.* Late Time Afterglow Observations Reveal a Collimated Relativistic Jet in the Ejecta of the Binary Neutron Star Merger GW170817 // . VI 2018. 120, 24. 241103.
- Lennarz D., Taboada I.* GRB 160509A: non-observation of VHE emission with HAWC. // GRB Coordinates Network. I 2016. 19423. 1.
- Levan A. J., Tanvir N. R., Cenko S. B., Perley D.* GRB 160509A Gemini North candidate afterglow. // GRB Coordinates Network. I 2016. 19410. 1.
- Leventis K., van der Horst A. J., van Eerten H. J., Wijers R. A. M. J.* Applying an accurate spherical model to gamma-ray burst afterglow observations // . V 2013. 431, 2. 1026–1038.

- Li Long-Biao, Huang Yong-Feng, Geng Jin-Jun, Li Bing.* A model of fast radio bursts: collisions between episodic magnetic blobs // *Research in Astronomy and Astrophysics*. Jun 2018. 18. 061.
- Li W., Chornock R., Leaman J., Filippenko A. V., Poznanski D., Wang X., Ganeshalingam M., Mannucci F.* Nearby supernova rates from the Lick Observatory Supernova Search - III. The rate-size relation, and the rates as a function of galaxy Hubble type and colour // *Astronomical Journal*. IV 2011. 412. 1473–1507.
- Li Ye, Zhang Bing.* A Comparative Study of Host Galaxy Properties between Fast Radio Bursts and Stellar Transients // *Chinese Journal of Astronomy*. VIII 2020. 899, 1. L6.
- Lien A., Sakamoto T., Gehrels N., Palmer D. M., Barthelmy S. D., Graziani C., Cannizzo J. K.* Probing the Cosmic Gamma-Ray Burst Rate with Trigger Simulations of the Swift Burst Alert Telescope // *Astronomical Journal*. III 2014. 783. 24.
- Lien Amy, Sakamoto Takanori, Barthelmy Scott D., Baumgartner Wayne H., Cannizzo John K., Chen Kevin, Collins Nicholas R., Cummings Jay R., Gehrels Neil, Krimm Hans A., Markwardt Craig. B., Palmer David M., Stamatikos Michael, Troja Eleonora, Ukwatta T. N.* The Third Swift Burst Alert Telescope Gamma-Ray Burst Catalog // *Astronomical Journal*. IX 2016a. 829, 1. 7.
- Lien Amy, Sakamoto Takanori, Barthelmy Scott D., Baumgartner Wayne H., Cannizzo John K., Chen Kevin, Collins Nicholas R., Cummings Jay R., Gehrels Neil, Krimm Hans A., Markwardt Craig. B., Palmer David M., Stamatikos Michael, Troja Eleonora, Ukwatta T. N.* The Third Swift Burst Alert Telescope Gamma-Ray Burst Catalog // *Astronomical Journal*. IX 2016b. 829, 1. 7.
- Lin Yiqing, Cheng Zaijun, Gan Liangqin.* Revisiting the neutron star-white dwarf binary model of FRB 121102 // *Scientia Sinica Physica, Mechanica & Astronomica*. Feb 2018. 48. 029501.
- Longo F., Bissaldi E., Bregeon J., McEnery J., Ohno M., Zhu S.* GRB 160509A: Fermi-LAT prompt detection of a very bright burst. // *GRB Coordinates Network*. I 2016a. 19403. 1.
- Longo F., Bissaldi E., Vianello G., Moretti E., Omodei N., Bregeon J., Dirirsa F., Yassine M., Kocevski D., Racusin J., McEnery J., Ohno M.* GRB 160509A: Fermi-LAT refined analysis. // *GRB Coordinates Network*. I 2016b. 19413. 1.
- Lorimer D. R., Bailes M., McLaughlin M. A., Narkevic D. J., Crawford F.* A Bright Millisecond Radio Burst of Extragalactic Origin // *Science*. XI 2007. 318. 777.
- Lorimer Duncan R.* A decade of fast radio bursts // *Nature Astronomy*. Oct 2018. 2. 860–864.
- Lu Wenbin, Kumar Pawan.* On the radiation mechanism of repeating fast radio bursts // *Astronomical Journal*. VI 2018. 477, 2. 2470–2493.

- Lu Wenbin, Kumar Pawan, Zhang Bing.* A unified picture of Galactic and cosmological fast radio bursts // . X 2020. 498, 1. 1397–1405.
- Lyubarsky Y.* A model for fast extragalactic radio bursts // . VII 2014. 442. L9–L13.
- Lyutikov M.* Radio Emission from Magnetars // . XI 2002. 580. L65–L68.
- MAGIC Collaboration , Acciari V. A., Ansoldi S., Antonelli L. A., Arbet Engels A., Baack D., Babić A., Banerjee B., Barres de Almeida U., Barrio J. A., et al.* . Teraelectronvolt emission from the γ -ray burst GRB 190114C // . XI 2019. 575, 7783. 455–458.
- MacFadyen A. I., Woosley S. E.* Collapsars: Gamma-Ray Bursts and Explosions in “Failed Supernovae” // . X 1999. 524, 1. 262–289.
- MacLachlan G. A., Shenoy A., Sonbas E., Dhuga K. S., Cobb B. E., Ukwatta T. N., Morris D. C., Eskandarian A., Maximon L. C., Parke W. C.* Minimum variability time-scales of long and short GRBs // . VI 2013. 432, 2. 857–865.
- MacLachlan G. A., Shenoy A., Sonbas E., Dhuga K. S., Eskandarian A., Maximon L. C., Parke W. C.* The minimum variability time-scale and its relation to pulse profiles of Fermi GRBs // . IX 2012. 425, 1. L32–L35.
- Manchester R. N., Hobbs G. B., Teoh A., Hobbs M.* VizieR Online Data Catalog: ATNF Pulsar Catalogue (Manchester+, 2005) // VizieR Online Data Catalog. V 2016. B/psr.
- Maoz D., Loeb A., Shvartzvald Y., Sitek M., Engel M., Kiefer F., Kiraga M., Levi A., Mazeh T., Pawlak M., Rich R. M., Tal-Or L., Wyrzykowski L.* Fast radio bursts: the observational case for a Galactic origin // . XII 2015. 454. 2183–2189.
- Marcote B., Paragi Z., Hessels J. W. T., Keimpema A., van Langevelde H. J., Huang Y., Bassa C. G., Bogdanov S., Bower G. C., Burke-Spolaor S., Butler B. J., Campbell R. M., Chatterjee S., Cordes J. M., Demorest P., Garrett M. A., Ghosh T., Kaspi V. M., Law C. J., Lazio T. J. W., McLaughlin M. A., Ransom S. M., Salter C. J., Scholz P., Seymour A., Siemion A., Spitler L. G., Tendulkar S. P., Wharton R. S.* The Repeating Fast Radio Burst FRB 121102 as Seen on Milliarcsecond Angular Scales // . I 2017. 834. L8.
- Margalit Ben, Metzger Brian D., Sironi Lorenzo.* Constraints on the engines of fast radio bursts // . VI 2020. 494, 4. 4627–4644.
- Margutti R., Alexander K. D., Xie X., Sironi L., Metzger B. D., Kathirgamaraju A., Fong W., Blanchard P. K., Berger E., MacFadyen A., Giannios D., Guidorzi C., Hajela A., Chornock R., Cowperthwaite P. S., Eftekhari T., Nicholl M., Villar V. A., Williams P. K. G., Zrake J.* The Binary Neutron Star Event LIGO/Virgo GW170817 160 Days after Merger: Synchrotron Emission across the Electromagnetic Spectrum // . III 2018. 856, 1. L18.

- Marshall F. E., Roegiers T. G. R.* GRB 160509A: Further Swift/UVOT Observations. // GRB Coordinates Network. I 2016. 19420. 1.
- Mazets E. P., Golentskii S. V., Ilinskii V. N., Aptekar R. L., Guryan I. A.* Observations of a flaring X-ray pulsar in Dorado // . XII 1979. 282. 587–589.
- McBreen S., Krühler T., Rau A., Greiner J., Kann D. A., Savaglio S., Afonso P., Clemens C., Filgas R., Klose S., Küpcü Yoldaş A., Olivares E. F., Rossi A., Szokoly G. P., Updike A., Yoldaş A.* Optical and near-infrared follow-up observations of four Fermi/LAT GRBs: redshifts, afterglows, energetics, and host galaxies // . VI 2010. 516. A71.
- McMullin J. P., Waters B., Schiebel D., Young W., Golap K.* CASA Architecture and Applications // Astronomical Data Analysis Software and Systems XVI. 376. 2007. 127.
- McQuinn M.* Locating the “Missing” Baryons with Extragalactic Dispersion Measure Estimates // . I 2014. 780. L33.
- Meegan C., Lichti G., Bhat P. N., Bissaldi E., Briggs M. S., Connaughton V., Diehl R., Fishman G., Greiner J., Hoover A. S., van der Horst A. J., von Kienlin A., Kippen R. M., Kouveliotou C., McBreen S., Paciesas W. S., Preece R., Steinle H., Wallace M. S., Wilson R. B., Wilson-Hodge C.* The Fermi Gamma-ray Burst Monitor // . IX 2009. 702. 791–804.
- Meegan C. A., Fishman G. J., Wilson R. B., Paciesas W. S., Pendleton G. N., Horack J. M., Brock M. N., Kouveliotou C.* Spatial distribution of γ -ray bursts observed by BATSE // . I 1992. 355, 6356. 143–145.
- Mereghetti S., Savchenko V., Ferrigno C., Götz D., Rigoselli M., Tiengo A., Bazzano A., Bozzo E., Coleiro A., Courvoisier T. J. L., Doyle M., Goldwurm A., Hanlon L., Jourdain E., von Kienlin A., Lutovinov A., Martin-Carrillo A., Molkov S., Natalucci L., Onori F., Panessa F., Rodi J., Rodriguez J., Sánchez-Fernández C., Sunyaev R., Ubertini P.* INTEGRAL Discovery of a Burst with Associated Radio Emission from the Magnetar SGR 1935+2154 // . VIII 2020. 898, 2. L29.
- Mészáros P., Rees M. J.* GRB 990123: reverse and internal shock flashes and late afterglow behaviour // . VII 1999. 306, 3. L39–L43.
- Mészáros P., Rees M. J., Wijers R. A. M. J.* Viewing Angle and Environment Effects in Gamma-Ray Bursts: Sources of Afterglow Diversity // . V 1998. 499, 1. 301–308.
- Metzger B. D., Giannios D., Thompson T. A., Bucciantini N., Quataert E.* The protomagnetar model for gamma-ray bursts // . V 2011. 413, 3. 2031–2056.

- Metzger Brian D., Beniamini Paz, Giannios Dimitrios.* Effects of Fallback Accretion on Protomagnetar Outflows in Gamma-Ray Bursts and Superluminous Supernovae // . IV 2018. 857, 2. 95.
- Metzger Brian D., Berger Edo, Margalit Ben.* Millisecond Magnetar Birth Connects FRB 121102 to Superluminous Supernovae and Long-duration Gamma-Ray Bursts // . V 2017. 841. 14.
- Metzger Brian D., Margalit Ben, Kasen Daniel, Quataert Eliot.* The diversity of transients from magnetar birth in core collapse supernovae // . XII 2015. 454, 3. 3311–3316.
- Metzger Brian D., Margalit Ben, Sironi Lorenzo.* Fast radio bursts as synchrotron maser emission from decelerating relativistic blast waves // . V 2019. 485, 3. 4091–4106.
- Metzger Brian D., Thompson Todd A., Quataert Eliot.* Proto-Neutron Star Winds with Magnetic Fields and Rotation // . IV 2007. 659, 1. 561–579.
- Mickaliger M. B., McLaughlin M. A., Lorimer D. R., Langston G. I., Bilous A. V., Kondratiev V. I., Lyutikov M., Ransom S. M., Palliyaguru N.* A Giant Sample of Giant Pulses from the Crab Pulsar // . XI 2012. 760. 64.
- Mooley K. P., Staley T. D., Fender R. P., Anderson G. E., Cantwell T., Rumsey C., Titterton D., Carey S. H., Hickish J., Perrott Y. C., Razavi-Ghods N., Scott P., Grainge K., Scaife A.* GRB 160509A: 15 GHz upper limits from AMI. // GRB Coordinates Network. I 2016. 19532. 1.
- Morsony Brian J., Lazzati Davide, Begelman Mitchell C.* Temporal and Angular Properties of Gamma-Ray Burst Jets Emerging from Massive Stars // . VIII 2007. 665, 1. 569–598.
- Nakahira S., Yoshida A., Sakamoto T., Kawakubo Y., Moriyama M., Yamada Y., Yamaoka K., Takahashi I., Asaoka Y., Ozawa S., Torii S., Shimizu Y., Tamura T., Ishizaki W., Cherry M. L., Ricciarini S., Marrocchesi P. S.* GRB 160625B CALET Gamma-Ray Burst Monitor detection. // GRB Coordinates Network. I 2016. 19617. 1.
- Negoro H., Tanimoto A., Nakajima M., Maruyama W., Sakamaki A., Mihara T., Nakahira S., Yatabe F., Takao Y., Matsuoka M., Kawai N., Sugizaki M., Tachibana Y., Morita K., Sakamoto T., Serino M., Sugita S., Kawakubo Y., Hashimoto T., Yoshida A., Ueno S., Tomida H., Ishikawa M., Sugawara Y., Isobe N., Shimomukai R., Ueda Y., Morita T., Yamada S., Tsuboi Y., Iwakiri W., Sasaki R., Kawai H., Sato T., Tsunemi H., Yoneyama T., Yamauchi M., Hidaka K., Iwahori S., Kawamuro T., Yamaoka K., Shidatsu M.* GRB 180720B: MAXI/GSC detection. // GRB Coordinates Network. I 2018. 22993. 1.

- Nicholl M., Williams P. K. G., Berger E., Villar V. A., Alexander K. D., Eftekhari T., Metzger B. D.* Empirical Constraints on the Origin of Fast Radio Bursts: Volumetric Rates and Host Galaxy Demographics as a Test of Millisecond Magnetar Connection // . VII 2017. 843. 84.
- Olivares F., Afonso P., Greiner J., McBreen S., Kruehler T., Rau A., Yoldas A., Kanbach G., Kloze S.* GRB 090902B: GROND NIR afterglow observations. // GRB Coordinates Network. I 2009. 9874. 1.
- Paczynski B.* Gamma-ray bursters at cosmological distances // . IX 1986. 308. L43–L46.
- Paczynski Bohdan.* Super-Eddington Winds from Neutron Stars // . XI 1990. 363. 218.
- Palaniswamy Divya, Li Ye, Zhang Bing.* Are There Multiple Populations of Fast Radio Bursts? // . II 2018. 854. L12.
- Palmer D. M., Barthelmy S., Gehrels N., Kippen R. M., Cayton T., Kouveliotou C., Eichler D., Wijers R. A. M. J., Woods P. M., Granot J., Lyubarsky Y. E., Ramirez-Ruiz E., Barbier L., Chester M., Cummings J., Fenimore E. E., Finger M. H., Gaensler B. M., Hullinger D., Krimm H., Markwardt C. B., Nousek J. A., Parsons A., Patel S., Sakamoto T., Sato G., Suzuki M., Tueller J.* A giant γ -ray flare from the magnetar SGR 1806 - 20 // . IV 2005. 434. 1107–1109.
- Panaitescu A.* Jet breaks in the X-ray light-curves of Swift gamma-ray burst afterglows // . IX 2007. 380, 1. 374–380.
- Panaitescu A., Kumar P.* Properties of Relativistic Jets in Gamma-Ray Burst Afterglows // . VI 2002. 571, 2. 779–789.
- Pandey S. B., Swenson C. A., Perley D. A., Guidorzi C., Wiersema K., Malesani D., Akerlof C., Ashley M. C. B., Bersier D., Cano Z., Gomboc A., Ilyin I., Jakobsson P., Kleiser I. K. W., Kobayashi S., Kouveliotou C., Levan A. J., McKay T. A., Melandri A., Mottram C. J., Mundell C. G., O'Brien P. T., Phillips A., Rex J. M., Siegel M. H., Smith R. J., Steele I. A., Stratta G., Tanvir N. R., Weights D., Yost S. A., Yuan F., Zheng W.* GRB 090902B: Afterglow Observations and Implications // . V 2010. 714, 1. 799–804.
- Pandey S. B., Zheng W., Yuan F., Akerlof C.* GRB 090902B: ROTSE-III detection of optical afterglow. // GRB Coordinates Network. I 2009. 9878. 1.
- Pe'er Asaf.* Physics of Gamma-Ray Bursts Prompt Emission // Advances in Astronomy. I 2015. 2015. 907321.
- Pei Yichuan C.* Interstellar Dust from the Milky Way to the Magellanic Clouds // . VIII 1992. 395. 130.

- Pen U.-L., Connor L.* Local Circumnuclear Magnetar Solution to Extragalactic Fast Radio Bursts // . VII 2015. 807. 179.
- Perley D. A., Cenko S. B., Corsi A., Tanvir N. R., Levan A. J., Kann D. A., Sonbas E., Wiersema K., Zheng W., Zhao X. H., Bai J. M., Bremer M., Castro-Tirado A. J., Chang L., Clubb K. I., Frail D., Fruchter A., Göğüş E., Greiner J., Güver T., Horesh A., Filippenko A. V., Klose S., Mao J., Morgan A. N., Pozanenko A. S., Schmidl S., Stecklum B., Tanga M., Volnova A. A., Volvach A. E., Wang J. G., Winters J. M., Xin Y. X.* The Afterglow of GRB 130427A from 1 to 10^{16} GHz // . I 2014. 781, 1. 37.
- Perley D. A., Kleiser I. K. W., Rex J. M.* GRB 090902B: optical afterglow candidate. // GRB Coordinates Network. I 2009. 9870. 1.
- Pescalli A., Ghirlanda G., Salafia O. S., Ghisellini G., Nappo F., Salvaterra R.* Luminosity function and jet structure of Gamma-Ray Burst // . II 2015. 447, 2. 1911–1921.
- Petroff E., Barr E. D., Jameson A., Keane E. F., Bailes M., Kramer M., Morello V., Tabbara D., van Straten W.* FRBCAT: The Fast Radio Burst Catalogue // Publications of the Astronomical Society of Australia. IX 2016. 33. e045.
- Petroff E., Hessels J. W. T., Lorimer D. R.* Fast radio bursts // . V 2019. 27, 1. 4.
- Petroff E., Keane E. F., Barr E. D., Reynolds J. E., Sarkissian J., Edwards P. G., Stevens J., Brem C., Jameson A., Burke-Spolaor S., Johnston S., Bhat N. D. R., Kudale P., Chandra S., Bhandari S.* Identifying the source of perytons at the Parkes radio telescope // . VIII 2015. 451, 4. 3933–3940.
- Piran Tsvi.* Magnetic Fields in Gamma-Ray Bursts: A Short Overview // Magnetic Fields in the Universe: From Laboratory and Stars to Primordial Structures. 784. IX 2005. 164–174. (American Institute of Physics Conference Series).
- Piran Tsvi, Shemi Amotz.* Fireballs in the Galactic Halo and Gamma-Ray Bursts // . II 1993. 403. L67.
- Planck Collaboration , Aghanim N., Akrami Y., Ashdown M., Aumont J., Bacigalupi C., Ballardini M., Banday A. J., Barreiro R. B., Bartolo N., Basak S., Battye R., Benabed K., Bernard J. P., Bersanelli M., Bielewicz P., et al. .* Planck 2018 results. VI. Cosmological parameters // arXiv e-prints. VII 2018. arXiv:1807.06209.
- Platts E., Weltman A., Walters A., Tendulkar S. P., Gordin J. E. B., Kandhai S.* A living theory catalogue for fast radio bursts // . VIII 2019. 821. 1–27.
- Popham Robert, Woosley S. E., Fryer Chris.* Hyperaccreting Black Holes and Gamma-Ray Bursts // . VI 1999. 518, 1. 356–374.

- Popov S. B., Postnov K. A.* Millisecond extragalactic radio bursts as magnetar flares // ArXiv e-prints. VII 2013.
- Racusin J. L., Liang E. W., Burrows D. N., Falcone A., Sakamoto T., Zhang B. B., Zhang B., Evans P., Osborne J.* Jet Breaks and Energetics of Swift Gamma-Ray Burst X-Ray Afterglows // . VI 2009. 698, 1. 43–74.
- Racusin J. L., Oates S. R., Schady P., Burrows D. N., de Pasquale M., Donato D., Gehrels N., Koch S., McEnery J., Piran T., Roming P., Sakamoto T., Swenson C., Troja E., Vasileiou V., Virgili F., Wanderman D., Zhang B.* Fermi and Swift Gamma-ray Burst Afterglow Population Studies // . Sep 2011. 738. 138.
- Readhead Anthony C. S.* Equipartition Brightness Temperature and the Inverse Compton Catastrophe // . V 1994. 426. 51.
- Ressler Sean M., Laskar Tanmoy.* Thermal Electrons in Gamma-Ray Burst Afterglows // . VIII 2017. 845, 2. 150.
- Rhoads James E.* The Dynamics and Light Curves of Beamed Gamma-Ray Burst Afterglows // . Nov 1999. 525, 2. 737–749.
- Rhodes L., van der Horst A. J., Fender R., Monageng I. M., Anderson G. E., Antoniadis J., Bietenholz M. F., Böttcher M., Bright J. S., Green D. A., Kouveliotou C., Kramer M., Motta S. E., Wijers R. A. M. J., Williams D. R. A., Woudt P. A.* Radio afterglows of very high-energy gamma-ray bursts 190829A and 180720B // . VIII 2020. 496, 3. 3326–3335.
- Roberts O. J., Fitzpatrick G., Veres P.* GRB 160509A: Fermi GBM Detection. // GRB Coordinates Network. I 2016. 19411. 1.
- Roberts O. J., Meegan C.* GRB 180720B: Fermi GBM observation. // GRB Coordinates Network. I 2018. 22981. 1.
- Roming Peter W. A., Kennedy Thomas E., Mason Keith O., Nousek John A., Ahr Lindy, Bingham Richard E., Broos Patrick S., Carter Mary J., Hancock Barry K., Huckle Howard E., Hunsberger S. D., Kawakami Hajime, Killough Ronnie, Koch T. Scott, McLelland Michael K., Smith Kelly, Smith Philip J., Soto Juan Carlos, Boyd Patricia T., Breeveld Alice A., Holland Stephen T., Ivanushkina Mariya, Pryzby Michael S., Still Martin D., Stock Joseph.* The Swift Ultra-Violet/Optical Telescope // . X 2005. 120, 3-4. 95–142.
- Ronchi M., Fumagalli F., Ravasio M. E., Oganesyan G., Toffano M., Salafia O. S., Nava L., Ascenzi S., Ghirlanda G., Ghisellini G.* Rise and fall of the high-energy afterglow emission of GRB 180720B // . IV 2020. 636. A55.
- Rossi Elena, Lazzati Davide, Rees Martin J.* Afterglow light curves, viewing angle and the jet structure of γ -ray bursts // . VI 2002. 332, 4. 945–950.

- Rossi Elena M., Lazzati Davide, Salmonson Jay D., Ghisellini Gabriele.* The polarization of afterglow emission reveals γ -ray bursts jet structure // . X 2004. 354, 1. 86–100.
- Ruderman M. A., Sutherland P. G.* Theory of pulsars: polar gaps, sparks, and coherent microwave radiation. // . II 1975. 196. 51–72.
- Ryan Geoffrey, Eerten Hendrik van, Piro Luigi, Troja Eleonora.* Gamma-Ray Burst Afterglows in the Multimessenger Era: Numerical Models and Closure Relations // . VI 2020. 896, 2. 166.
- Ryan Geoffrey, van Eerten Hendrik, MacFadyen Andrew.* Fitting Afterglows With Multi-Dimensional Simulations // arXiv e-prints. VII 2013. arXiv:1307.6334.
- Ryan Geoffrey, van Eerten Hendrik, MacFadyen Andrew, Zhang Bin-Bin.* Gamma-Ray Bursts are Observed Off-axis // . I 2015. 799, 1. 3.
- Sari Re'em.* Beaming and jets in gamma-ray bursts // Gamma-ray Bursts, 5th Huntsville Symposium. 526. IX 2000. 504–513. (American Institute of Physics Conference Series).
- Sari Re'em, Narayan Ramesh, Piran Tsvi.* Cooling Timescales and Temporal Structure of Gamma-Ray Bursts // . XII 1996. 473. 204.
- Sari Re'em, Piran Tsvi.* Predictions for the Very Early Afterglow and the Optical Flash // . VIII 1999. 520, 2. 641–649.
- Sari Re'em, Piran Tsvi, Halpern J. P.* Jets in Gamma-Ray Bursts // . Jul 1999. 519, 1. L17–L20.
- Sari Re'em, Piran Tsvi, Narayan Ramesh.* Spectra and Light Curves of Gamma-Ray Burst Afterglows // . IV 1998. 497, 1. L17–L20.
- Sasada M., Nakaoka T., Kawabata M., Uchida N., Yamazaki Y., Kawabata K. S.* GRB 180720B: Kanata 1.5m optical/NIR observation. // GRB Coordinates Network. I 2018. 22977. 1.
- Savchenko V., Ferrigno C., Panessa F., Bazzano A., Ubertini E., Kuulkers P., Keane E.* INTEGRAL gamma-ray upper limits on FRB180311 // The Astronomer's Telegram. Mar 2018a. 11431. 1.
- Savchenko V., Ferrigno C., Panessa F., Bazzano A., Ubertini P. E. Kuulkers, Keane E.* INTEGRAL gamma-ray upper limits on FRB180309 // The Astronomer's Telegram. Mar 2018b. 11387. 1.
- Savchenko V., Panessa F., Ferrigno C., Keane E., Bazzano A., Burgay M., Kuulkers E., Petroff E., Ubertini P., Diehl R.* INTEGRAL serendipitous upper limits on FRB180301 // The Astronomer's Telegram. Mar 2018c. 11386. 1.

- Schilizzi Richard T., Dewdney Peter E. F., Lazio T. Joseph W.* The square kilometre array // Ground-based and Airborne Telescopes III. 7733. VII 2010. 773318. (Society of Photo-Optical Instrumentation Engineers (SPIE) Conference Series).
- Schlafly Edward F., Finkbeiner Douglas P.* Measuring Reddening with Sloan Digital Sky Survey Stellar Spectra and Recalibrating SFD // . VIII 2011. 737, 2. 103.
- Scholz P., Bogdanov S., Hessels J. W. T., Lynch R. S., Spitler L. G., Bassa C. G., Bower G. C., Burke-Spolaor S., Butler B. J., Chatterjee S., Cordes J. M., Gourdji K., Kaspi V. M., Law C. J., Marcote B., McLaughlin M. A., Michilli D., Paragi Z., Ransom S. M., Seymour A., Tendulkar S. P., Wharton R. S.* Simultaneous X-Ray, Gamma-Ray, and Radio Observations of the Repeating Fast Radio Burst FRB 121102 // . IX 2017a. 846. 80.
- Scholz P., Bogdanov S., Hessels J. W. T., Lynch R. S., Spitler L. G., Bassa C. G., Bower G. C., Burke-Spolaor S., Butler B. J., Chatterjee S., Cordes J. M., Gourdji K., Kaspi V. M., Law C. J., Marcote B., McLaughlin M. A., Michilli D., Paragi Z., Ransom S. M., Seymour A., Tendulkar S. P., Wharton R. S.* Simultaneous X-Ray, Gamma-Ray, and Radio Observations of the Repeating Fast Radio Burst FRB 121102 // . IX 2017b. 846.
- Scholz P., Spitler L. G., Hessels J. W. T., Chatterjee S., Cordes J. M., Kaspi V. M., Wharton R. S., Bassa C. G., Bogdanov S., Camilo F., Crawford F., Deneva J., van Leeuwen J., Lynch R., Madsen E. C., McLaughlin M. A., Mickaliger M., Parent E., Patel C., Ransom S. M., Seymour A., Stairs I. H., Stappers B. W., Tendulkar S. P.* The Repeating Fast Radio Burst FRB 121102: Multi-wavelength Observations and Additional Bursts // . XII 2016. 833. 177.
- Sfaradi I., Bright J., Horesh A., Fender R., Motta S., Titterton D., Perrott Y.* GRB 180720B: AMI-LA 15.5 GHz observation. // GRB Coordinates Network. I 2018. 23037. 1.
- Shahmoradi Amir, Nemiroff Robert J.* Short versus long gamma-ray bursts: a comprehensive study of energetics and prompt gamma-ray correlations // . VII 2015. 451, 1. 126–143.
- Shemi Amotz, Piran Tsvi.* The Appearance of Cosmic Fireballs // . XII 1990. 365. L55.
- Shull J. M., Smith B. D., Danforth C. W.* The Baryon Census in a Multiphase Intergalactic Medium: 30% of the Baryons May Still be Missing // . XI 2012. 759. 23.
- Siegel M. H., Burrows D. N., Deich A., Gropp J. D., Kennea J. A., Laporte S. J., Lien A. Y., Moss M. J., Page K. L., Palmer D. M., Sbarufatti B., Tohuwavohu A.* GRB 180720A: Swift detection of a burst. // GRB Coordinates Network. I 2018. 22973. 1.

- Sironi Lorenzo, Spitkovsky Anatoly.* Particle Acceleration in Relativistic Magnetized Collisionless Electron-Ion Shocks // . I 2011. 726, 2. 75.
- Sironi Lorenzo, Spitkovsky Anatoly, Arons Jonathan.* The Maximum Energy of Accelerated Particles in Relativistic Collisionless Shocks // . VII 2013. 771, 1. 54.
- Sivula Tuomas, Magnusson Måns, Vehtari Aki.* Uncertainty in Bayesian Leave-One-Out Cross-Validation Based Model Comparison // arXiv e-prints. VIII 2020. arXiv:2008.10296.
- Sonbas E., MacLachlan G. A., Shenoy A., Dhuga K. S., Parke W. C.* A New Correlation between GRB X-Ray Flares and the Prompt Emission // . IV 2013. 767, 2. L28.
- Spergel D., Gehrels N., Baltay C., Bennett D., Breckinridge J., Donahue M., Dressler A., Gaudi B. S., Greene T., Guyon O., Hirata C., Kalirai J., Kasdin N. J., Macintosh B., Moos W., Perlmutter S., Postman M., Rauscher B., Rhodes J., Wang Y., Weinberg D., Benford D., Hudson M., Jeong W. S., Mellier Y., Traub W., Yamada T., Capak P., Colbert J., Masters D., Penny M., Savransky D., Stern D., Zimmerman N., Barry R., Bartusek L., Carpenter K., Cheng E., Content D., Dekens F., Demers R., Grady K., Jackson C., Kuan G., Kruk J., Melton M., Nemati B., Parvin B., Poberezhskiy I., Peddie C., Ruffa J., Wallace J. K., Whipple A., Wollack E., Zhao F.* Wide-Field Infrared Survey Telescope-Astrophysics Focused Telescope Assets WFIRST-AFTA 2015 Report // arXiv e-prints. III 2015. arXiv:1503.03757.
- Spitler L. G., Cordes J. M., Hessels J. W. T., Lorimer D. R., McLaughlin M. A., Chatterjee S., Crawford F., Deneva J. S., Kaspi V. M., Wharton R. S., Allen B., Bogdanov S., Brazier A., Camilo F., Freire P. C. C., Jenet F. A., Karako-Argaman C., Knispel B., Lazarus P., Lee K. J., van Leeuwen J., Lynch R., Ransom S. M., Scholz P., Siemens X., Stairs I. H., Stovall K., Swiggum J. K., Venkataraman A., Zhu W. W., Aulbert C., Fehrmann H.* Fast Radio Burst Discovered in the Arecibo Pulsar ALFA Survey // . VIII 2014. 790. 101.
- Spitler L. G., Scholz P., Hessels J. W. T., Bogdanov S., Brazier A., Camilo F., Chatterjee S., Cordes J. M., Crawford F., Deneva J., Ferdman R. D., Freire P. C. C., Kaspi V. M., Lazarus P., Lynch R., Madsen E. C., McLaughlin M. A., Patel C., Ransom S. M., Seymour A., Stairs I. H., Stappers B. W., van Leeuwen J., Zhu W. W.* A repeating fast radio burst // . III 2016. 531. 202–205.
- Stappers B. W., Caleb M., Driessen L. N.* Fast Radio Transients: From Pulsars to Fast Radio Bursts // Southern Horizons in Time-Domain Astronomy. 339. VIII 2019. 27–32.
- Steele Iain A., Smith Robert J., Rees Paul C., Baker Ian P., Bates S. D., Bode Michael F., Bowman Mark K., Carter Dave, Etherton Jason, Ford Martyn J., Fraser Stephen N., Gomboc A., Lett Robert D. J., Mansfield Anthony G.,*

- Marchant Jonathon M., Medrano-Cerda Gustavo A., Mottram Christopher J., Raback D., Scott A. B., Tomlinson M. D., Zamanov R.* The Liverpool Telescope: performance and first results // *Ground-based Telescopes*. 5489. X 2004. 679–692. (Society of Photo-Optical Instrumentation Engineers (SPIE) Conference Series).
- Stratta G., D’Elia V., Perri M.* GRB090902B: Swift XRT refined analysis. // *GRB Coordinates Network*. I 2009. 9876. 1.
- Strausbaugh Robert, Butler Nathaniel, Lee William H., Troja Eleonora, Watson Alan M.* Evidence for a Bright-edged Jet in the Optical/Near-infrared Afterglow of GRB 160625B // . III 2019. 873, 1. L6.
- Striani E., Tavani M., Piano G., Donnarumma I., Pucella G., Vittorini V., Bulgarelli A., Trois A., Pittori C., Verrecchia F., Costa E., Weisskopf M., Tennant A., Argan A., Barbiellini G., Caraveo P., Cardillo M., Cattaneo P. W., Chen A. W., De Paris G., Del Monte E., Di Cocco G., Evangelista Y., Ferrari A., Feroci M., Fuschino F., Galli M., Gianotti F., Giuliani A., Labanti C., Lapshov I., Lazzarotto F., Longo F., Marisaldi M., Mereghetti S., Morselli A., Pacciani L., Pellizzoni A., Perotti F., Picozza P., Pilia M., Rapisarda M., Rappoldi A., Sabatini S., Soffitta P., Trifoglio M., Vercellone S., Lucarelli F., Santolamazza P., Giommi P.* The Crab Nebula Super-flare in 2011 April: Extremely Fast Particle Acceleration and Gamma-Ray Emission // . XI 2011. 741. L5.
- Sun Hui, Zhang Bing, Li Zhuo.* Extragalactic High-energy Transients: Event Rate Densities and Luminosity Functions // . X 2015. 812, 1. 33.
- Svinkin D., Golenetskii S., Aptekar R., Frederiks D., Oleynik P., Ulanov M., Tsvetkova A., Lysenko A., Kozlova A., Cline T.* Konus-Wind observation of GRB 160625B. // *GRB Coordinates Network*. I 2016. 19604. 1.
- Swenson C. A., Stratta G.* GRB 090902B: Swift/UVOT refined analysis. // *GRB Coordinates Network*. I 2009. 9877. 1.
- Takami H., Kyutoku K., Ioka K.* High-energy radiation from remnants of neutron star binary mergers // . III 2014. 89, 6. 063006.
- Tanvir N. R., Levan A. J., Cenko S. B., Perley D., Cucchiara A., Roth K., Wiersema K., Fruchter A., Laskar T.* GRB 160509A Gemini North redshift. // *GRB Coordinates Network*. I 2016. 19419. 1.
- Tendulkar S. P., Bassa C. G., Cordes J. M., Bower G. C., Law C. J., Chatterjee S., Adams E. A. K., Bogdanov S., Burke-Spolaor S., Butler B. J., Demorest P., Hessels J. W. T., Kaspi V. M., Lazio T. J. W., Maddox N., Marcote B., McLaughlin M. A., Paragi Z., Ransom S. M., Scholz P., Seymour A., Spitler L. G., van Langevelde H. J., Wharton R. S.* The Host Galaxy and Redshift of the Repeating Fast Radio Burst FRB 121102 // . I 2017. 834. L7.

Tendulkar S. P., Kaspi V. M., Patel C. Radio Nondetection of the SGR 1806-20 Giant Flare and Implications for Fast Radio Bursts // . VIII 2016. 827. 59.

Terada Y., Tashiro M., Endo A., Onda K., Sugasahara T., Iwakiri W., Yamaoka K., Sugita S., Ohno M., Suzuki M., Kokubun M., Takahashi T., Nakagawa Y. E., Tamagawa T., Ohmori N., Daikyuji A., Sonoda E., Kono K., Hayashi H., Noda K., Nishioka Y., Yamauchi M., Vasquez N., Urata Y., Hanabata Y., Uehara T., Fukazawa Y., Enoto T., Nakazawa K., Makishima K., Hong S. GRB 090902B: Suzaku WAM observation of the prompt emission. // GRB Coordinates Network. I 2009. 9897. 1.

The CHIME/FRB Collaboration , : , Amiri M., Bandura K., Bhardwaj M., Boubel P., Boyce M. M., Boyle P. J., Brar C., Burhanpurkar M., Cassanelli T., Chawla P., Cliche J. F., Cubranic D., Deng M., Denman N., Dobbs M., Fandino M., Fonseca E., Gaensler B. M., Gilbert A. J., Gill A., Giri U., Good D. C., Halpern M., Hanna D. S., Hill A. S., Hinshaw G., Höfer C., Josephy A., Kaspi V. M., Landecker T. L., Lang D. A., Lin H. H., Masui K. W., Mckinven R., Mena-Parra J., Merryfield M., Michilli D., Milutinovic N., Moatti C., Naidu A., Newburgh L. B., Ng C., Patel C., Pen U. L., Pinsonneault-Marotte T., Pleunis Z., Rafiei-Ravandi M., Rahman M., Ransom S. M., Renard A., Scholz P., Shaw J. R., Siegel S. R., Smith K. M., Stairs I. H., Tendulkar S. P., Tretyakov I., Vanderlinde K., Yadav P. A Second Source of Repeating Fast Radio Bursts // arXiv e-prints. I 2019. arXiv:1901.04525.

The CHIME/FRB Collaboration , : , Amiri Mandana, Andersen Bridget C., Bandura Kevin, Berger Sabrina, Bhardwaj Mohit, Boyce Michelle M., Boyle P. J., Brar Charanjot, Breitman Daniela, Cassanelli Tomas, Chawla Pragya, Chen Tianyue, Cliche J. F., Cook Amanda, Cubranic Davor, Curtin Alice P., Deng Meiling, Dobbs Matt, Fengqiu , Dong , Eadie Gwendolyn, Fandino Mateus, Fonseca Emmanuel, Gaensler B. M., Giri Utkarsh, Good Deborah C., Halpern Mark, Hill Alex S., Hinshaw Gary, Josephy Alexander, Kaczmarek Jane F., Kader Zarif, Kania Joseph W., Kaspi Victoria M., Landecker T. L., Lang Dustin, Leung Calvin, Li Dongzi, Lin Hsiu-Hsien, Masui Kiyoshi W., Mckinven Ryan, Mena-Parra Juan, Merryfield Marcus, Meyers Bradley W., Michilli Daniele, Milutinovic Nikola, Mirhosseini Arash, Münchmeyer Moritz, Naidu Arun, Newburgh Laura, Ng Cherry, Patel Chitrag, Pen Ue-Li, Petroff Emily, Pinsonneault-Marotte Tristan, Pleunis Ziggy, Rafiei-Ravandi Masoud, Rahman Mubdi, Ransom Scott M., Renard Andre, Sanghavi Pranav, Scholz Paul, Shaw J. Richard, Shin Kaitlyn, Siegel Seth R., Sikora Andrew E., Singh Saurabh, Smith Kendrick M., Stairs Ingrid, Tan Chia Min, Tendulkar S. P., Vanderlinde Keith, Wang Haochen, Wulf Dallas, Zwaniga A. V. The First CHIME/FRB Fast Radio Burst Catalog // arXiv e-prints. VI 2021. arXiv:2106.04352.

The Chime/FRB Collaboration B. C. Andersen, Bandura K. M., Bhardwaj M., Bij A., Boyce M. M., Boyle P. J., Brar C., Cassanelli T., Chawla P., Chen T., Cliche J. F., Cook A., Cubranic D., Curtin A. P., Denman N. T., Dobbs

- M., Dong F. Q., Fandino M., Fonseca E., Gaensler B. M., Giri U., Good D. C., Halpern M., Hill A. S., Hinshaw G. F., Höfer C., Josephy A., Kania J. W., Kaspi V. M., Landecker T. L., Leung C., Li D. Z., Lin H. H., Masui K. W., McKinven R., Mena-Parra J., Merryfield M., Meyers B. W., Michilli D., Milutinovic N., Mirhosseini A., Münchmeyer M., Naidu A., Newburgh L. B., Ng C., Patel C., Pen U. L., Pinsonneault-Marotte T., Pleunis Z., Quine B. M., Rafiei-Ravandi M., Rahman M., Ransom S. M., Renard A., Sanghavi P., Scholz P., Shaw J. R., Shin K., Siegel S. R., Singh S., Smegal R. J., Smith K. M., Stairs I. H., Tan C. M., Tendulkar S. P., Tretyakov I., Vanderlinde K., Wang H., Wulf D., Zwaniga A. V.* A bright millisecond-duration radio burst from a Galactic magnetar // . XI 2020. 587, 7832. 54–58.
- Thompson Christopher, Duncan Robert C.* The soft gamma repeaters as very strongly magnetized neutron stars - I. Radiative mechanism for outbursts // . VII 1995. 275, 2. 255–300.
- Thompson Todd A., Chang Philip, Quataert Eliot.* Magnetar Spin-Down, Hyperenergetic Supernovae, and Gamma-Ray Bursts // . Aug 2004. 611. 380–393.
- Thornton D., Stappers B., Bailes M., Barsdell B., Bates S., Bhat N. D. R., Burgay M., Burke-Spolaor S., Champion D. J., Coster P., D’Amico N., Jameson A., Johnston S., Keith M., Kramer M., Levin L., Milia S., Ng C., Possenti A., van Straten W.* A Population of Fast Radio Bursts at Cosmological Distances // Science. VII 2013. 341. 53–56.
- Troja E., Lipunov V. M., Mundell C. G., Butler N. R., Watson A. M., Kobayashi S., Cenko S. B., Marshall F. E., Ricci R., Fruchter A., Wieringa M. H., Gorbovskoy E. S., Kornilov V., Kuttyrev A., Lee W. H., Toy V., Tyurina N. V., Budnev N. M., Buckley D. A. H., González J., Gress O., Horesh A., Panasyuk M. I., Prochaska J. X., Ramirez-Ruiz E., Rebolo Lopez R., Richer M. G., Roman-Zuniga C., Serran-Ricart M., Yurkov V., Gehrels N.* Significant and variable linear polarization during the prompt optical flash of GRB 160625B. // . VII 2017. 547. 425–427.
- Troja E., Piro L., Ryan G., van Eerten H., Ricci R., Wieringa M. H., Lotti S., Sakamoto T., Cenko S. B.* The outflow structure of GW170817 from late-time broad-band observations // . VII 2018. 478, 1. L18–L23.
- Troja E., van Eerten H., Ryan G., Ricci R., Burgess J. M., Wieringa M. H., Piro L., Cenko S. B., Sakamoto T.* A year in the life of GW 170817: the rise and fall of a structured jet from a binary neutron star merger // . X 2019. 489, 2. 1919–1926.
- Troja E., van Eerten H., Zhang B., Ryan G., Piro L., Ricci R., O’Connor B., Wieringa M. H., Cenko S. B., Sakamoto T.* A thousand days after the merger: continued X-ray emission from GW170817 // arXiv e-prints. VI 2020. arXiv:2006.01150.

- Vehtari Aki, Gelman Andrew, Gabry Jonah.* Practical Bayesian model evaluation using leave-one-out cross-validation and WAIC // arXiv e-prints. VII 2015. arXiv:1507.04544.
- Vieyro F. L., Romero G. E., Bosch-Ramon V., Marcote B., del Valle M. V.* A model for the repeating FRB 121102 in the AGN scenario // . Jun 2017. 602. A64.
- Vink Jorick S., de Koter A., Lamers H. J. G. L. M.* Mass-loss predictions for O and B stars as a function of metallicity // . IV 2001. 369. 574–588.
- Vreeswijk P. M., Kann D. A., Heintz K. E., de Ugarte Postigo A., Milvang-Jensen B., Malesani D. B., Covino S., Levan A. J., Pugliese G.* GRB 180720B: VLT/X-shooter redshift. // GRB Coordinates Network. I 2018. 22996. 1.
- Wang Xiang-Yu, Liu Ruo-Yu, Zhang Hai-Ming, Xi Shao-Qiang, Zhang Bing.* Synchrotron Self-Compton Emission from External Shocks as the Origin of the Sub-TeV Emission in GRB 180720B and GRB 190114C // . X 2019. 884, 2. 117.
- Warren Donald C., Barkov Maxim V., Ito Hirotaka, Nagataki Shigehiro, Laskar Tanmoy.* Synchrotron self-absorption in GRB afterglows: the effects of a thermal electron population // . XI 2018. 480, 3. 4060–4068.
- Watanabe Sumio.* Asymptotic Equivalence of Bayes Cross Validation and Widely Applicable Information Criterion in Singular Learning Theory // arXiv e-prints. IV 2010. arXiv:1004.2316.
- Williams P. K. G., Berger E.* No Precise Localization for FRB 150418: Claimed Radio Transient Is AGN Variability // . IV 2016. 821. L22.
- Willingale R., Starling R. L. C., Beardmore A. P., Tanvir N. R., O’Brien P. T.* Calibration of X-ray absorption in our Galaxy // . V 2013. 431, 1. 394–404.
- Woosley S. E.* Gamma-Ray Bursts from Stellar Mass Accretion Disks around Black Holes // . III 1993. 405. 273.
- Woosley S. E., Bloom J. S.* The Supernova Gamma-Ray Burst Connection // . IX 2006. 44, 1. 507–556.
- Woosley S. E., Heger A., Weaver T. A.* The evolution and explosion of massive stars // Reviews of Modern Physics. XI 2002. 74, 4. 1015–1071.
- Woosley S. E., Heger Alexander.* Long Gamma-Ray Transients from Collapsars // . Jun 2012. 752. 32.
- Wu Yiyang, MacFadyen Andrew.* Constraining the Outflow Structure of the Binary Neutron Star Merger Event GW170817/GRB170817A with a Markov Chain Monte Carlo Analysis // . XII 2018. 869, 1. 55.

- Xie Xiaoyi, Zrake Jonathan, MacFadyen Andrew.* Numerical Simulations of the Jet Dynamics and Synchrotron Radiation of Binary Neutron Star Merger Event GW170817/GRB 170817A // . VIII 2018. 863, 1. 58.
- Xu D., Malesani D., Fynbo J. P. U., Tanvir N. R., Levan A. J., Perley D. A.* GRB 160625B: VLT/X-shooter redshift. // GRB Coordinates Network. I 2016. 19600. 1.
- Xu D., de Ugarte Postigo A., Leloudas G., Krühler T., Cano Z., Hjorth J., Malesani D., Fynbo J. P. U., Thöne C. C., Sánchez-Ramírez R., Schulze S., Jakobsson P., Kaper L., Sollerman J., Watson D. J., Cabrera-Lavers A., Cao C., Covino S., Flores H., Geier S., Gorosabel J., Hu S. M., Milvang-Jensen B., Sparre M., Xin L. P., Zhang T. M., Zheng W. K., Zou Y. C.* Discovery of the Broad-lined Type Ic SN 2013cq Associated with the Very Energetic GRB 130427A // . X 2013. 776, 2. 98.
- Yamazaki Ryo, Sato Yuri, Sakamoto Takanori, Serino Motoko.* Less noticeable shallow decay phase in early X-ray afterglows of GeV/TeV-detected gamma-ray bursts // arXiv e-prints. X 2019. arXiv:1910.04097.
- Yang Yuan-Pei, Zhang Bing.* Bunching Coherent Curvature Radiation in Three-dimensional Magnetic Field Geometry: Application to Pulsars and Fast Radio Bursts // . XI 2018. 868, 1. 31.
- Yoshida A., Sakamoto T., Kawakubo Y., Moriyama M., Yamada Y., Yamaoka K., Nakahira S., Takahashi I., Asaoka Y., Ozawa S., Torii S., Shimizu Y., Tamura T., Ishizaki W., Cherry M. L., Ricciarini S., Marrocchesi P. S.* GRB 160509A: CALET Gamma-Ray Burst Monitor detection. // GRB Coordinates Network. I 2016. 19424. 1.
- Zhang B.* A Cosmic Comb Model of Fast Radio Bursts // . II 2017. 836. L32.
- Zhang B. B., Zhang B., Castro-Tirado A. J., Dai Z. G., Tam P. H. T., Wang X. Y., Hu Y. D., Karpov S., Pozanenko A., Zhang F. W., Mazaeva E., Minaeva P., Volnova A., Oates S., Gao H., Wu X. F., Shao L., Tang Q. W., Beskin G., Biryukov A., Bondar S., Ivanov E., Katkova E., Orekhova N., Perkov A., Sasyuk V., Mankiewicz L., Żarnecki A. F., Cwiek A., Opiela R., Zadrożny A., Aptekar R., Frederiks D., Svinkin D., Kusakin A., Inasaridze R., Burhonov O., Rumyantsev V., Klunko E., Moskvitin A., Fatkhullin T., Sokolov V. V., Valeev A. F., Jeong S., Park I. H., Caballero-García M. D., Cunniffe R., Tello J. C., Ferrero P., Pandey S. B., Jelínek M., Peng F. K., Sánchez-Ramírez R., Castellón A.* Transition from fireball to Poynting-flux-dominated outflow in the three-episode GRB 160625B // Nature Astronomy. XI 2018. 2. 69–75.
- Zhang Bin-Bin, van Eerten Hendrik, Burrows David N., Ryan Geoffrey Scott, Evans Philip A., Racusin Judith L., Troja Eleonora, MacFadyen Andrew.* An Analysis of Chandra Deep Follow-up Gamma-Ray Bursts: Implications for Off-axis Jets // . VI 2015. 806, 1. 15.

- Zhang Bing.* A Possible Connection between Fast Radio Bursts and Gamma-Ray Bursts // . Jan 2014. 780. L21.
- Zhang Bing.* Mergers of Charged Black Holes: Gravitational-wave Events, Short Gamma-Ray Bursts, and Fast Radio Bursts // . Aug 2016. 827. L31.
- Zhang Bing.* The physical mechanisms of fast radio bursts // . XI 2020. 587, 7832. 45–53.
- Zhang Bing, Dai Xinyu, Lloyd-Ronning Nicole M., Mészáros Peter.* Quasi-universal Gaussian Jets: A Unified Picture for Gamma-Ray Bursts and X-Ray Flashes // . II 2004. 601, 2. L119–L122.
- Zhang Bing, Fan Y. Z., Dyks Jaroslaw, Kobayashi Shiho, Mészáros Peter, Burrows David N., Nousek John A., Gehrels Neil.* Physical Processes Shaping Gamma-Ray Burst X-Ray Afterglow Light Curves: Theoretical Implications from the Swift X-Ray Telescope Observations // . V 2006. 642, 1. 354–370.
- Zhang Bing, Mészáros Peter.* High-Energy Spectral Components in Gamma-Ray Burst Afterglows // . Sep 2001. 559. 110–122.
- Zhang Bing, Mészáros Peter.* Gamma-Ray Burst Beaming: A Universal Configuration with a Standard Energy Reservoir? // . VI 2002. 571, 2. 876–879.
- Zhang C. F., Jiang J. C., Men Y. P., Wang B. J., Xu H., Xu J. W., Niu C. H., Zhou D. J., Guan X., Han J. L., Jiang P., Lee K. J., Li D., Lin L., Niu J. R., Wang P., Wang Z. L., Xu R. X., Yu W., Zhang B., Zhu W. W.* A highly polarised radio burst detected from SGR 1935+2154 by FAST // The Astronomer’s Telegram. V 2020. 13699. 1.
- Zhou B., Li X., Wang T., Fan Y.-Z., Wei D.-M.* Fast radio bursts as a cosmic probe? // . V 2014. 89, 10. 107303.
- Zwart J. T. L., Barker R. W., Biddulph P., Bly D., Boysen R. C., Brown A. R., Clementson C., Crofts M., Culverhouse T. L., Czeres J., Dace R. J., Davies M. L., D’Alessandro R., Doherty P., Duggan K., Ely J. A., Felvus M., Feroz F., Flynn W., Franzen T. M. O., Geisbüsch J., Génova-Santos R., Grainge K. J. B., Grainger W. F., Hammett D., Hills R. E., Hobson M. P., Holler C. M., Hurley-Walker N., Jilley R., Jones M. E., Kaneko T., Kneissl R., Lancaster K., Lasenby A. N., Marshall P. J., Newton F., Norris O., Northrop I., Odell D. M., Petencin G., Pober J. C., Pooley G. G., Pospieszalski M. W., Quy V., Rodríguez-González C., Saunders R. D. E., Scaife A. M. M., Schofield J., Scott P. F., Shaw C., Shimwell T. W., Smith H., Taylor A. C., Titterington D. J., Velić M., Waldram E. M., West S., Wood B. A., Yassin G., AMI Consortium .* The Arcminute Microkelvin Imager // . XII 2008. 391, 4. 1545–1558.
- de Naurois M.* GRB190829A: Detection of VHE gamma-ray emission with H.E.S.S. // The Astronomer’s Telegram. VIII 2019. 13052. 1.

- de Palma F., Bregeon J., Tajima H.* GRB 090902B: Fermi LAT detection. // GRB Coordinates Network. I 2009. 9867. 1.
- van Eerten H. J.* Simulation and physical model based gamma-ray burst afterglow analysis // Journal of High Energy Astrophysics. IX 2015. 7. 23–34.
- van Eerten Hendrik, Zhang Weiqun, MacFadyen Andrew.* Off-axis Gamma-ray Burst Afterglow Modeling Based on a Two-dimensional Axisymmetric Hydrodynamics Simulation // . X 2010. 722, 1. 235–247.
- van Eerten Hendrik, van der Horst Alexander, MacFadyen Andrew.* Gamma-Ray Burst Afterglow Broadband Fitting Based Directly on Hydrodynamics Simulations // . IV 2012. 749, 1. 44.
- van Eerten Hendrik J., MacFadyen Andrew I.* Gamma-Ray Burst Afterglow Scaling Relations for the Full Blast Wave Evolution // . III 2012. 747, 2. L30.
- van der Horst A. J., Kamble A. P., Wijers R. A. M. J., Kouveliotou C.* GRB 090902B: WSRT radio observation. // GRB Coordinates Network. I 2009. 9883. 1.
- von Kienlin A., Meegan C. A., Paciesas W. S., Bhat P. N., Bissaldi E., Briggs M. S., Burns E., Cleveland W. H., Gibby M. H., Giles M. M., Goldstein A., Hamburg R., Hui C. M., Kocevski D., Mailyan B., Malacaria C., Poolakkil S., Preece R. D., Roberts O. J., Veres P., Wilson-Hodge C. A.* The 4th Fermi-GBM Gamma-Ray Burst Catalog: A Decade of Data // arXiv e-prints. II 2020. arXiv:2002.11460.